Experimental Characterization of Electrical Discharges and Formation of the Ignition Kernel. Application to the Study of Performances of Aeronautical Igniters

Carlos Javier Benito Parejo

To cite this version:

Carlos Javier Benito Parejo. Experimental Characterization of Electrical Discharges and Formation of the Ignition Kernel. Application to the Study of Performances of Aeronautical Igniters. Other. ISAE-ENSMA Ecole Nationale Supérieure de Mécanique et d'Aérotechique - Poitiers, 2019. English. NNT : 2019ESMA0021 . tel-02860055

HAL Id: tel-02860055
https://theses.hal.science/tel-02860055v1

Submitted on 8 Jun 2020

THÈSE

POUR L'OBTENTION DU GRADE DE

DOCTEUR DE L'ÉCOLE NATIONALE SUPERIEURE DE MECANIQUE ET D'AEROTECHNIQUE

(DIPLOME NATIONAL – ARRETE DU 25 MAI 2016)

ECOLE DOCTORALE :
SCIENCES ET INGENIERIE EN MATERIAUX, MECANIQUE, ÉNERGETIQUE ET AERONAUTIQUE
SECTEUR DE RECHERCHE : ÉNERGETIQUE, THERMIQUE, COMBUSTION

PRÉSENTÉE PAR :

Carlos Javier BENITO PAREJO

Experimental characterization of electrical discharges and formation of the ignition kernel. Application to the study of performances of aeronautical igniters.

DIRECTEUR DE THESE : JULIEN SOTTON
CO-ENCADRANT : CAMILLE STROZZI

SOUTENANCE PREVUE LE 28 OCTOBRE 2019
DEVANT LA COMMISSION D'EXAMEN

JURY

PRESIDENT		
M. Philippe GILLARD	Professeur des Universités	Université d'Orléans
RAPPORTEURS		
M. Bruno RENOU	Professeur des Universités	INSA Rouen
M. Carlo Nazareno GRIMALDI	Full Professor	Université de Pérouse
MEMBRES DU JURY		
M. Bénédicte CUENOT	Chercheuse Sénior	CERFACS
M. Gabriele DISCEPOLI	Assistant Professor	Université de Pérouse
M. Marc BELLENOUE	Professeur des Universités	ISAE-ENSMA Poitiers
M. Julien SOTTON	Professeur des Universités	ISAE-ENSMA Poitiers
M. Camille STROZZI	Maître de Conférences	Université de Poitiers

Acknowledgments

This thesis has been a very enriching experience and a great challenge. Anyone who has gone through difficult challenges will understand the difficulty of expressing on paper the genuine gratitude felt towards the people who supported them. This is not, therefore, a payment for their generosity, but a sincere tribute to record, even in a few words, that they did not go unnoticed in my life. As I write these lines, I remain fully aware of the times when I could never have completed this work without them.

First and foremost, I would like to thank the research team. I have been very fortunate to work in the best research team that I know of: professor Julien Sotton, professor Marc Bellenoue, and doctor Camille Strozzi. Their guidance, support and the great atmosphere that reigns in the combustion team have helped enormously to the outcome of this work. Thanks to them I have learned a lot, both as a researcher and as a person.

I want to thank the members of the jury: professor Philippe Gillard for presiding the jury; professor Bruno Renou and professor Carlo Grimaldi for reviewing the dissertation; and doctor Bénédicte Cuenot and doctor Gabriele Discepoli for being part of the jury of this thesis.

I am also grateful to colleagues at the laboratory, who have greatly facilitated the realization of this project, both on a logistical and a personal level: Alain Claverie, Hervé Doreau, Nicolas Papin, Jean Carl Rousseau, Jean-Christophe Jouvanneau, Yann Thomas, Vincent Montassier and Maxime Caron. I want to thank laboratory and university staff, who helped in so many things during these years, being always available and with a smile: Marie-Cannelle Eysseric, Jocelyne Bardeau, Catherine Lavallade, Audrey Veron, Cécile Boye, Bénedicte Cuenot et Céline Portron.

One of the things that added to this experience was the great atmosphere I found in the establishment, thanks to others from PhD, postdocs, thanks to Moez, Allassane, Clément and Stéphane, Maxime, Anthony, Geoffrey, Paul, Luc, Saïd, Cyprien for so many years shared in this beautiful journey. Thank to closer companions with whom I worked side by side, Quentin, Hugo and Nicolas. Special mention to Romain, Geoffrey and André, for the great time we had both in the routine and in special occasions.

Finally, I thank my family and friends. Thank to my closest friends who have always been there no matter the physical distance between us. My siblings, who have accompanied me in so many moments. And I thank my parents, for without their continuous sacrifice and support I would not have had the chances nor the aptitudes to engage and fulfill this great project.

Abstract

Spark ignition systems are generally defined by the electrical energy input used to operate them. However, the physical characteristic that directly affects the ignition process is the energy deposit supplied to the fluid by the system. This work focuses on the development of two proposed methodologies for the characterization of the thermal energy deposit of electrical discharges produced by different ignition systems, and their implementation through a parametric study. An experimental device is developed for this purpose, using simultaneously a non-optical technique, constant volume calorimetry, and an optical technique, SBOS (Speckle-based Background-Oriented Schlieren). The experimental techniques are first validated in a reference configuration: a pair of pin-to-pin electrodes with an automobile-type inductive ignition system.

Constant volume calorimetry measures a thermal energy deposit supplied to the fluid via the pressure rise inside a reduced volume chamber. The ratio between thermal energy deposit and electrical energy supply represents the efficiency of energy transfer, which is between 15 and 40% for the reference configuration. Energy deposit and efficiency are higher as pressure and inter-electrode gap increase. Tests with an inert propane-nitrogen mixture show that energy deposit is greater in the presence of fuel than in clean air.

SBOS is an optical method that quantifies changes in the optical index generated by the phenomenon under study. This technique is adapted in this work to the spatial and temporal specificity of an electrical discharge. Image-processing procedure is developed to obtain density, temperature and local energy fields at the time of image acquisition. The volume of the hot kernel produced by the plasma and the energy deposit are deduced from it. These properties are measured at different times during the evolution of the kernel. Temperatures in the hot kernel reach higher values (up to 1400 K) at longer inter-electrode gaps and higher pressures, or in the presence of gaseous fuel. Energy deposit measurements performed by SBOS are in good agreement with calorimetry results.

Finally, both methodologies are adapted to the study of different ignition systems. Two igniters were tested: an innovative multi-filament radiofrequency discharge igniter and a capacitive helicopter engine igniter. For the latter, the energy deposit is measured for different initial pressures and gas mixtures to simulate the actual engine conditions. In standard conditions, the electrical energy input is 2 J, the electrical energy measured at the electrodes is 625 mJ and finally the thermal energy deposited in the gas is about 85 mJ. The estimated efficiency of 14% is not very pressure dependent. The SBOS technique is used to estimate the temperature in the hot kernel at the first moments of discharge (around 3700 K) and the thermal energy deposit, which is in good agreement with the calorimetric measurement.

Keywords: Aeronautics, Ignition, Calorimetry, Electric discharges, Energy transfer, Motors--Combustion, Speckle-Based Background-Oriented Schlieren (SBOS).

Résumé

Les systèmes d'allumage par étincelle sont généralement définis par l'énergie électrique utilisée pour leur fonctionnement. Cependant, la caractéristique physique qui affecte directement le processus d'allumage est l'énergie déposée dans le fluide par le système. Ce travail porte sur le développement de deux méthodologies proposées pour la caractérisation du dépôt d’énergie thermique de décharges produites par différents systèmes d’allumage et de leur mise en œuvre au travers d’une étude paramétrique. Un dispositif expérimental est mis au point afin de développer et mettre en œuvre simultanément une technique optique et une non optique. Les méthodes sont validées d’abord dans une configuration de référence d’un allumeur inductif alimentant une paire d’électrodes pointe-pointe.

La calorimétrie à volume constant mesure un dépôt d'énergie thermique fournie au fluide par l’analyse de la montée en pression à l'intérieur d'une chambre de petit volume. Le rapport entre le dépôt d'énergie thermique et l'apport d'énergie électrique représente l'efficacité du transfert d'énergie, qui est comprise entre 15 et 40% pour la configuration de référence. Le dépôt d'énergie et l'efficacité du transfert d’énergie sont plus élevés à mesure que la pression et l'écart inter-électrode augmentent. Des essais avec un mélange inerte azote-propane montrent que le dépôt d'énergie est plus important en présence de carburant que dans l'air pur.

La SBOS (Speckle-based Background-Oriented Schlieren) est une méthode optique permettant de quantifier les variations d’indice optique générés par le phénomène étudié. Cette technique est ici adaptée aux contraintes d’échelles spatiale et temporelle d’une décharge électrique. Une procédure de traitement a été développée afin d’obtenir les champs de masse volumique, de température et l'énergie locale au moment de l'acquisition de l'image. Le volume du noyau chaud produit par le plasma et le dépôt d'énergie en sont déduits. Ces propriétés sont mesurées à différents instants de l'évolution du noyau. Dans la configuration de référence, les températures dans le noyau chaud atteignent des valeurs plus élevées (jusqu’à 1400 K) pour des distances inter-électrodes et des pressions plus élevées ou en présence de carburant. Des mesures simultanées de dépôt d’énergie par SBOS et calorimétrie montrent un très bon accord.

Enfin, les deux méthodologies sont adaptées à l'étude de différents systèmes d'allumage. Ainsi, deux allumeurs ont été testés, un allumeur à décharge radiofréquence multi filamentaires innovant et un allumeur capacitif typique d’un moteur d’hélicoptère. Pour ce dernier, le dépôt d'énergie est mesuré pour différentes pressions initiales et mélanges gazeux afin de simuler les conditions réelles du moteur. Dans des conditions standard, l’énergie électrique est de 2 J, l’énergie électrique mesurée aux électrodes de 625 mJ et enfin l’énergie thermique déposée dans le gaz de l’ordre de 85 mJ. Le rendement du 14% semble peu dépendant des conditions thermodynamiques du mélanges. La technique SBOS est utilisée pour estimer la température dans le noyau chaud aux premiers instants de la décharge (jusqu’á 3700 K) et le dépôt d’énergie thermique qui est en bon accord avec la mesure calorimétrique.

Mots-clés : Aéronautique, Allumage, Calorimétrie, Décharges électriques, Transfert d’énergie, Moteurs--Combustion, Speckle-Based Background-Oriented Schlieren (SBOS).

Resumen

Los sistemas de ignición por chispa se definen generalmente por la energía eléctrica utilizada para su funcionamiento. Sin embargo, la característica física que afecta directamente al proceso de ignición es la energía depositada en el fluido por el sistema. Este estudio se centra en el desarrollo de dos metodologías (calorimetría y SBOS) propuestas para la caracterización de la energía térmica depositada por descargas eléctricas, producidas por diferentes sistemas de ignición, y su aplicación mediante un estudio paramétrico. Se describeel desarrollo de un dispositivo experimental para emplear simultáneamente una técnica óptica y otra no óptica. Los métodos se validan primero en una configuración de referencia de un sistema inductivo que suministra un par de electrodos punta-punta.

La calorimetría a volumen constante mide un depósito de energía térmica suministrado al fluido, analizando el aumento de presión dentro de una cámara de volumen reducido. La relación entre la energía térmica depositada y el suministro de energía eléctrica representa la eficiencia de la transferencia de energía, que se encuentra entre el 15% y el 40% para la configuración de referencia. El depósito de energía y la eficiencia son mayores a medida que aumenta la presión y el espacio entre electrodos. Ensayos con una mezcla inerte de propano-nitrógeno muestran que el depósito de energía es mayor en presencia de combustible que en aire puro.

La SBOS (Speckle-based Background-Oriented Schlieren) es una técnica óptica que cuantifica los cambios en el índice de refracción generados por el fenómeno de estudio. Esta técnica se ha adaptado específicamente a la distribución espacial y temporal de una descarga eléctrica. Además, se ha desarrollado un post-tratamiento de imágenes para obtener la densidad, la temperatura y los campos de energía locales en el instante de la adquisición de la imagen. Del post-tratamiento se deduce el volumen del núcleo caliente producido por el plasma y la energía depositada, propiedades que son medidas en distintos momentos de la evolución del núcleo. Las temperaturas en el núcleo caliente alcanzan valores más altos (hasta 1400 K) a mayor espacio entre electrodos y presiones más altas, o en presencia de combustible gaseoso. Mediciones simultaneas de la energía depositada por SBOS y por calorimetría son consistentes.

Finalmente, ambas metodologías son adaptadas al estudio de diferentes sistemas de ignición. Se han probado dos bugías: un innovador sistema de descarga de radiofrecuencia multifilamento y un sistema capacitivo típico de un motor de helicóptero. En el caso de este último, se mide el depósito de energía para diferentes presiones iniciales y mezclas de gases para simular las condiciones reales del motor. En condiciones estándar, la energía eléctrica de entrada es de 2 J, la energía eléctrica medida en los electrodos es de 625 mJ y, finalmente, la energía térmica depositada en el gas es de unos 85 mJ. La eficiencia, el 14%, no depende mucho de las condiciones termodinámicas de la mezcla. La técnica SBOS se ha utilizado para estimar la temperatura en el núcleo caliente en los primeros momentos de descarga (alrededor de 3700 K) y la energía térmica depositada, que es consistente con la medición calorimétrica.

Palabras clave: Aeronáutica, Ignición, Calorimetría, Descargas eléctricas, Transferencia de energía, Motores—Combustión, Speckle-Based Background-Oriented Schlieren (SBOS).

Contents

List of Figures

List of Tables

Bilan de thèse (français)

Introduction

L'allumage est un point critique dans la conception des moteurs d'avion. En effet, le processus d'allumage d'une moteur aéronautique doit pouvoir s'effectuer dans une large gamme de conditions aérodynamiques et thermodynamiques (allumage au sol, rallumage en vol...) et de préférence dans les délais les plus courts possibles.

La fonction du système d'allumage est de générer le noyau initial et de l'aider à survivre le plus longtemps possible grâce à une énergie transmise au fluide la plus élevée possible. Les systèmes actuellement utilisés sont basés sur une bougie d'allumage à arc électrique placée dans la paroi de la chambre de combustion à proximité d'un injecteur de carburant. Ce type d'allumeur à haute énergie produit donc une décharge de surface durant quelques centaines de microsecondes, assurant ainsi la génération d'un plasma à très haute température (plusieurs dizaines de milliers de Kelvins). La diffusion des espèces intermédiaires produites et la haute température générée permettent le déclenchement des réactions chimiques de combustion, formant un noyau d'allumage. Le noyau d’allumage est plus ou moins résistant à la dissipation turbulente permettant ou non sa survie et sa propagation. Ce processus, qui a lieu dans la paroi proche de la chambre de combustion, nécessite que le combustible soit dirigé dans sa direction.

Les systèmes d'allumage par étincelle sont généralement décrits par l'énergie électrique utilisée pour les faire fonctionner. Cependant, la caractéristique physique qui affecte directement le processus d'allumage est le dépôt d'énergie fourni au fluide par le système. Le dépôt d'énergie dans le fluide n'est qu'une partie de l'énergie électrique fournie. Le reste de l'énergie est perdu, dissipé pendant le stockage et l’adaptation de l’énergie électrique dans système d’allumage et pendant le transfert d’énergie depuis l’énergie électrique fournie aux électrodes à l’énergie thermique fournie au fluide. Le dépôt d'énergie thermique fourni au fluide n'est pas simple à estimer, et sa mesure nécessite des techniques expérimentales spécifiques de calorimétrie.

Le dépôt d'énergie thermique et d'autres effets liés à l'allumage par décharges électrique ont été étudiés dans des configurations académiques et, dans une moindre mesure, dans des applications automobiles. Cependant, peu d'informations ont été publiées sur les caractéristiques des décharges électriques dans les applications des moteurs à turbine à gaz. Une meilleure compréhension de la décharge électrique et du dépôt d'énergie produits par les systèmes d'allumage aéronautiques est donc nécessaire pour assurer un allumage correct, et représente donc une connaissance essentielle pour la simulation de la combustion et pour la conception de nouveaux moteurs.

Ce travail se concentre sur le développement de méthodologies proposées pour la caractérisation du dépôt d'énergie thermique des décharges électriques. Une étude paramétrique originale est ensuite menée pour différents systèmes d'allumage. Les techniques expérimentales sont d'abord appliquées à l'étude des décharges électriques produites par une configuration de référence en conditions de repos, à différents mélanges de gaz inertes et à différentes pressions. Les méthodologies développées sont ensuite appliquées à la fois à un système d'allumage radiofréquence et à un allumeur d'hélicoptère. Ces travaux de thèse ont été réalisés à l'Institut Pprime et financés par la région Nouvelle Aquitaine, et ont collaboré avec le projet de recherche industrielle CAPA et les programmes de recherche Radiµs.

Objectives de l'étude

Le but principal de cette investigation est de développer une méthodologie pour caractériser les décharges électriques et les systèmes d'allumage. Pour ce faire, différentes propriétés des décharges électriques doivent être mesurées avec précision :

- Le courant et la tension électrique, la durée de la décharge et l'énergie électrique fournie aux électrodes.

- Dépôt d'énergie délivré au fluide par une décharge électrique.

- Distribution spatiale des propriétés du gaz à la décharge : évolution du noyau de la décharge dans le temps, y compris le volume et les propriétés du noyau (champs de température et de masse volumique).

Les techniques de mesure devraient être adaptées ou mises au point pour cette tâche et validées sur une configuration de référence, comme les électrodes pin-pin. L'influence des conditions extérieures sur ces propriétés devrait aussi être étudiée. Enfin, l'objectif est d'adapter les méthodologies développées à différents systèmes d'allumage, y compris un allumeur d'avion, afin de mieux comprendre leurs performances et leur comportement.

I. Décharges électriques et allumage par étincelle : théorie et littérature

Dans ce chapitre, nous présentons les bases de l'étude des décharges électriques dans l'allumage par étincelle.

Dans une première partie, la théorie des décharges électriques est brièvement expliquée, décrivant la décharge de plasma chaud et comment elle produit l'allumage [2-19]. Le type de décharge électrique le plus utilisée pour l'allumage est la décharge de plasma en équilibre, produite en augmentant la tension électrique DC entre les bornes d'une paire d'électrodes. Lorsque la tension électrique augmente, le champ électrique dans l'espace inter-électrodes augmente pareillement. Quand la tension atteint la valeur de claquage pour les conditions de gaz, le gaz dans l'espace est ionisé et un canal conducteur se forme. L'énergie électrique stockée dans l'espace inter-électrodes se décharge alors dans la phase de claquage, et si le circuit électrique connecté aux électrodes a plus d'énergie stockée, cette énergie stockée se décharge dans les phases d'arc et de glow suivantes. L'énergie électrique est alors transformée en énergie thermique au niveau du noyau chaud de la décharge, produisant également des espèces ionisées de molécules de gaz qui amorcent et favorisent la combustion.

Les systèmes d'allumage des automobiles commerciales utilisent soit une capacité électrique (systèmes CDI) soit une bobine (systèmes TCI) pour produire des décharges électriques, tandis que les allumeurs de moteurs à turbine à gaz sont constitués d'un système capacitif à haute énergie et d'une bougie coaxiale. D'autres systèmes d'allumage, actuellement en phase finale de développement, utilisent des plasmas hors équilibre ou un laser pour l'allumage [20-36].

Dans une seconde partie, une revue bibliographique non exhaustive donne une idée de l'état de l'art en matière d'allumage par étincelle. Elle présente des études portant sur l'effet des décharges électriques sur l'allumage et sur la façon dont les décharges sont caractérisées pour la combustion [37-46]. Cette partie présente aussi des modèles d'allumage par étincelle avec les principales caractéristiques de décharge dont ils ont besoin en entrée et leurs principaux résultats [47-63]. Des études expérimentales sur les décharges électriques et l'allumage par étincelle sont également passées en revue, notamment la métrologie utilisée pour la détermination du dépôt d'énergie [64-74], les méthodes de visualisation pour étudier le noyau de décharge et la formation de la flamme [75-89], et les essais sur les systèmes d'allumage [19, 64, 90-99].

Enfin, nous présentons la conclusion du chapitre et la motivation de ce travail de thèse en rapport avec l'état de l'art : Les décharges électriques pour l'allumage par étincelle ont été largement étudiées. Pourtant, dans de nombreuses études d'allumage, l'énergie de l'étincelle est caractérisée comme étant l'énergie électrique fournie aux électrodes (E_{el}) ou l'énergie stockée dans le condensateur du circuit électrique (E_c), au lieu de l'énergie délivrée au fluide par la décharge. Ce dépôt d'énergie est estimé comme l'augmentation de l'énergie thermique dans le gaz (E_{th}), et n'a fait l'objet que de quelques études. Pour la modélisation de la décharge électrique et de l'allumage, le dépôt d'énergie thermique est nécessaire pour démarrer les simulations ou vérifier les résultats, ainsi que l'évolution spatiale précoce du noyau. Le transfert d'énergie est produit différemment dans les différentes phases de décharge, avec peu d'études qui ont mesuré les efficacités d'arc et de glow.

Bien que de nombreux travaux publiés sur les décharges électriques caractérisent les propriétés de la décharge, l'évolution du noyau et - dans une moindre mesure - le transfert d'énergie de l'alimentation électrique au dépôt thermique, les travaux expérimentaux sur les systèmes d'allumage disponibles étudient rarement de façon simultanée le dépôt d'énergie thermique et l'évolution du noyau. Il y a aussi un vrai manque d'études qui portent sur les caractéristiques des décharges produites par les systèmes d'allumage aéronautiques. Les auteurs ont trouvé qu'une méthodologie capable de caractériser complètement les décharges électriques et la formation du noyau de la décharge est souhaitable pour l'étude des systèmes d'allumage, notamment pour les systèmes aéronautiques et des systèmes innovants.

II. Matériaux et montage expérimental

Ce chapitre décrit les systèmes d'allumage et ses décharges électriques étudiées dans cette thèse et le choix des méthodes expérimentales, des matériaux et des montages.

Dans un premier temps, ce chapitre présent les systèmes d'allumage et ses décharges électriques. Pour la génération d'une décharge électrique un système d'allumage trois éléments basiques sont requis : une bougie, une source d'alimentation et un circuit électronique capable de fournir à la bougie l'énergie nécessaire dans les conditions correctes pour produire la décharge. Pour notre étude on a utilisé trois systèmes différents, qui sont décrits en détail dans ce chapitre :

Le premier système produit une décharge académique canonique pour l'étude des décharges électriques, qui permet donc de valider les méthodes expérimentales. Il s'agit d'une bobine-crayon (circuit inductive TCI) avec une paire d'électrodes pointe-pointe, produisant une décharge avec une énergie électrique associée de l'ordre de 50 mJ dans un temps caractéristique de 3 ms. Le deuxième système est un allumeur d'hélicoptère standard, qui se compose d'une bougie cylindrique coaxiale, un circuit électrique capacitif. La décharge produite par l'allumeur d'hélicoptère a une énergie électrique de l'ordre de 700 mJ et une durée de quelques 100 µs. Le troisième système est un allumeur à radiofréquence qui produit une décharge à plasma froid. Cet allumeur utilise une bougie avec un seul électrode avec courant et tension électriques changeant de polarisation avec une fréquence ~5 MHz. L'énergie électrique fournie à la bougie par le système électrique peut être régulé avec une large plage d'énergies et durées de décharge, avec une valeur typique de 70 mJ pour une décharge de 200 µs.

Ensuite, la deuxième partie du chapitre introduit les méthodes expérimentales utilisées pour étudier les décharges et le dimensionnement du montage expérimental. La décharge électrique est caractérisée principalement par comparaison de l'énergie électrique fournie aux électrodes avec le dépôt d'énergie thermique dans le fluide. L'énergie électrique (E_{el}) fournie à la bougie est mesurée à partir des mesures des sondes de tension et courant électriques. Le dépôt d'énergie thermique (E_{th}) est mesuré par calorimétrie à volume constant : à partir de la mesure de la montée de pression pendant et après la décharge dans une chambre à volume constant. Au même temps une technique optique, la Speckle-based Background-Oriented Schlieren (SBOS), permet de caractériser l'effet des décharges électriques sur le gaz en mesurant quantitativement la masse volumique et la température du fluide à différents instants de la décharge. Le choix d'un équipement de mesure approprié et le dimensionnement du dispositif expérimental sont justifiés par les conditions requises pour optimiser les mesures par les méthodes expérimentales décrites.

Enfin, la troisième partie du chapitre décrit les sondes de mesure, les chambres expérimentales et les différentes configurations du montage. Le dispositif expérimental se compose d'une chambre d'essai qui loge les électrodes et un transducteur de pression différentielle piézo-résistif. Différentes chambres d'essai sont disponibles, avec un volume intérieur de 6 ou 20 ml, afin de réduire les incertitudes de mesure pour les décharges à basse ou haute énergie. La chambre d'essai est placée dedans une chambre plus grande qui sert de pression de référence, avec un plus grand volume intérieur (0,64 L). Les deux chambres sont reliées par une vanne de dérivation, qui reste ouverte pour changer la pression ou le gaz pour les expériences et fermée pendant les essais. Des sondes électriques mesurent la tension et le courant aux électrodes. Le système a un accès optique par des fenêtres situées sur les côtés des deux chambres, ce qui permet de mettre en œuvre la méthode SBOS simultanément aux mesures de calorimétrie en pression. L'installation comprend une série d'objectifs, un diaphragme et une caméra CCD intensifiée ; placés à différentes distances pour régler le grandissement optique du système, la taille des taches du motif de fond et la distance de défocalisation. Le motif du fond subjectif est généré par l'interaction d'un faisceau laser collimaté provenant d'un laser continu pompé par diode, d'un verre dépoli, des lentilles et du capteur de la caméra.

III. Calorimétrie des décharges électriques pour les électrodes pin-pin

Dans ce chapitre, la calorimétrie à volume constant est appliquée à l'étude des décharges électriques sur une configuration de référence académique.

Un système calorimétrique à volume constant est développé pour caractériser le dépôt d'énergie des décharges électriques. Un allumeur standard à bobine de crayon TCI avec des électrodes pin-pin est utilisé. Pendant la décharge, l'énergie électrique est surveillée à partir des signaux électriques mesurés aux électrodes. Le dépôt d'énergie dans le fluide est estimé à partir de l'augmentation transitoire de la pression dans la chambre à volume constant de 6 ml, mesurée avec un capteur piézo-résistif. Les incertitudes de mesure sont inférieures à 15% pour E_{th} et inférieures à 4,1% pour E_{el}.

L'application de la calorimétrie dans notre dispositif expérimental s'appuie sur plusieurs hypothèses, liées à l'influence du noyau chaud sur les décharges ultérieures, la durée de l'effet de l'onde de choc et la surface de contact des électrodes avec le noyau chaud. Les hypothèses de la méthode sont vérifiées en utilisant la strioscopie : volume de plasma négligeable par rapport au volume total de gaz, coefficient de capacité thermique constant et pertes de chaleur négligeables à travers des parois. Également, les pertes de chaleur après la fin de la décharge sont estimées par calorimétrie à partir de la chute de pression.

Les effets des paramètres de contrôle E_{el} et de l'écart inter-électrodes sur la décharge électrique sont étudiés dans l'air dans des conditions atmosphériques (1 bar et 293 K). L'énergie électrique E_{el} est contrôlée par le temps de charge de la bobine TCI. Le temps de charge de la bobine varie de 0,5 à 5 ms, avec une saturation du TCI à 3,5 ms et aucun changement pour les temps de charge plus longs que le temps de saturation. E_{el} augmente avec le temps de charge de 6 à 42 mJ, et E_{th} augmente également de 2 à 10 mJ. Le rapport E_{th}/E_{el}, qui est l'efficacité du transfert d'énergie η, diminue pour de temps de charge, passant de 34% à 25%. Les premiers résultats sont cohérents avec ceux d'autres études et valident la technique calorimétrique pour notre montage expérimental.

L'écart entre les électrodes affecte énormément le transfert d'énergie, car plus l'écart est long, plus il y a de molécules de gaz entre les électrodes et la tension de claquage augmente. Les valeurs de l'E_{el} et de l'E_{th} augmentent avec l'augmentation de l'écart : de 37 et 7,5 mJ respectivement pour 1 mm d'écart à 45 et 15 mJ pour 3 mm d'écart ; en moyenne. L'efficacité du transfert d'énergie η augmente également avec l'écart, passant de 19 % à 1 mm d'écart à 33 % à 3 mm. L'analyse des phases de la décharge montre que pour une plus grande distance d'écart, il y a une plus grande portion de l'énergie transférée en phase d'arc et moins en phase de glow. Ceci affecte l'efficacité globale de la décharge, ainsi que la diminution des pertes d'énergie avec l'augmentation de l'écart comme le montrent des images simultanées de strioscopie. Les efficacités pour chaque phase de décharge sont estimées pour différentes distances d'écart, avec η_{arc} et η_{glow} de 55 % et 25 % respectivement pour un écart de 2 mm.

Les valeurs d'énergie électrique présentent une dispersion importante pour les mêmes conditions expérimentales, alors que le dépôt d'énergie thermique reste le même avec peu de variation.

Les effets de la pression et de la composition du gaz sur la décharge sont également étudiés. Des essais sont effectués à 0,5, 1, 1,5 et 2 bar ; dans l'air et dans deux mélanges inertes azote-propane avec différentes concentrations de propane. La pression affecte la décharge de la même manière que l'écartement : pour une pression initiale plus élevée, E_{th} et η augmentent et une plus grande partie de la décharge se produisait en mode arc. L'énergie de claquage est également plus élevée pour une pression plus élevée. En présence de carburant, la même tendance est observée avec la pression. La proportion de la phase d'arc de la décharge totale augmente en présence de combustible, avec plus de 80% d'E_{el} correspondant à la phase d'arc à des pressions plus élevées et des mélanges de propane, alors que cette valeur est inférieure à 60% dans l'air.

La contribution des différentes phases de la décharge à la valeur du dépôt d'énergie transférée et l'efficacité de la décharge correspondante sont analysées pour la première fois par calorimétrie. Ces résultats permettent de mieux comprendre la nature de la diffusion des résultats expérimentaux : pour une plus longue durée de décharge, il y a plus d'énergie fournie en mode glow, et l'efficacité totale est donc plus faible. Les changements de la quantité d'énergie électrique fournie dans chaque phase de la décharge, c'est-à-dire un rapport arc/glow plus élevé, n'affectent que l'efficacité du transfert et non le dépôt d'énergie dans le fluide. L'efficacité des différentes phases de la décharge est également affectée par les conditions expérimentales (écart, pression, composition du gaz), ce qu'il faut tenir en compte lors de la modélisation des décharges électriques ou des systèmes d'allumage dans différentes conditions.

Le dépôt d'énergie devrait être utilisé comme l'énergie caractéristique d'un système d'allumage, au lieu de l'énergie électrique qu'il utilise, car il serait plus précis et utile pour les applications liées au fluide comme l'allumage, la combustion ou la dynamique des fluides. Les effets de l'écartement entre les électrodes, de la pression et de la composition du gaz modifient le dépôt d'énergie et l'efficacité du transfert d'énergie et sont étudiés dans ce chapitre.

IV. Calorimétrie optique de décharges électriques utilisant la SBOS

Ce chapitre décrit le développement de la technique SBOS (Speckle-based Background Oriented Schlieren) pour son application aux décharges électriques produites par une paire d'électrodes pin-pin, et les mesures de la distribution spatiale instantanée des propriétés du gaz dans le noyau de décharge dans différentes conditions.

La technique BOS est basée sur la dépendance de la masse volumique du gaz à l'indice de réfraction, comme donné par la relation Gladstone-Dale pour les gaz. Les points d'un motif de fond se déplacent lorsqu'il y a des gradients de masse volumique entre le fond et la caméra de l'observateur. Le déplacement des points du motif est observé si le phénomène produisant le gradient de masse volumique se trouve à une distance de défocalisation éloignée du plan focal. Le déplacement est calculé par une corrélation croisée multi-étape entre une image de référence du motif de fond et une image lors d'un phénomène impliquant des gradients de masse volumique. Dans la SBOS, l'utilisation d'un motif de fond moucheté généré par laser améliore la résolution, en particulier dans les applications avec tailles caractéristiques réduites, comme les décharges électriques.

La technique et le traitement d'images sont développés pour les décharges électriques : le patron de fond moucheté est généré par l'interaction entre un laser, un verre dépoli, le diaphragme du système optique et le capteur de la caméra. Le montage est configuré pour obtenir un patron de fond moucheté avec la bonne taille moyenne des taches du motif. Ensuite deux images sont prises, une image de référence et l'image d'essai au délai de temps souhaité après le début de la décharge. L'image du motif de fond de référence est comparée à l'image du motif perturbé par la décharge par corrélation croisée, ce qui donne le champ de déplacement des points du motif. Le champ de déplacement est intégré, en résolvant une équation de Poisson, pour obtenir la masse volumique intégrée le long de la ligne de vue. Pour les champs axisymétriques, une rétroprojection filtrée permet d'obtenir le champ de masse volumique. Avec un comportement semi-idéal du gaz, le champ de température est obtenu directement à partir du champ de masse volumique, puis la distribution locale de l'enthalpie est évaluée. La taille du noyau chaud de la décharge, en particulier son rayon maximum et son volume, est estimée à partir du champ de température. Enfin, l'intégrale volumique de la distribution d'enthalpie donne le dépôt d'énergie, calculé comme l'augmentation de l'enthalpie totale par rapport aux conditions initiales.

La méthodologie est d'abord validée pour un cas de référence : un jet de CO_2 de même taille et avec des gradients de masse volumique absolus identiques à ceux attendus dans les décharges électriques. Un ensemble de 100 tests est réalisé sur le jet, permettant d'obtenir les champs de déplacement et les distributions de masse volumique. Comme au centre du jet la masse volumique doit être celle du CO_2, les résultats sont comparés à cette valeur. L'analyse de l'influence des différents paramètres et des incertitudes de mesure, ainsi qu'une moyenne temporelle des résultats, donnent une incertitude de 6,2% pour la distribution de la température et de la masse volumique. L'incertitude du dépôt d'énergie obtenu par SBOS (E_{BOS}) était de l'ordre de ~12%.

La technique SBOS est ensuite appliquée aux décharges électriques. Des essais en conditions atmosphériques (dans l'air à 1 bar) montrent que pour un écart inter-électrodes plus important, la température du noyau à la fin de la décharge est plus élevée, puisqu'elle atteignait 900 K pour un écart de 2 mm et 750 K pour un écart de 1 mm. Également la taille du noyau est plus grande pour. L'évolution du noyau de la décharge est également étudiée, avec une série d'essais dès 0,5 à 2,5 ms de délai (temps après le début de la décharge), pour un écart de 2 mm. La température du noyau de gaz chaud est plus élevée aux premiers instants de la décharge, avec une température maximale de 1200 K pour un délai de 0,5 ms. Ensuite le noyau se refroidit à mesure qu'il se dilate, avec 1000 K de température maximale à 2,5 ms, même quand la décharge se poursuivit à cet instant. Il se dilate plus rapidement aux premiers instants de la décharge que par la suite, car la diffusion régit la dilatation du noyau, bien qu'il y ait une grande influence du transport convectif induit par l'onde de choc initiale. L'E_{BOS} est mesuré pendant l'évolution du noyau, augmente jusqu'à sa valeur maximale à la fin de la décharge. Les résultats de la SBOS pour l'évolution du dépôt d'énergie sont comparés avec des mesures simultanées par calorimétrie. Même si la SBOS surestime légèrement le dépôt d'énergie, les différences entre l'E_{BOS} et l'E_{th} sont de l'ordre des incertitudes de mesure, de sorte que les deux techniques fournissent de bonnes estimations du dépôt d'énergie.

Les essais dans l'air sont complétés par un changement de la pression initiale, de 0,5 à 2,0 bar. La distance de défocalisation du dispositif est adaptée à chaque pression pour obtenir un déplacement adéquat. La température du noyau chaud augmente avec la pression : à la fin de la décharge, la température du noyau est d'environ 900 K pour 2 bar, alors qu'elle était inférieure à 600 K à 0,5 bar dans l'air. Le volume du noyau diminue toutefois pour les pressions plus élevées, ce qui s'explique par la masse volumique plus élevée : à 2,0 bar, le volume du noyau à la fin de la décharge est la moitié du volume du noyau à 0,5 bar.

Enfin, l'influence de la présence de carburant est étudiée. Les mélanges propane-azote, à des fractions molaires de 0,04 et 0,06 ; sont soumis à des essais pour des écartements de 1 mm et 2 mm et des pressions initiales de 0,5 à 2,0 bar. Les constantes de Gladstone et de Dale des différents mélanges sont d'abord obtenues. Les essais sont effectués dans 8 conditions différentes (2 distances d'écartement et 4 pressions initiales), pour les deux mélanges de gaz. Pour des pressions plus élevées, la température atteint des valeurs supérieures à celles des mêmes décharges dans l'air (1100 K à 2 bar), sans une influence appréciable des changements dans la concentration de propane. La répétabilité des décharges est plus faible à des pressions plus élevées en présence de propane, avec une proportion plus importante de distributions asymétriques des noyaux et de structures 3D, ce qui exclut ces tests pour le traitement SBOS. La taille du noyau diminue de façon linéaire avec la pression. La composition du gaz n'a pas d'effet significatif sur le volume du noyau, bien qu'on observe une grande variabilité du rayon maximal due à des différences de forme des noyaux.

Le dépôt d'énergie est estimé pour les différents mélanges de propane, et avec les résultats dans l'air, ces résultats sont comparés aux résultats de mesures simultanées par calorimétrie. Les données SBOS et calorimétriques montrent la même tendance : le dépôt d'énergie est plus élevé pour les distances d'écartement plus longues et les pressions plus élevées, et il augmente en présence de carburant. D'un point de vue quantitatif, les deux techniques de mesure de l'énergie diffèrent en moyenne de 13 %, ce qui se situe dans la plage des incertitudes cumulées pour les deux méthodes.

V. Caractérisation expérimentale de différents systèmes d'allumage

Dans ce chapitre, nous visons à caractériser les systèmes d'allumage contemporains en utilisant les techniques expérimentales développées dans les chapitres précédents.

En effet, la calorimétrie à volume constant et la SBOS sont appliquées à un allumeur de moteur d'hélicoptère et à un allumeur à radiofréquence. Les décharges produites par ces allumeurs sont étudiées en mesurant l'énergie électrique qu'ils délivrent à la bougie d'allumage, le dépôt d'énergie thermique dans le fluide, l'efficacité du transfert d'énergie et la caractérisation spatiale de la décharge.

L'énergie déposée dans le fluide par l'allumeur du moteur d'hélicoptère Ardiden 3 est mesurée par calorimétrie, dans l'air et différents mélanges de gaz, pour une gamme de 8 pressions initiales de 0,25 à 2,0 bar. Tant l'énergie électrique fournie à la bougie d'allumage que le dépôt d'énergie restant dans le fluide à la fin de la décharge diffèrent des valeurs qui décrivent généralement le système d'allumage, qui est l'apport d'énergie pour le système :

Pour notre système d'allumage avec une entrée électrique de 2 J (provenant de la source d'alimentation), l'énergie électrique à la bougie d'allumage est en moyenne $E_{el}=624\pm49$ mJ (± une déviation standard). Le dépôt d'énergie dans le gaz par la décharge, mesuré pour la première fois par calorimétrie, est $E_{th}=85\pm7$ mJ, pour une durée de décharge de 250 μs. La décharge est trop courte pour permettre un suivi temporel du dépôt d'énergie au cours de la décharge, de sorte que l'énergie est estimée comme le dépôt global après la fin de la décharge. Cela donne un rendement de $\eta=13{,}7\pm0{,}4\%$ pour le transfert d'énergie des électrodes de l'allumeur au fluide.

L'allumeur de l'hélicoptère n'est pas affecté de manière significative par les changements des conditions expérimentales, par rapport aux électrodes broche à broche et à la configuration TCI. Des essais dans l'air à des différentes pressions initiales montrent que le dépôt d'énergie augmente en moyenne de 74±8 mJ à 0,25 bar à 94±8 mJ à 1,75 bar, avec des valeurs d'E_{th} qui se chevauchent à différentes pressions. L'augmentation de η n'est que de 2 %, de 0,25 à 2,0 bar. Le revêtement semi-conducteur de l'isolation de la bougie d'allumage est la raison du faible effet de la pression : le semi-conducteur régule la tension de claquage à environ 700 V, qui autrement varie fortement avec la pression. La présence de carburant, testée par des expériences sur des mélanges propane-azote, réduit le dépôt d'énergie d'environ 10 mJ et le rendement d'environ 2 %.

L'allumeur Ardiden 3 est également étudié par SBOS, après avoir adapté la méthodologie aux caractéristiques de la décharge en termes de taille, d'énergie et d'émission de lumière. L'évolution du noyau de décharge montre la structure du noyau dans les premiers instants de la décharge, de 20 μs à 8,5 ms après le début de la décharge. La reconstruction du champ de température par SBOS nécessite d'une distribution axisymétrique du champ, donc à partir des images de l'évolution du noyau, nous fixons la plage de délai d'acquisition des images valable pour le traitement SBOS complet entre 25 et 100 μs. Les distributions de l'indice de réfraction, de la température, de la masse volumique et de l'enthalpie sont estimées pour les décharges dans l'air à différentes pressions, ainsi que le dépôt d'énergie. L'influence de la pression initiale sur l'énergie de décharge est trop faible pour être observée dans les résultats, puisqu'il y a une variabilité du dépôt d'énergie. Néanmoins, la pression initiale affecte directement la taille du noyau de décharge, car le volume du noyau et la profondeur de pénétration du noyau diminuent pour des pressions initiales plus élevées.

Un allumeur à radiofréquence est aussi caractérisé par calorimétrie pour une décharge de 0,5 ms. L'allumeur à radiofréquence produit une décharge de plasma hors équilibre qui se développe en une structure tridimensionnelle multibranche. Cette structure asymétrique nous empêche de mesurer les conditions de gaz par SBOS pour cet allumeur. Des mesures de calorimétrie donnent différentes énergies dans l'air pour différentes configurations, avec des E_{el} allant de 45 à 78 mJ d'entrée électrique à l'étincelle, et des E_{th} allant de 25 à 50 mJ. Ces valeurs sont obtenues en modifiant la durée de décharge et la tension d'alimentation. L'efficacité de ce type de décharge est beaucoup plus élevée que pour les étincelles classiques, avec un rendement de la bougie d'allumage de $\eta > 60\%$, notamment par la réduction des pertes de chaleur liée aux caractéristiques du plasma froid hors équilibre, l'utilisation d'une seule électrode et la structure de la décharge.

Conclusion

Nous avons développé et adapté deux méthodologies pour l'étude des décharges électriques : la calorimétrie à élévation de pression, qui a fourni une mesure globale du dépôt d'énergie dans le gaz E_{th} ; et la SBOS, qui a permis de calculer les distributions spatiales de la masse volumique, de la température et de l'enthalpie à un moment choisi après le début de la décharge, ainsi que le dépôt d'énergie dans le gaz jusqu'à ce moment E_{BOS}.

La calorimétrie a été appliquée aux décharges dans une configuration d'électrodes pin-pin et de TCI. Le dépôt d'énergie E_{th} qui a été transféré au fluide par une décharge électrique a varié de 7 à 18 mJ, avec une énergie électrique fournie aux électrodes E_{el} de 33 à 48 mJ. L'efficacité du transfert d'énergie η était d'environ 20 à 40%. L'E_{th} et η ont augmenté avec la pression et la distance entre les électrodes. L'augmentation de l'efficacité était due à la réduction des pertes avec une pression ou un écartement élevé et à une plus grande proportion de la décharge produite en mode arc. La présence de combustible, testée avec des mélanges propane-azote, a encore augmenté le dépôt énergétique E_{th} et l'efficacité η.

La SBOS a été développée pour l'étude des décharges dans la même configuration pin-pin de référence. Les distributions de l'indice de réfraction, de la masse volumique et de la température du noyau de décharge ont été obtenues pour différents moments de la décharge dans l'air et à la fin de la décharge dans de multiples conditions expérimentales de pression et de mélanges de gaz. La température est plus élevée au début de la décharge, et elle est affectée par la pression initiale, l'écartement inter-électrodes et la composition du gaz, atteignant plus de 1400 K dans certaines conditions. Le dépôt d'énergie E_{BOS} a été estimé et comparé aux résultats obtenus simultanément par calorimétrie. L'estimation du dépôt d'énergie par deux méthodes basées sur des propriétés physiques différentes a donné de bons résultats, avec des différences dans l'intervalle d'incertitude des méthodes.

Pour la première fois, ces méthodes ont été appliquées à l'étude d'un allumeur de moteur à turbine à gaz : l'allumeur de moteur d'hélicoptère Ardiden 3. Ce système d'allumage avait une énergie nominale d'entrée dans le circuit électrique de 2 J. Cependant, les mesures par calorimétrie ont montré que l'énergie électrique fournie aux électrodes par décharge était d'environ 625 mJ, et le dépôt d'énergie dans le gaz était de 85 mJ ; avec une efficacité inférieure à 14 %, même pour la courte durée de 250 μs. Un revêtement semi-conducteur sur l'isolation de la bougie d'allumage réduit et fixe la tension de claquage, ce qui réduit considérablement l'influence de la pression et de la composition du gaz sur les caractéristiques de la décharge.

Le noyau de décharge produit par l'allumeur de l'hélicoptère a été étudié également par SBOS. Les températures à l'intérieur du noyau ont été mesurées pour atteindre 3700 K, 50 μs après le début de la décharge. Cette décharge n'a pas été affectée de façon significative par les changements de pression.

Introduction

Research and development in air transport is nowadays oriented towards increasing efficiency and reducing pollutant emissions. To limit the effects of global warming, European regulations set objectives in this respect: air transport agents have to reduce fuel consumption and CO_2 emissions per kilometer and passenger 75% in 2050 of their reference values from year 2000; and to reduce NOx emission 90% in 2050 [1].

Aircraft propulsive systems, that employ the Brayton thermodynamic cycle, have been optimized during the last decades to a point where there is little margin for further improvement. Indeed, optimization of the different components of the engine and the use of leaner combustion are both limited physically. The necessary solution lays on new engine concepts that are currently under development, such as the Rotative Detonation Engine or the Constant Volume Combustion engines. These engine concepts work in different thermodynamic cycles that are potentially more efficient.

Ignition is a critical point in the design of aircraft engines. Indeed, the certification of an aircraft engine is only acquired if it has demonstrated its ability to restart in altitude conditions (20 to 30 kft), i.e. for low pressures (around 0.3 to 0.4 bar) and low temperatures (around -50 °C). These conditions are particularly severe for the processes of fuel atomization (low injection pressure), vaporization (low temperature) and ignition of the fuel/air mixture (low fuel vapor available). This critical phase of ignition is even more crucial to control, as nowadays the aim is to:

- increase the ignition ceiling (maximum altitude) to extend the flight range (e. g. for dual jets)
- increase the ignition range (in terms of engine speed)
- hybridize helicopter turbines: This results in the standby or even total shutdown of one of the two turbines equipping the aircraft, which must nevertheless be able to be restarted extremely quickly and reliably in flight (fast restart < 10 s).

Therefore, the ignition process of a gas turbine must be able to be carried out in a wide range of aero- and thermodynamic conditions (ground ignition, re-ignition at altitude...) and preferably within the shortest possible time.

The function of the ignition system is to generate the initial kernel and to help it survive as long as possible thanks to the highest possible energy transmitted to the fluid. The systems currently in use are based on an electric arc spark plug placed in the combustion chamber wall near a fuel injector. This type of high energy igniter therefore produces a surface discharge lasting a few hundred microseconds, thus ensuring the generation of a plasma at very high temperature (several tens of thousands of Kelvins). The diffusion of the intermediate species produced and the high temperature generated allow the triggering of the chemical combustion reactions, forming an ignition kernel. This kernel is more or less resistant to turbulent dissipation allowing or not its survival and propagation. This process, which takes place in the near wall of the combustion chamber, requires the fuel to be directed in its direction.

Spark ignition systems are generally described by the electrical energy input used to operate them. However, the physical characteristic that directly affects the ignition process is the energy deposit supplied to the fluid by the system. The energy deposit in the fluid is only a portion of the electrical energy input. The rest of the energy is lost, with two kind of energy losses: electrical circuit losses and electrical discharge losses.

Electrical circuit losses occur inside the ignition system from the storage point up to the electrodes. The electrical circuit of the ignition system stores the energy input, and then adapts and delivers the electrical energy to the spark plug electrodes to produce the discharge. Some of the input energy is employed to adapt the low-power energy input of the to the high-power electrical energy at the electrodes during a short time to produce the discharge. Another part is dissipated in the circuit or lost because storage is not completely efficient. Electrical circuit losses can be easily estimated by measuring electric voltage and current at the ignition system input and output, i.e. the power source and the spark plug electrodes respectively.

Electrical discharge losses occur in the energy transfer from the electrical energy at the electrodes of the spark plug to thermal energy deposit in the fluid. In this process there are different sources of energy loss: energy is dissipated by radiation, heat conduction to the electrodes, anode and cathode falls, and shockwave production. The remaining thermal energy deposit is not simple to estimate, and its measurement requires specific calorimetry experimental techniques.

The thermal energy deposit and other effects related to ignition produced by electrical discharges have been studied in academic configurations, and to a lesser extent in automobile applications. However, little information has been published about the electrical discharge characteristics in gas-turbine engine applications. A better understanding of the electrical discharge and energy deposit produced by aeronautic ignition systems is therefore necessary to ensure the correct ignition, and thus represents essential knowledge for combustion simulation and for the design of new engines.

This work focuses on the development of proposed methodologies for the characterization of the thermal energy deposit of electrical discharges. An original parametric study is then conducted for different ignition systems. Experimental techniques are first applied to the study of electrical discharges produced by a reference configuration in quiescent conditions, at different inert gas mixtures and pressures. The methodologies developed are then applied to both a radio-frequency ignition system and a helicopter igniter.

Objectives

The main goal of this investigation is to develop a methodology to characterize electrical discharges and ignition systems. To do so, different properties of the electrical discharges need to be accurately measured:

- Electrical current and voltage, discharge duration and electrical energy supplied to the electrodes.
- Energy deposit delivered to the fluid by an electrical discharge.
- Spatial distribution of gas properties at the discharge: discharge kernel evolution over time, including kernel volume and properties (temperature and density fields).

Measurement techniques should be adapted or developed for this task and validated on a reference configuration, such as pin-to-pin electrodes. The influence of external conditions on these properties should be studied too. Finally, the aim is to adapt the developed methodologies to different ignition systems, including an aircraft igniter, to provide better understanding of their performance and behavior.

Thesis outline

Chapter 1 presents the principles of electrical discharges and spark ignition. It includes background information on spark ignition theory, ignition systems and previous numerical and experimental investigations of electrical discharges. The experimental setups used in this work are presented in Chapter 2.

The application of pressure rise calorimetry to the measurement of the thermal energy deposit in the fluid is presented in Chapter 3. This chapter explains the pressure rise calorimetry methodology, which coupled with electrical measurements globally characterize the pin-to-pin electrodes electrical discharge. It also presents the experiments carried out in different conditions and the discussion on the results, for the case of pin-to-pin electrodes.

Chapter 4 covers the development of the Speckle-based Background-Oriented Schlieren (SBOS) technique for electrical discharges and the measurement of the instantaneous spatial distribution of gas properties in the discharge kernel. Density, temperature and enthalpy fields are obtained at different moments of the pin-to-pin electrodes discharge and in different conditions, simultaneously with calorimetry measurements.

The developed methodologies are applied to the characterization of a gas turbine engine igniter in Chapter 5. Both calorimetry and SBOS techniques are first adapted to the characteristics of the igniter, and then employed to the study of the discharge. Thermal energy deposit is obtained by calorimetry, and spatial distribution of thermodynamic properties in the spark kernel by SBOS.

Finally, the investigations carried out in this thesis are summarized and future works are proposed in the conclusion section.

Chapter 1

Electrical discharges and spark ignition: theory and literature

Contents

1 Electrical discharges and spark ignition: theory and literature

In this chapter we present the basis for the study of electrical discharges at spark ignition. In a first part, the theory of electrical discharges is briefly explained, describing the hot plasma discharge and how it produces the ignition. The commercial ignition systems that use this discharge are described as well. Non-equilibrium plasma discharges and laser ignition are also commented. In a second part, a non-exhaustive bibliographic review gives an idea of the state-of-the-art in spark ignition. It presents studies of the effect of electrical discharges on ignition and how discharges are characterized for combustion, and spark ignition models with the main discharge characteristics they need as inputs and their main findings. Experimental investigations on electrical discharges and spark ignition are also reviewed, including metrology used for the determination of the energy deposit, visualization methods to study the discharge kernel and early flame, and tests on ignition systems. Finally, we present the chapter conclusion and the motivation for this thesis work related to the state-of-the art.

1.1 Theory: Electrical discharges and spark ignition

An electrical discharge is the most used form of transferring electrical energy to a fluid in form of thermal energy. It is produced when the electric field in a region is strong enough to ionize the fluid, which then turns into an electrical conductor (plasma). The thermal energy deposit provides the gas mixture with the activation energy necessary to start the combustion chemical reactions and to compensate heat losses, starting a chain reaction.

The most common type of electrical discharge for ignition applications is the hot plasma discharge, which use dates back more than a century. To produce it, DC voltage is increased at the electrode tips until fluid in the inter-electrode gap is ionized and forms a conductive plasma channel. Then the high voltage drops, and energy is released. Fluid in the conductive channel reaches high temperatures (electronic temperature of ~60,000 K) and is ionized, in form of plasma in thermal equilibrium (hot plasma). At the frontier of the conductive channel there are the right conditions (temperature, radicals, fuel and oxidizer presence) for combustion to start.

Other type of electrical discharges used for ignitions are Low-Temperature Plasmas (LTP). They are produced when voltage is increased fast enough to produce ionization before the hot plasma discharge is produced, and then they employ different mechanisms to maintain the plasma in a non-equilibrium state instead of allowing a hot plasma discharge to develop. Nanosecond Pulsed Repetitive Discharges (NRPD) and radio-frequency resonating discharges are examples of LTP.

In this section, first we describe physical phenomena during hot plasma discharge and spark ignition. Then, we present the commercial ignition systems that use hot plasma discharges. Next we describe non-equilibrium plasma discharges, and finally we comment other existing ignition mechanisms.

1.1.1 Hot plasma discharge: physical phenomena and phases of the discharge

The equilibrium plasma discharge has been used at spark plugs spark plug for igniting gas mixtures inside internal combustion engines for more than one century. It is also found in nature, as in lightnings or in electrostatic discharges. In engines it is used as the energy source which ignites the gas mixture and starts combustion.

Spark ignition has been widely studied and is explained in depth in Maly's work [2], [3]. The physical description of the process at the fluid and plasma physics is found in Raizer's book [4]. A global description of the hot plasma discharge and its role in spark ignition process is explained next.

Increasing the electric potential between two electrodes rises the electric field in the inter-electrode gap. When the electric field is strong enough, the fluid is ionized in that area setting up a conductive channel. The period preceding the moment of ionization is called the "pre-breakdown" phase. It is followed by the discharge of the energy stored between the electrode tips, which act as a capacity during the breakdown phase. Energy from cables and the electrical circuit connected to the electrodes is discharged later in either arc or glow phase, depending on electrical and gas conditions.

Figure 1-1 shows a schematic representation of typical voltage and current signals during a discharge, produced by a commercial transistorized coil ignition system (TCI), showing their approximative values during each phase of the discharge. The exact values and distribution in time can vary depending on gas, gas conditions (pressure, temperature, flow conditions), electrode geometry, electrical circuit components [5].

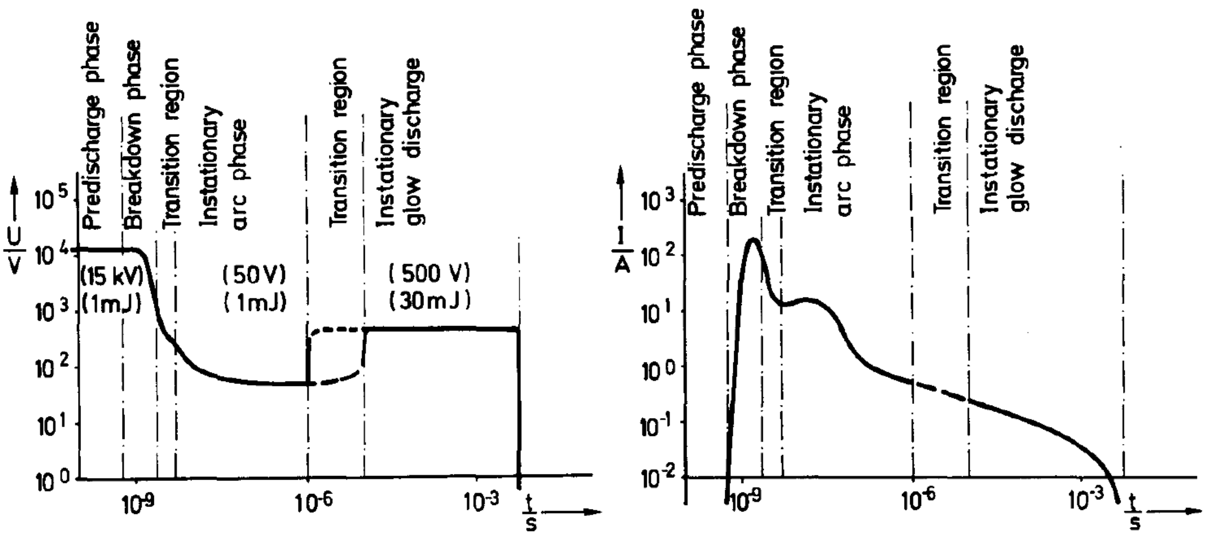

Figure 1-1: Voltage (U) and current (I) of technical ignition systems versus discharge time. Typical values are given in parentheses [5]

1.1.1.1 Pre-breakdown phase:

During this phase voltage and electric field at the electrodes gap rise, until the electrical field is strong enough to ionize the gas in the inter-electrode gap and form a conductive channel. Two processes take place in the formation of the conductive channel: electronic avalanches and streamer propagation.

Gas in the gap acts initially as a perfect insulator. Randomly existing electrons in the fluid -from cosmic X-ray radiation- are accelerated towards the anode colliding with fluid neutral species. Collisions produce more electrons and ions, which are accelerated by the electric field too and contribute further to collisions; this is the primary electron avalanche, firstly described by Townsend [6]. Electrons are collected by the anode, but other processes produce more electrons:

As ionization occurs there is excitation of gas atoms in short lifetime estates ($\sim 10^{-13}\ s$) that emit photons in every direction when relaxing. Then photons are absorbed by molecules by photoionization, liberating an electron. If there is enough photoionization, 2nd generation auxiliary avalanches are produced, not necessarily in the original channel direction, and even 3rd generation and more consecutive avalanches. Deviation from the original channel lines and branching are explained by this effect [7].

When the electric field is high enough (50-100 kV/cm) the electron avalanche becomes a self-sustained process and reaches the anode. The electronic avalanche formation is illustrated in Figure 1-2 (a) [3]. The electronic avalanche across the gap does not constitute a conductive channel, as it is not fully ionized [8]. The fluid is highly ionized next to the anode only, as a result of the electronic avalanche. Then a fast ionization wave propagates from the anode towards the cathode: a positive streamer. When the streamer reaches the cathode, the conductive channel is formed, and breakdown starts. The transition from the electronic avalanche to the conductive channel is schematized in Figure 1-2 (b).

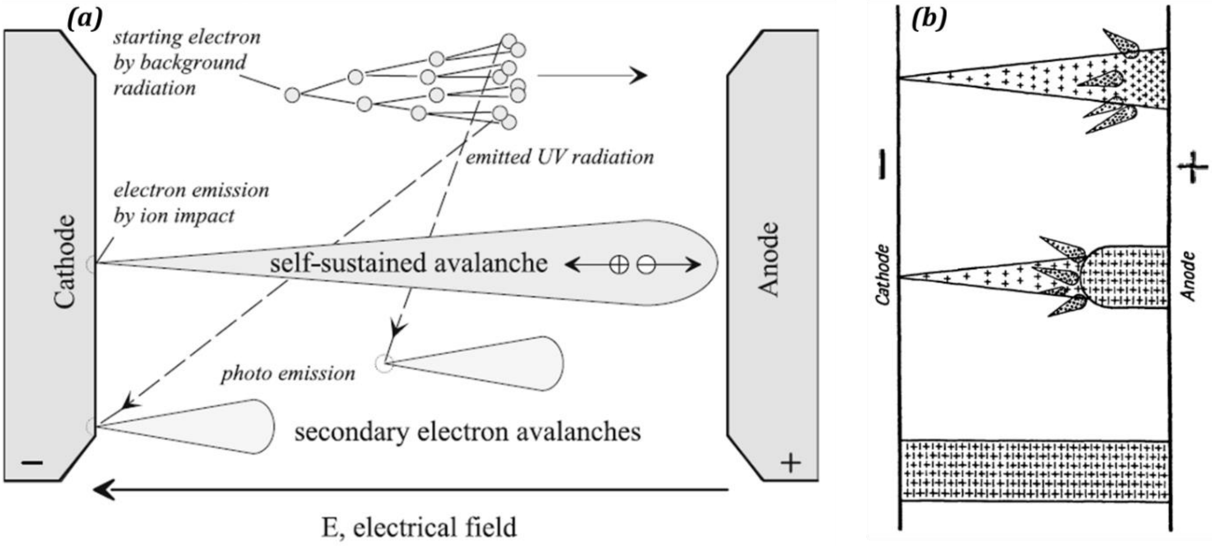

Figure 1-2: Formation of a primary electron avalanche (a) and transition electronic avalanche - positive streamer - conductive channel (b) [5] [8].

When all the fluid in the inter-electrode gap is ionized, it constitutes a conductive plasma channel. Then the breakdown phase begins.

1.1.1.2 Breakdown phase:

The energy stored in form of voltage difference between the electrode tips (as a gas capacitor) discharges through the conductive channel. Discharge current increases over exponentially –up to tens or hundreds amperes depending on circuit and gas conditions- as the insulator gas in the gap becomes conductive. Voltage and electric field drop rapidly to low values (from several kV to hundreds of V). This process is fast, in the timescale of tens of ns. Minimum energy to produce a complete breakdown is estimated as 0.3 mJ for air at atmospheric conditions. Breakdown voltage depends on gas properties and gap distance (the product $p \cdot d$), following the Paschen's Law in most common applications [4]. Deviations from Paschen's Law are produced only when the product $p \cdot d$ is high for some gases, for pulsed discharges, non-equilibrium discharges [9], or when the gap is in the order of μm [10], [11]; which are far from modern igniters working in engine conditions.

The ion density in the discharge region increases, as the gas is completely ionized in the conductive channel (100% ionization). Energy exchange between electrons and ions by Coulomb forces is the dominating process for energy loss for the accelerated electrons, although energy is transferred to the fluid efficiently (estimated transferred efficiency of 90% of the electrical energy)[12]. The conductive channel is highly ionized, forming a plasma channel, with high temperatures (~60000 K) and pressure (>200 bar) that produces a shockwave [2].

As breakdown is a very fast process the cathode remains globally cold, although the high current passing through concentrated points (of the size of the conductive channel) at the cathode surface form hot spots. These hot spots produce material evaporation and electron emission, which serve to sustain the conductive channel in the arc mode.

Electrical and gas conditions determine the nature of the process which will sustain the conductive channel. Whether it occurs as an arc or a glow mode depends on the physical phenomenon providing electrons for the discharge: thermal emission (from hot spots in the cathode) in the arc phase, or radiation emission (ionic bombardment of the cathode liberating electrons plus photo-electronic effect) in the glow phase.

1.1.1.3 Arc phase:

Arc phase takes place after breakdown. In discharges with mainly glow phase after breakdown, arc phase lasts up to hundreds of µs. The hot spots in cathode surface produce electrode material to melt and evaporate, emitting electrons. This is the main source of electrons, which sustain the conductive channel in the arc mode, but material melting produces high electrode erosion.

Arc phase is characterized by low voltage (in the order of 100 V), which splits into the cathode fall, the anode fall, and the conductive channel fall. Current during arc phase is higher than 100 mA for air at 1 bar (high current to produce the cathode hot spots). Energy transfer to the fluid is produced at the conductive channel fall only, as energy dissipated at electrode falls is transferred to the electrodes as heat [13]. Electrode falls, or sheath regions, happen because around each electrode a cloud of charged particles form –ions for the cathode or negative electrode, and electrons for the anode-. This screens the plasma from the electrodes and lowers the potential at the electrodes. During the arc phase, gas ionization in the conductive channel is around 0.1%.

Energy is dissipated as electrode fall losses, heat conduction from the hot kernel to the electrodes, and radiation emission. Energy transfer efficiency is estimated to be around 50% [12], varying with discharge conditions (gas, gap, pressure and temperature, and electrode material, size and shape). Despite its high efficiency arc phase erodes the electrodes, so it is limited in automobile applications (where spark plugs are used in each engine cycle) to extend spark plug life.

1.1.1.4 Glow phase:

In the glow phase the electrons that maintain the conductive channel are produced through electron emission by ion impact, i.e. an ionic bombardment of the cathode liberating electrons and producing photo-electronic effect. The cathode is colder than in arc phase, as there are no hot spots in its surface, and electrode wearing is much lower.

Electron liberation by ion impact is not efficient, so current is low during glow phase, around 100 mA. A higher voltage than during arc phase is necessary to sustain the conductive channel, in the order of 500 V at atmospheric conditions. Gas ionization during the glow phase is weak, around 0.01% ionization [2].

Sources of energy loss are dissipation at the electrode falls, radiation, and electrode heating at the contact of the hot kernel with electrodes. Energy transfer efficiency at the glow mode is estimated at 30% at atmospheric conditions [12].

1.1.1.5 Hot kernel evolution

Spark channel ionization produces a sudden rise in temperatures (~60000 K) as gas is ionized in few nanoseconds in the thin area of 40 μm of diameter initially. Plasma is initially out of equilibrium (rotational, vibrational and translational temperatures differing) but after first tens of nanoseconds it reaches local thermal equilibrium [2]. Energy transferred to the fluid is stored initially as potential energy in the radicals N, O, H and C, dissociated from the molecules in the initial gas mixture. As the hot kernel cools down that potential energy transforms into thermal energy (when radicals recombine, and hot kernel is in equilibrium), as indicated in Figure 1-3 for a breakdown phase [3]. Figure 1-4 shows the characteristic timescales and sequence of the main physical processes during an electrical spark, in this case a pulsed breakdown discharge [14].

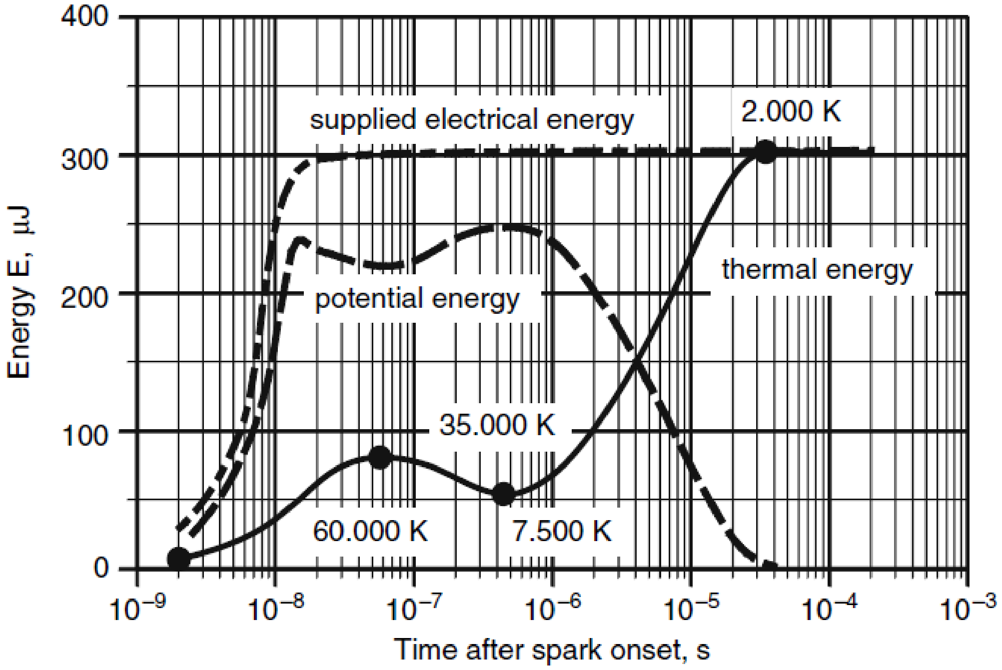

Figure 1-3: Temporal redistribution of the electrically supplied energy in a breakdown phase from initially potential energy (dissociation, ionization) into thermal energy

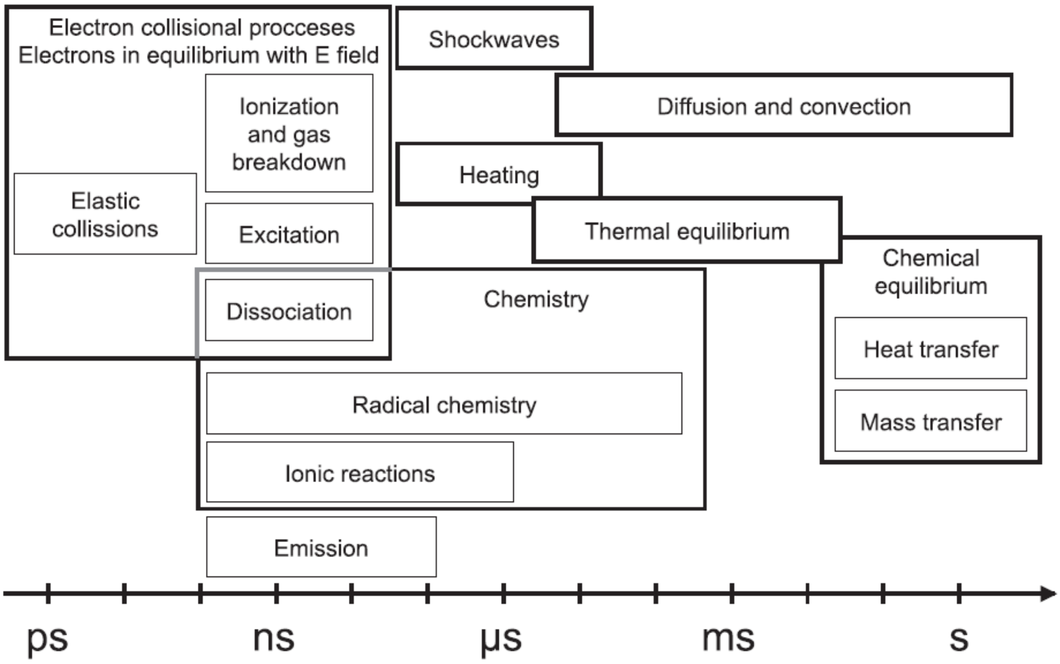

Figure 1-4: Timescales of relevant collisional and transport processes in atmospheric pressure plasmas for a pulsed breakdown discharge [14].

High temperature and pressure inside the conductive channel produce an expansive shockwave as the surrounding gas is at initial conditions. Shockwave carries away a fraction of the energy discharged at breakdown (estimated around ~30%[2]), but a part of it is regained later: shockwaves transfer their energy fast to gas molecules in a small sphere (2 mm Ø) and the conductive channel expands later [5]. A part of this dissipated energy isn't useful for ignition although reabsorbed by the fluid [15]. The shockwave expands and attenuates to a sound wave few microseconds after it is produced.

The plasma channel from breakdown expands and cools down, becoming the spark's hot kernel. Its initial size depends on breakdown energy deposit, and it expands more as more energy is transferred in arc and glow phase. The low-pressure gas in the center of the hot kernel, after shockwave expansion, entrains cold gas from outside the kernel to flow next to the electrode walls towards the kernel center. This way, the initially cylindrical kernel transforms into a toroidal shape.

Chemical reactions happen few nanoseconds after the spark onset, still during breakdown. They take place in the border of the plasma channel, as inside it all molecules are dissociated. Energy from those chemical reactions add up to the plasma energy. Combustion starts and takes place at the hot kernel surface after the plasma channel expands. As the hot kernel expands the flame in its border expands with it. Combustion becomes self-sustained if the energy released at the chemical reactions compensate heat losses produced by conduction and radiation with surrounding fluid, otherwise the flame will extinguish. There are other external influences that may lead to flame propagation failures [16]: energy losses to electrodes or walls, flow field effects, mixture properties, thermodynamic conditions, and dependence of turbulent scales.

Energy from chemical reactions increases with hot kernel size. The critical radius (or minimum ignition radius) is the minimum radius the hot kernel must reach to start a self-sustained flame, and therefore success at igniting the mixture in the engine combustion chamber. The electrical energy supplied to the spark plug to produce an electrical discharge that reaches the critical radius is known as the minimum ignition energy (MIE), which is used to characterize gas mixtures in different conditions [17].

1.1.2 Commercial ignition systems

The ignition system is formed by the spark plug and the electric circuit which adapts the energy supply to it. All the ignition systems can be represented by an equivalent circuit with a high voltage transformer and impedances, capacitances and inductances on the primary and secondary circuits. The spark plug acts as a capacitance at the high voltage loop before breakdown (as the gas in the inter-electrode gap is an insulator), and as an impedance once the conductive channel forms.

There are two kinds of ignition systems, depending on the main element used to store energy: Transistorized Coil Ignition (or Transistor Controlled Ignition, TCI), for ignition systems using a coil and a transistor; and Capacitive Discharge Ignition (CDI). They are both used for low energy applications: motorbikes, little oil engines (e.g. chainsaw) use CDIs, while most cars use TCIs. High power applications, i.e. gas turbines and aircraft engines, use CDI systems.

An example of CDI system equivalent circuit and the electrical discharge events are represented in figure 1.1 [15]: the charging of the capacitor in a), firing of the ignition system in b), formation of the conductive channel at breakdown in c), and formation of electric arc in either arc of glow phase in d). The images in the figure correspond to pictures of the inter-electrode gap of the automobile spark plug in that ignition system.

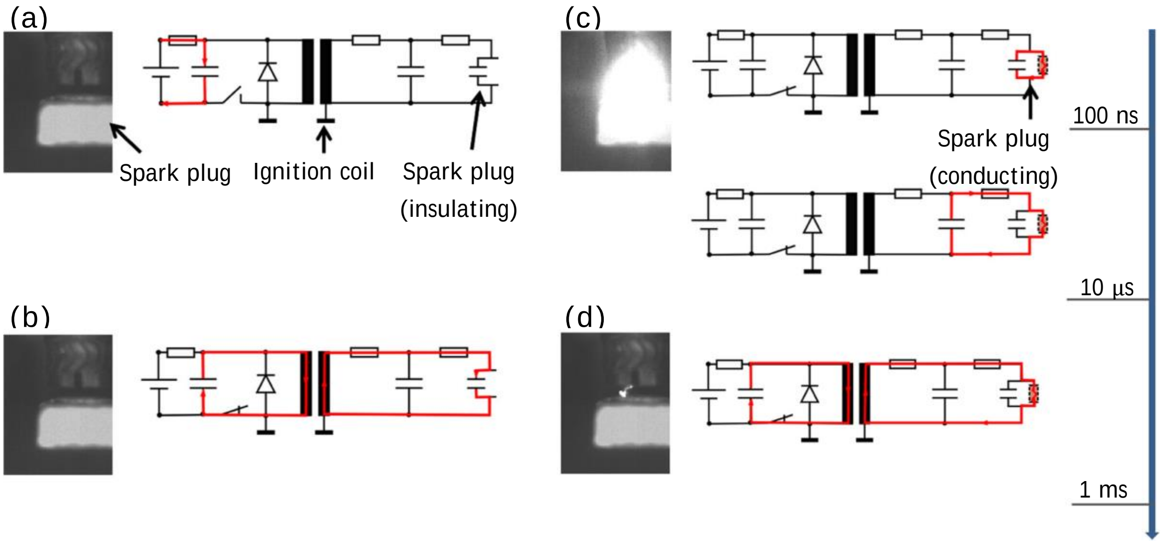

Figure 1-5: Events during spark discharge for a CDI. Timeline applies to breakdown and arc-glow phases (c and d). [15]

Aeronautical CDI use a capacitive exciter to store and adapt voltage and current, a lead –coaxial wire- to deliver energy to the igniter, and the spark plug. The exciter periodically charges its capacitance and produces a discharge several times per second (~ 5 Hz) at engine ignition. The ignition system stops when there is a stable flame at the combustion chamber. In gas turbines and aircraft engines there are flame detectors to that end.

These igniters produce less discharges in total engine working life cycle than automobile TCIs: a successful ignition in aircraft conditions is assured by high energy and power discharges. Electrical energy is in the order of 2 J as input for the exciter, and 600 mJ at the igniter. This high energy causes more erosion in the spark plug than in automobile applications. Though, erosion is of less importance as the number of total discharges that aeronautic igniters produce is reduced in comparison. The discharge lasts around 100 µs in this setup [18], [19]. Working conditions change, as in normal ignition, on-flight re-lighting or high-altitude engine start.

Automobile TCI use a coil to rise voltage in the system, and when the transistor is triggered by the spark controller it starts the discharge. This kind of discharge is mostly in glow phase to reduce electrode wearing and lasts several milliseconds. A resistive spark plug is commonly used to reduce EMI (electromagnetic interference) with other electronic devices in the car, even when that resistance dissipates a portion of the energy.

Electrical energy supplied to the spark plug by these systems is in the order of 50 mJ (typical for commercial “top-plug” or “pencil-coil” systems). In an automobile engine these systems operate several times per second, e.g. 3.600 rpm correspond to 30 Hz for each ignition cycle in four-stroke engines. In the inter-electrode gap, gas would be at high pressures and presenting a turbulent flow. Electrodes are at temperatures between 500 and 800 °C during normal engine functioning.

1.1.3 Non-equilibrium plasma ignition.

In the non-equilibrium state of the plasma, an imbalance exists between ion and electron temperatures. As in the transient pre-breakdown phase, electrons reach high temperatures (tens of thousands K of electronic temperature) as they are accelerated by the electric field, while ions move much slower. The energy is mainly carried by the electrons while atoms and ions remain much colder, which is why they are also called Low Temperature Plasmas (LTP). Thermal diffusion losses are very low in this process. Furthermore, the accelerated electrons produce free radicals in the gas by electron ionization of the gas, which is more efficient than thermal dissociation as in hot plasma discharges [20].

A strong electric field is needed to accelerate the electrons, which requires high voltages across a pair of electrodes. If the voltage is applied slowly, a hot plasma takes place. But, as discovered by Meek and Raether independently around 1940 [8], if an excess of voltage is applied to the electrodes before the electronic avalanche reaches the anode, the electronic avalanche does not reach the opposite electrode. Instead, because of the excess in the electric field in the gap, the electron avalanche produces a mid-gap streamer that propagates towards both electrodes. The streamer tips propagate by the effect of photo-ionization of molecules next to the streamer, which is an isotropic process, so the streamer does not always follow a straight line and is prone to branching. This process, depicted in Figure 1-6 (a-d), starts sooner the higher is the overvoltage applied, and it is much faster than the avalanche alone.

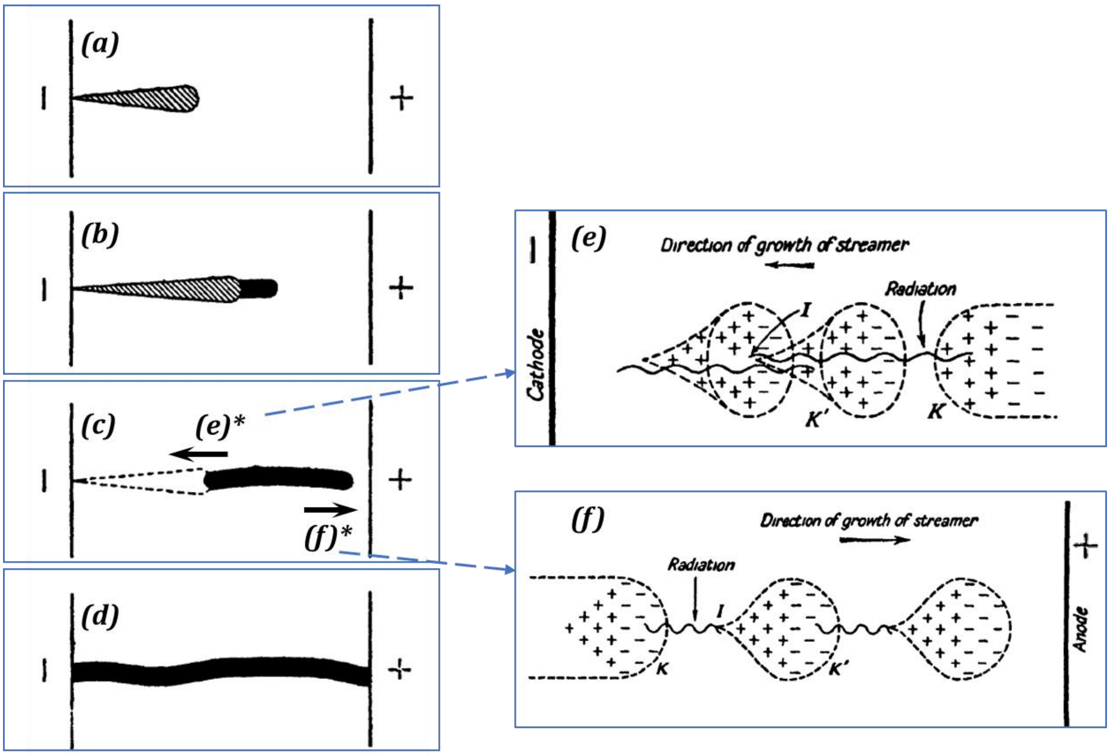

Figure 1-6: Formation of a conductive channel voltage in excess of the minimum for breakdown: the electronic avalanche (a) produces a mid-gap streamer (b) which propagates towards the electrodes (c) forming the conductive channel (d). The streamer propagates towards the cathode as a positive streamer (e) and towards the anode as a negative streamer (f)[8].

Different mechanisms produce propagation of the positive and the negative streamers: ahead of the positive streamer (cathode-directed, Figure 1-6 (e)) photons produce photoelectrons that start new avalanches towards the tip of the streamer (charged positively). These avalanches extend the tip of the streamer, which propagates towards the cathode. The negative streamer (anode-directed, Figure 1-6(f)) grows as the result of avalanches developing away from the streamer tip, from electrons from the streamer or from photoelectrons produced ahead of the tip. A detailed explanation of these processes can be found in Meek's book [8].

Starikovskaia [20] presented an in-depth review about the physics of non-equilibrium plasmas, with experimental and theoretical analyses of various non-equilibrium plasmas and their applications on ignition and combustion. It was further expanded by [21], including discharge kinetics and applications in low and high speed propulsion (automotive and aerospace applications). Later, Starikovskaia included in [22] more recent results on LTP, focusing on ignition. Finally, Ju and Sun revised works about enhancement pathways of plasma assisted combustion and fundamental phenomena in plasma assisted combustion experiments [23], focusing on discharge and chemical kinetics.

The non-equilibrium plasma is present only during the transient stage of the formation of a conductive channel, and an arc plasma – not to be confused with the arc phase of the equilibrium discharge – is obtained if a high-voltage pulse is applied to a pair of electrodes. The passage to gas breakdown can be avoided modifying either the system of electrodes or the shape of the high voltage. Different plasma discharges are obtained for different overvoltage levels and electrode configurations: streamer discharge, Dielectric Barrier Discharge (DBD), Pulsed Nanosecond Discharge (PND), atmospheric-pressure glow discharge, and microwave discharge. An in-depth description of these systems, which are pictured in Figure 1-7 [21] can be found in the aforementioned reviews.

Another type of LTP discharge, the radio-frequency resonating discharge, has been developed recently. It employs a polarized high voltage on the tip of a single electrode. The effect of the fast change in polarization of the voltage produce the formation of streamers and gas ionization in a multi-branch cold-plasma discharge. The discharge energy is delivered to a number of streamers, so the discharge affects a large volume of gas compared to the conventional equilibrium discharge. In Auzas PhD dissertation [24] a radio-frequency system is developed, and applied to engine-like conditions in Prevost PhD [25], and also independently in Mariani et al. studies [26], [27].

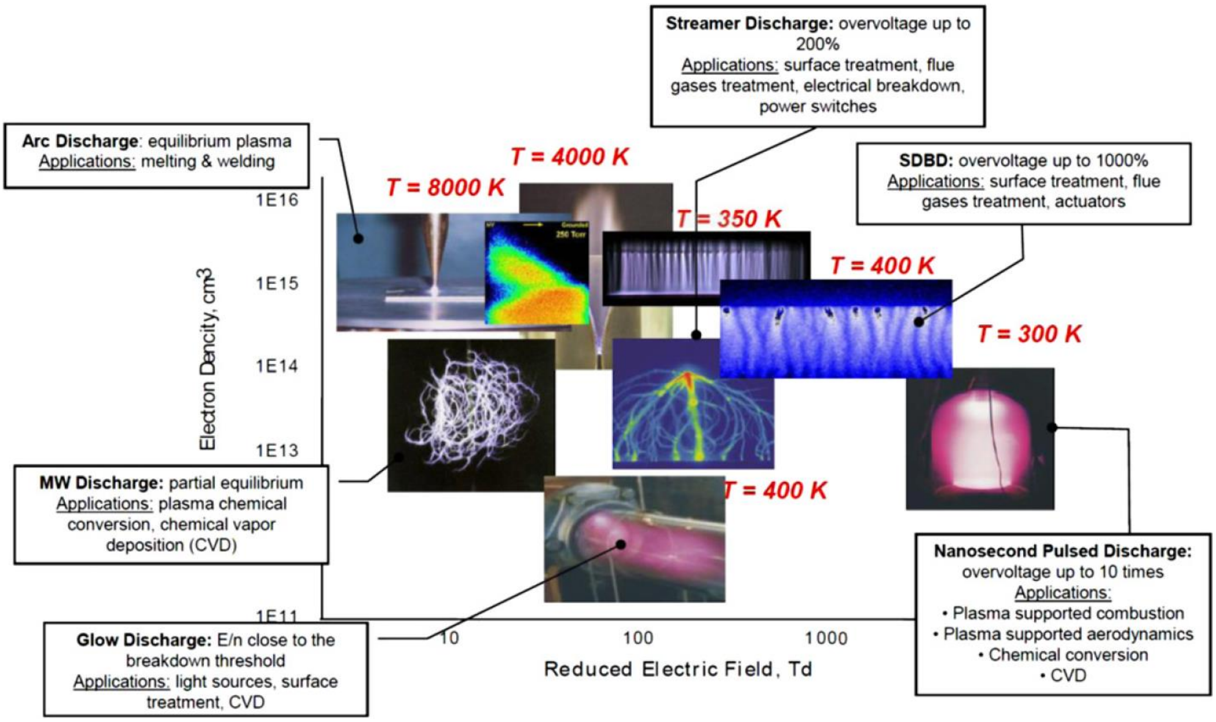

Figure 1-7: Discharge development and plasma generation for different applied overvoltages and their applications [21]

1.1.4 Other ignition mechanisms

1.1.4.1 Plasma Jet

Plasma jet igniters produce an energetic discharge inside a small pre-chamber, where the gas is ionized and projected at high pressure inside the combustion chamber. The plasma jet, with high thermal energy and concentration of radicals, starts the combustion in the chamber efficiently [28]. The pre-chamber presents durability issues due to sustaining the high energy discharge [29].

1.1.4.2 Laser discharge

Another process for initiating combustion is using a concentrated laser to create a hot kernel inside the fluid. This method is optimal for placing the flame kernel at the desired place, i.e. the most favorable position in the combustion chamber in terms of gas mixture and aerodynamics, with no losses to close structures such as chamber walls or electrodes. The energy deposit is properly controlled by the laser power and can be delivered in a short time.

However, laser ignition needs optical access to the chamber, through a small window which must stand structural and thermal charges during the combustion cycle, and with little optical losses. This promising system is still under development, currently under many research works, as by Letty [30], Mulla [31], or Renou [32], [33]. More details about laser ignition can be found in O'Briant's review [34] and in Phuoc's review [35]; and an in depth analysis and application for aeronautic propulsion in George's PhD [36].

1.2 Literature review

In this paragraph we present a general review of the state of the art in spark ignition to the author's knowledge, with focus on the electrical discharge process and the different experimental studies performed on electrical discharges, related to this thesis.

1.2.1 Combustion: successful ignition and MIE.

The ignition process has been widely studied. A minimum energy deposit is needed to start the combustion process, as the initial ignition kernel needs to reach a minimum radius (critical radius, r_c) to initiate a self-sustained flame [37]. It is the role of the ignition system to deliver to the fluid an energy deposit enough to produce an ignition kernel that expands beyond r_c. This value of the energy deposit is known as the Minimal Ignition Energy (MIE), and it depends on gas conditions (pressure, temperature, fuel and gas employed, equivalence ratio, flow conditions…). Furthermore, the energy deposit also influences the initial kernel expansion speed or initial flame speed in the laminar case, until kernel radius reaches values from 5 to 10 mm, as in [38], [39].

MIE has been widely studied, as it is a determining parameter for successful ignition for different fuels [40]. Still, in many MIE studies, the reference parameter is the electrical energy stored at the capacitor (E_C) in a short capacitive discharge [17], obtained from breakdown voltage U and circuit and spark gap capacity C, as in equation (1.1). MIE is often estimated as $MIE \sim E_c$ value with 50% ignition probability in a series of tests (or with lower probabilities for risk analysis issues). Although breakdown energy transfer efficiency is around 90%, breakdown phase only lasts for tens of ns, and discharges for typical MIE experiments last in the order of 100 ns. With a subsequent arc phase with lower efficiency, the energy deposit in the fluid is not truly addressed by this energy estimation.

$$E_C = {}^{1}\!/_{2}\, C U^2 \tag{1.1}$$

The influence of spark discharge characteristics on MIE was studied by Ballal and Lefebre [41]. The setup used was a closed channel, allowing for flowing gases up to 100 m/s, with windows for direct visualization of the successful combustion event. They used pin-to-pin electrodes with a capacitive circuit, varying the energy supplied to the electrodes E_{el} from 0 to 105 mJ, discharge duration from 1 to 105 µs and electrode gap from 1.5 to 19.0 mm. They tried different electrode diameters, with cross-sectional areas from 10^{-4} to 0.2 cm^2. The energy release was estimated empirically from electrical current and voltage measurement at the electrodes – see equation (1.2). They also estimated the energy losses in the energy transfer due to forced convection and shockwave in flowing gases from E_{el} measurements, although they used a fluid mechanics expression of the gas flow for the forced convection losses and an empirical estimation for the shockwave losses. E_{el} was found to be proportional to gap width, increasing slightly with pressure and velocity. The measurements of energy release were used as MIE values, for a 50% igniting probability, in diverse conditions: MIE presented almost no variation with turbulence intensity, but vary with pressure, velocity and mixture strength; and is reduced with low conductivity and low boiling point electrode materials.

$$E_{el} = \int I\,U\,dt \tag{1.2}$$

The risk of electrostatic discharges in aircraft fuel tanks motivated studies of MIE of Jet A [42][43]. They measured the minimal energy that could ignite fuel mixtures during flight conditions: from 0.3 bar to 0.98 bar (corresponding to 14 kft height and seal level respectively), for different equivalent ratios. A pair of pin-to-pin electrodes were used with a capacitive circuit, to produce spark energies from under 1 mJ to 100 J of E_C with 3.3 mm and 5.4 mm gaps and duration under 30 µs. The ignition energy was estimated from the circuit capacitance, E_C; in the first study [42], but in the second part of the study [43] the spark energy was estimated from the electrical energy E_{el} minus losses in the spark circuit resistances. This improves the measurement, but it does not address the energy deposit in the gas. They used simple statistical tools to relate MIE to spark energy measurements, and expressed it as a mean and a standard deviation.

Other spark ignition studies estimate energy as the electrical energy supplied to the electrodes minus the remaining energy in the capacitor after the discharge, from breakdown voltage and spark current as in equation (1.3). This was done first by Moffett and his co-workers [44], who developed and characterized a low-energy capacitive spark ignition system that can produce repeatable sparks near MIE values for aviation (0.1 to 1 mJ, in ~50 ns). They used a statistical approach to better characterize MIE as an ignition probability curve rather than a single threshold value, for Jet A (using data from [42], [43]).

$$\begin{gathered} E_{spark} \sim E_C - E_{residual} = \frac{1}{2} C U_{bd}{}^2 - \frac{1}{2}\frac{Q_{residual}{}^2}{C} \\ where\ Q_{residual} = Q_{stored} - Q_{spark} = C U_{bd} - \int I_{spark}(t)dt \end{gathered} \tag{1.3}$$

Later, Bane [45], [46] continued the lane of work with other fuels and refining the statistical approach by the use of energy density, or spark energy over gap distance E_{spark}/d as reference. The spark energy was measured as before (equation (1.3)), with inter electrode gap from 1 to 11 mm, energies from 50 µJ to 2.4 mJ and discharge duration under 100 ns, for H_2-O_2-Ar mixtures, kerosene, C_6H_{14} and H_2.

As presented, many ignition studies employ only electrical measurements (E_{el} or E_c) as reference value for the discharge energy. But the electrical energy supplied to the electrodes or stocked in a capacitance differs from the value of the energy deposit in the fluid, as there are energy losses and electrical discharge characteristics that affect the energy transfer. Furthermore, changes in the electrical energy or discharge duration could change the energy deposit or the energy transfer efficiency. The energy deposit in the fluid would be a better choice as reference for combustion initiation.

1.2.2 Spark discharge and ignition modeling

Electrical discharges have been modeled by many studies, some of them oriented to provide initial conditions for combustion simulations, and few of them specifically about the electrical discharge phase. A complete model for the electrical discharge is very complicated to obtain, as the different processes involved in the discharge have very different natures and timescales. As represented schematically in Figure 1-4, these different processes are electron collisions (statistical events), plasma dynamics, ionization, chemistry, fluid dynamics... Most combustion simulations are based on an initial energy deposit or temperature profiles, and kernel volume as initial conditions [47].

Maly developed a thermal model for ignition and the early phase of flame front growth [48]. As a criterion for ignition was imposed that the energy balance within the outer shell of a spark plasma sphere should be identical to that found in a self-supporting, quasi-stationary expanding flame front. Neglecting diffusion and radiation, he related flame front growth to ignition energies and minimum ignition radii, assuming flame temperature (~2000 K) at the plasma shell. He estimated the temperature profiles for three possible discharge devices with the same E_{el} (30 mJ), only in breakdown mode, or mostly in arc or glow (with a 3 mJ breakdown in arc and glow cases). This illustrated how the discharge mode can affect ignition. Figure 1-8 shows a schema of the thermal model employed (a) and the temperature profiles of the flame kernels produced by different devices (b).

Using this model, he concluded that ignition energy is derived only from a narrow shell at the surface of the discharge plasma of width in the order of the flame front thickness. The time for transport of ignition energy is limited by the developing flame front velocity. Then not all the spark energy is useful for ignition, only the portion that can transfer to the outer shell of the expanding plasma. Also, a minimum plasma radius is required for successful ignition, independently of plasma geometry. To enhance ignition, energy should be introduced at the highest power and lowest duration possible. An excess in the energy deposit produces an increase in the initial reaction velocity.

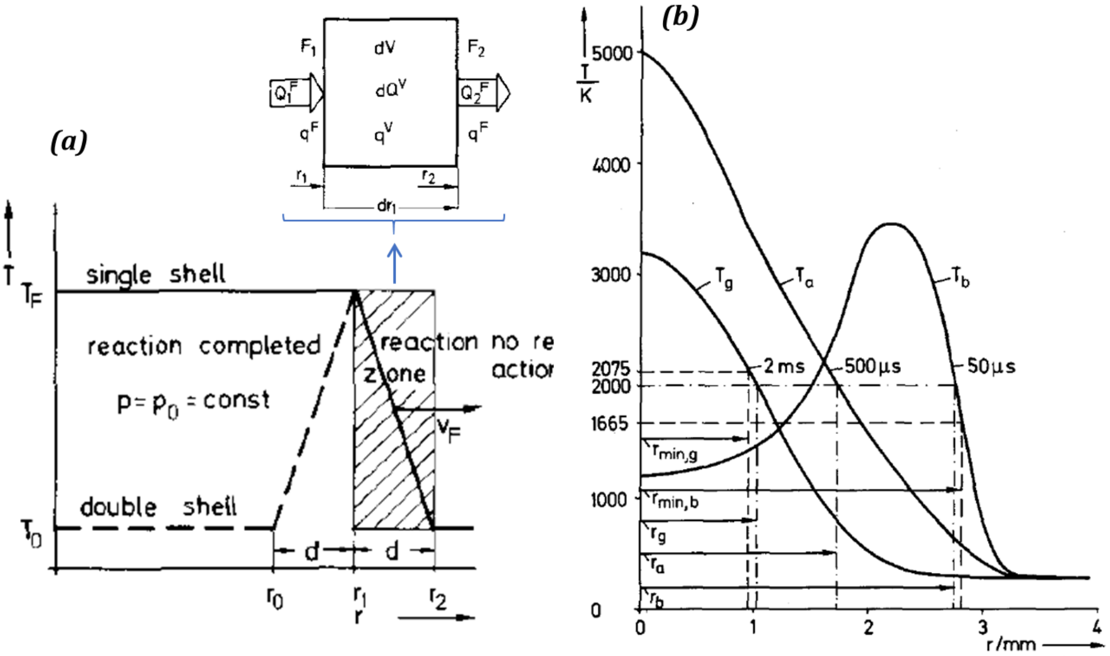

Figure 1-8: Thermal model or the plasma outer shell-reaction zone (a) and radial temperature profiles for three ignition devices at the indicated points of time after spark onset in methane-air (b)[48]. In (b), T_b= 30 mJ breakdown in 60 ns; T_a= CDI with 3 mJ for 100 µs + 30 mJ in arc for 230 µs, and Tg= 3 mJ for 100 µs + 30 mJ glow for 770 µs.

Sher and Keck simulated the evolution with time of a spark channel into a combustion wave [49], and studied the establishment period of the flame growth. A larger hot kernel volume in a shorter time increases the probability of self-sustained flame. The initial growing of the flame depends also on the methane-air mixture equivalence ratio (Φ), breakdown energy E_{bd} and spark duration. This model excluded the breakdown phase and used breakdown energy as input.

In the model developed by Ko [50], also for methane-air mixtures, kernel growth was simulated, taking into account breakdown. They based their model on their previous experimental results [51], employing a two-step process: a first step as a blast wave for $t < 10^{-5}\ s$; and a second step as a thermal diffusive growth with an electrical input power. Diffusive growth was formulated by integral approach, involving temperature dependence overall reaction kinetics and thermodiffusion model, quenching, discharge duration and electrode fall energy. They estimated the characteristic radius of the blast wave due to the quasi-instantaneous energy release by dimensional arguments.

Later, Sher and coworkers [7] used a 2 phases model for the electrical discharge. They evaluated thermodynamic properties and transport coefficients of the plasma arc, taking into account in their mathematical model molecular dissociation, ionization and various modes of energy stored in a molecule. The model consisted on a first phase ($t < 10^{-6}\ s$) as energy deposit in constant volume, followed by a sudden expansion phase after the shock wave. They established the initial conditions after the breakdown phase, depending on E_{bd} and maximum plasma temperature.

Another thermodynamical model of ignition and flame growth was developed by Anbarasu and co-workers [52] for different ignition systems (TCI and CDI). They modeled breakdown with a 1-D cylindrical unsteady lagrangian shock flow equation, and arc and glow phases as thermal diffusion phase. They treated the flame kernel as an open system, including the input discharge energy, heat loss to the spark plug, chemical heat release and expansion of the kernel; although they did not consider radiation nor shockwave losses. They found that pressure rise rate increases with increasing breakdown energy, and that a CDI system (higher power and less E_{el} than TCI) produces the same pressure peak as a TCI system.

Akram [53], [54] revised the macroscopic models for discharges, comparing and validating the eulerian and lagrangian approaches, and corrected the model from Plooster for the shockwave [55]–[57], who introduced an artificial viscosity term to the model to simulate the shockwave. The evolution of spark in air after breakdown was studied, taking breakdown energy as the initial input condition and electrical power input after breakdown accounted for in the energy balance. Their simulation provided results for temperature, density, gas flow and pressure from t = *5 to 100 µs* after the discharge onset, equivalent to short discharges under 100 µs duration. The influence of the shockwave was studied, tracking its radial position and introducing possible reflections in walls close to the spark. In another paper, Akram [58] presented the modeling of ultrafast electrical discharge during the early phase of its evolution (10 ns – 40 µs). It showed that electrode geometry is responsible for the development of flow structure, and that the heat transfer after 2 µs is dominated by convective diffusion.

Studies by Thiele et al. [59], [60] presented a numerical simulation of spark ignition including detailed chemistry, electrodynamics and ionization. Their model investigated times from the blast wave formation through to the early stages of flame development in methane/air mixtures.

Later, in 2007 Ekici *et al.* [61] presented a theoretical model to simulate spark discharge, for ultra-fast discharges (90 ns). They revised and compared different existing thermodynamic models, and compared their results for energy deposit (~14 mJ), blast wave radius and mass density. Figure 1-9 (b) represent the simulated evolution for hot kernel (T<2000 K) and shock wave after breakdown. A comparison of 1-D and 2-D models revealed that 1-D models predict well the evolution of high temperature regions until the recirculating flows begin (around ~10 μs after discharge start), which is observed in 2-D models. They estimated radiation losses to be around ~0.2 mJ and to happen mostly in the first instants, for the 14 mJ energy deposit. Conduction losses to the electrodes, observed only in 2-D models, represent almost a third of the energy deposit (~4 mJ). The results reported for shockwave and plasma radii evolution, temperature, flow velocity and pressure profiles in the first instants (up to $t = 15\,\mu s$) provide a good understanding of the dynamics of the spark discharge right after breakdown.

A theoretical study on flame formation by Eisazadeh-Far et al. [13] found that, for a high voltage capacitor discharge (equivalent to a CDI) a large part of the discharge energy is dissipated by cathode fall energy losses, and that radiation from the plasma is the most important source of energy losses. They developed a thermodynamical model of the spark, and verified its results with direct visualization. Inputs for this model were kernel radius, temperature and discharge energy. The efficiency of the energy transfer from E_{el} to E_{th} was estimated and compared to experimental results, as it shown in Table 1-1 for two different electrical energy levels. The efficiency values reported by two other references are reported as well.

	E_{el} = 24 mJ	E_{el} = 81 mJ
Cathode-Anode fall losses	26.6%	26%
Thermal boundary layer conduction	0.4%	1%
Radiation losses	48%	62%
Efficiency [13]	25%	11%
Teets and Sell [62]	24%	14%
Maly [2]	30%	-

Table 1-1: Sources of loss in the energy transfer and transfer efficiency [13] and comparison with other authors [2], [62].

The impact of plasma chemical kinetics was addressed by Collin-Bastiani and co-workers [63], who modeled the transition from plasma to an early flame kernel in a propane-air mixture by direct numerical simulation (DNS). The use of Analytically Reduced Chemistries (ARCs) allowed them to couple low temperature chemistry (representative of combustion) and plasma kinetics. They concluded that, as dissociation and ionization reactions are endothermic, taking into account those reactions lower the peak temperature in the ignition kernel. They remarked the sensitivity to input parameters such as the diameter of energy deposition in the cylindrical volume, which explained discrepancies of their results with experimental data.

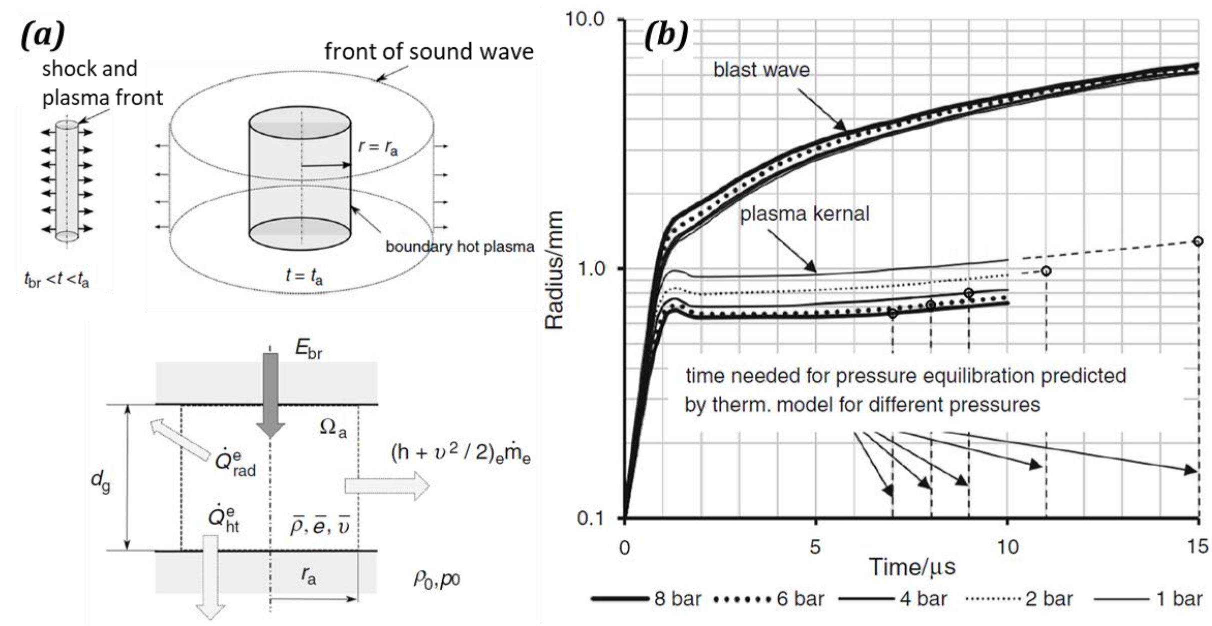

Figure 1-9: Thermodynamic model used by Meyer [15](a) and temporal evolution of plasma and blast wave radii at different pressures together with time needed for pressure equilibration [15], [61](b)

Recently, a thermodynamic model for the resulting gas conditions after a breakdown discharge was developed by Meyer and Wimmer [15]. A good review of the spark models is presented in their work, mentioning that the spark models had evolved little in the last 30 years and proposed an updated 0-D model, capable of providing a good estimation of the temporal evolution of gas properties during and after breakdown. They remarked that the efficiency of the energy transfer useful for ignition during breakdown is η_{bd} ~0.82, which cannot be measured experimentally. Their results for pressure, temperature and radius of the kernel over time, at different pressures, were contrasted with those of previous works [61]. They confirmed that changes in the breakdown energy had no influence in mean kernel temperatures, that only changed with pressure. A schema of the 0-D thermodynamical model is shown in Figure 1-9 (a), together with hot kernel and plasma radii temporal evolution from Ekici [61], showing Meyer's remarks on the time needed for pressure equilibration after the discharge in different conditions Figure 1-9 (b), which is estimated as $t = 15\ \mu s$ at 1 bar. The blastwave separates from the plasma kernel at around ~1 μs after discharge onset.

Modeling results provide a good insight on physical phenomena occurring during spark ignition, although simulations need reliable data as initial conditions and to verify the results.

1.2.3 Experiments on electrical discharges and ignition systems

Experimental investigations on spark ignition and electrical discharges are presented next, focusing on their metrology and main results. First, we review different studies that measured the energy deposit in the gas by electrical discharges using different calorimetry methods, which is described first. Second, we present works that measured discharge kernel properties and evolution employing different visualization techniques. And last, we summarize investigations that studied discharges produced by different ignition systems, both from automobile and from aeronautic applications.

1.2.3.1 Energy deposit - Calorimetry

Calorimetry measures the energy increase associated to a thermal event. In the case of electrical discharges, calorimetry has been employed to estimate the deposit of thermal energy in the fluid; i.e. the electrical energy supplied to the electrodes after transfer losses.

Principally, calorimetry is performed inside a caloric vessel, where one measures the increase in temperature, pressure or volume caused by a discharge to later calculate the associated energy deposit.

First calorimetry measurements of spark discharges date from almost one century ago. A first attempt to measure the thermal energy deposited by ignition sparks was performed in 1920 [64]. They measured the heat energy of aviation igniters for alternative engines of that time, with an inter-electrode gap of 2.1 mm. They employed a repetitive discharge inside a metallic chamber at 500 to 2500 runs per minute for at least 10 minutes, measured the increase in temperature of the metallic chamber after the test, and averaged the energy deposit for one spark. The issue with this method is that repetitive discharges at that rate are influenced by previous discharges, with changes in gas conditions (temperature, presence of metastable molecules), and differences between two single sparks are neglected this way. Kumagai [65] used a similar approach, although in a heat-conductive chamber surrounded with water and at lower rates.

Roth and co-workers [66] used for the first time constant volume and constant pressure calorimetry for electrical discharges: Constant volume calorimetry (or pressure rise calorimetry) measures the transient pressure increase inside a closed vessel using a pressure transducer, and constant pressure calorimetry measures the volume change in the vessel by the movement of a droplet in a capillarity tube attached to the vessel. They employed these techniques to measure discharge energy deposits and estimate losses to electrodes in monoatomic gases, for low energy discharges ($E_{el} = 0.1 - 2\,mJ$) and Pt electrodes. They found that heat loss rate increased with decreasing pressure and gap length, and with increasing electrode diameter and gas conductivity.

Merritt [67] adapted the pressure rise calorimeter from Roth to the usage of a common differential pressure transducer, and proposed the adapted usage with commercial available elements for the measurement of the energy released by a single spark, in air or other gas. The technique was used by Saggau [12] to measure the energy transfer efficiency, η, for different electrode materials and for the three discharge modes individually, with the highest value for breakdown and the lowest for the glow discharge and varying with the energy supply, as in Figure 1-10 (a).

Pressure rise calorimetry was also employed by Teets and Sell [62] for different spark plugs: a commercial TCI (non-resistive), a commercial TCI with sharpened electrodes, a plasma jet and an ultra-short discharge igniter (breakdown only). They varied the electrical energy E_{el} and pressure, from 1 to 7 bar. For the conventional TCI the energy delivered to the gas was found to depend strongly on the pressure and the gap spacing. The results ranged from 1.4 mJ for

1 atm and a 1 mm gap to 15.8 mJ for 7 atm and a 2 mm gap. The corresponding efficiencies were 5% and 65%, respectively, as shown in Figure 1-10 (b).

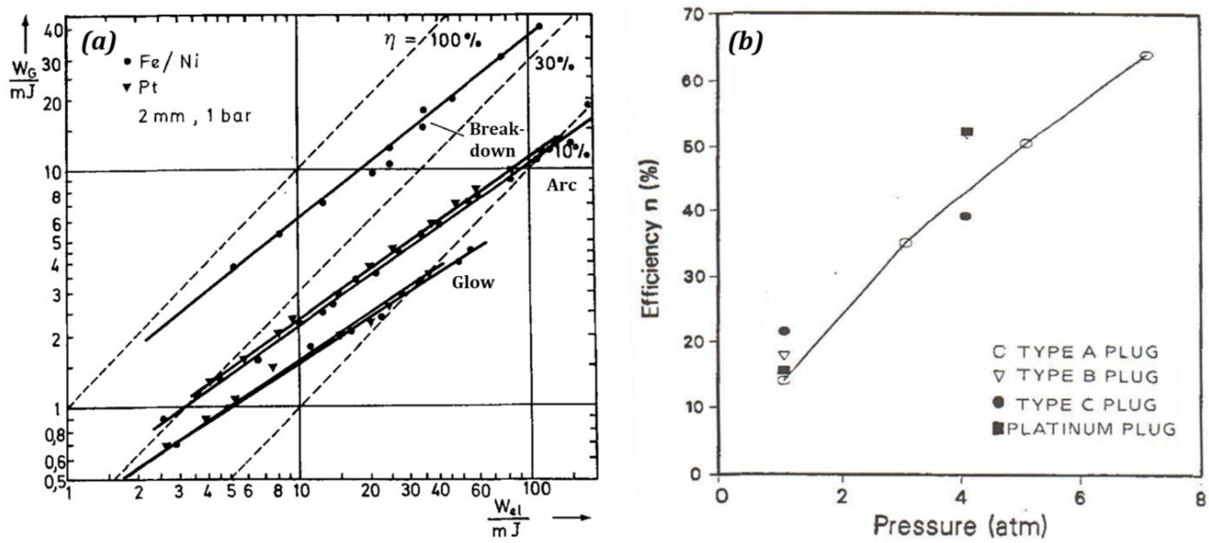

Figure 1-10: Electrical discharge efficiency for the three discharge modes (a)[12] and for different pressures (b)[62].

Pressure rise calorimetry has been applied to other discharge systems, as did Reinmann and Akram [68] to validate a thermodynamic model of the discharge for ultra-fast discharges. They employed a small volume caloric chamber (1 cm^3) and pin-to-pin electrodes, although the electrode diameter in their experiment was half of the diameter they employed at their model, so it was not a reliable comparison as electrode geometry affect the electrical discharges.

Other ignitions systems have been studied for their application on internal combustion engines. Wolk and Ekoto [69] studied Pulsed Nanosecond Discharges (PND) at high pressures by pressure rise calorimetry and atomic oxygen Laser Induced Fluorescence. Single and multi-pulse PND discharges are compared to discharges with secondary streamer breakdown. In a first study [69], a pair of pin-to-pin electrodes with 1 to 5 mm gaps are tested, in a range from 1 to 5 bar of pressure. The PND discharge produced almost no heating of the gas, with little energy transformed into the energy deposit (with $E_{th} < 5\% \ E_{el}$). Instead, O-LIF results showed that substantial O-atom populations are generated for hundreds of μs, which enhances combustion. In a second study [70], the impact of variations in the gas was assessed. They performed calorimetry and O-LIF experiments in CO_2-O_2-H_2O mixtures, varying their mole fractions, at up to 9 bar and 70 ºC. The anode-only configuration was compared to the anode-cathode configuration. While with the anode only configuration PND were more consistent, the anode-cathode configuration produced more radicals in the fluid, as excited O-atom production is concentrated near the anode and the cathode.

The energy deposited in air by three different ignition systems was studied recently by Grimaldi and co-workers [71]. They tested a single spark system, a multiple spark system and an Advanced Corona Ignition System (radio-frequency igniter with $f_R \sim 1\ MHz$); at three chamber pressures (1, 5 and 10 bar). The electrical energy was measured at the primary circuit, as the aim of the study was to measure the performance of the full ignition system and not only the electrical to thermal energy transfer at the electrodes. The single and multiple spark systems showed an increase in E_{th} with increasing pressure. For the radio-frequency corona system only the supply voltage offset was varied, with a different appropriate voltage offset window – which produce a non-arced discharge - for each pressure. E_{th} depends on the offset voltage, with a large interval of available energy deposit between 0.2 and 65 mJ.

1.2.3.1.1 Shockwave energy

During the breakdown phase, part of the energy delivered to the fluid is lost to the generated shockwave. The expansion rate of the shockwave caused by electrical discharges was described by [72], simulated in several models and it can be seen in the first moments of the discharge in visualization experiments (1 to tens of µs); but the energy dissipated in the shockwave E_{sw} is complicated to measure.

Liu and Zhang [73] estimated this energy for high energy electrical capacitive discharges (with an E_C of 10 to 1000 J, with the E_C defined in eq. (1.3)). They only tested high energy sparks because the aim of the study was to provide a tool for calculating the shock wave energy for detonation initiation from electrical energy measurements. The shock wave energy released from the electric spark discharge process was calculated by using the overpressure values at different measurement points near the electric spark discharge center (2 to 11 cm away), applying weak shock wave theory. The electrical energy E_{el} was measured from the current signal and the spark resistance; E_{el} was found to be between a 69 and 82% of the stored energy E_C. The shockwave energy is only a small fraction of the electrical energy: E_{sw} = 2% - 2.2% E_{el} for the high energy sparks tested.

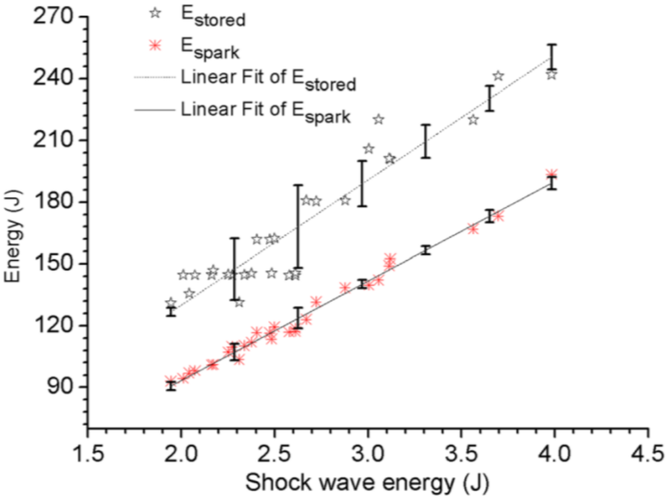

Figure 1-11: Variations in E_c and E_{el} with Shock wave energy E_{sw} (for a capacitance C100J=3.998 µF) [73]

Recently, Peters et al. [74] investigated laser-induced shock waves in air, CH_4/N_2, CH_4/air and biogas/air experimentally (visualization) and by CFD simulation. They used the blast wave theory by Jones to capture the mechanics of the shock waves and to estimate the energy required for shock generation. Single-color interferometry measurements showed that reactive mixtures showed a stronger shock front and larger low-density region in the plasma kernel. Two-color interferometry was utilized to obtain density profiles through a cross section of the plasma kernel for various times after breakdown. An extremely low density was measured in the center of the plasma kernel, increasing sharply until peaking at the shock front. Shock wave energy was estimated to be a large portion of the energy absorbed by the fluid (with values of up to 90%) for laser ignition.

1.2.3.2 Discharge kernel and early flame visualization – Optical methods

Many optical methods have been applied to the study of the electrical discharges and the early flame kernel. Some of these studies are mentioned here, remarking their main findings but without an in-depth description of the experimental methods. For more details about the optical methods and their application one can refer to [75], [76].

In a first approach by interferometry, three discharge modes were tested by Maly and Vogel [5] in methane-air mixtures at 4 bar. The interferometry image fringes displacement allow a measurement of the refractive index, which was related to density. Using an inverse Abel transformation, they measured the hot kernel temperature distribution, for temperatures up to 2500 K. For higher temperatures, they measured rotational temperature by spectroscopy. They found that temperature does not depend on breakdown energy; instead an increase in breakdown energy increases the conductive channel diameter. Temperatures in the expanding shell for high enough energy inputs are of ~ 4000 K. They concluded that as the flame starts around t ~ 30 μs, energy in glow discharge does not reach the inflammability zone, while energy in arc mode produced an increase in the active zone radius. Representative interferograms are shown in Figure 1-12(a).

Ziegler, Wagner and Maly [77] then used electrical measurements and schlieren visualization to estimate the energy in the electrode falls and in the positive column, for pin-to-pin electrodes of different materials (Al, Cd, Cu, Pt, W) and in methane-air mixtures. Measurements indicated that energy dissipated in the anode and cathode fall is completely lost to the electrodes, whereas the energy of the positive column determines the flame initiation process. Ko [51] employed the same methods (schlieren and electrical measurements) in CH4-air mixtures. The work was focused on the equivalent kernel radius, near MIE conditions for different gaps and discharge durations, to investigate the influence of the critical radius on kernel growth and to develop a spark ignition model based on their results [50].

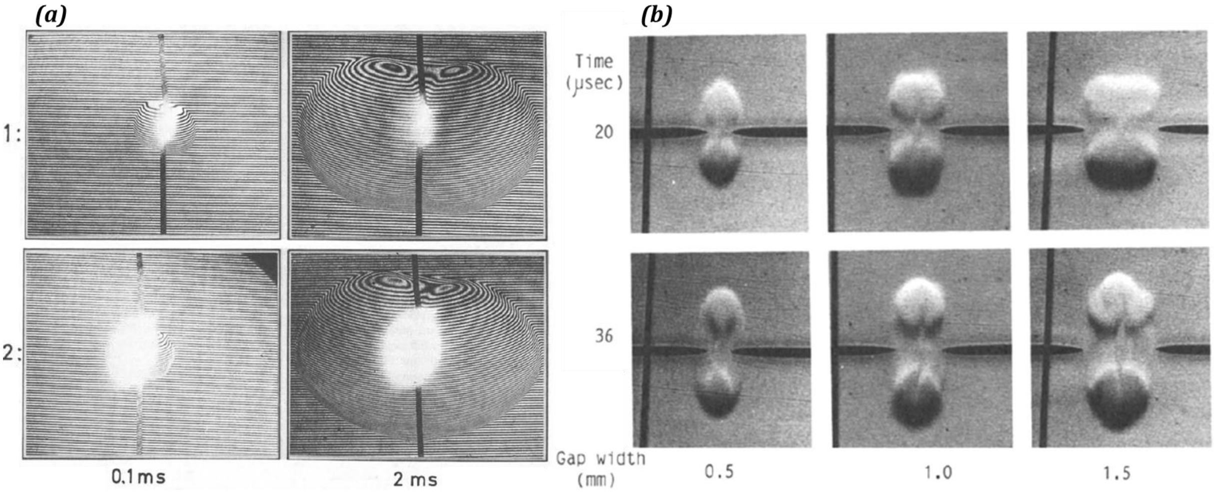

Figure 1-12: Interferograms of differently activated volumes in CH_4-air mixture at 4 bar, where 1: 3 mJ CDI and 2: 3 mJ CDI + 30 mJ arc (a)[5]; and Schlieren photographs of spark kernels in air for different gaps and a 4.6 mJ discharge (b)[78].

Kono and co-workers [78] investigated the kernel originated by short sparks (E_{el} < 5 mJ, duration < 0.3 μs). They developed a 2-D cylindrical model for kernel formation, which was validated by experiments. They observed by schlieren the kernel structure and validated the modeled velocity fields, and measured the temperature field by interferometry. It was shown that gas flow produced by secondary effect of shockwave is the main cause for specific kernel configurations: kernel shape in incipient stage is either a torus, a torus with a groove within the ring, or a non-toroidal shape. Toroidal kernel development is shown in Figure 1-12(b).

Borghese et al. [79] employed Rayleigh light scattering technique to measure density distributions for the first moments of the discharge (t < 15 μs), and schlieren technique to obtain a qualitative description of the perturbed gas volume. The electrical discharge studied was a fast discharge (t<100 ns), with an energy of no more than 14 mJ, a pair of pin-to-pin electrodes and in pure nitrogen. In their experimental conditions the time scales of the nitrogen recombination and of the establishment of fresh gas recirculation into the excited kernel turn out to be comparable (tens of microseconds): thus the energy transfer from the excited species to cold gas is not limited to the outer shell of the hot channel, but occurs also inside the hot kernel.

An optical method for measuring the energy deposit was presented by Verhoeven [80], the interferometric spark calorimetry. With a good estimated accuracy, this method limitations lay in the laser ray crossing in high pressures or at the first moments of the discharge. It was thus possible to measure at 1-5 ms in atmospheric conditions, but only after 10 ms in higher pressures; and also in the interference with the electrodes, so an image reconstruction is necessary in discharges without flowing gas. In [81] he presented a parametric study varying flow speed (0 to 6 m/s), electrode gap (1-3 mm), electrode diameter (0.5-2 mm) pressure (1-8 bar) and gas (air or propane-nitrogen mixture). Thermal energy is calculated after the reconstruction of a phase shift map from three different images, using a quasi-heterodyne technique and three different images with different relative phases. The estimated thermal efficiency was of 26% for a 2 mm gap and 2 mm diameter electrodes, which disagrees with data from other authors, and the partial efficiencies for arc and glow phases were estimated at 30% and 33%, also differing from estimations for Saggau [12]. They employed a TCI system, which presented run-to-run variability because of changes in the arc and glow percentage in the discharge. Arc phase detection was done by a time window and not voltage levels, and little variation in arc and glow % were observed.

Dreizler [82] employed planar laser-induced fluorescence of the OH to characterize spark ignition, obtaining flame front velocities and OH radical distributions at different instants of time per test. Their research team studied spark ignition of H_2-air [83], comparing results of a 2-D model, shapes of the early flame kernels from PLIF-OH imaging and temperature measurements within the flame kernel from vibrational coherent anti-Stokes Raman spectroscopy (CARS) of nitrogen. The electrical sparks they employed consisted on a 150 ns breakdown plus a 55 or 110 μs arc phase, with an electrical energy of E_{el}=8.7 mJ (and estimated E_{th} ~4.5 mJ). They investigated heat conduction to the electrodes, for different electrode shapes, and different equivalent ratios.

The effect of electrode geometry on spark ignition was also studied by Bane et al. [84], who modeled and observed with high speed schlieren a low energy (~2 mJ) fast discharge (< 100 ns duration) in H_2-O_2-Ar mixtures. They compared three different electrode geometries: thin cylindrical, conic, and flanged electrodes; and discussed the influence of pressure gradients, viscous effects and flow confinement on kernel early development. Fluid dynamics in the spark kernel were analyzed, showing the initial blast wave followed by a rarefaction wave, which produces the creation of two vortex (toroidal vortex) close to each other next to each electrode tip. Schlieren images and simulation results are shown in Figure 1-13.

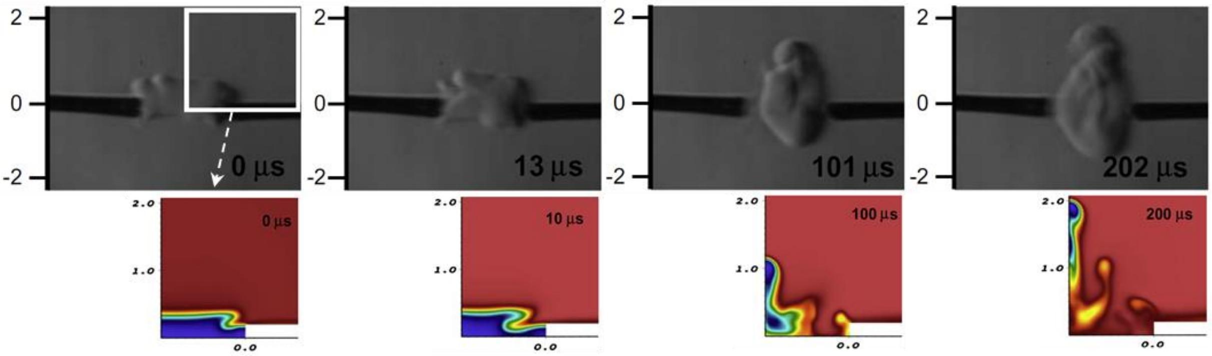

Figure 1-13: Images from high-speed schlieren visualization (upper row) and simulation (lower row) for a 2 mJ spark discharge in air with cylindrical electrodes [84].

Gas temperature of capacitance spark discharges in air was measured by Ono [85], for low energy fast discharges (E_{el}~0.03-1 mJ, duration < 100 ns). The rotational and vibrational temperatures of the nitrogen molecule were measured by spectrometry, and estimated to be 500 and 5000 K respectively, and independently of the discharge energy. Laser-Induced Fluorescence of OH radicals was employed also to measure the gas temperature after discharge, and it was found to increase after discharge until it reached 1000 K at 3 ms after the discharge.

For high energy short duration sparks, Sforzo [86] presented simulation and visualization results for size, shape and temperature of the kernel, up to 200 μs after discharge onset. The discharges were produced by a capacitive system, of $E_{el} \sim 0.25$ J, with a duration of 0.3 to 0.5 μs and in cross-flow conditions. The development of the discharge kernel was visualized using high-speed schlieren for $t < 300$ μs. For the energetic discharge, similar in order of E_{el} to aircraft igniters, it was found that superequilibrium O atom levels remain significant even at lower temperature (800 K), which enhances ignition even at that temperature.

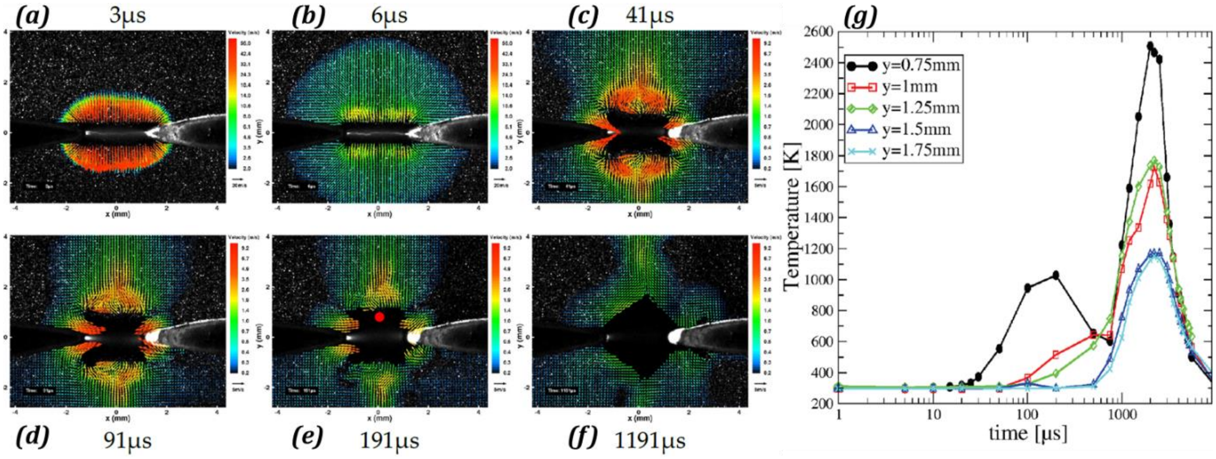

Figure 1-14: Gas velocity fields surrounding the spark after breakdown in quiescent air measured by PIV (a-f) and temperature evolution with time along a vertical profile in the center plane measured by SRS (g); all from [87].

In a study by Lacour and co-workers, [87] a discharge generated by a commercial automobile TCI pencil coil is characterized in a laminar flow. Gas velocity is measured using Particle Image Velocimetry, and temperature fields using Spontaneous Raman Scattering (SRS). The discharge electrical energy is 81 mJ, and it is produced between pin-to-pin electrodes with a 3 mm gap. PIV observations showed a strong modification of gas flow surrounding the spark, with fresh air entering toward the spark central area after the shock wave and rarefaction wave. SRS measurements of the time evolution of temperature show a first convective heating of the gas surrounding the spark, induced by the rapid expansion of the hot gas channel leaving the gap following the shock wave. A second temperature rise corresponds to the conductive heating of the gas by the remaining glow discharge. Figure 1-14 shows velocity fields in quiescent air obtained by PIV – where one can observe the initial shockwave and the cold gas recirculation- and the temperature evolution in the central plane (red dot in image (e)) measured by SRS.

PIV was also employed by Singh et al. [88] to quantify the velocity field induced by a spark discharge plasma. The effect of the electrode gap on the induced flow field was studied for electrode gaps of 2, 5 and 8 mm. They identified three stages of flow evolution for the longer gaps: first, the appearance of coherent vortices near the electrode tips (100 μs for the 5 mm gap); second, the entrainment of flow along the electrodes, resembling two axial jets (200 μs); and third, the jets collide in the electrode gap, with a decay in overall vorticity. In a recent study [89] they coupled the PIV method with a numerical study and Background Oriented Schlieren (BOS) measurements, for Nanosecond Repetitive Pulsed Discharges (NRPD) in conic end electrodes and a 5 mm gap. For the first stages of the discharge (t <100 μs), the induced flow was studied via numerical simulation and planar PIV at 100 kHz. For later stages

(t >100 µs), Stereoscopic PIV at 10 kHz and BOS were employed to obtain the velocity fields and density distribution respectively. In the first moments they observed the formation of a cylindrical shockwave, which was one of the primary sources of vorticity generation and induced high speed radial motion at t<10 µs. They also detected vorticity patches near the surface of the electrodes in addition to vorticity in the larger flow structures (the pair of vortex rings) around 60 µs after spark onset. Kernel density was obtained with BOS measurements (using Abel inversion and Dirichlet boundary conditions), with the minimum kernel density decreasing with increasing energy deposited in the plasma.

1.2.3.3 Ignition systems tested

Many studies focused on the characterization of ignition systems, either regarding their ignition capabilities directly (related to combustion and MIE with those igniters or if they perform properly in lean mixtures, for example) or regarding the properties of the electrical discharge that they produce. First, studies with automobile applications and characteristic sparks are presented, and then, studies with aircraft engine applications.

1.2.3.3.1 Automotive applications

Dale et al. [90] reviewed progress on alternative ignition systems that supply higher energy sparks and sparks with a more efficient energy transfer to the gas. TCI and CDI systems are presented and compared together with high energy breakdown ignition systems, and plasma jet igniters.

In a study by Franke and Reinmann [91], the energy deposited in the gas by a broad range of ignition systems was measured by calorimetry. Electrical energy was measured before the spark plug, which was a commercial automobile spark plug (NGK, 4.7 kΩ of internal resistance, 1 mm gap and 2.5 and 2.8 mm of electrode diameters). They tested two capacitive systems and three inductive systems. The experiments were performed in nitrogen, and in pressures from 1 to 16 bar. The electrical power input was compared to the thermal deposit, and instantaneous and global conversion efficiency was estimated. The energy deposit measured ranged from 0.5 to 2.5 mJ at 1 bar and from 1 to 4 mJ at 2 bar, and low efficiency characterizes this spark plug due to the high internal resistance, which serves to dump electromagnetic interference and reduce the arc phase to reduce electrode wearing.

Mitianiec [92] studied factors that determine ignition and efficient combustion, studying the application of compressed natural gas (CNG) to internal combustion engines. Experimental works were performed with CNG in a caloric chamber in normal engine conditions, which is ~25 bar for CNG. The automobile igniter used presented thermal efficiencies lower than 1% at 1 bar and up to 15% at 25 bar, with an increase in efficiency when thin electrodes are used. The energy balance during ignition was presented, with a thermal energy of ~7% and calculated losses: radiation (12.7%), ionization during breakdown (11.8%), heat transfer to the electrodes (50.8%), kinetic energy (turbulence, 14.7%); although without considering directly electrode fall losses (included in the heat transfer) or shockwave losses, and a part of the ionization energy is actually useful for ignition.

For conventional internal combustion engines, recent works have presented optical studies of spark ignition, as the work from Kastengren et al. [93]. They presented X-Ray measurements, at different points in space, averaged for each point over several discharges for the same conditions. Using the X-ray, they obtained an averaged density distribution, the displaced path-length of ambient gas, and the total integrated volume displacement of gas. From the total integrated volume displacement, they estimated the thermal energy increase (~E_{th}) of 2 mJ. Their electrical measurements could not provide the E_{el} supply, as current was measured at the primary circuit and voltage at the secondary. They found that the spatial structure of the plasma varied between Ar and air, suggesting that the ionization potential of the gas may be an important factor. Thermal energy and volume displacement peaked around 1 ms after discharge onset and relaxed back to equilibrium after tens of milliseconds.

Kawahara and coworkers [94] coupled a conventional spark plug with optical fiber and performed measurements of the emission intensities from OH, NH and CN radicals produced during spark discharge. A fiber-optic spark-plug sensor was developed for application to practical spark-ignition engines. They employed this setup in another study [95] to investigate the spark discharge ignition process using simultaneous temperature measurements of the spark discharges and the initial flame kernel. They measured a time series of emission spectra from the spark discharge and initial flame kernel inside a spark-ignition engine (a Compression-Expansion Machine). The plasma vibrational temperature of the spark discharge was measured using time series emission spectra from the CN* radical, and the gas rotational temperature of the initial flame kernel was measured using emission spectra from OH* radicals. Plasma vibrational temperature of the spark discharge was nearly 6800 K, and gas temperature of the initial flame kernel approached that of the adiabatic flame temperature.

1.2.3.3.2 Aircraft ignition systems

First measurements of the heat energy of aviation alternative ignition systems were found in [64], with ignition systems resembling commercial automobile systems. Foster and Straight [96] tested various igniters and their effect on MIE, including surface-type aircraft igniters, although only E_{el} was measured in this study.

In modern aircraft engines, the “sunken igniter” configuration is employed. It consists on a high energy capacitive ignition system, with coaxial electrodes: the central electrode being the high voltage electrode and the cylinder wall the mass electrode. A ceramic part is used as insulator, with a dielectric part on it in some configurations to lower breakdown voltage. A high energy discharge is produced at the surface of the spark plug. It is depicted inside the combustion chamber in Figure 1-15, from a patent for the ignition start design [97].

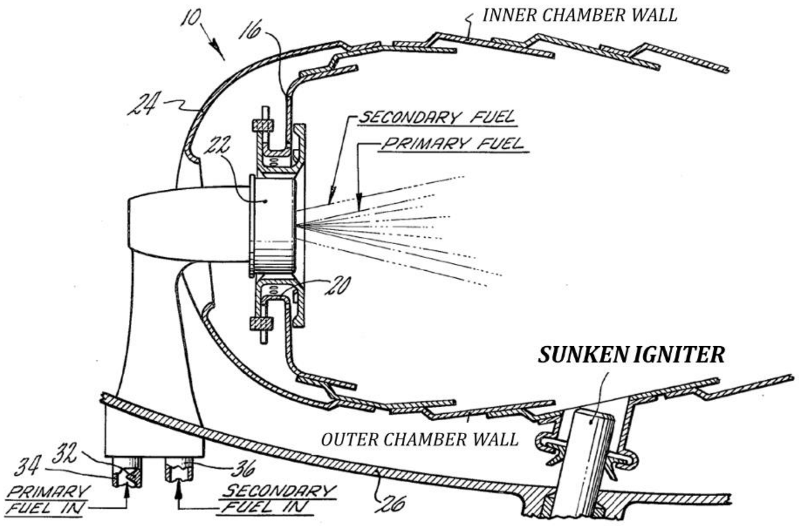

Figure 1-15: Gas Engine combustion chamber and sunken igniter [97]

Naegeli and Lee carried out an ignition study using a gas turbine combustor [98]. They employed a modified combustor from the T63 aircraft engine and employed high-speed photography and a hot film anemometer to study ignition conditions for gas turbines. The igniter spark electrical energy E_{el} was 0.87 J, and it worked at 8 Hz. Gas velocities near the igniter gap were measured with a modified igniter, in which the inner electrode was replaced by the anemometer. Gas velocities near the gap were found to be proportional to reference gas velocity in the combustor. From the high-speed photography, they observed brightness up to 2 ms for spark duration. Then tests showed significant delays (< 13 ms) from the formation of the ignition kernel to the onset of visible flame radiation for the limiting ignition condition, which led them to the conclusion that many of the critical steps for ignition occur at temperatures lower than the adiabatic flame temperature.

A different visualization method was applied to discharges by Blunck et al. [99]: using an infrared camera, narrowband radiation intensity measurements can be treated by an inverse deconvolution to obtain the energy and path integrated temperature of the hot kernel. In this study, they measured temperature, energy, energy decay and kernel structure over time for a plasma jet igniter.

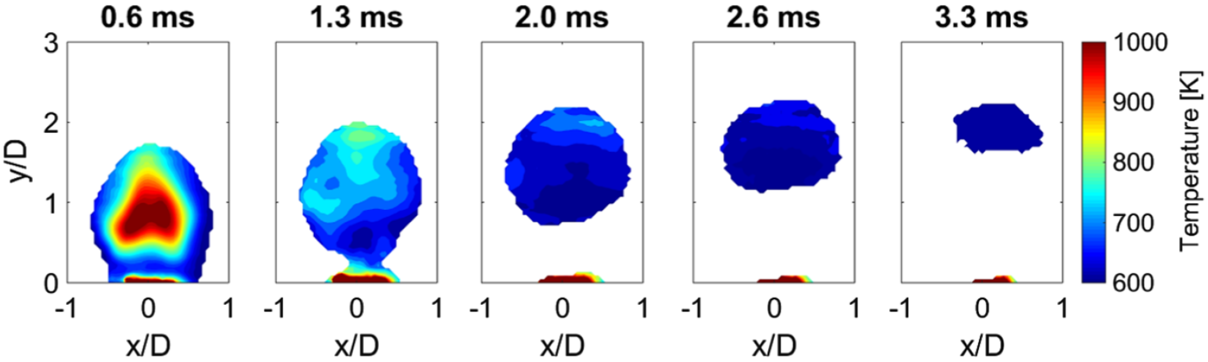

Figure 1-16: Phase averaged temperatures for the sunken igniter discharge kernel in air[19]

The infrared camera and narrowband radiation intensity measurements were also employed later by the same research team to study a gas turbine engine igniter [19], with an input E_{el} of ~10 J per pulse. Because of an intense light emission at the first moments of the discharge, measurements were made only after 0.6 ms, and up to 3.3 ms after discharge start. They found averaged temperatures T ~1250 K at t=0.6 ms after discharge, although this value was underestimated in around 100 K as a result of the deconvolution step. The kernel developed into a toroidal structure both in quiescent and crossflow conditions. Figure 1-16 depicts the phase averaged temperatures at different times after discharge onset [19]. One can observe kernel projection away from the igniter (with igniter surface on the bottom of the images), as well as the toroidal development of the kernel.

1.3 Conclusion and Motivations

When the electrical voltage between two electrodes increases, the electrical field in the inter-electrode gap rises. As the voltage reaches the breakdown value for the gas conditions, the gas in the gap is ionized and a conductive channel forms. Electrical energy stored in the gap discharges then in the fast breakdown phase, and if the electrical circuit connected to the electrodes has more energy stored, this stocked energy discharges in the following arc and glow phases. Commercial automobile ignition systems use either an electrical capacity (CDI systems) or a coil (TCI systems) to produce electrical discharges, while gas turbine engine igniters consist on a high energy capacitive system and a coaxial spark plug. Other ignition systems, currently in the final steps of development, utilize non-equilibrium plasmas or laser for ignition.

Electrical discharges for spark ignition have been widely studied. Still, in many ignition studies the spark energy is characterized as the electrical energy supply to the electrodes (E_{el}) or the energy stored in the capacitor of the electrical circuit (E_c), instead of the energy delivered to the fluid by the discharge. This energy deposit is estimated as the thermal energy increase in the gas (E_{th}), and was the subject of only a few studies. For electrical discharge and ignition modeling, the thermal energy deposit is needed to start the simulations or verify the results, together with early kernel spatial evolution. The energy transfer is produced differently in the different discharge phases, with few studies that measured arc and glow efficiencies.

Although many published works on the electrical discharges characterize discharge properties, kernel evolution, and – to a lesser extent– energy transfer from electrical supply to thermal deposit; experimental works on available ignition systems rarely study simultaneously the thermal energy deposit and kernel evolution. The authors found that a methodology able to fully characterize electrical discharges and kernel formation is desirable for the study of new ignition systems.

Chapter 2

Materials and Experimental setup

Contents

2 Materials and Experimental setup

This chapter describes the ignition systems, materials and experimental setup that are employed in this study. Firstly, we present the ignition systems and its electrical discharges, in §2.1. Secondly, we introduce the experimental methods used to study the discharges. The choice of appropriate measurement equipment and the dimensioning of the experimental setup are justified in §2.2. Finally, the measuring probes, the experimental vessels and configurations are described in §2.3.

2.1 Electrical discharge generation systems

To generate an electrical spark three basic elements are needed: a spark plug, a power source, and an electric circuit able to supply the spark plug with proper conditions for the discharge. In this study we used three discharge generation systems: pin-to-pin electrodes associated with an inductive circuit, helicopter igniter using a capacitive circuit, and finally a radio frequency spark plug supplied with a high frequency high voltage circuit.

2.1.1 Pin-to-pin electrodes

Discharge is produced between two tungsten E3® electrodes. With a 2 mm diameter and a conic tip that has an 11.25° half angle, their axes are aligned. A Transistorized Coil Ignition system (or TCI, pencil coil ZSE 041, BERU) transforms the 12 V DC electric voltage into transient high voltage at the electrodes. A Selectronic SL-1730SL20A DC source provides the 12 V, and a rectangular signal generator is used to trig the electrical discharge. The trigger signal controls the TCI coil charging time: the charge starts with the leading edge of the square trigger signal and ends with the trailing edge, when the electrical discharge starts, or with coil saturation if the trigger square signal lasts longer than the coil full charge duration. The energy supply to the electrodes can then be regulated by varying trigger signal width.

Pin-to-pin electrodes represent the canonical academic case for electrical discharge study. This setup is usually chosen to validate the experimental setup and for reference results. It represents the convenient configuration for visualization techniques as the conductive channel is always located at the same place. Commercial applications do not use pin-to-pin electrodes due to the high wearing of the electrode tips, but the inductive TCI system is the same that one can find in automotive applications.

The TCI system delivers around 50 mJ of electrical energy at the electrodes per discharge. Duration of the discharges is of the order of 2.5 ms. Electrical voltage and current are, respectively, lower than 400 V and 2 A for most of the discharge, with an initial voltage peak of tens of kV during breakdown phase.

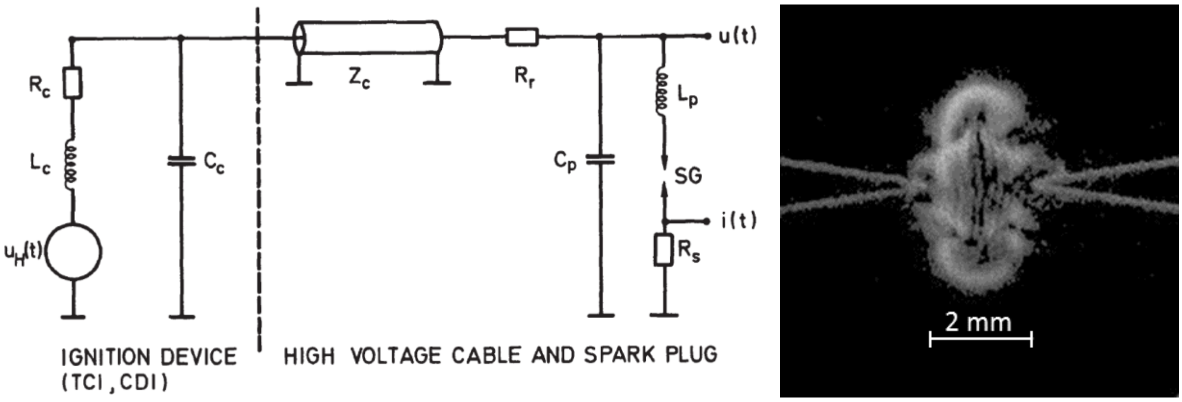

Figure 2-1: Schematic equivalent circuit of technical ignition systems[2] and schlieren image of a pin-to-pin electrodes discharge with TCI circuit and a 2 mm inter-electrode gap.

Figure 2-1 shows, on the left, the equivalent circuit for TCI and CDI systems, as described by Maly [2]. For the circuit: $u_H(t)$ represents the high-voltage signal, L_C the coil inductance, R_C the coil resistance, C_C the coil capacitor, Z_C the high-voltage cable impedance, R_r the radio interference damping resistor, C_p the plug capacitor, L_p the plug inductance, and R_s the current shunt (if present for measuring purposes); and for the spark gap: SG represents the spark gap, $u(t)$ the spark voltage, and $i(t)$ the spark current. On the right a schlieren visualization of a pin-to-pin electrodes discharge with a TCI circuit, for a 2 mm inter-electrode gap.

2.1.2 Coaxial spark plug discharge

This discharge is produced by a standard helicopter igniter (helicopter Ardiden 3G, Meggitt ignition system). This consists of a spark plug and a capacitive circuit. The spark plug is cylindrical, with the cylinder wall as the ground electrode and the cylinder axis as the high voltage electrode (see Figure 2-2). The electrodes are isolated by ceramic reducing the requirement of insulation during engine working conditions at high temperatures. A semi-conductive deposit on the ceramic insulator surface between electrodes reduces the spark voltage required for breakdown (down to around 750 V).

The spark plug is shown in Figure 2-2(left), together with a schematic view of the electrode setup (middle) and a schlieren visualization of the discharge (right) which creates a strong shockwave due to its high power. The diameter of the plug is 8 mm. The in-built capacitive circuit supplies the high voltage for the electrical discharge with a frequency from 5 to 10 Hz in the standard configuration. Frequency of the discharge is controlled by the DC voltage input, which can be from 12 to 24 V – higher voltage corresponds to higher frequency-. An electrical relay is added at the electronic device entry to enable a single spark trigger and to insure an accurate control of the discharge timing. In some cases, an adapter was included between the high voltage coaxial wire and the spark plug to allow electrical measurements. The power source and equivalent electric circuit are similar to that of the pin-to-pin electrodes (Figure 2-1), as it represents both a TCI (pencil coil) and a CDI system (helicopter igniter).

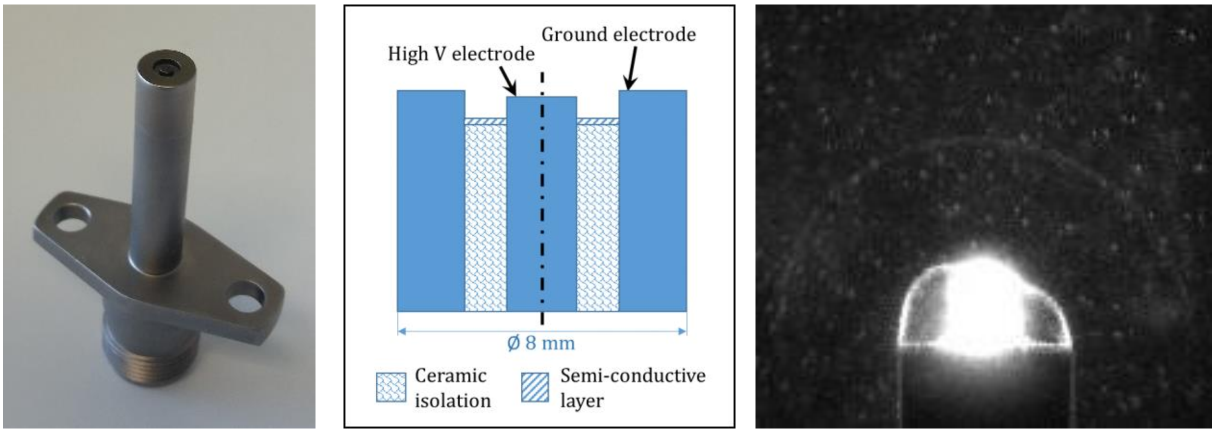

Figure 2-2: Ardiden 3 helicopter engine igniter spark plug (left), spark plug cutaway view (middle) and schlieren acquisition of an electrical discharge (right).

R. George studied a similar spark plug in his PhD thesis [36]. This device corresponds to an earlier version (1991) than the one used in our study, but electrical energy and discharge duration are representative for this type of discharge. Indeed, a discharge requires around 700 mJ of electrical energy supplied to the electrodes, and the magnitude order of its duration is 100 µs. Voltage peaks up to several kV at the beginning of the discharge (~5 kV during breakdown for their device), and electrical current is high, up to few hundreds of amperes.

2.1.3 Radiofrequency discharge

Cold plasma discharge is produced by a radiofrequency spark plug. This device works producing high voltage at one electrode tip to produce a streamer. Then it changes voltage polarization to propagate the streamer. Changing voltage polarization at high frequency (~5 MHz) makes the streamer grow and bifurcate, increasing discharge volume and maintaining a cold plasma channel. An in-depth work from Auzas [24] characterizes the functioning of this spark plug. The high frequency electrical voltage and current change polarization at ~5 MHz, with an amplitude of tens of kV for the voltage, and tens of mA for the current. Discharge duration can be regulated from hundreds of µs to few ms, and the electrical energy supplied to the electrode varies with duration. Typically, an energy of 70 mJ is reported for a 200 µs discharge [24]. Figure 2-3 shows a schematic equivalent circuit of the RF igniter (left) and a picture of a radiofrequency discharge in air in atmospheric conditions (right), with ~1 cm length discharge filaments at 1 bar.

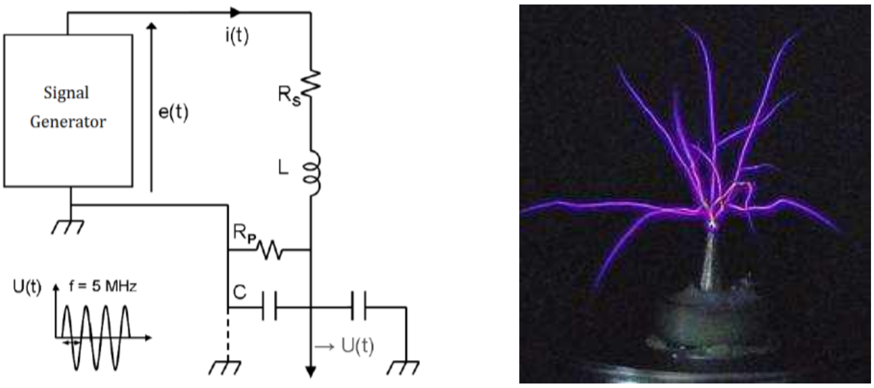

Figure 2-3: Radio-frequency igniter equivalent electric circuit (left) and picture of a radio-frequency discharge in air and atmospheric conditions (right) [24].

2.2 Experimental setup design

We want to characterize electrical discharge ignition systems, so we will measure the electrical energy supplied to the electrodes and compare it to the thermal energy deposit in the gas. A visualization technique is also employed to study the spatial dimension of the discharge and how the gas properties change during the discharge. Experimental setup is designed following the experimental methods requirements, as described in this section.

2.2.1 Requirements: experimental methods

2.2.1.1 Electrical measurements

Electrical energy is obtained integrating the product of voltage and current, see Eq. (2.1). Voltage and current can be measured at the electric circuit entry, or at the electrodes. The difference between these options corresponds to losses in the circuit impedance. Electrical efficiency of an igniter is the ratio of energy supplied to the electrodes after passing through the igniter electrical circuit (E_{el}) to total electrical energy supplied to the igniter for producing the discharge [29]. This efficiency is different from the energy transfer efficiency (η), studied in this work, which relates remaining energy at the fluid after the electrical discharge (E_{th}) to electrical energy supplied to the electrodes (E_{el}).

$$E_{el} = \int_0^{t_d} I\,U\,dt \tag{2.1}$$

Electrical signal measurements will be made at the electrodes or spark plug, so it is necessary to connect separately the electrical probes for voltage and current.

2.2.1.2 Pressure-rise calorimetry

Calorimetry technique measures the amount of thermal energy released by a process. In spark ignition, the electrical discharge is the energy source.

The energy deposit by an electrical discharge E_{th} can be calculated from the internal energy variation of the gas inside the chamber volume, as in equation (2.2).

$$E_{th} = \int_V \delta u\,dV = \int_V \rho\,c_v\,\Delta T\,dV \tag{2.2}$$

Considering the gas inside the chamber as an ideal gas, temperature variation is related to pressure variation by the ideal gas relation and can come out of the integral $(\rho c_v \Delta T = (c_p/(R\,/\,Mm))\Delta p)$. Integrating for the control volume; i.e., all the gas in the chamber, E_{th} is obtained as a function of chamber volume and the pressure rise inside the chamber:

$$E_{th} = \left(\frac{c_p}{R}\right) V\,\Delta p = \frac{1}{\gamma - 1} \Delta p\,V \tag{2.3}$$

Pressure rise calorimetry is applied to the study of electrical discharges in §3; where hypothesis will be explained in depth and verified. Pressure-rise calorimetry requires then a constant volume vessel and a pressure transducer to estimate the thermal energy deposit.

2.2.1.3 Speckle-based Background-Oriented Schlieren (SBOS) and Schlieren

Speckle-based Background-Oriented Schlieren (SBOS) is a visualization technique which allows quantitative measurements of the density and temperature distributions in the observed region of a fluid. As the schlieren technique, it is based on the variation of the refractive index due to density gradients. Schlieren has been mostly used to obtain qualitative measurements, but different schlieren techniques can be employed to obtain quantitative data, see for instance Hargather and Settles [100]. One of these techniques is Background-Oriented Schlieren. It uses a background image as a reference image to measure quantitatively changes on it. A laser-generated speckle background can be used (SBOS) to adapt background resolution to the required scale and optical magnification. The development and application of SBOS methodology to quantitative measurements in electrical discharges is explained in depth in Chapter 4.

Schlieren technique is used in this work to observe phenomena involved in ignition processes: shockwave expansion, hot kernel size and contact between kernel and the electrodes. By SBOS, density and temperature distributions are obtained, and under the right conditions, the energy deposit E_{th}.

Schlieren and SBOS techniques require visual access of the studied phenomenon, i.e. optical windows on the experimental chamber walls.

2.2.2 Setup dimensioning

Access to the electrodes/spark plug for the electrical probes and optical access to the chambers are taken into account for the design of the test chambers. In this section we explain the choice of pressure transducer and chamber volume that fit better for our study.

Two constraints limit the chamber volume: the maximum pressure that can be measured in the linear range of the pressure transducer, and the sensitivity of the measurement. An energy deposit in the gas inside a closed vessel produces a pressure rise inversely proportional to vessel volume, see equation (2.3). The maximum admissible pressure of the transducer limits the minimum volume of the chamber. Also the size of the hot kernel must be small enough compared to chamber volume to avoid wall effect. The upper limit to the chamber volume is the measurement chain sensitivity, as a small pressure rise increases the noise-signal ratio and measurement uncertainty.

A large volume is desirable for several reasons: to keep a minimum distance between the electrical discharge plasma and hot kernel and the pressure transducer, to avoid wall effect during hot kernel evolution (heat transfer), and to have a small plasma volume relative to the total chamber volume during the discharge (so the volume can be considered practically as an inert gas). A large chamber volume would require a high sensitivity pressure transducer, as the pressure rise is inversely proportional to chamber volume.

The pressure transducer signal is amplified by a signal amplifier, and finally recorded with an oscilloscope. The chain of measurements increases the intrinsic uncertainty of the pressure transducer, through the amplifier gain and noise and the oscilloscope uncertainty related to the 11 bit sampling (the oscilloscope registers at 8 bit the signal, with a +3 bit oversampling filter).

We found the Meggitt differential pressure transducers in the 8510B series to be optimal for this application, as they have the highest sensitivity that we found. They work with the coupled amplifier model 136 with adjustable gain. Three different models are compared, referred to as their maximum pressure difference measurable in the linear range: 1, 2 and 5 psi; with sensitivities of 200, 100 and 60 mV/psi respectively (1 psi = 68.9 mbar). A lower sensitivity pressure transducer would have more measurement uncertainty a priori, but the higher pressure range may allow to use the same chamber (and chamber volume) for different ignition systems.

Measurement uncertainties are calculated as a function of chamber volume, for different hypothetical energy deposits and the three pressure transducers. The Δp caused by the energy deposit is estimated with equation (2.3). It is then converted to the corresponding electrical signal in mV with each pressure transducer sensitivity. The maximum uncertainty associated to each transducer is calculated for the electrical signal, using the uncertainty from the transducers specifications. The signal and its uncertainty are multiplied by the amplifier gain. Amplifier adds a fixed value to the amplified signal uncertainty. Finally, the oscilloscope 11 bit resolution is taken into account for global signal uncertainty.

By these estimations, we plot the measurement uncertainty related to chamber volume, so we can choose the best options for the setup: ideally, we would like only one chamber volume and pressure transducer for all the tests, with minimum uncertainty for the measurement. The results are plotted in Figure 2-4, with energy deposits value expected from the ignition systems: 10-30 mJ for the pin-to-pin electrodes, 100 mJ for the radiofrequency discharge, and 500 mJ for the coaxial spark plug discharge. Discontinuities in the curves correspond to changes in the amplifier gain (in calculations set to 10, 100 or 1000 to have possible maximum gain possible respecting the maximum tension output of the amplifier). Only uncertainty values under 10% are considered valid.

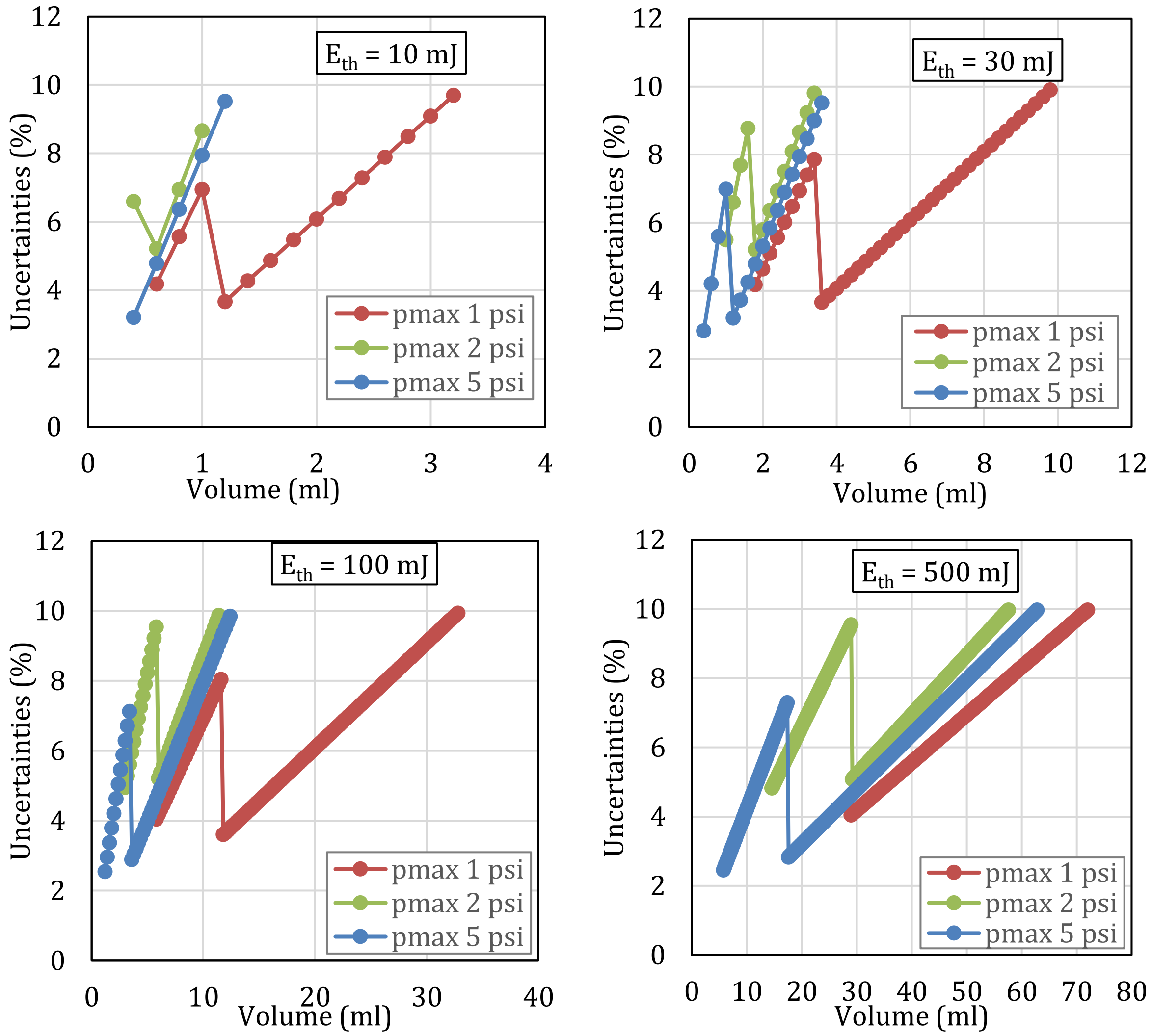

Figure 2-4: Uncertainties versus chamber volume for different pressure transducers. Energy deposits are, from left to right and top to bottom, 10, 30, 100, and 500 mJ.

The 1 psi maximum pressure transducer is chosen. As it has the best sensitivity, low energy deposits can be measured in a small volume: 3 ml represents a 1 cm height 1 cm radius cylindrical chamber. For higher energy deposits it requires a larger volume, thus, different chambers for different igniters have to be realized. As the high energy discharges we want to study present also high power (more energy delivered in a shorter time) a bigger chamber distances the pressure transducer from the discharge kernel, which is safer for the transducer.

Regarding the chamber volumes, a 6 ml volume chamber is chosen for the low energy discharges. For the coaxial spark plug discharge, which requires around 700 mJ of electrical energy, preliminary tests are made in a 60 ml atmospheric plastic chamber, see chapter 5, as the efficiency is unknown and a high energy deposit without enough chamber volume would damage the pressure transducer. As a result, the coaxial spark plug energy deposit (thermal energy) is in the order of 100 mJ. For the high energy discharges, a 20 ml chamber volume is chosen to decrease measurement maximum uncertainty.

2.3 Experimental setup

2.3.1 Probes and transducers

During electrical discharges, voltage and current variations occur in the order of tens of ns (e. g., hot plasma discharge breakdown voltage drop in tens of ns), so wideband electrical probes are required. The Tektronix P6015A is chosen as high voltage probe, with a 75 MHz bandwidth and measuring voltage peaks up to 40 kV. For electrical intensity measurement, several probes are chosen depending on the maximum current reached in the discharge. For the study of the classical pin-to-pin electrodes discharge we used the probe LeCroy CP031, with a 100 MHz bandwidth and measuring intensity peaks up to 50 A. The Pearson current monitor model 101 is used for applications where higher currents are expected, it measures up to 50 kA with a 4 MHz bandwidth.

The high voltage probe Tektronix P6015A presents a DC attenuation of 1000:1 ± 3%. The current probe LeCroy CP031 is accurate to 1% at low frequency. Operating at 20 MHz, the current probe presents an AC noise under 2.5 mA (under 100 ns). Uncertainty for voltage and current are then 3% and 1% respectively.

The transient pressure increase produced by an electrical discharge is of a few mbar. The piezo-resistive differential pressure transducer Meggitt 8510B-1 measures up to 70 mbar (1 psi) pressure differences. It is connected to a Meggitt DC Amplifier model 136, which also adapts and filters the pressure signal, with an integrated 10 kHz Butterworth physical filter. Signals are recorded by a LeCroy waverunner 104Xi high speed sampling oscilloscope (sampling from 200 MHz to 1 GHz at tests).

2.3.2 Experimental vessels

The experiments are conducted inside a closed volume. Chambers are made with isolating non-conductive plastic materials (POM, POM-C) to reduce heat losses through the walls.

Different chambers are needed to obtain good sensitivity measurements for different electrical discharges in all conditions, as described in §2.2.2: a volume of 6 ml is chosen for the pin-to-pin electrodes discharge (estimated of 30 mJ of energy deposit) while a 20 ml volume fits better more energetic discharges as produced by the aeronautical igniter (around 100 mJ). Chamber volume is determined by filling it with water with a volumetric syringe, so volume is measured with ± 0.2 ml uncertainty.

As differential pressure sensors are used, a pressurized system is developed for experiments involving different gas mixtures and reference pressures. It consists of an outer metallic chamber which contains an inner chamber with the chosen volume for calorimetry tests (see Figure 2-5, Figure 2-6).

The outer chamber is made of stainless steel, measuring 120x76x70 mm^3, with 0.64 l inner volume. It serves as reference pressure for the piezo-resistive pressure transducer employed in calorimetry.

A gas entry in the base, closed by a valve, allows to fill and empty the volume with gas at different pressures. Two opposite sides of the chamber hold 125x75 mm² windows for visualization diagnostics. An adaptive plastic wall made of Polyacetal [POM-C] closes the last chamber opening. This plastic wall supports the inner test chamber, instruments and the spark plug; and is referred to as the inner chamber ensemble. The outer chamber is airtight, which is assured by flat rubber gaskets.

Two different inner chamber ensembles are designed to support different spark plugs and adapted inner cylindrical chambers, with the volumes chosen in §2.2.2:

The 6 ml chamber (Ø 17.4 mm x 25 mm), with two electrodes: a fixed electrode holder and an electrode holder adjustable from outside the experimental setup, allowing to set the inter-electrode gap distance with a precision of 0.1 mm. The cylinder wall is made of POM-C, and the cylinder bases are 25 mm diameter two surfaces anti-reflection coated laser silica window (W2-PW1-2506M-UV-1064-0), with a steel support. A metallic part connects the inner fixed electrode with the outer chamber wall, working as ground connection. This chamber ensemble is shown in Figure 2-5.

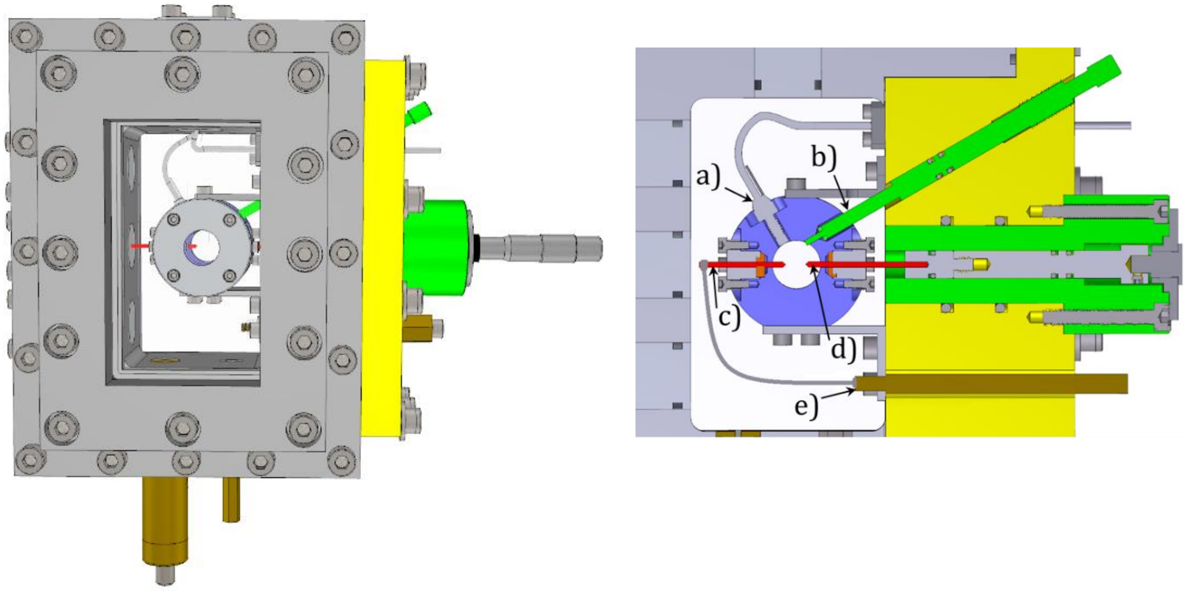

Figure 2-5: Pressurized ensemble 3D view (left), and transversal cut (right). (blue) 6 ml inner volume chamber, a) differential pressure transducer, b) by-pass valve, c) ground electrode (red), d) high V electrode attached to millimetric positioner, e) electric ground.

The 20 ml chamber (Ø 32 mm x 25 mm) is equipped with a helicopter spark plug holder. The cylinder wall is made of POM-C, and the cylinder bases are two polished surfaces quartz windows supported by a stainless steel piece. Figure 2-6 shows this setup.

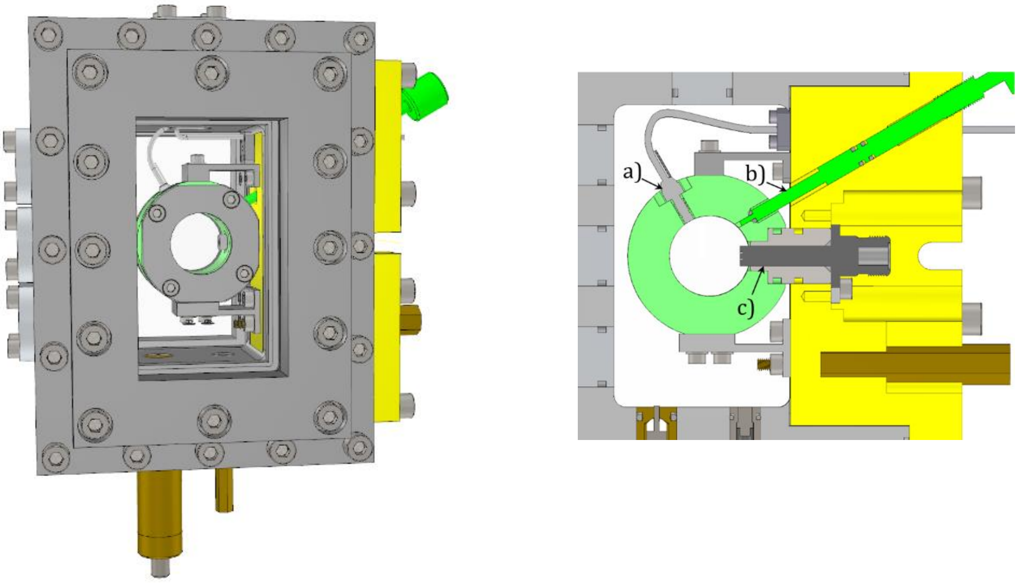

Figure 2-6: Pressurized ensemble 3D view (left), and transversal cut (right). (light green) 20 ml inner volume chamber wall, a) pressure transducer, b) by-pass valve, c) helicopter spark plug.

The design of the inner chamber ensembles includes passages for the electrical device (electrodes or spark plug) from outside the outer chamber into the inner chamber. Both include a valve which communicates or isolates the inner and the reference volumes. It is controlled from outside the outer vessel. Air tightness is assured for the inner chambers by rubber O rings between chamber windows and walls.

2.3.3 Experimental setups

The experimental setups are described next, for each experimental method.

2.3.3.1 Pressure rise calorimetry

For calorimetry experiments, the spark plug (electrodes, radio frequency or corona discharge plug) is placed inside a constant volume vessel. The piezo-resistive differential pressure transducer measures the pressure rise inside the chamber, while the current and voltage probes measure electric signals. The differential pressure transducer Meggitt 8510B-1 is connected to the Meggitt DC Amplifier model 136.

The pressure transducer is located at least 1 cm from the electrodes tips. It is protected to reduce the direct impact from the shockwave at breakdown: by a cotton disc in the pin-to-pin setup, and by a porous metallic disc (around 50% porosity) in the high energy discharge setup. Figure 2-7 shows the calorimetry setup, including probe connections and chamber scheme for pin-to-pin electrodes.

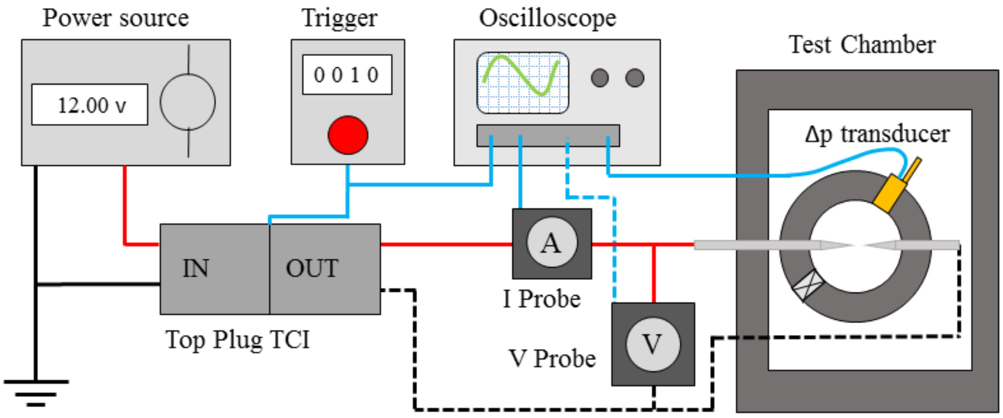

Figure 2-7: Pressure-rise calorimetry experimental setup.

Electrical probes measure electric current and voltage at the electrodes. Differential pressure signal from the amplifier, electrical signals and trigger signal are recorded with the oscilloscope. Calorimetry principles, tests and results are discussed in depth in §3.

2.3.3.2 Visualization techniques

2.3.3.2.1 Schlieren

A SA5 Photron fast camera and a 5W Argon Spectra-Physics 2017 laser are used to obtain schlieren images at 90 kHz. An optical blade (lens with an opaque spot in the center) and two lenses are used to control the focal point, magnification and contrast of the images, as in [101].

2.3.3.2.2 SBOS

The coherent source is a diode-pumped continuous solid-state laser (MxL-F, $\lambda = 532\, nm$, 3 W). The emission power is stabilized for steady conditions at 1%. The beam is expanded through a collimator. Parallel beams that are expanded to a 45 mm diameter impact a 1 mm wide ground glass, which produces the speckle by scattering effects (Figure 2-8).

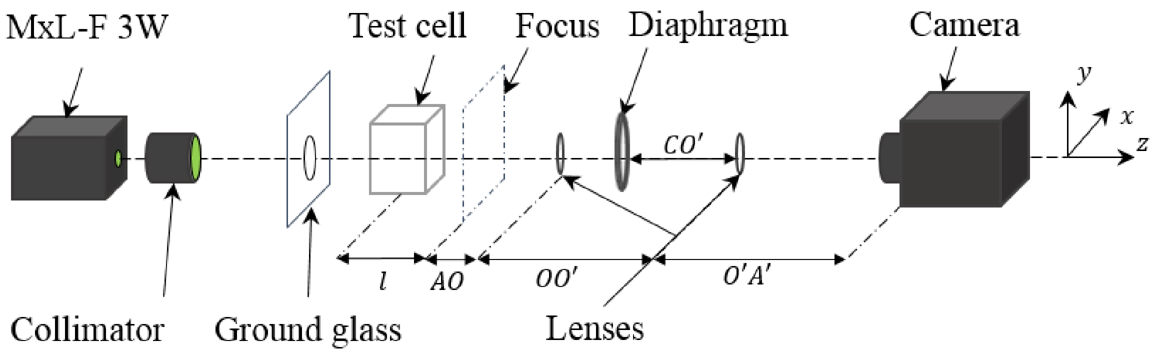

Figure 2-8: SBOS optical configuration.

The optical collection system consists of two lenses, whose respective focal length and center are O and $f_1 = 500\, mm$ and O' and $f_2 = 300\, mm$, and a diaphragm. Speckle light is directly focused on the naked camera sensor plan. The camera used is a PiMax 1k GenII RB-SG, CCD intensified camera with a 1 Hz acquisition, which meets the requirements for short exposure time (1 µs).

Intensification is channeled using fiber optic coupling, which greatly reduces loss of resolution and distortion.

Under laminar conditions, refraction index field is assumed to be sufficiently axisymmetric to use a single view in tomography. The average pixel size is $c = 13\,\mu m$. Although the overall discharge process takes approximately 2.5 ms, rapid advection movement occurs; therefore, the shortest possible exposure time is selected. The best trade-off, imaging-wise, is found for a $1\,\mu s$ exposure time.

The lens positioning is set depending on the desired optical magnification. For the pin-to-pin electrodes study it is $AO = 170\,mm$, $OO' = 492\,mm$, and $O'A' = 500\,mm$, which ensures a global magnification ratio of $M = 1.0$. The diaphragm positioned at C is closed at 5 mm in diameter, which at a distance $CO' = 45\,mm$ yields an effective exit pupil diameter of $D{\sim}5{,}32\,mm$. This configuration yields a speckle size of $61.6\,\mu m$, which is approximately 4.7 px, and which meets PIV software requirements. The defocusing distance is adapted to the discharge energy, from $l = -80\,mm$ to $l = -30\,mm$ for the pin-to-pin electrodes (see chapter 4), and $l = -100\,mm$ for the helicopter igniter (see chapter 5), to regulate speckle pattern displacement. For higher energy electrical discharges (the case of the helicopter engine igniter), lens positioning is modified to obtain a smaller magnification ratio of $M = 0.5$. For this case, distances are $AO = 170\,mm$, $OO' = 942\,mm$ and $OA' = 400\,m$.

The electric discharge study is done with the calorimetry chamber as the test cell, with the spark plug at its center. Delay is ensured by a pulse and delay generator (DG535, Stanford Research Systems) that synchronizes the camera, the oscilloscope, and the spark plug. Images are recorded at different instants after the discharge onset. The heated gas is intended to be air of ambient composition and pressure, to which we apply semi-ideal behavior. This means that the ideal gas law applies, and calorific capacity is temperature-dependent, which is taken as the standard Gordon-McBride polynomial form (see chapter 4).

The test cell is fitted with two different windows: one for the inner and one for the outer chamber, between the discharge zone and the optical setup. These windows- affect the optical setup by shifting the focal point and reference $\Delta z = -11.5\,mm$. It is compensated by simply displacing that Δz the test cell and the reference for defocusing distance. Windows have negligible influence in angle variations of the light beam and in the measured pattern point displacement at the camera sensor. This is verified both theoretically and experimentally in Appendix A.

Chapter 3

Calorimetry of electrical discharges for pin-to-pin electrodes

Contents

3 Calorimetry of electrical discharges for pin-to-pin electrodes

In this chapter pressure rise calorimetry is applied to the study of electrical discharges on an academic reference configuration. A pair of pin-to-pin electrodes and a TCI system are employed to that end. Calorimetry basics are discussed in §3.1. Then the calorimetry measurements and data processing are explained in §3.2. Results in atmospheric conditions are discussed in §3.3, and tests with different pressure and gas mixtures in §3.4. Finally, conclusions are presented in §3.5.

3.1 Introduction

Calorimetry technique aims at measuring the amount of thermal energy released by a process. In spark ignition, the electrical discharge is the energy source. There are two types of calorimetry: constant pressure calorimetry and constant volume calorimetry, both used as early as 1951 [66]. In constant pressure calorimetry, a capillary is attached to the calorimeter volume, and energy is obtained from the volume change. In constant volume calorimetry though, the transient pressure rise in the constant calorimeter volume is used to calculate the energy.

Constant volume calorimetry is the most used technique for spark ignition applications. It was used by Roth et al. [66] to study the influence of electrode geometry and gas properties on the discharge, breakdown voltage and energy. Other authors confirmed his data [2] , Elisazadeh-Far [13]). Merritt [67] used a constant volume calorimeter with a differential pressure transducer and the atmospheric air as reference pressure. Another closed volume can be used as reference pressure to perform tests using different pressures and gases. This setup is more common in other studies [91].

3.1.1 Principles and hypotheses

As explained in Chapter 1, electrical energy transforms into thermal energy during the discharge. Thermal energy remaining in the fluid (E_{th}) is measured by constant volume calorimetry. The high pressure inside the plasma channel at the onset of the discharge is transmitted to the rest of the chamber by a shockwave and the resulting acoustic wave which is damped after several reflections on the vessel walls. When these acoustic effects end, a transient pressure rise is measured while more energy is being provided by the discharge. The total discharge time ranges from less than 100 μs to more than 3 ms depending on the discharge system and experimental conditions, whereas acoustic resonations are already damped in the experimental vessel after hundreds of microseconds. After this moment, E_{th} rise is obtained during the discharge from the pressure signal.

The estimation of E_{th} supposes that shockwave energy has transformed into a global pressure and temperature rise, e.g. the pressure field is supposed to be uniform. The volume of plasma during the discharge (in the order of 0.05 ml = 50 mm^3, as the inter-electrode gap volume) is negligible in comparison to the chamber volume (> 5 ml), and is far from the chamber walls. Therefore global temperature rise is negligible in most part of the vessel, and consequently there is no heat transfer through the walls (except to the electrodes, but this energy is part of the energy loss in the transfer). For these reasons, all the chamber volume is considered to behave as a confined gas with homogeneous properties, and in particular a constant gas heat capacity ratio γ. To summarize, the hypothesis assumed for the calorimetry measurements are:

H1. The volume of plasma is negligible in comparison to the chamber volume.
H2. Heat capacity ratio of the gas inside the chamber is constant.
H3. There is no heat transfer through the walls.

As introduced in chapter 2, the thermal energy is measured as a function of chamber volume and pressure rise, using equation (2.3):

$$E_{th} = \frac{1}{\gamma - 1} \Delta p\, V \tag{2.3}$$

The thermal energy measured (E_{th}) is then the energy deposit in the fluid by the electrical discharge. In the energy transfer from E_{el} to E_{th} there are several sources of energy loss [2], [13]:

- Electrode heating, by two processes: dissipation of anode and cathode fall (voltage drop) energies, and conduction to electrodes by thermal boundary layer (contact with the hot kernel in the gas).
- Radiation: the plasma and hot kernel produced by the discharge lose energy in form of radiation to their surroundings due to the high temperature difference. This effect is more important at high discharge energies, as they present larger kernel areas and higher temperatures.
- Shockwave generation: the plasma channel created at the breakdown phase produces a shockwave due to the high local pressure (see §1.1.1). Part of this energy is reabsorbed by the expanding kernel, but another fraction is dissipated.

We measure the thermal energy deposit that remains in the fluid after the mentioned losses in the discharge process.

3.1.2 Advantages and Limitations

As one of the objectives of this study is to determine energy transfer from complex geometrical ignitors, pressure rise calorimetry technique is optimal for this purpose. Indeed, it should work for any kind of electrical discharge, measuring with good accuracy Δp and E_{th} over time. It is simple to implement as the main requirement is a known closed volume and an appropriate pressure gauge.

There are some details to consider about calorimetry:

- Calorimetry quantifies the total amount of energy supplied to the gas but cannot provide information about the efficiency of the supplied energy for the initiation of combustion itself (Meyer), as there are many other factors involved. Calorimetry provides no spatial information about discharge properties (discharge volume, gas properties).
- Electrode heating by high currents can affect measurements (see 5.1.2.4).
- Electromagnetic interference (EMI): The high electric field during breakdown, and parasitic noise during arc-glow transitions affect measurements and/or equipment in some cases. We have observed a high antenna effect at the signal amplifier. EMI hides the differential pressure signal a short period after breakdown (~150 μs), so pressure data is unavailable during that time.

3.2 Methodology - Constant volume calorimetry

Three quantities are measured during the calorimetry experiments: differential pressure, voltage and current. They are used to calculate the electrical energy supplied to the electrodes (E_{el}), the thermal energy deposit into the fluid (E_{th}) and energy transfer efficiency (η). Input signals p, I and U are measured with the probes and setup described in Chapter 2. The main assumptions made in calorimetry are validated by visualization via schlieren technique.

3.2.1 Pressure, current and voltage measurements

The typical measured signals for calorimetry are described in this paragraph for a representative test for 1 mm inter-electrode gap at atmospheric conditions (293 K, 1 bar). First, Figure 3-1 shows the experimental setup used for calorimetry tests, with a detail on the inner chamber. The different components are presented in §2.3.

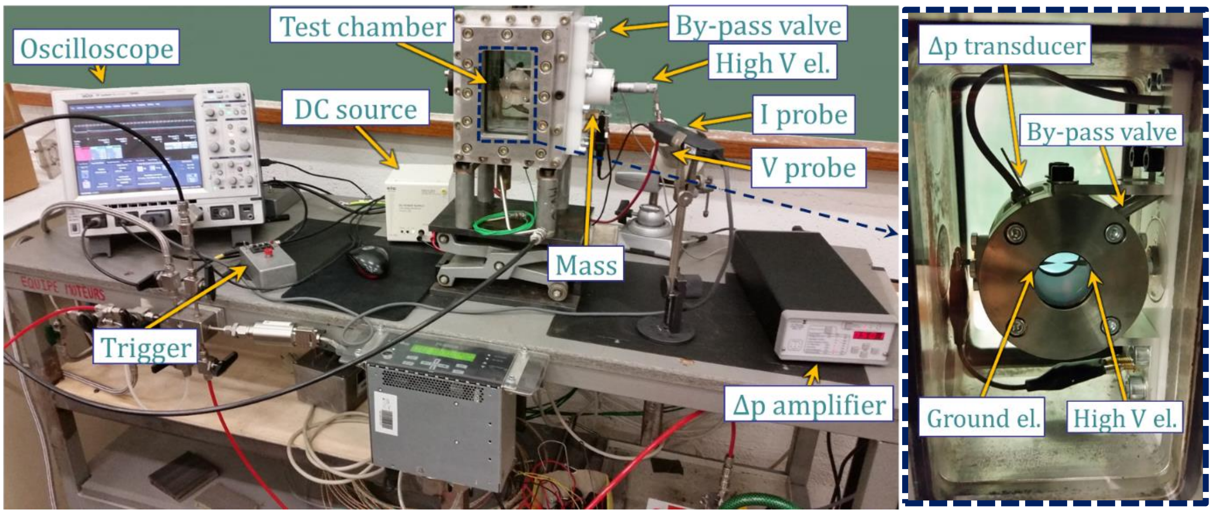

Figure 3-1: Pin-to-pin electrodes calorimetry experimental setup and detail on the inner chamber.

3.2.1.1 Electrical signals

Voltage signal is reported in Figure 3-2. The different phases of the discharge can be observed: breakdown, arc and glow; as described in §1.1. Figure 3-3 (left) shows voltage evolution during discharge time, excluding the TCI coil charging time. Voltage peaks at the beginning of the discharge reaching several kilovolts, corresponding to the breakdown phase. It is followed by the glow or the arc phase: if the voltage is over 350 V (typically 400 V) it is a glow phase (see §1.1). For lower values (around 200 V), this is an arc phase. Arc and glow voltage levels are affected by discharge properties, e.g. they vary for different gas mixtures or higher pressure levels.

The corresponding current signal is displayed in Figure 3-2. An intense peak is recorded at breakdown (up to 0.5 A). Then current gradually decreases from 0.1 A to almost zero at the end of the discharge. One can see current signal in detail in Figure 3-3 (right), which corresponds to the same discharge plotted during the spark duration.

As a TCI circuit is employed without any electrical limiters, fast transitions between both discharge modes occur, producing peaks in the electrical signals. At the end of the discharge, voltage oscillates as it lowers in the resonating the RCL circuit. Current and power at this point are very low, and negligible in comparison to the ones during the rest of the discharge. To exclude this effect at energy calculation, integration is stopped at the onset of oscillations (t = 2.8 ms in Figure 3-2). This instant is considered as the end of the discharge.

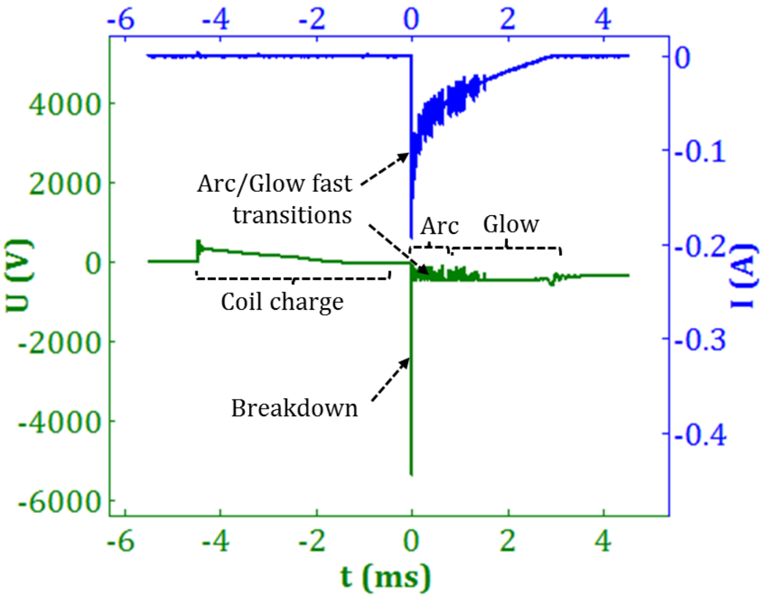

Figure 3-2: Electrical signals for a 1 mm gap and E_{el} = 39 mJ.

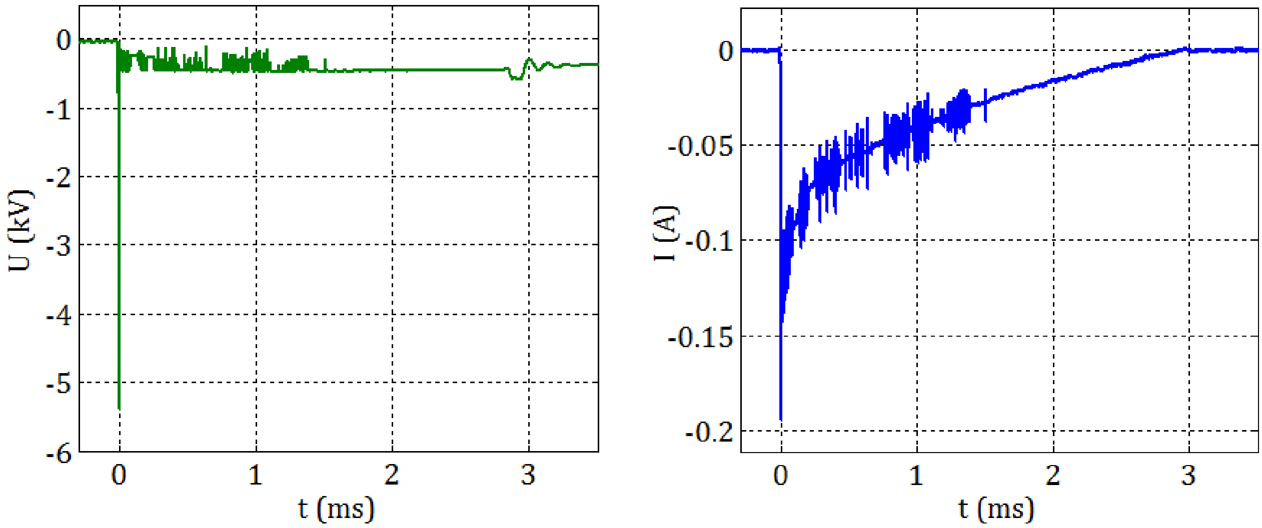

Figure 3-3: Voltage (left) and Intensity (right) during spark duration (from 0 to 3 µs in the precedent figure).

As a remark, when measuring electrical signals using a TCI system, coil charge duration must be included in the recorded time range, as the voltage level after coil charge and before breakdown is not equal to initial offset value before coil charge.

3.2.1.2 Pressure evolution

The piezo-resistive differential pressure transducer measures the differential pressure between the inside and the outside of the measurement chamber during the discharge. Signal amplifier processes the pressure signal: it amplifies the signal with an adjustable gain, which is set to 10^3; and filters with its integrated physical Butterworth 10 kHz filter. Filtering reduces the influence of resonance of diverse phenomena: acoustics (17 kHz for the first mode of the 6 ml vessel), transducer resonance (55 kHz) and chamber structure resonance (40 kHz). Pressure signal is recorded by the oscilloscope and post-processed by the Matlab® program that we developed.

Signal post-processing adjusts measurement units and possible offset disparities to obtain the differential pressure signal. Signal is multiplied by a correcting factor to take into account amplifier gain and unit change: pressure transducer sensitivity is 187.5 mV/PSI, which is converted to bar. Then this signal is reset to zero before the discharge.

Differential pressure evolution measured for a 1 mm gap and 39 mJ E_{el} is represented in Figure 3-4. An initial peak of few microseconds width (2 μs) is observed at the time corresponding to breakdown phase. This is signaled as the detail a) in the figure. It is produced by the intense electromagnetic field during the discharge and an antenna effect of the signal amplifier (it is not a real pressure peak, but EMI), and it can be either positive or negative.

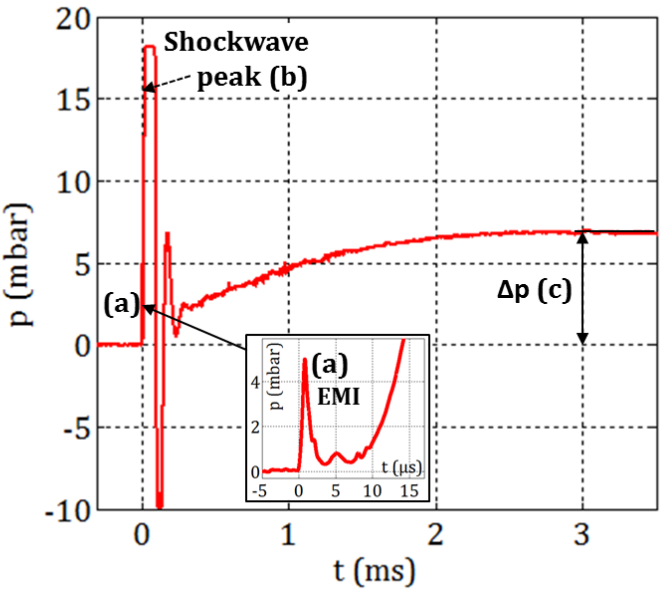

Figure 3-4: Differential pressure evolution measured for a 1.0 mm gap and 39 mJ of electrical energy. (a) Antenna effect and high electromagnetic field. (b) Shockwave peak arrival to the pressure transducer. (c) Maximum mean pressure.

The discharge produces a shockwave, which arrives at the transducer around 15 μs after spark onset –see detail b) in the figure-. To verify this assertion, images of the beginning of the discharge were recorded by schlieren technique (Figure 3-5). After filtering and background subtraction, the shockwave can be observed only in one or two frames, with a time difference between images of 11 μs. At these instants, strong pressure heterogeneities exist in the chamber and therefore Eq. (2.3) can not be employed to estimate the amount of energy deposited in the gas.

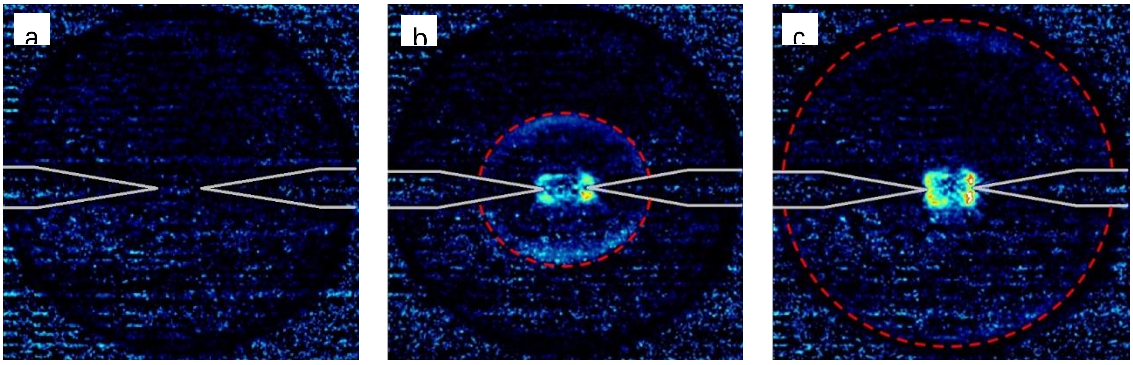

Figure 3-5: Schlieren images of the beginning of the discharge, filtered and after background subtraction, with dt = 11 µs. Electrodes position pointed out in grey, shockwave front in red. At (a.) discharge starts, shockwave is observed 11 µs later at (b.) and it has already bounced at the wall 11 µs later at (c).

Shockwave pressure peak saturates the pressure transducer. Pressure waves following the shockwave (acoustic effects) produce oscillations in the pressure signal. After 200 µs, pressure waves are damped by the multiple reflections and propagations within the chamber. From this instant, pressure transducer provides a good estimate of the mean pressure inside the vessel.

Mean pressure rises up to its maximum at the end of the discharge and decreases again as a result of heat losses. Therefore, thermal energy supplied to the gas is obtained from the difference between the maximum mean pressure during the discharge and the initial pressure, following Eq. 2.3.

The effect of heat transfer is not negligible: pressure decreases slowly after the end of the discharge. It is attributed to heat exchange between the hot kernel and the electrodes: compression-induced temperature rise is negligible at these instants at the total chamber volume –lower than 1 K for an average pressure rise of 5 mbar, from ideal gas equations-. From the pressure decays after spark end, this heat transfer is estimated to be lower than 0.6 Watt, which is much lower than the heat transfer during the discharge (an average value of 5 Watt). These power values suggest the pressure rise measurement is a good estimate of the energy deposit into the fluid. Nevertheless, it represents more exactly the energy remaining into the fluid after the discharge, see 3.1.1.

Hypothesis H1 is justified with the results in Figure 3-5, where one can observe that the hot kernel is small compared to the measurement chamber size. The temperature rise in the chamber is estimated to be lower than 1 K, which verifies the second hypothesis H2, as gas heat capacity ratio can then be considered constant, and H3, as there is almost no heat transfer to the walls.

3.2.2 Energy calculation

From electrical and pressure signals, a temporal tracking of E_{el} and E_{th} is performed. Energy transfer efficiency is calculated over time too.

Electrical and thermal energy are obtained from equations (2.1) and (2.3). As reported in [12], E_{el} is supplied with different efficiencies for the different phases of the discharge. In a standard discharge, around 3 mJ are supplied in less than 1 µs to the electrodes during breakdown, corresponding to the energy stocked in the inter-electrode gap capacitance. This represents from 5 to 10% of the total energy. Then, during the next milliseconds E_{el} gradually rises up to the total cumulated value, which depends on test conditions (20 - 55 mJ).

$$E_{el} = \int_0^{t_d} I\, U\, dt \tag{2.1}$$

$$E_{th} = \frac{1}{\gamma - 1} \Delta p\, V \tag{2.3}$$

Pressure difference $\Delta p(t)$, at the instant t, is the pressure signal at t minus reference initial pressure. Energy deposit $E_{th}(t)$ is obtained using equation (2.3). The total amount of energy deposited in the fluid is E_{th} at the end of the discharge. Instantaneous pressure difference $dp(t)$ is obtained as $p(t_i)$-$p(t_{i-1})$ and represents the instantaneous pressure rise, useful to analyze the thermal energy deposit rate with time. Thermal energy E_{th} cannot be measured until the effect of the shockwave on the signal has dissipated, which happens 200 µs after the shockwave peak at the pressure signal (see Figure 3-4).

E_{th} and E_{el} cumulated over time and energy transfer efficiency are shown in Figure 3-6, for a 1 mm gap, saturated coil and 39 mJ electrical energy discharge. They are estimated in function of time, while the energy transfer is still going on. The ratio of E_{th} over E_{el} represents the energy transfer efficiency (η), as in Eq. (3.1). Efficiency is also represented in the figure.

$$\eta = \frac{E_{th}}{E_{el}} \tag{3.1}$$

Instantaneous E_{el} rising rates are different depending on the discharge phase, which is studied later in 3.3.4. At the end of the discharge, the measure of energy remaining in the fluid reaches 10 mJ (E_{th}) whereas 39 mJ is supplied to the electrodes (E_{el}). It can be noticed that the cumulative efficiency decays as the discharge duration increases. This is due to efficiency variations over time, which is explained later.

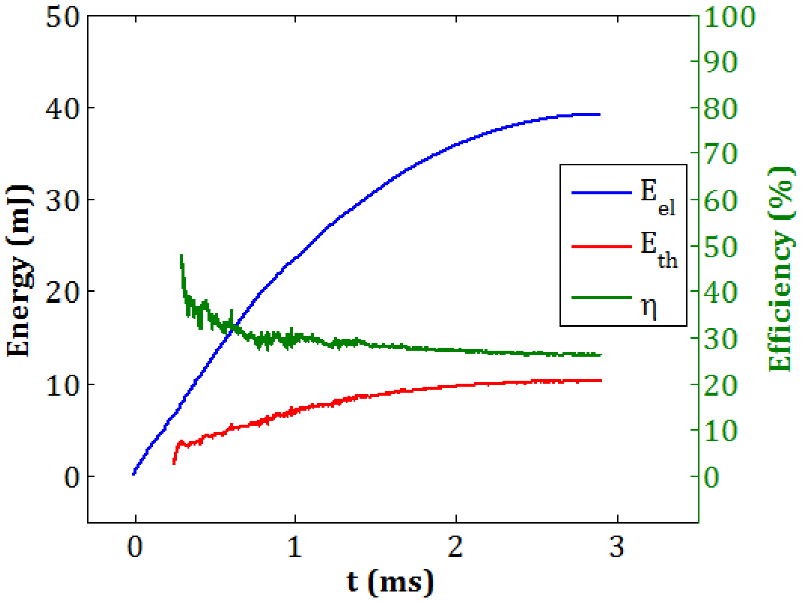

Figure 3-6: Evolution of energies and efficiency vs. time, for a 1.0 mm gap, saturated coil and 39.2 mJ electrical energy discharge. Total discharge energy and efficiency are as at the end of the discharge, at 3 ms: E_{el} = 39.2 mJ, E_{th} = 10.2 mJ and η = 26.2%.

During breakdown phase, E_{el} is estimated similarly from equation (2.1). Breakdown voltage peaks for up to 12 kV in some conditions. Voltage peak is detected during signal processing, from first voltage rise until it decreases to glow voltage value. This phase lasts for less than 1 µs (600 ns). During breakdown, E_{th} cannot be estimated instantaneously by calorimetry, as the energy deposit is concentrated in the plasma channel and the pressure wave. First E_{th} values calculated from mean pressure rise take place 150 to 200 µs after breakdown and include breakdown energy deposit. Breakdown transfer efficiency estimated as 90% [15].

3.2.3 Measurement uncertainties

Measurement uncertainties are determined from the specifications of the measuring equipment:

3.2.3.1 Electrical energy

The high voltage probe Tektronix P6015A presents a DC attenuation of 1000:1 ± 3%. The current probe LeCroy CP031 is accurate to 1% at low frequency, and operating at 20 MHz presents an AC noise under 2.5 mA (under 100 ns). Uncertainty for voltage and current are then 3% and 1% respectively.

The LeCroy waverunner 104Xi oscilloscope analogic sampling is at 8 bit resolution, with an incorporated +3 bit signal enhancement. This means an uncertainty, from oscilloscope resolution, of $1/2^{11}$, or 0,05%.

Globally, for electrical power and E_{el}, measurement uncertainty is estimated to be 4,1%.

3.2.3.2 Thermal energy deposit

As thermal energy is one of the main results of this study, a low uncertainty is required from the measurement chain. Chamber volume and the differential pressure transducer model were chosen to minimize E_{th} uncertainty, from first measurement estimations:

An energy deposit value is chosen, as expected for the ignition system (13 mJ). Then, from chamber volume (6 ml) and pressure transducer sensitivity (184 mV/PSI or 2.66 mV/mbar) the value of the signal is calculated in mV, using eq. 2-9. If this value is higher than the transducer linearity operation limit, volume should be bigger. Smaller volumes allow a better signal/noise ratio and lower uncertainty.

Pressure transducer measure has a 1.5% uncertainty from Full Scale Output (200 mV), then it presents a 3 mV uncertainty. The next step in the measurement chain is the signal amplifier, which has a 0.5% of Full-Scale accuracy. Signal amplifier full scale is 10 V, so the output uncertainty is 50 mV. Amplifier multiplies transducer pressure signal times gain parameter, which is 10^3 for most tests. Then at amplifier output total uncertainty is of 3050 mV. Compared to the amplified pressure signal the amplifier output uncertainty is of 13%.

Taking into account oscilloscope uncertainty from the 11 bit resolution, and the volume uncertainty of 0.1 ml (1.6%), a maximum global uncertainty of ~15% is estimated for thermal energy deposit measurement in the pin-to-pin electrodes setup.

After covering the methodology, hypothesis and uncertainties associated, next we present the first measurements we performed with calorimetry.

3.3 Measurements in atmospheric conditions

Electrical discharges are studied for different E_{el}, varying the coil charge of the TCI pencil coil. Series of 10 discharges in air, at 1 bar and room temperature (293 K), were recorded. Tests were performed in the 6.0 ml pressurized vessel. The influence of inter-electrode gap is also analyzed. The effect of the control parameters over E_{th} and η are commented first. Efficiencies of arc and glow phases and discharge duration are then estimated.

Different parameters control experimental conditions: pressure and gas composition chosen in the pressurized vessel. Additionally, for pin-to-pin electrodes setup E_{el} and gap can be varied. Moreover, electrical energy supplied to the electrodes (E_{el}) is modified by the charging time of the coil inside the TCI system.

At least five seconds are waited between two consecutive experiments. This time is chosen to ensure the stabilization of gas species after breakdown ionization [102] and also to obtain the same initial pressure level (obtained after 2 s).

3.3.1 Supplied electrical energy

For a fixed gap value, the amount of supplied electrical energy is controlled by varying the charging time of the coil of the TCI. Prolonging the charging time increases the electrical energy, then affects also the energy transferred to the fluid. The coil charge is commanded by a rectangular trigger signal, which duration varies from 1 to 5 ms. The supplied energy remains constant for charging duration longer than 3.5 ms as a result of coil saturation. With the TCI system, supplied energy affects the discharge as follows: more energy stored in the electric circuit leads to higher supplied energy values, via longer discharges for such kind of igniter. Variation of electrical energy and supplied energy with the coil charging time are shown in Figure 3-7, for a 1 mm gap.

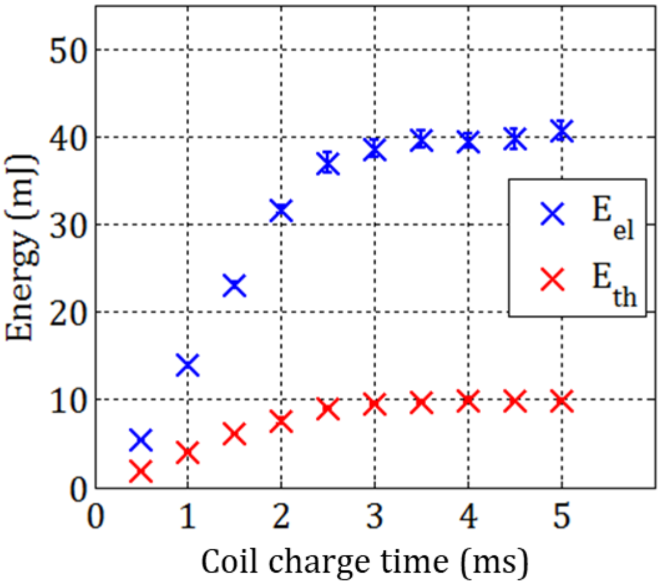

Figure 3-7 : Energy versus TCI coil charging time, for a 1 mm gap, at atmospheric pressure. From the minimum charging time to trigger a discharge (0.5 ms), to saturation time (3.5 ms), both E_{el} and E_{th} increase, with bars for one std.

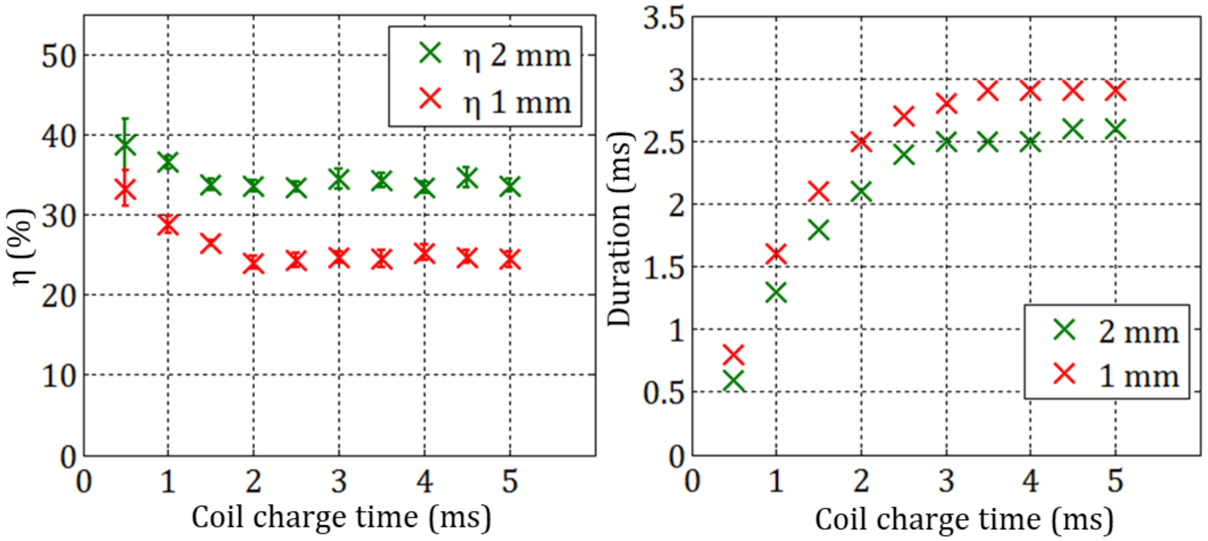

Figure 3-8: Efficiency η (left) and Discharge duration (right) versus coil charge time, for 1 and 2 mm gap.

Overall Efficiency (η), as defined in Eq. (3.1), decreases for higher electrical energies E_{el}, for different conditions (gap) as Figure 3-8 shows. In our configuration the increase of energy is associated to the discharge duration: longer discharges usually have more glow phase fraction, and glow phase is less efficient than arc or breakdown. As there is more glow phase, global efficiency diminishes when increasing the discharge duration and energy. Efficiency is almost 10% higher for a 2 mm gap than for 1 mm. This is studied in detail in section 3.3.3.

3.3.2 Discharge duration

Discharge duration Δt is determined from voltage signals: from maximum voltage until the onset of voltage oscillations –after 0.5 to 3.5 ms, when current value is almost zero-. For each test condition, it is measured for several voltage signals. The uncertainty of discharge duration measurements is of 0.1 ms, with little scattering (same as uncertainty value). Then Δt is used as input for the data processing program, as the moment to stop energy calculation.

Coil charge variation affects mostly discharge duration: breakdown energy depends on gas density and electrodes geometry –and gap (Maly). Low coil charge produces shorter discharges. As coil charging time increases the electrical discharge lasts longer, as one can see in Figure 3-8: from 0.5 ms for the minimum coil charge time of 0.5 ms, to 2.6 ms at saturated coil, for a 2 mm gap.

Gap influences discharge duration: as shown in Figure 3-8, discharges for a 2 mm gap are 0.3 ms shorter than for a 1 mm gap, which is studied in next section.

3.3.3 Inter-electrode gap

Gap distance between the electrode tips has great influence on the energy supplied to the discharge E_{el}, as it affects directly the voltage and the energy needed to generate and maintain an electrical discharge. This is linked to the fluid inside the conductive channel that behaves as an extra capacitance of the total circuit. For a longer channel (longer gap distance) or a higher pressure, there will be more particles that have to be ionized to form the conductive channel.

Then more voltage and more energy will be needed for unleashing and sustaining the discharge. This effect is described, for the breakdown, by Paschen's Law [4].

For a saturated coil different gap distances are tested, see Figure 3-9 representing mean values and standard deviation of thermal and electrical energies over 10 tests at each point. E_{th} increases with the gap, and for a gap value there is little dependence of E_{th} on supplied E_{el}. Stochastic variability of discharges for identical conditions change the supplied electrical energy: this causes the scatter of E_{el} reported in the Figure 3-10 for all the tests. Despite the scattering, E_{th} deposited into the fluid only depends on the gap, for the same fluid initial conditions. Thermal energy increases from 7 to 16 mJ when the gap varies from 1 to 3 mm, see Figure 3-10.

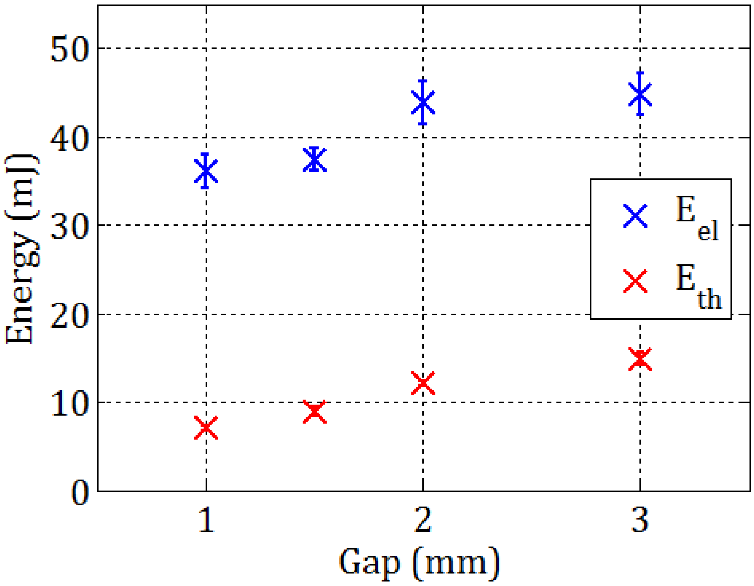

Figure 3-9: Thermal energy and electrical energy for different gap distances. E_{th} increases with gap distance.

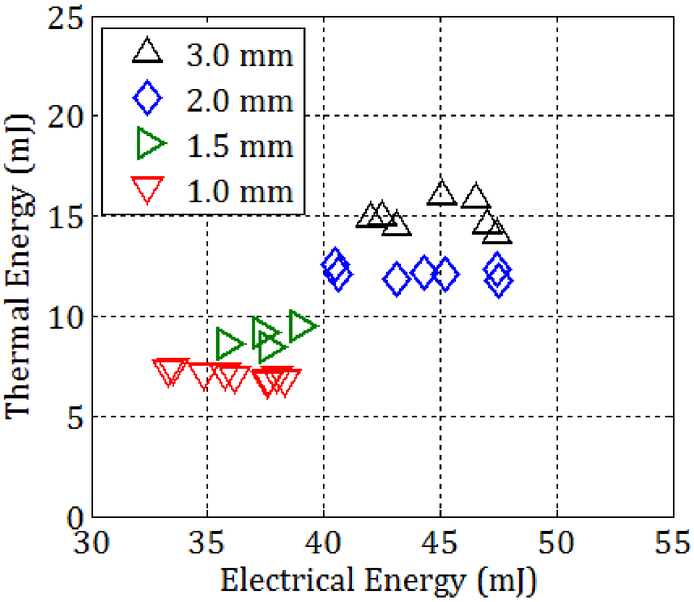

Figure 3-10: E_{th} versus E_{el} for different gap distances. Each point corresponds to one test.

Energy transfer efficiency also rises with the gap (cf. Figure 3-8 and Figure 3-12). Larger gap distance reduces the contact surface of the hot kernel with the conic ends electrodes relative to the total hot kernel area. From schlieren images recorded 0.63 ms after the onset of the discharge (cf. Figure 3-11) the average contact surface is estimated 0.63 ms after discharge onset as 3.2 mm^2 at 1 mm gap, 2 mm^2 at 2 mm gap and 0.8 mm^2 at 3 mm gap. This effect, among other phenomena [2], lower heat losses at high gap values, and higher efficiencies are obtained. For each tested gap distance, variations in the electrical energy produce little change in thermal energy supplied. For a nearly constant thermal energy, higher electrical energies for the same gap result then in lower efficiency.

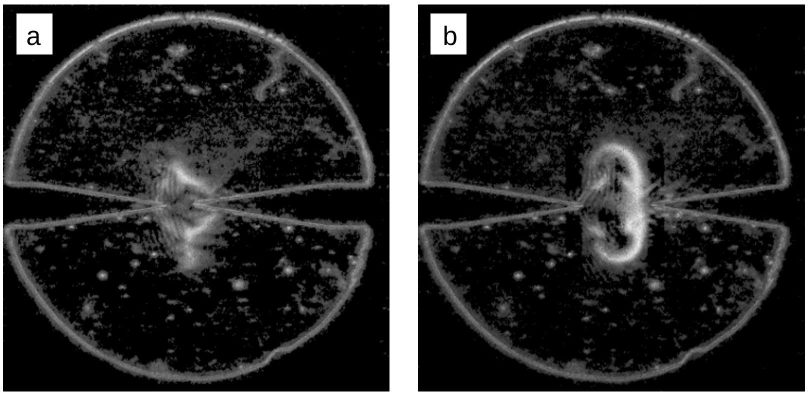

Figure 3-11 : Schlieren images 0.633 ms after discharge. Hot kernel is in contact with electrode tips for 1 mm gap (a) but mostly between electrode tips for a 3 mm gap (b).

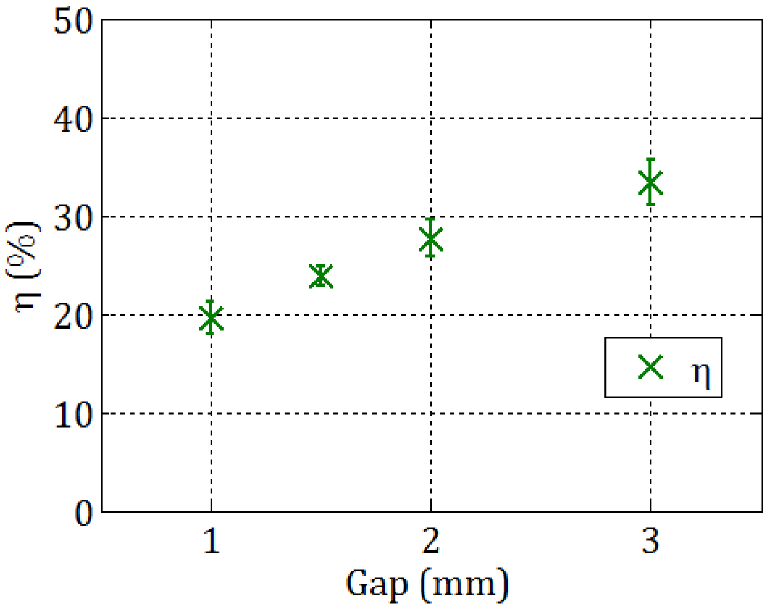

Figure 3-12: Energy transfer efficiency versus gap distance

Efficiency increases with gap distance, as shown in Figure 3-12. This is in good agreement with results from other studies with TCI systems [62] as it can be observed in Table 3-1 and Table 3-2. Main differences between results are probably caused by differences in electrical circuit and electrodes: Teets and Sell [62] employed 0.5 mm diameter Ti wire as electrodes. Despite the differences in absolute values, they all follow the same trends.

	Teets and Sell [62]	Present study (average)
E_{el} (mJ)	50	44
E_{th} (mJ)	11.5	12
η (%)	23%	27%

Table 3-1: Energy and efficiency data comparison, for a TCI system and 2 mm gap at atmospheric conditions

Gap	Teets and Sell [62]	Present study
1 mm	18%	19%
2 mm	23%	28%
3 mm	34%	33%

Table 3-2: Efficiency comparison for different gaps in air and atmospheric conditions

For the same experimental conditions, there is scattering of E_{el} for the same E_{th} deposit (see Figure 3-10). This motivates an in-depth analysis of each discharge phase contribution to the discharge, which has never been done for these calorimetry results and is the topic of next section.

3.3.4 Phase efficiency

Pin-to-pin electrical discharges are highly unsteady phenomena, and their analysis requires the identification and the characterization of their different phases: breakdown, arc and glow. Furthermore, the relative contribution of the different phases of a discharge may vary for identical control parameters as a result of the stochastic nature of electrical discharges. Such a scattering in the duration and thus in energetic contribution of the phases is usually observed. It can be due to small changes in the plasma channel, as it is a part of the electrical circuit that is not completely repeatable. Also there is influence of very small changes in the experimental conditions, as erosion on the electrodes, different location of the arc-glow fast transitions, and small variations in the plasma channel.

Discharge phases contribution is analyzed here through the voltage signal. Efficiency of each phase is also studied.

Breakdown energy is considered as E_{el} during high voltage levels at the initial moments of the discharge (when $V > V_{arc}$), which typically lasts up to 150 μs, and is around 3 mJ (E_{el}). The rest of the discharge occurs in arc and glow phase: a voltage around 400 V corresponds to glow, and 100 V to arc [2]. As multiple arc-glow transitions may occur, the electrical energies are cumulated for each phase, leading to the total electrical energy in arc mode and glow mode. Phase detection is made using a voltage threshold ($U_{threshold}$) of 350 V: when voltage is lower than the threshold value, the energy supplied E_{el} is also counted as electrical energy for arc mode E_{arc}, and similarly for E_{glow} when U is over threshold value. Voltage signal with phase detection is depicted in Figure 3-13. Characteristic values of arc and glow voltage vary with test conditions, i.e. pressure or gas mixture. Hence, the threshold voltage is adapted, see 3.4.2.

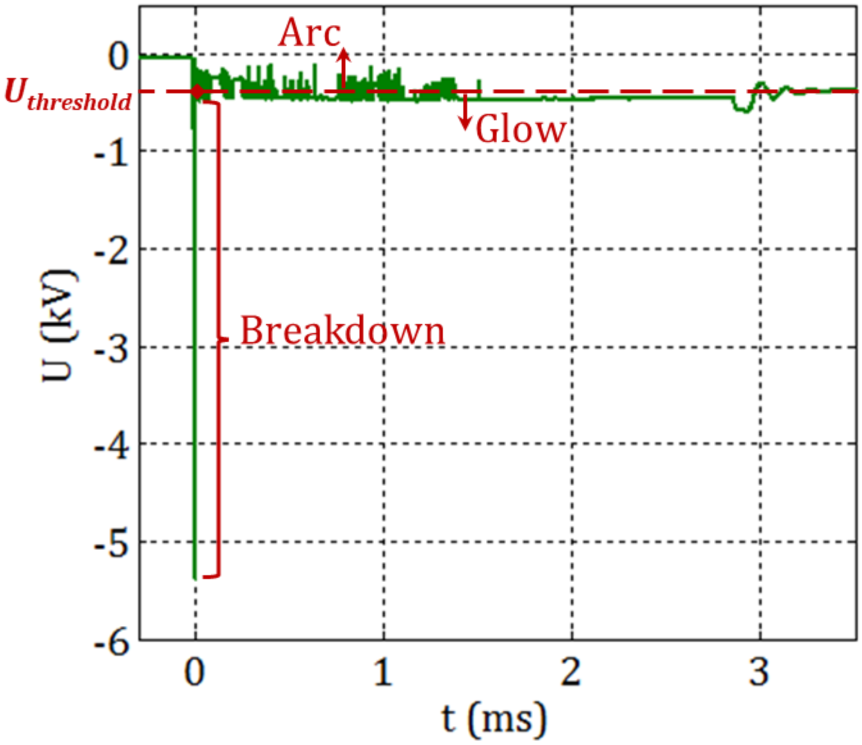

Figure 3-13: Voltage signal with voltage threshold and discharge phase detection.

In a first step, the observed discharges are described by reporting the relative contributions of the arc phase, both in terms of duration and energy fraction. These quantities are reported as a function of gap, for atmospheric conditions, see Figure 3-14 and Figure 3-15 respectively. Tests are made for a saturated TCI (4 ms charging time), to make sure that the maximum E_{el} for the circuit is supplied at each test.

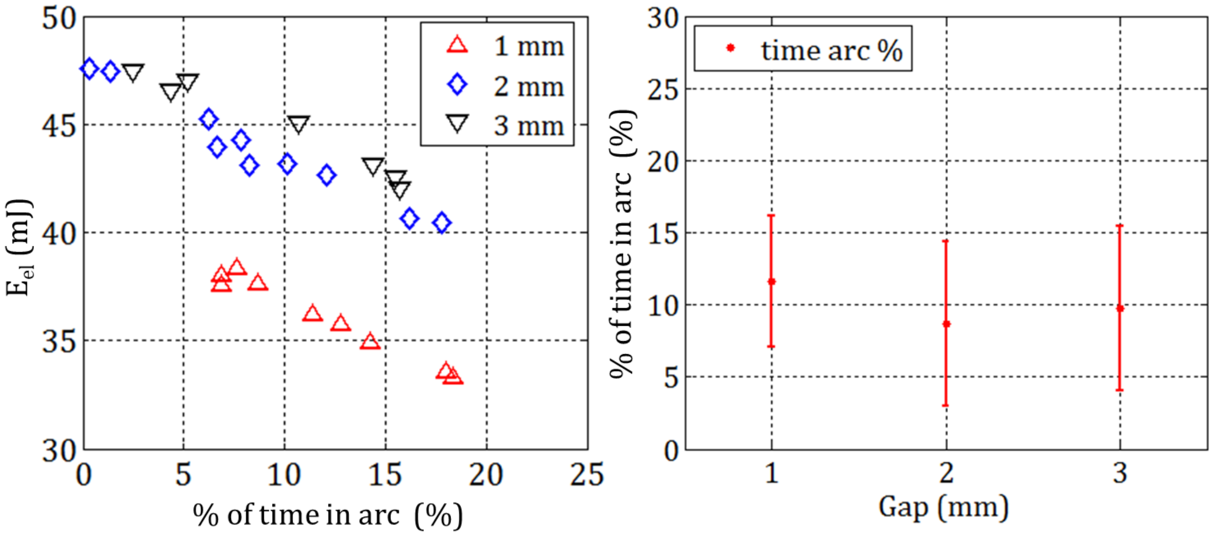

Figure 3-14: Arc duration as a fraction of the total discharge time (arc phase time over global discharge duration). On the left, E_{el} versus time % in arc mode; on the right, time % in arc mode for different gaps.

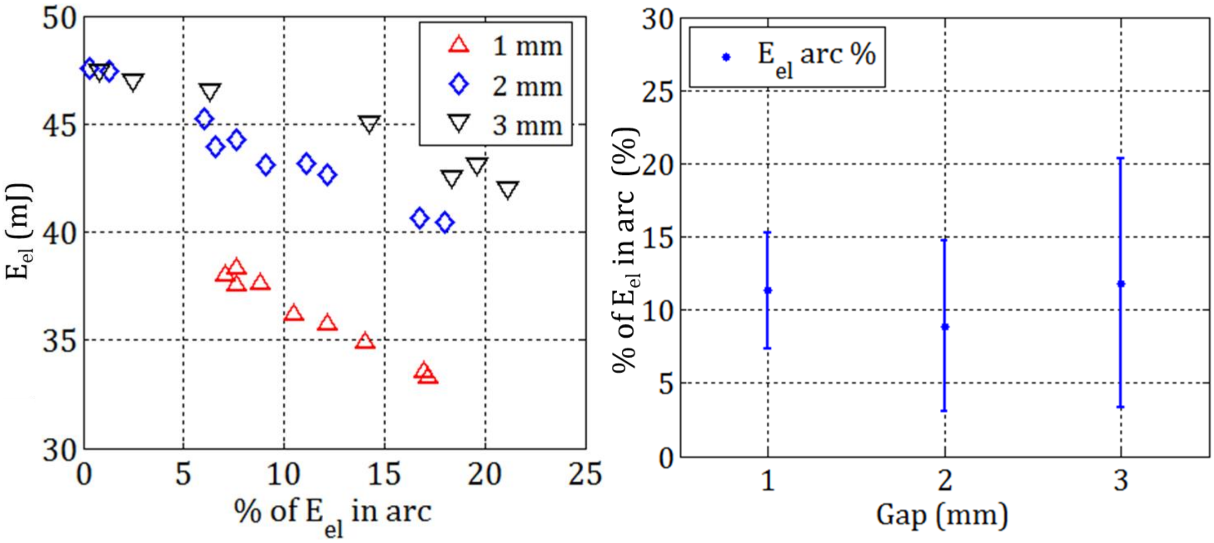

Figure 3-15: Arc phase energetic contribution (fraction of the electrical energy supplied in arc phase). On the left, E_{el} versus E_{el} % in arc mode; on the right, E_{el} % in arc mode for different gaps.

Figure 3-15 shows important variability of E_{el} for each gap. It shows also that this variability seems correlated to the proportion of arc phase, both as time % or in energy %. So higher electrical energy discharges have lower arc fraction, and lower energy discharges happen for higher arc fraction. For some cases, in particular at high gap values, almost the complete discharge is in glow mode (arc percentage close to zero). The higher the percentage of the discharge is in glow mode, the higher the supplied E_{el} is, for the same experimental conditions. This trend is present either regarding the fraction of time of the discharge in arc phase over total discharge duration (Figure 3-14), or regarding the fraction of energy supplied in arc mode over total discharge energy (Figure 3-15).

In a second step, efficiency of each phase of the discharge is estimated, to confirm consistency of these data. For each test, time evolutions of phase composition fraction, thermal energy and electrical energy are related. As in equation (3.2), total energy transfer is obtained by adding the efficiency of each phase (η_{ar}, η_{gl}, η_{bd} for arc, glow and breakdown respectively) multiplied by the fraction of electrical energy in that phase (*A*, *G*, *B* for arc, glow and breakdown respectively). *A*, *G* and *B* are obtained for a set of tests, then multi-fitting allows solving the resulting problem, represented by equation (3.3). This approach was used for interferometric calorimetry by Verhoeven [81], but in this study it is applied to constant volume calorimetry technique with a phase detection voltage threshold. Breakdown efficiency is considered as $\eta_{bd} = 0.9$, as reported by Meyer [15]. As the fraction of E_{el} in breakdown phase (B) is low this induces little uncertainty.

$$A\,\eta_{ar} + G\,\eta_{gl} + B\eta_{bd} = \eta_{th} \tag{3.2}$$

$$\frac{\eta_{th} - 0.9\,B}{G} = \frac{A}{G}\eta_{ar} + \eta_{gl} \tag{3.3}$$

$$With\ A = \frac{E_{ar}}{E_{el}}; B = \frac{E_{bd}}{E_{el}}; G = \frac{E_{glo}}{E_{el}}; \eta = \frac{E_{th}}{E_{el}};\ \eta_{bd} \sim 0.9$$

$$E = Energy; and\ \eta = efficiency.\ Subscripts: el = Total\ Electrical;\ th = Thermal$$

Eq. (3.2) leads to eq. (3.3), where glow and arc efficiencies, η_g and η_a, are the unknowns to be determined. They are supposed to be independent of time and identical for all the tests. *A*, *B*, *G* (fractions of total electric energy delivered by each phase, from the onset of the discharge to the time t under consideration) and η are obtained in each test from the signals, as functions of time. The system is over-dimensioned as there are as many equations as sampling points, i.e. several points for each test and only two variables. Values of cumulated energies are related, at the end of the discharge for at least 10 tests, and a least square fitting provides the glow and arc efficiencies. An example of the fitting for 7 tests is shown in Figure 3-16.

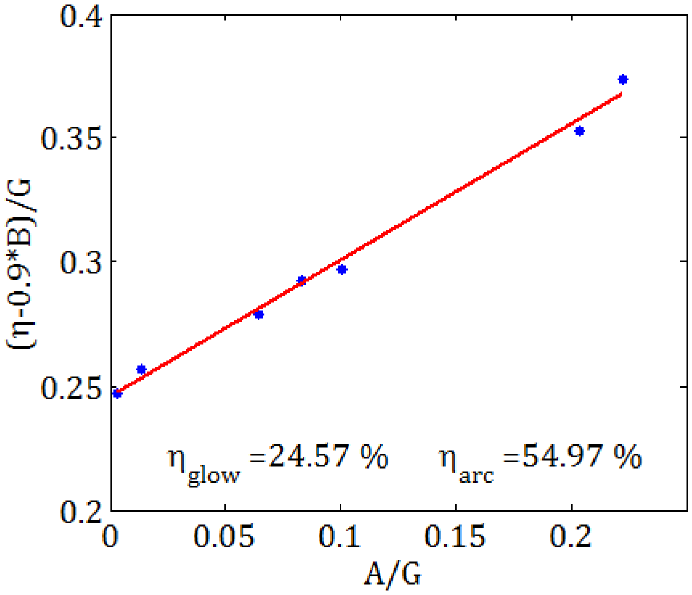

Figure 3-16: Phase efficiency data fitting for a 2 mm gap at the end of the discharge

Table 3-3 shows the obtained values that are consistent with other studies [2], [81]. Nevertheless, results from Maly [2] were obtained from single-mode discharges (only arc or glow phase) and results from Verhoeven [81] were obtained with a low velocity cross-flow of 3.8 m/s, which emphasize the originality of our results. This approach could introduce wrong results if the proportions of arc or glow (*A, G*) are too small (around 5%) or if they are the same for all the tests.

	Maly [2], [12]	Verhoeven [81]	Present study (average)
η_a (%)	50	33	55
η_g (%)	30	30	25

Table 3-3: Glow and arc efficiencies as obtained from different sources.

Arc and glow efficiencies are affected by discharge conditions too. A longer gap increases global discharge efficiency, as well as glow efficiency. Arc and glow efficiency are obtained for 1, 2 and 3 mm gap, see Figure 3-17. Glow efficiency increases from 14.8% at 1 mm gap to 29.6% at 3 mm, while arc efficiency decreases slightly with gap distance, from 54% at 1 mm gap to 50% at 3 mm.

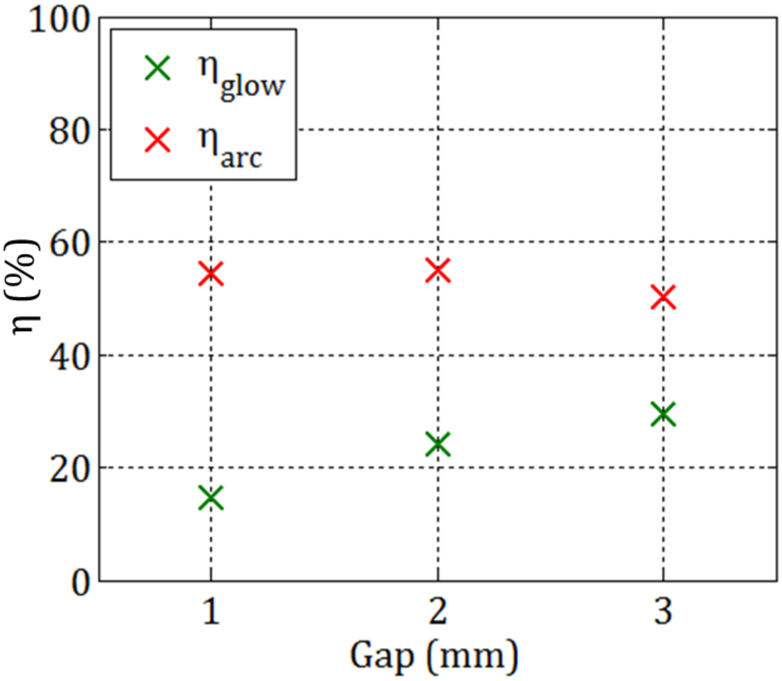

Figure 3-17: Arc and glow efficiencies versus gap.

3.4 Measurements: effects of varying pressure and gas composition

Sets of 10 tests are performed for a pressure range of 0.5 to 2 bar. Air, nitrogen and propane are employed to study the presence of fuel in the gas mixture over spark characteristics. Influence of gaseous mixture composition is investigated as well: experiments are carried out in air, nitrogen, and two nitrogen-propane mixtures of different concentration. The latter represent a stoichiometric and rich mixture where nitrogen replaces oxygen. Indeed, it was found necessary to avoids combustion, as its heat release perturbs calorimetry measurements.

Energies and energy transfer efficiency are measured for each test condition, as well as discharge phase efficiency and discharge duration.

3.4.1 Effect of pressure

Electrical discharges inside engines are produced in a range of temperatures and pressures, which can influence the discharge. In aircraft engine conditions, on-flight reignition takes place at low pressures.

Pressure influences directly energy deposit. E_{th} rises linearly with p, as one can see in tests made in air from 0.5 to 2 bar for 1 and 2 mm gap for a saturated coil (see Figure 3-18). E_{el} varies with pressure in lower extent than E_{th} does (E_{el} increases or decreases by 10% of its value at 1 bar, while E_{th} varies more than 50%). A low scatter of E_{el} values is observed for given experimental conditions while E_{th} remain the same, as it is represented in Figure 3-18 by the mean values from 10 tests at each point, and corresponding standard deviation bars. Efficiency rises with pressure as well, see Figure 3-19.

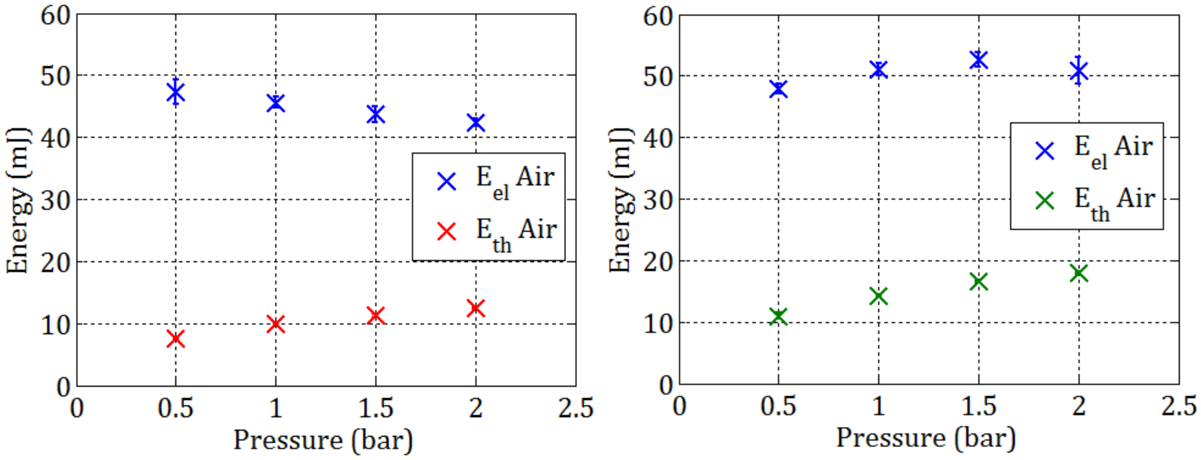

Figure 3-18 : Energy versus pressure in air, gap 1 mm (left) and 2 mm (right).

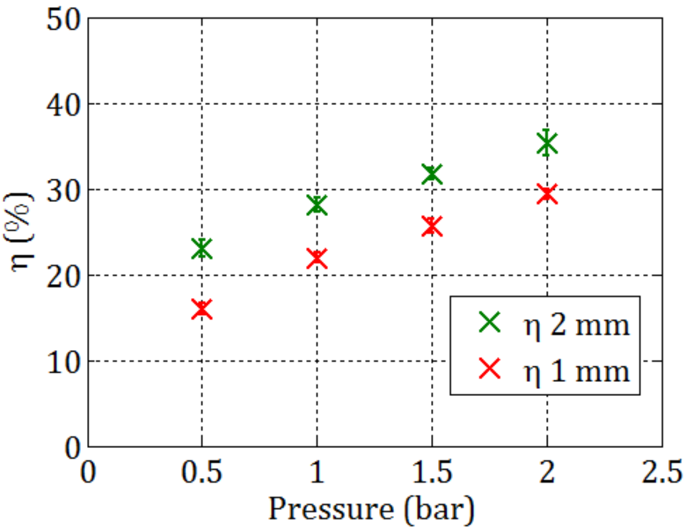

Figure 3-19: Energy transfer efficiency versus pressure for 1 and 2 mm gap

Pressure affects discharges in a similar way than temperature, i.e. through gas density. Together with gap distance, gas density determines discharge characteristics. Electrical discharges properties vary with pressure: at higher pressure, the voltage needed for breakdown rises -according to Paschen's Law as mentioned in 3.3.2-, size and duration of the discharges become smaller, and efficiency increases [62]. Conditions in higher pressure favor arc phase, which lasts longer [2].

One may think that the change in one parameter (gap) could be compensated by the change in the other one (density-pressure): see for instance that for 0.5 bar and 2 mm and 1.0 bar and 1 mm E_{el}, E_{th} and η are very close. The so-called "similarity rules" indicate that the parameter that characterizes a discharge is the electric field reduced with the parameter *pd*, *E/(pd)*, where *E* is the electric field, *p* the gas pressure and *d* the gap distance. Other discharge characteristics –e.g. volume, dynamic effects, or heat transfer- may change in particular conditions, such as for little gap distances or in non-equilibrium discharges [9]–[11].

3.4.2 Gas mixture

Electrical discharges properties vary depending on gas composition: electrical conductivity and resistivity of the gas in the inter-electrode region, species dissociation and/or recombination during the discharge –different ionization energies- and excited species residence time. After characterizing discharges in air, we aim at getting closer to real engine conditions, where hydrocarbon chains may have an effect on the energy transfer at the electrical discharge.

To analyze how the presence of hydrocarbon molecules affect electrical discharges we use a mixture of propane and nitrogen at different concentrations. It is necessary to use an inert mixture (nitrogen in this case) to avoid any energy release produced by oxidation reactions: fuel would react with oxygen releasing energy if an electrical discharge is produced in a propane-air mixture environment, even in lean conditions under the flammability limit.

There is little difference between air and pure nitrogen regarding electrical discharges (cf figure 3.21). Despite the presence of oxygen and its possible recombination –formation of oxides and/or ozone- during the discharge, this process is too fast compared to measurement time. Tests in air and nitrogen give same results, as in Figure 3-20.

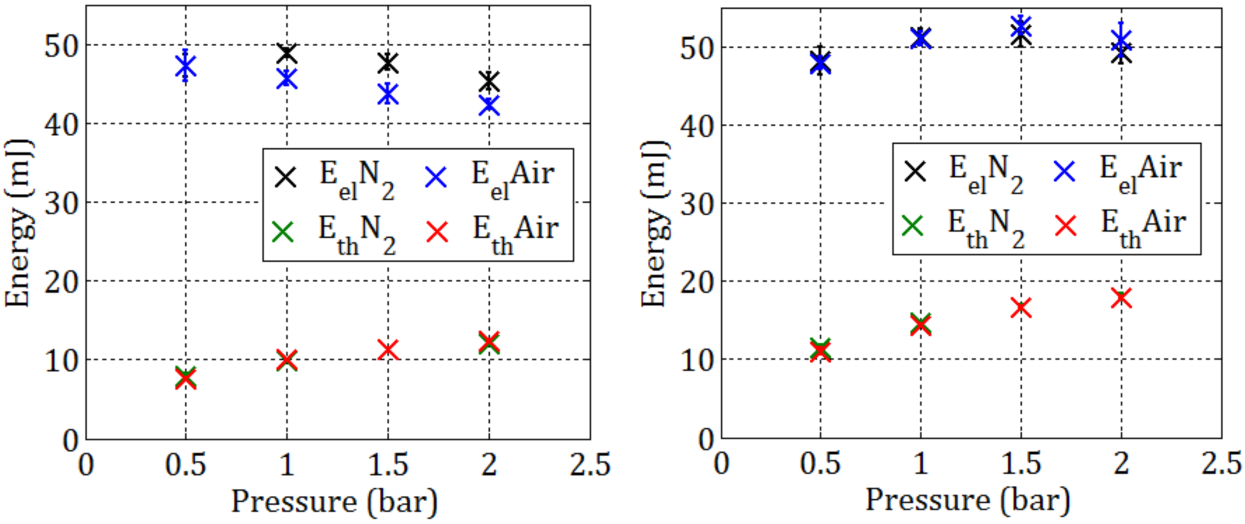

Figure 3-20: E_{el} and E_{th} versus pressure in air and nitrogen, for 1 (left) and 2 (right) mm gap.

We use two different fuel concentrations to represent stoichiometric and rich fuel/air mixtures at equivalent ratio (ϕ) of 1.0 and 1.5; although using nitrogen instead of air as mentioned before (keeping the same molar ratio fuel to total gas mixture). Fuel molar concentration for those propane/nitrogen mixtures were $40.31 \cdot 10^{-3}$ for $\phi = 1.0$, and $59.27 \cdot 10^{-3}$ for $\phi = 1.5$.

Experimental conditions are room temperature (20 °C), 0.5 to 2.0 bar and 1 and 2 mm gap. Here again, ten measurements are performed for each condition, represented as a mean value with its standard deviation bars in figures 3-22 to 3-24.

Energy deposit E_{th} rises in presence of fuel. One can observe the plot of E_{th} as a function of pressure in Figure 3-21, for 1 and 2 mm gap and the three mixtures employed. Discharges in the presence of propane differ from those without the fuel as many properties vary, e. g. ionization energy, gas conductivity, or particle collision cross section. These properties influence the discharge process prioritizing arc phase over glow ones at higher pressures and increasing the arc and glow voltage [4]. E_{el} supplied by the TCI to the electrodes varies from 35 to 42 mJ for 1 mm gap. This variation with pressure is not linear and non-monotonic with pressure. Nevertheless, for a 2 mm gap E_{el} increases with pressure, see Figure 3-22. Because of the higher E_{th} and the lower E_{el}, the energy transfer efficiency η improves with pressure and in the presence of fuel (Figure 3-23).

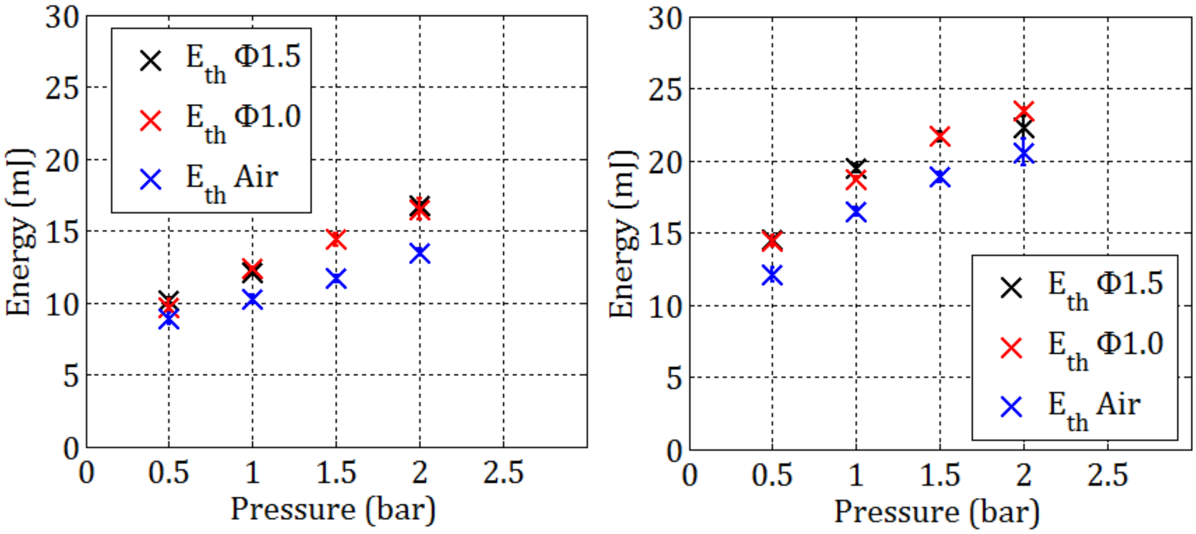

Figure 3-21: E_{th} vs pressure for different mixtures, at 1 mm (left) and 2 mm (right) gap.

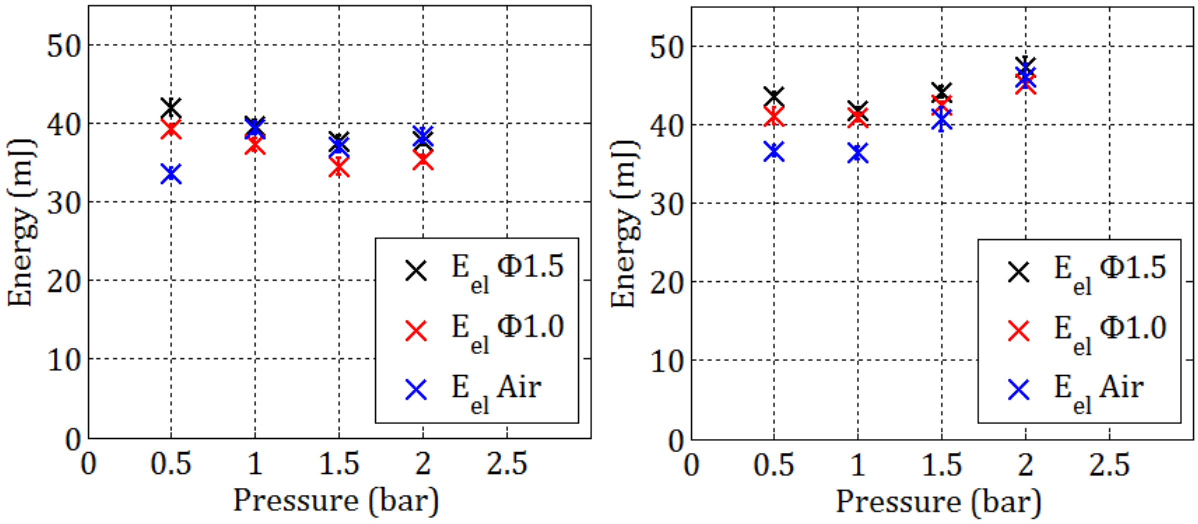

Figure 3-22: E_{el} vs pressure for different mixtures, at 1 mm (left) and 2 mm (right) gap.

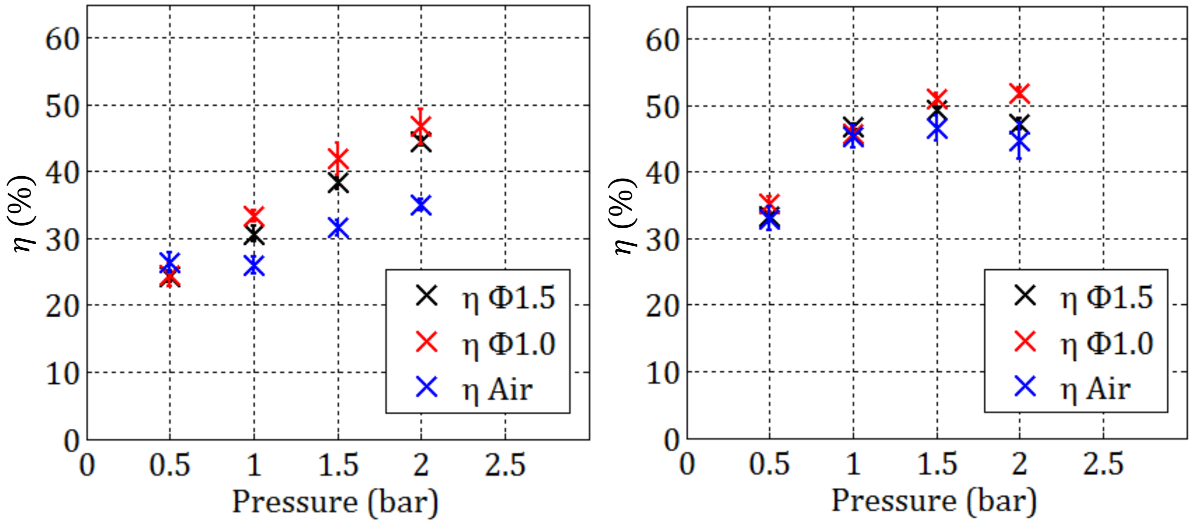

Figure 3-23: Efficiency vs pressure for different mixtures, at 1 mm (left) and 2 mm (right) gap.

It is observed electrical energy varies with pressure and mixture composition. This is explained by the fact the gas between the electrodes is a part of the electrical circuit, and changing its properties affect the discharge from the electrical point of view.

Breakdown voltage doubles when increasing pressure from 0.5 to 2.0 bar. One can see the different voltage levels in Figure 3-24 for air, and Figure 3-25 for nitrogen-propane mixtures (ϕ = 1.0 left figure, ϕ = 1.5 in the right). Voltage is presented inversed (positive values) for clarity in these figures. The voltage increase in the presence of fuel in both arc and glow phase is caused by the different chemical composition, as propane molecular bonds must break at ionization [2].Voltage level is higher in presence of fuel than in air, and for higher pressures: glow voltage reaches 1000 V for a discharge in 2 bar in any of the fuel-nitrogen mixtures while it remains in 300 V at 2 bar in air.

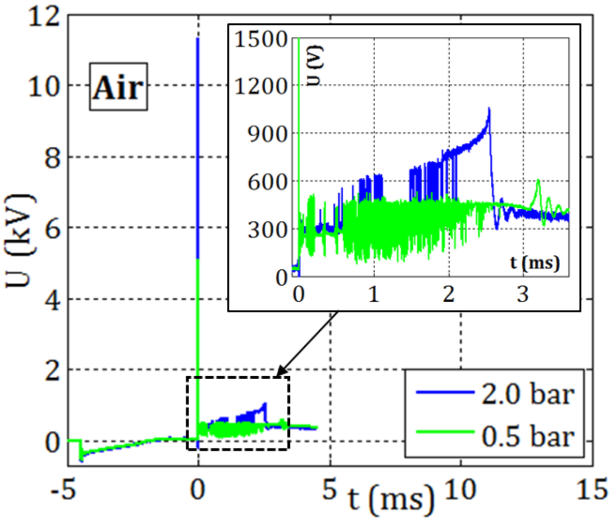

Figure 3-24: Voltage at 0.5 and 2 bar for a 2 mm gap in air.

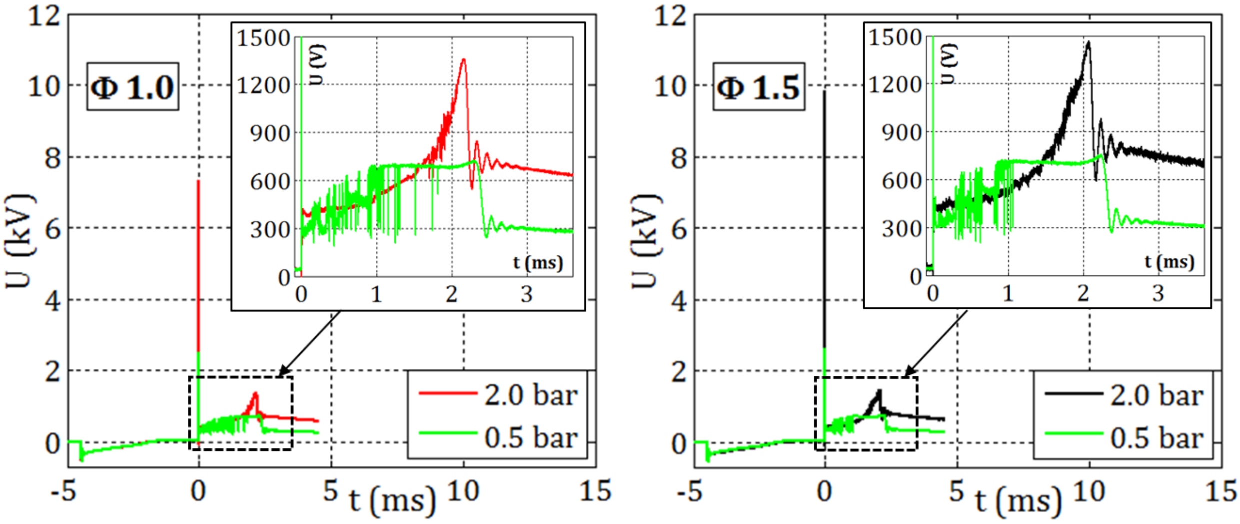

Figure 3-25: Voltage at 0.5 and 2 bar for a 2 mm gap in C_3H_8-N_2 at Φ =1.0 (left) and Φ = 1.5 (right).

3.4.3 Phase efficiency and discharge duration

3.4.3.1 Phase efficiency

As a result of these changes in discharge physics, arc phase prevails over glow phase in the presence of fuel. The fraction of E_{el} deposited in arc phase rises with pressure and fuel concentration, reaching an almost complete arc discharge at higher pressure values for $\phi = 1.0$ and 1.5, see Figure 3-26.

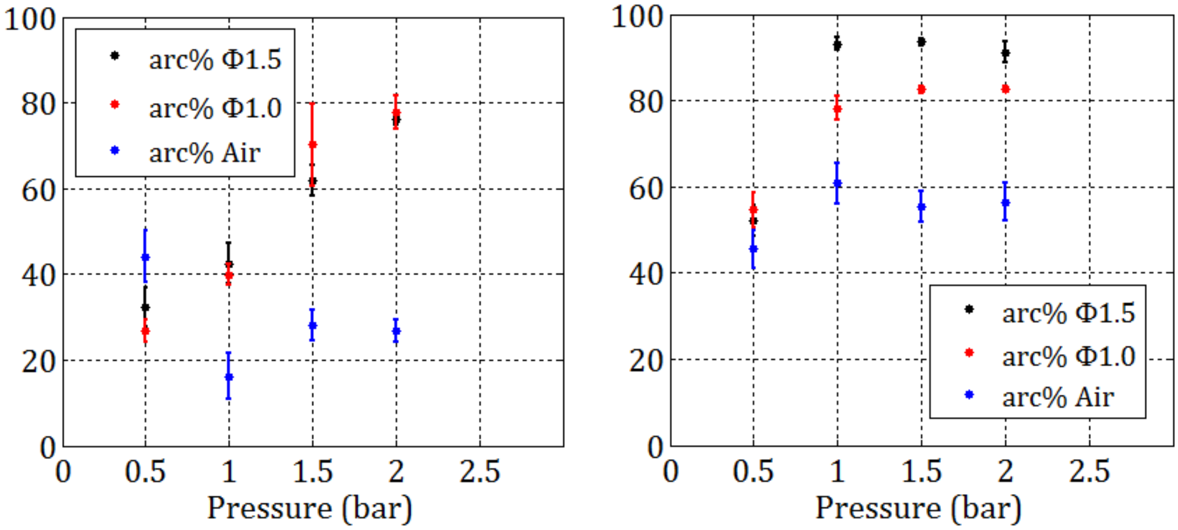

Figure 3-26: Arc phase fraction of total E_{el} vs pressure for different mixtures, at 1 mm (left) and 2 mm (right) gap.

Efficiency calculation of the discharge phases for different pressures and mixtures is estimated as described in 3.3.4. For propane-nitrogen mixtures at pressures from 1 to 2 bar, most of the discharge is in arc mode, as in Figure 3-26. For these conditions only the efficiency of arc phase can be estimated. It is represented in Figure 3-27, where for 1 mm gap arc efficiency increases with pressure for air and the Φ=1.0 mixture, but not for the rich mixture. Values of arc efficiency range between 35 and 55%.

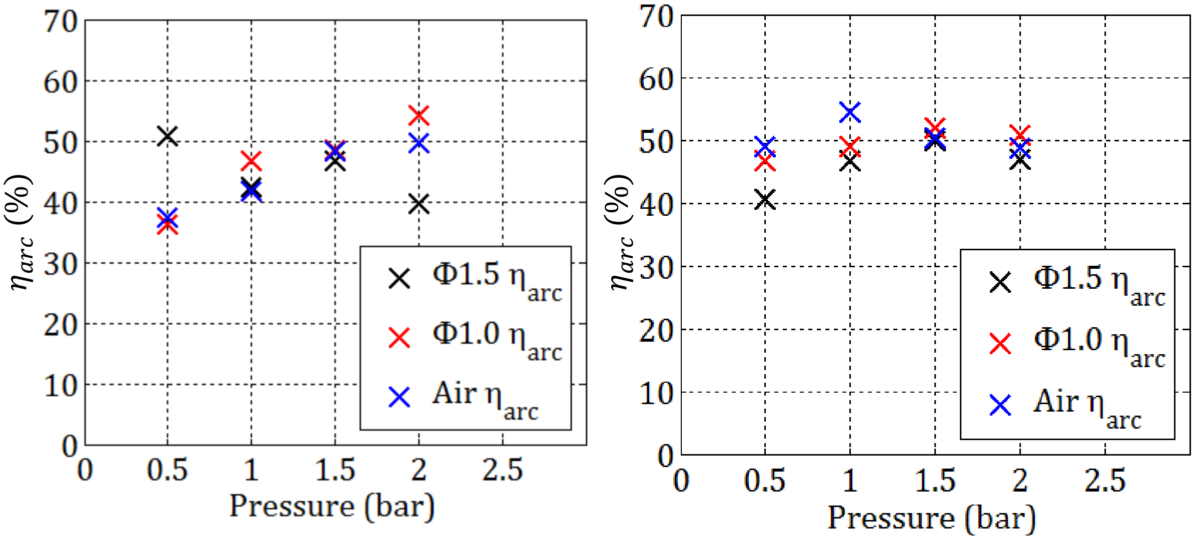

Figure 3-27: Arc phase efficiency versus pressure, for 1 mm (left) and 2 mm (right) gap.

3.4.3.2 Discharge duration

Spark discharges shorten for higher pressures, and they are shorter in presence of propane. In propane-nitrogen mixtures, electrical discharges are between 0.3 and 1 ms shorter, see Figure 3-28.

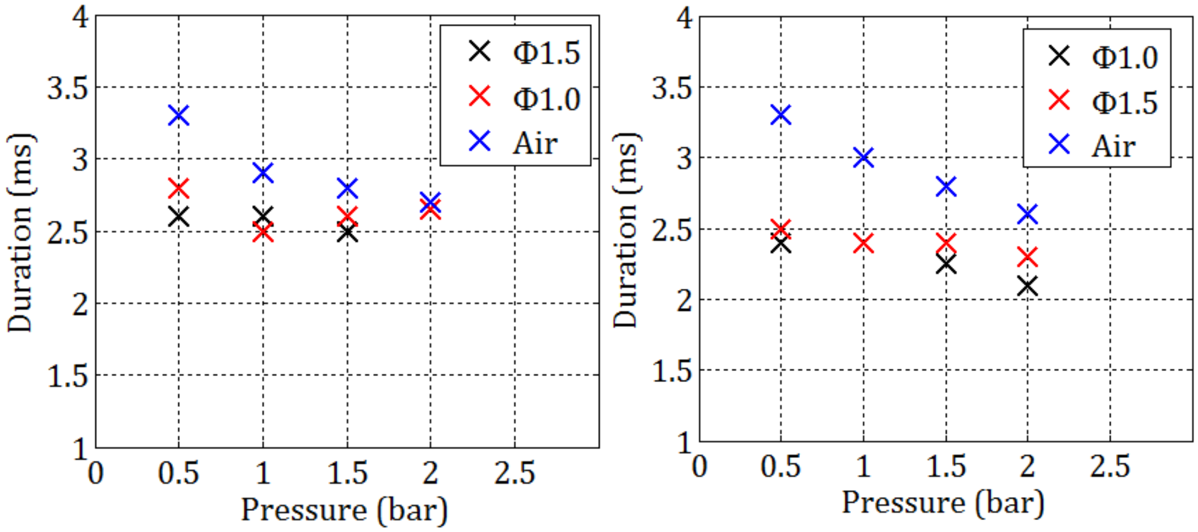

Figure 3-28: Discharge duration for 1 mm (left) and 2 mm gap (right).

The different composition of the discharge explains the different discharge duration, as there is a higher proportion of the discharge in arc phase (more efficient than glow phase) in presence of propane and higher pressure. The difference in discharge duration is explained by the energy needed to produce the discharge: higher voltage is needed for increasing pressure and in the presence of gas. At the same time, the energy available at the secondary circuit of the ignition system remains almost constant, as it depends on the electrical circuit only, so this available energy runs out faster [87]. Thus, the discharge is sustained for a shorter time.

3.5 Conclusion

A constant-volume calorimetric system is developed for characterizing the energy deposit of electrical discharges. A standard TCI pencil coil igniter with pin to pin electrodes is employed. During the discharge, electrical input energy is monitored from the electric signals measured at the electrodes, and the energy deposit in the fluid is estimated from the transient pressure rise in the constant volume vessel.

Electrical energy supplied to the discharge is controlled by the coil charging time. For 0.5 to 3.5 ms the coil is under-saturated, producing shorter discharges with less energy deposit than with fully saturated coil but with a higher efficiency. Schlieren technique is also used to verify method hypothesis as influence of the hot kernel on subsequent discharges, shockwave effect duration and kernel-electrodes contact surface. Method hypotheses are verified: plasma volume negligible compared to total gas volume, constant heat capacity ratio and negligible heat losses through the walls.

Heat transfer after the end of the discharge is estimated from the pressure decay. Thermal energy deposit in the fluid and transfer efficiency increase with gap, as the voltage rises for longer gap and there is a smaller proportion of contact surface between electrodes and the hot kernel, as it is observed by the schlieren images. First results are consistent with those from other studies and validate the calorimetric technique for our setup.

Electrical energy values present important scattering for the same experimental conditions, while thermal energy deposit remains the same with little variation. Energy deposit should be used as the characteristic energy of an ignition system, instead of the electrical energy it uses, as it would be more accurate and useful for applications related to the fluid such as ignition, combustion or fluid dynamics. The effects of inter-electrode gap, pressure and gas composition modify the energy deposit and energy transfer efficiency and have been investigated in this chapter.

Both energy deposit and energy transfer efficiency increase with pressure. The presence of fuel affects also electrical discharges, increasing the energy deposit, improving efficiency, and changing the portion of the discharge occurring in arc mode. Contribution of the different phases of the discharge to the transferred energy value and the related discharge efficiency are analyzed by calorimetry for the first time. These results provide a better understanding of the nature of scattering of the experimental results: for longer discharge duration there is more energy supplied in glow mode, and the total efficiency is lower as a result. Changes in the amount of electrical energy supplied in each phase of the discharge, i.e. higher ratio arc to glow, only affects the transfer efficiency and not the energy deposit in the fluid. Efficiency of different discharge phases are also affected by experimental conditions (gap, pressure, gas composition), which should be taken into account when modelling electrical discharges or ignition systems in different conditions.

Chapter 4

Optical calorimetry of electrical discharges using SBOS

Contents

4 Optical calorimetry of electrical discharges using SBOS

This chapter describes the application of Speckle-based Background Oriented Schlieren (SBOS) to electrical discharges produced by a pair of pin-to-pin electrodes.

First optical concepts and theories are introduced in §4.1. Schlieren techniques bases are presented, as well as the optical principles of schlieren, the theory development for Background Oriented Schlieren (BOS) and the advantages of the speckle background in SBOS.

Then SBOS measurement methodology is described step-by-step, applying it for an electrical discharge in atmospheric conditions in §4.2: from speckle generation and image acquisition to calculation of local energy distribution (volumetric energy distribution) and global energy (energy deposit). Spatial distributions of refractive index, density and temperature are obtained through the process.

The method is validated in section §4.3, through a reference case with similar density gradients as those found in a spark discharge kernel: the analysis of a laminar flow Reynolds CO_2 jet. These results allow for uncertainty and noise investigations of the method. Main advantages and limitations of the application of SBOS to electrical discharges are commented.

Electrical discharge experiments with pin-to-pin electrodes are reported in different conditions in §4.4. Energy deposit, spatial distribution of gas properties and kernel size are compared at different instants and for different gap values. The effect of pressure and gas mixture is studied as well. The SBOS energy deposit measurements are compared to pressure-rise calorimetry results.

Finally, chapter conclusion is presented in §4.5, together with notes about the method.

4.1 Principles of the Speckle-based Background-Oriented Schlieren

In this section, we introduce the optical concepts and theories that bind the integrated refractive index to the measured displacement field, as in [103]. The optical configuration is similar to the one described in [104].

4.1.1 Gladstone-Dale relation and Schlieren method

Schlieren method translates light phase differences into amplitude differences that we can see [105]. It is based on the dependency of the refractive index on the fluid density, as described by the Lorentz-Lorenz equation. It is simplified for gases in the Gladstone-Dale relation:

$$n - 1 = \rho K \tag{4.1}$$

K is the Gladstone-Dale constant, which can be found in tables or calculated based on refractive index measurements and density calculations for the respective conditions. The same variation of n is observed in K, and depends primarily on both the fluid composition and wavelength.

Gladstone-Dale relation for a gas mixture of several constituents is given by (4.2).

$$n - 1 = \sum_i K_i \rho_i \tag{4.2}$$

This linearity also applies for the case of an ionized gas, as in Eq. (4.3) [106]:

$$n - 1 = \rho[(1 - \alpha_I)K_A + \alpha_I K_I] + N_e K'_e \tag{4.3}$$

Where K_A and K_I are the Gladstone-Dale constants of the atom and the ion gas respectively. N_e is the electron number density, and K'_e, the constant of the electron gas, has dimensions different from those of K_A and K_I.

Principle of schlieren imaging is the following: density variations at some point of the light path imply refractive index variations, which deviate light beams from their initial path. Non-deviated light beams are stopped by an optical blade so they do not reach the camera, as it is shown in Figure 4-1. The illuminance level in a schlieren image responds to the first spatial derivative of the refractive index [105].

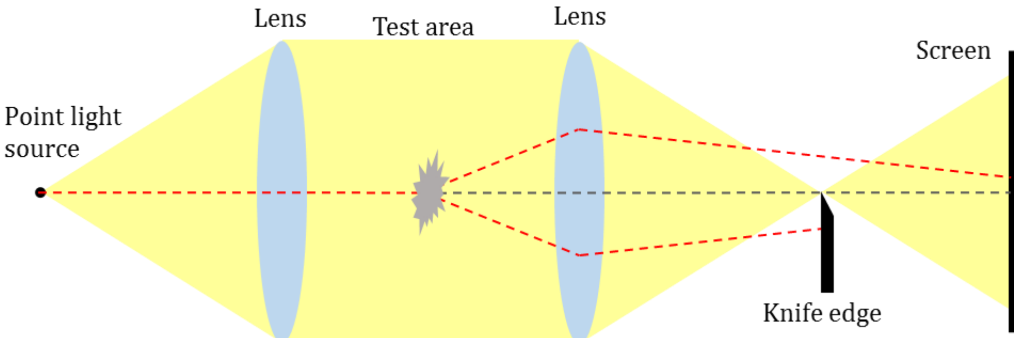

Figure 4-1: Diagram of a schlieren system [105]

4.1.2 Background-Oriented Schlieren (BOS)

As a schlieren method, it is based on the principle that when a light ray propagates through an optically heterogeneous medium, its trajectory bends according to the refractive index gradient. This behavior is mathematically modeled by the eikonal equation [105], [107]. If one assigns the z-axis of a right-handed Cartesian x,y,z coordinate system as the direction vector of the undisturbed light ray –see Figure 4-2- the eikonal equation yields the following curvature:

$$\begin{cases} \dfrac{\partial^2 x}{\partial z^2} = \dfrac{1}{n}\dfrac{\partial n}{\partial x} \\ \dfrac{\partial^2 y}{\partial z^2} = \dfrac{1}{n}\dfrac{\partial n}{\partial y} \end{cases} \tag{4.4}$$

Where n is the refraction index. In the limit of small angles, the intrinsic angular ray deflections write $\varepsilon_x \approx \frac{\partial x}{\partial z}$, $\varepsilon_y \approx \frac{\partial y}{\partial z}$. Integrating eq. (4.4) along light path $\mathcal{C}$ yields the schlieren intrinsic angular ray deflection ε and its components along x and y:

$$\begin{cases} \varepsilon_x = \dfrac{1}{n}\displaystyle\int_{\mathcal{C}} \dfrac{\partial n}{\partial x} dz \\ \varepsilon_y = \dfrac{1}{n}\displaystyle\int_{\mathcal{C}} \dfrac{\partial n}{\partial y} dz \end{cases} \tag{4.5}$$

Since ε is obtained as a result of integration, knowledge of the boundary conditions is required to achieve an absolute measurement. One can estimate the expected maximum value of ε based on the deviation that would occur at the extremity of the gas sphere of a refractive index n placed in a fluid of refractive index n_0, based on Keagy's [108] calculations. This is approximated as

$$\varepsilon_{max} \sim 2(n/n_0 - 1) \tag{4.6}$$

Usually, the refractive index is not the measurement of interest. Using the Gladstone-Dale equation one can use the refractive index to obtain gas density ρ (Eq. (4.1)).

In BOS configurations, the angular intrinsic deflection is materialized on a screen by amplification through the optical collection configuration (Figure 4-2).

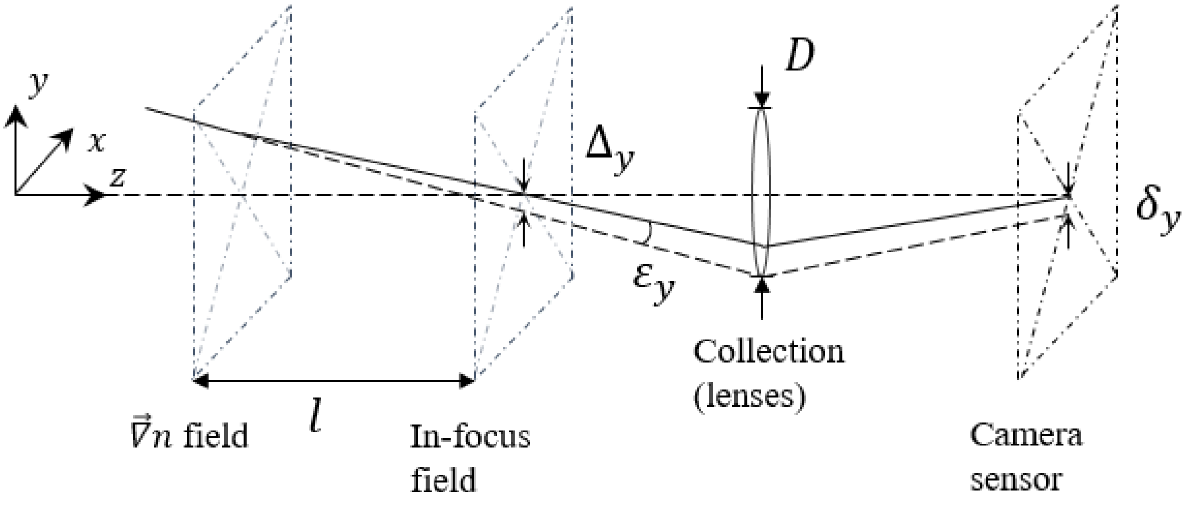

Figure 4-2: Geometry of SBOS configuration with negative focus to subject field distance [103]

In most BOS pictures, the in-schlieren plane objects appear blurry because of the defocusing required to induce the signal. In the classical BOS method, the focal plane corresponds to the background. But with SBOS, the focal plane can be virtual, therefore it can be positioned anywhere, ranging from the speckle generator up to negative distance in front of the transparent object of interest (Figure 4-2). Simple geometrical considerations based on the Figure 4-2 (assuming optical Gaussian conditions and near-axes ray light) yield the expression of the integrated displacement vector field $\vec{\delta}$ as

$$\vec{\delta} = lM\vec{\varepsilon} \tag{4.7}$$

where M is the optical magnification of the optical system (i.e., the magnification measured in the in-focus field) and l is the defocusing distance. $A = lM$ can be considered to be the optical amplification constant.

Blur adds a sliding averaging window convolution to the signal, the width of which is d_{av} dimensions [109] (Figure 4-3), resulting in a loss of spatial resolution.

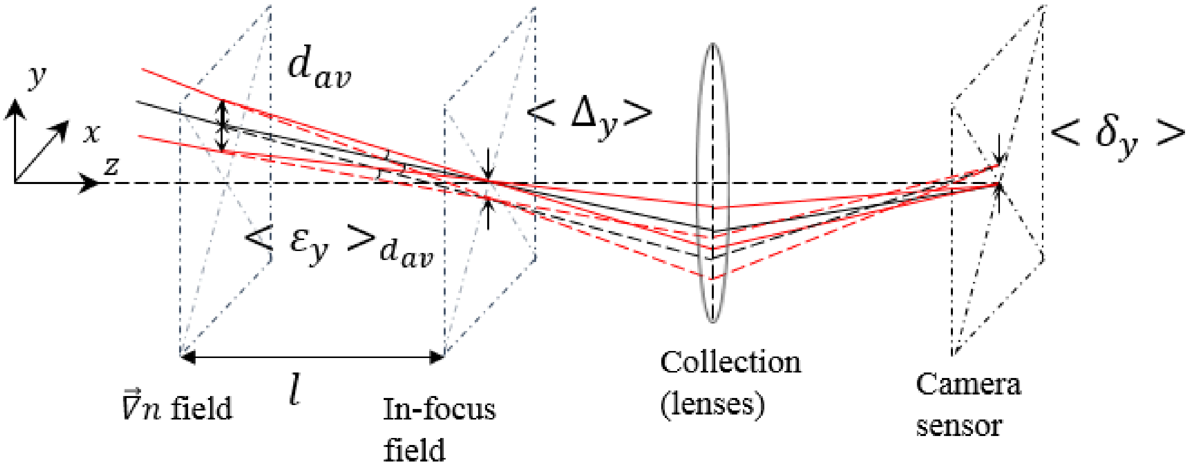

Figure 4-3: Scheme similar to Figure 4-2, where defocusing blur affected by ray tracing is added (in red). For simplicity of representation, ε_y (x,y) for each ray is taken as an average (< > operator) ε_y (x,y) over d_{av} resulting in an averaged Δy and averaged δy [103]

From geometric considerations, one can easily establish [109] a simple expression for d_{av}:

$$d_{av} = \frac{l}{N}\frac{M}{1+\mathrm{M}} \tag{4.8}$$

where N is the f-number of the optical system ($\mathrm{N} = f/D$), D is the optical system effective aperture diameter, and f the focal length of the aperture lens. M is the absolute value of magnification. Depending on the optical configuration, d_{av} may differ slightly from the observed optical blur, considering the focus rays traced back from the refractive plan. A direct consequence of Eq. (4.8) is that the blur effect decreases with decreasing aperture diameter D.

When looking for an optimal BOS configuration, one should then notice that the blur spatial averaging scales proportionally to the defocusing distance. Given an expected maximum spatial resolution, (4.7) and (4.8) then yield an upper limitation to the BOS signal amplification value A.

Implementing BOS is quite simple, as it technically requires only a background and camera. Afterwards, cross-correlation algorithms from PIV applications are typically used to compute the optical displacement field. Therefore, any background which looks like a PIV-seeded flow will provide good results in BOS. For qualitative and visualization purposes, it is easily observed that any background with sufficient contrast will work with the algorithm. Several backgrounds have been used to obtain quantitative density measurements, such as dot-printed black and white patterns [110], printed black and white wavelet noise [111], or regular colored grids (CGBOS [112]).

More recently, the work of Meier and Roesgen [104] introduced the use of laser speckle as a background choice. This is the Speckle-based Background Oriented Schlieren (SBOS). If using a subjective speckle (which is explained in next section), as emphasized by Meier, the imaging lens aperture itself is considered as the source of the speckle pattern, not the BOS reference screen nor the surface used to generate the speckle. Speckle photography already used similar configurations [107], but the computation capacity and required algorithms were not available when it was considered.

Eq. (4.7) still stands in speckle configurations. Furthermore, one can currently work with negative defocusing distance values, speckle being observed in the focal plane. In BOS setups, the background pattern is placed at the focal plane, and the $\vec{\nabla} n$ field (the phenomenon of study) placed between the focal plane and the camera sensor (positive defocus distance l). As in SBOS the background is subjective, it is observed at the location of the focal plane, even if it the focal plane is placed between the $\vec{\nabla} n$ field and the camera sensor (negative defocus distance l). According to Meier and Roesgen [104], working with negative distances greatly increases sensitivity relative to an equal but positive distance. Such configurations considerably reduce the distance needed to achieve equivalent sensitivity for a positive distance.

The practical application of the SBOS technique to the measurement of gas properties and energy deposit in electrical discharges is described next.

4.2 Methodology

In this section, the SBOS methodology is described step-by-step, from a practical point of view, from the experimental procedure up to the data processing as applied in measurements of properties of pin-to-pin electrical discharges.

The method starts by the generation of a background image and image acquisition, which are explained first (§4.2.1). Then the displacement field is calculated using DaVis® program and a Particle Image Velocimetry–like processing (§4.2.2). Matlab® program is used for the rest of the data processing. It consists in: calculation of the divergence of the displacement field, its integration to solve the resulting Poisson equation (§4.2.3), a filtered backprojection to obtain the refractive index and temperature field (§4.2.4), and calculation of the enthalpy variation induced by the discharge (§4.2.5). Lastly, control parameters are discussed (§4.2.6), and the SBOS advantages and limitations are analyzed (§4.2.7).

4.2.1 Image acquisition

First a speckle background is generated by the interaction of a laser beam, a ground glass, the lenses and camera sensor. SBOS requires at least two images: a reference background pattern, and a test image. The reference image can be used for different tests in the same conditions. A reference image of the background pattern is recorded at initial conditions for the test. A second image is captured at a chosen time after discharge onset. Background pattern is disturbed by refractive index gradients in the optical path produced by the electrical discharge. This process is described in detail next:

4.2.1.1 Speckle generation

There are two ways to generate a speckle pattern, as described in the Speckle physics book by Fomin [107]. The first one is by reflection of coherent light from a rough surface, which reflects with different angles in different points of the surface. The second one is by transmission of the light through a transparent medium with a randomly fluctuating refractive index distribution, such as a ground glass, and the subsequent 3D multiple beam interference.

In the chosen optical configuration (Figure 2-8), speckle pattern is generated by transmission through a transparent medium: laser light passes through the ground glass changing its phase, as the ground glass surface is irregular. On the optical setup focal plane, i.e. the plane where the camera sensor is focused, light is observed with heterogeneous phase distribution, forming speckle patterns with similar appearance where light is in the same phase.

Speckle patterns are interferential in nature. They are formed when scattered (i.e., spatially randomly phased) coherent light interferes with a sensor surface. It can be shown [107] that when a speckle is acquired through an optical system, the speckle mean dot “diameter” (i.e., characteristic size, Δ_s) is described by:

$$\Delta_s \approx 1.22\lambda N\frac{1+M}{M} \tag{4.9}$$

where λ is the wavelength of the coherent light. In (4.9), Δ_s increases for a decreasing pupil diameter of the collection system exit ($\mathrm{N} = f/D$), which is easily verified experimentally. Multi-pass cross-correlation software criteria advise using 2-5 pixel/dots to achieve optimum results (sub-pixel interpolation). At a fixed magnification, speckle mean size is tunable, even beyond what can be achieved with physical printed backgrounds. It is particularly well suited for high magnification applications where printing resolution becomes an issue (i.e., beyond 1200 dpi).

For each magnification, an optimal diaphragm opening must be found with both sufficient contrast and light and a small enough speckle size, while keeping spatial resolution as high as possible, as given in Eq. (4.9). Depth of field decreases with an increasing diaphragm opening, i.e. the blur effect decreases with decreasing aperture diameter D, as in (4.8). The amount of light that reaches the camera sensor is higher for bigger diaphragm openings. One can see the effects of D on the speckle reference fields in Figure 4-4: for $D = 6\,mm$ (Figure 4-4, left) speckle size is bigger and chamber and electrode edges are less blurry than for a $D = 10\,mm$ (Figure 4-4, right). In the figure, the images correspond to a square window with a 13.18 mm side.

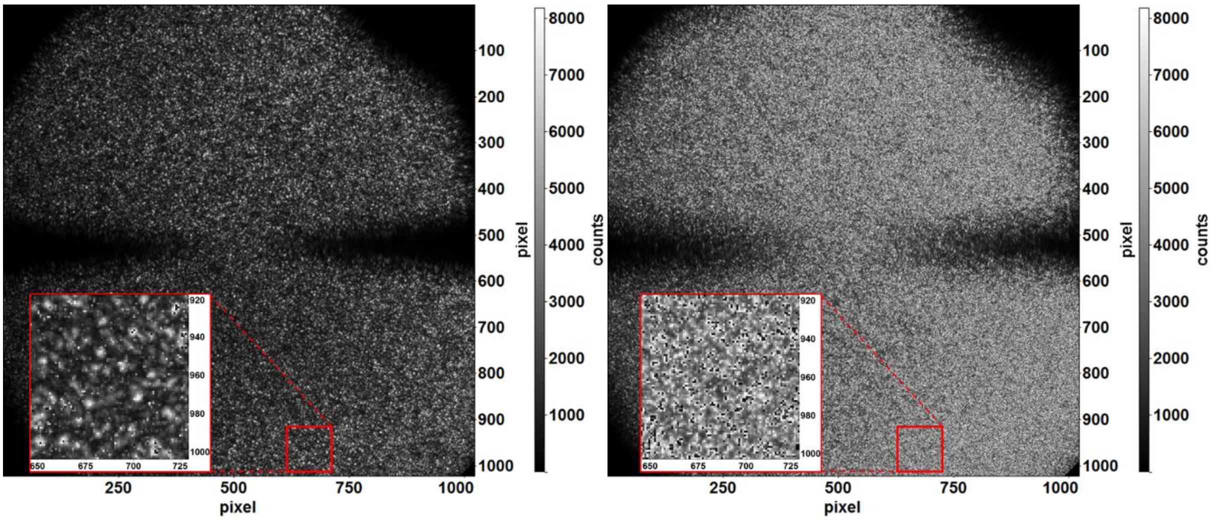

Figure 4-4: Different speckle backgrounds for different diaphragm opening diameters: 6 mm (left) and 10 mm (right). Pin-to-pin electrodes with 1 mm gap, at 2 bar with defocus distance l -80 mm.

4.2.1.2 Test images

Image acquisition is controlled by WinView32 program. Camera shutter speed (camera sensor exposure time), image capture delay and light intensity gain are adjusted to experimental conditions.

Defocus distance l is set to have an adequate speckle point displacement. This causes image details, such as electrode edges, to be blurry. This effect is shown for $l = -80\,mm$ in Figure 4-5, which compares the test chamber and the electrode tips at 1 and 2 mm gap without defocus (l = 0 mm) and with a defocus distance of $l = -80\,mm$.

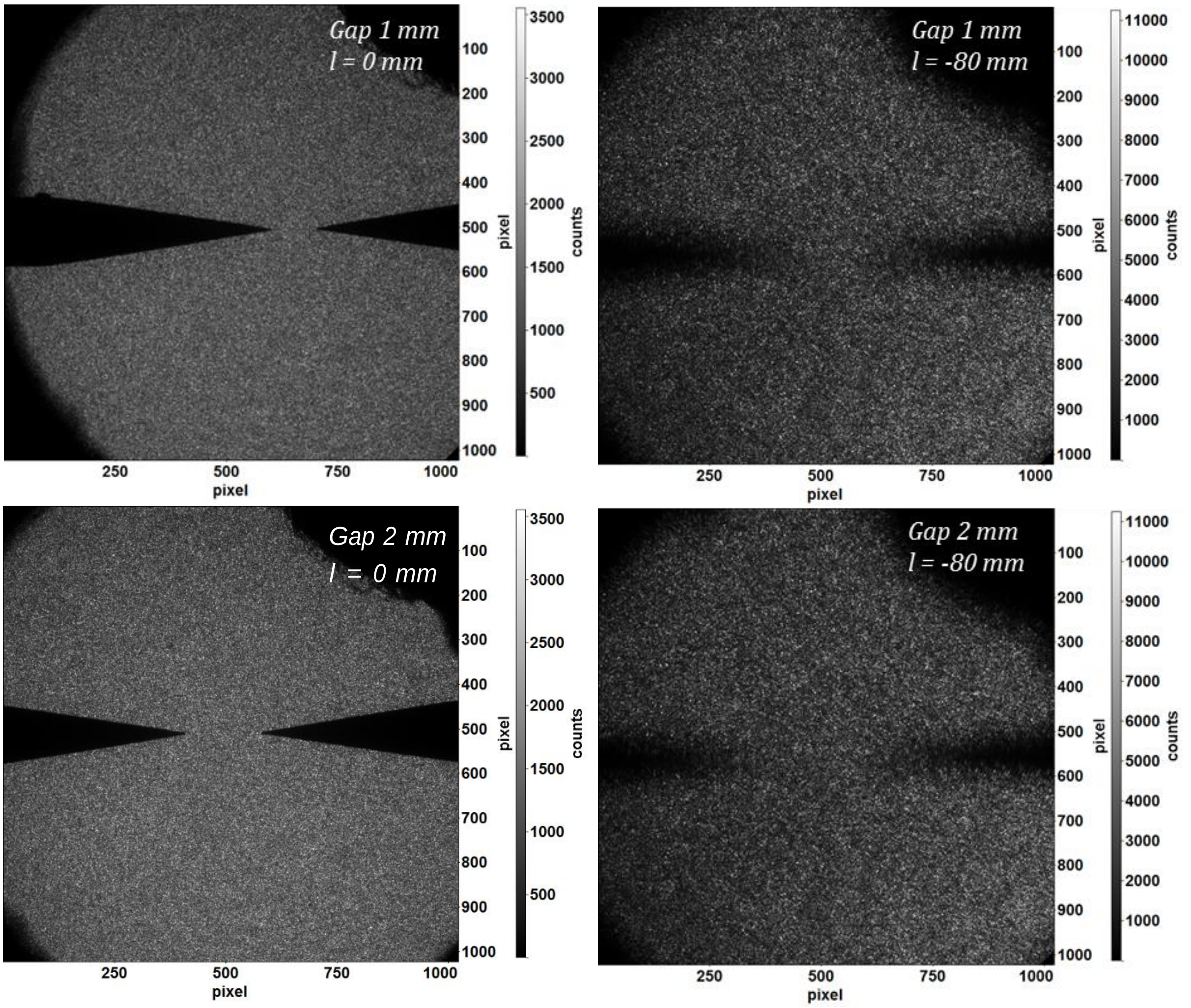

Figure 4-5: Effect of defocus distance on speckle and background elements. Top, 1 mm gap, bottom, 2 mm gap. Left, electrodes in the focal plane (l = 0 mm), Right: defocus l = -80 mm (further from the camera). Focused image: calibration, gate width 1 ms, low laser power (~0.5 W). Defocused: test conditions, maximum laser power (3 W), gate width 1 µs.

Test chamber images without defocus ($l = 0$) are used to calibrate the optical system: by measuring optical magnification M and finding the focal plane. M is the ratio of the observed reference distance ($number\ of\ pixels \cdot pixel\ size$) over the measured distance. In practice, M is obtained using the electrode gap or the electrode diameter as reference. M is obtained using the electrode gap or the electrode diameter as reference. The focal plane is located displacing the test chamber to minimize the blur on the electrode tips, until they appear sharp.

In our experiments, the same reference image is used for series of experiments performed in the same conditions. The reference pattern remains the same at the beginning and the end of experiments.

Test images are obtained using the discharge trigger as input for the camera system as well. One can see a pair reference-test images in Figure 4-6, before and 3 ms after the onset of an electrical discharge in air at 1 bar and 1 mm gap. In the central area, there is a displacement of points in the background pattern, although it difficult to directly identify it visually.

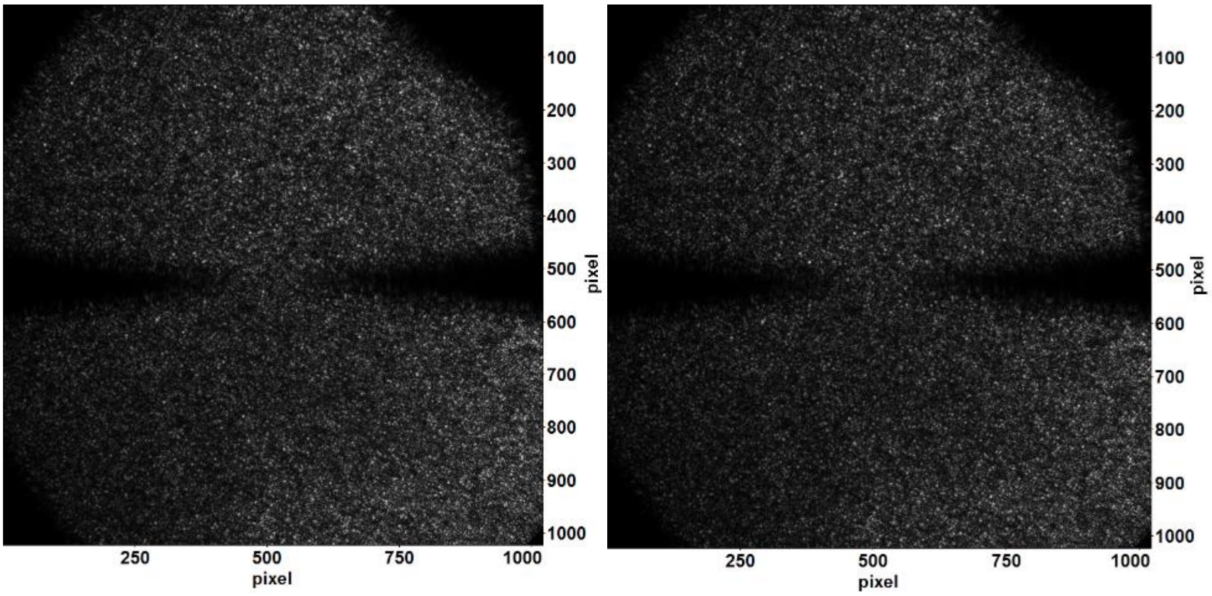

Figure 4-6: SBOS images of an electrical discharge in air and atmospheric conditions, with l = -80 mm and 1 mm gap. Left: Reference speckle pattern image, before the discharge event. Right: Caption 3.0 ms after discharge onset, with speckle pattern influenced by the hot discharge kernel.

4.2.2 Displacement field

As explained in §4.1.2, light rays deviate an angle $\vec{\varepsilon}$ due to refractive index (n) gradients in the light path, see Eq. (4.5). From optical calculations at the optical setup, this angle is related to the displacement of the points of the reference image $\vec{\delta}$ through optical magnification M and defocusing distance l, as in Eq. (4.7).

The reference image pattern points is compared to the test image by a multi-pass cross-correlation processing algorithm using DaVis 8.0 program. Background point displacement is detected by multi-pass cross-correlation between reference and test image. For a maximum displacement $\delta_{max} = 5\,px$, cross-correlation is performed using first a single pass with a 64x64 pixel window and 25% overlap, followed by 3 passes with a 16x16 pixel window and 75% overlap. For more details, DaVis program user guide can be consulted.

The multi-step cross-correlation with overlap reduces matrix size, from 1024x1024 pixels of the background image resolution to 255x255 pixels for the displacement field: each point of the displacement field corresponds to the mean displacement of 4 points of the original image. This detail is considered when re-scaling gas properties fields to mm and when calculating energy volume integration. The spatial resolution achieved is $\Delta x = 0.208\,mm$, based on the final interrogation window size. Resulting displacement field for an electrical discharge is represented in Figure 4-7 (scalar displacement field $|\vec{\delta}|$, δ_x and δ_y).

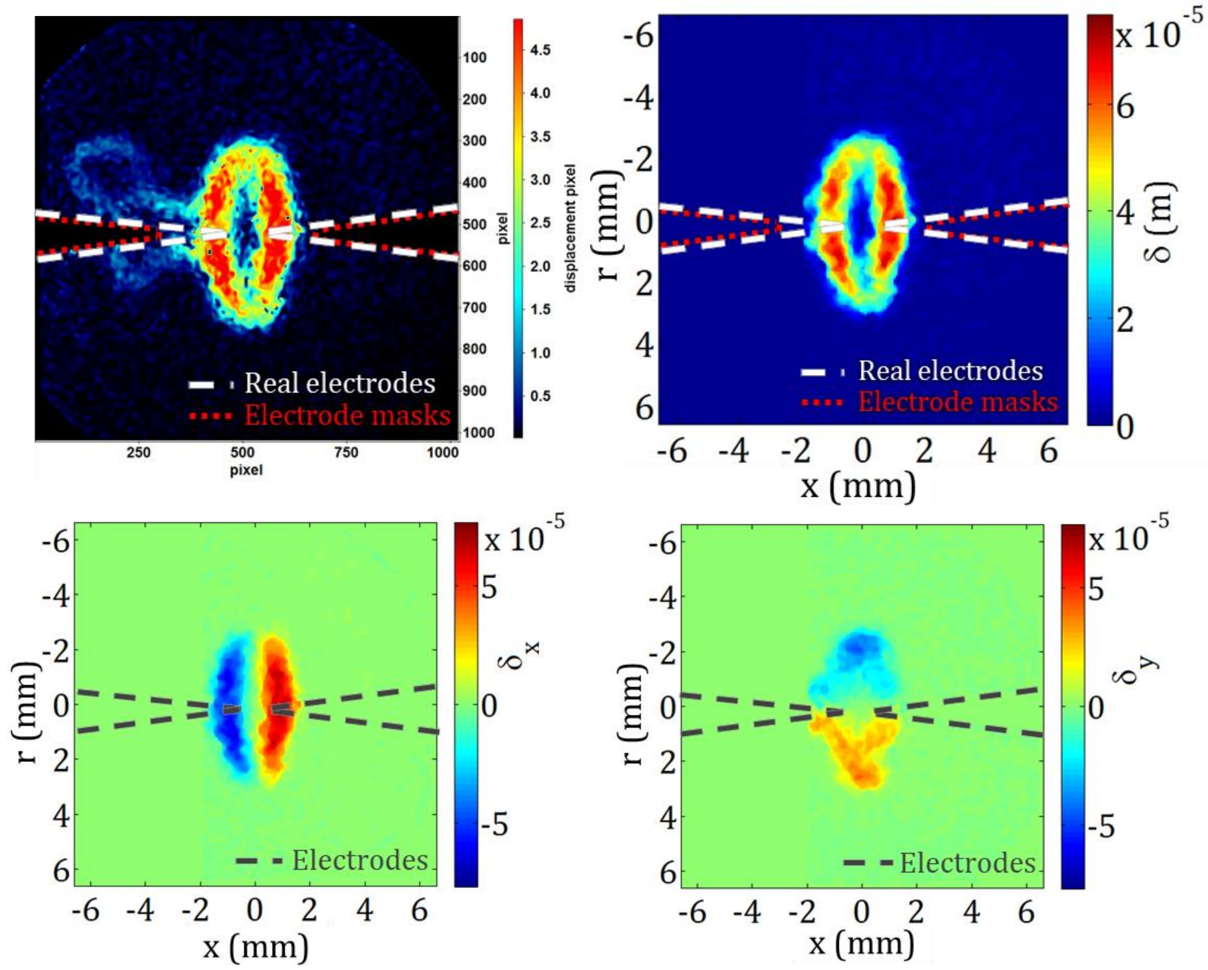

Figure 4-7: Displacement fields: (a) Original scalar δ field, (b) δ filtered and re-scaled, (c) δ_x, (d) δ_y

Geometric masks hide the electrode shades at the cross-correlation. The masked electrode shades correspond to electrode edges, without the blur border area which appears induced by defocus: the blur scatters information in a small area, causing the background speckle pattern to overlap with electrode edges, and thus carrying information about pattern displacement.

The resulting displacement field $\vec{\delta}$ provides an idea of the kernel size, but it is more particularly interesting because it contains information about the refractive index gradient. The latter can be transformed into a refractive index distribution and eventually density field. Combining equations (4.5) and (4.7) one obtains equation (4.10). In this equation s_p represents pixel scale ($s_p = 13\,\mu m/pixel$) converting $\vec{\delta}$ from pixels to m.

$$\vec{\delta} = \frac{lMs_p}{n_0}\int_{\mathcal{C}} \vec{\nabla} n \, dz \tag{4.10}$$

The equation above represents the relation between the displacement field and the gradient of the refractive index integrated through the line of sight $\mathcal{C}$. At this point there are two possible ways to obtain the refractive index field. The first one is to solve first the tomography problem (integral through $\mathcal{C}$) to obtain the refractive index gradient field, and then integrate the gradient field. The other form profits of the axisymmetric geometry and the optical setup configuration: integration of the gradient $\vec{\nabla} n$ is orthogonal to the derivation of the integral $\int_{\mathcal{C}} dz$ (tomography problem), so it is possible to integrate before solving the tomography problem. We chose the latter, as tomography induces more uncertainty, as discussed later in the uncertainties section (§4.3.2).

Displacement field $\vec{\delta}$ is then processed using Matlab®. Image post-processing is summarized in equation (4.11), and explained in detail in following sections 4.2.3 to 4.2.5.

$$\vec{\boldsymbol{\delta}} \overset{(a)}{\rightarrow} \vec{\boldsymbol{\nabla}}_{x,y}.\vec{\boldsymbol{\delta}} \overset{(b)}{\rightarrow} \int_{\boldsymbol{C}} \boldsymbol{n}\, \boldsymbol{dz} \overset{(c)}{\rightarrow} \boldsymbol{n}(\boldsymbol{x},\boldsymbol{y}) \overset{(d)}{\rightarrow} \begin{Bmatrix} \boldsymbol{\rho}(\boldsymbol{x},\boldsymbol{y}) \\ \boldsymbol{T}(\boldsymbol{x},\boldsymbol{y}) \end{Bmatrix} \overset{(e)}{\rightarrow} \boldsymbol{dH}(\boldsymbol{r}) \overset{(f)}{\rightarrow} \boldsymbol{H} = \boldsymbol{E_{SBOS}} \tag{4.11}$$

4.2.3 Integration of the displacement field, calculation of refractive index and density field.

Integration of the displacement field yields the refractive index field integrated through the line-of-sight ((4.11).b). Before integrating though, one can make use of the Gladstone-Dale relation (4.1) to switch the refractive index for the density, so the resulting field is the density field. This is possible only in the applications where Gladstone-Dale relation is linear, which depends on whether electron density is significant or negligible in equation (4.3). For our case in electrical discharges, this is discussed next.

4.2.3.1 Refractive index field and density field relation

In electrical discharges, the hot kernel contains ionized gas at the first moments of the discharge, and then temperature decreases. In ionized gas, ions and electrons affect the refractive index of the gas, as presented in §4.1.1. We want to capture images at different moments of the discharge, mainly at the end of the discharge –so a significant amount of energy has been deposited in the fluid- but also at earlier stages of the discharge to analyze kernel evolution (0.5 to 3.0 ms after discharge onset). Then we must estimate electron contribution first.

Maly [2] estimates the glow discharge electron density to be $N_e{\sim}2.10^{14}\ cm^{-3}$. The contribution to the refractive index [113] of the electron is given by

$$(n-1)_e \approx -4.46.10^{-14} N_e \lambda^2 \tag{4.12}$$

Therefore, $(n-1)_e = -2.52.10^{-8}$, which should be compared to the difference expected with air temperature elevation for a reference of at least 700 K. K_{air} for the laser wavelength of 532 nm is selected from tables[114], with $K_{air} = 0.2274\, cm^3/g$, and a refractive ambient air index of $20°C$ and $p = 1\, bar$, $n_0 = 1.00027$, one finds $n_{700K} - n_{293K} = -1.63.10^{-4} \gg (n-1)_e$. Thus, during the glow phase, electron contribution is expected to be negligible. Furthermore, the contribution of electrons to the refractive index is 20.5 times higher than that of the ions [113]. Therefore, the refractive index only depends on the neutral gas species temperature.

Equation (4.3) describes the G-D relation for an ionized gas. Assuming an equilibrium plasma, the electron contribution to the refractive index is taken into account with the electronic density as a function of temperature. The electronic density $N_e(T)$ is calculated for each temperature using the NASA9 model for air and a Cantera module integrated into our Matlab® program.

Refractive index function is sampled between 275 and 5000 K, with and without the electronic density term, to analyze the resulting difference with temperature. Figure 4-8 shows the effect of electronic density on the refractive index for higher temperatures in air, assuming an equilibrium plasma: $[n-1=f(\rho)]$ is the G-D relation without ionization, and $[n-1=f(\rho,N_e)]$ with ionization.

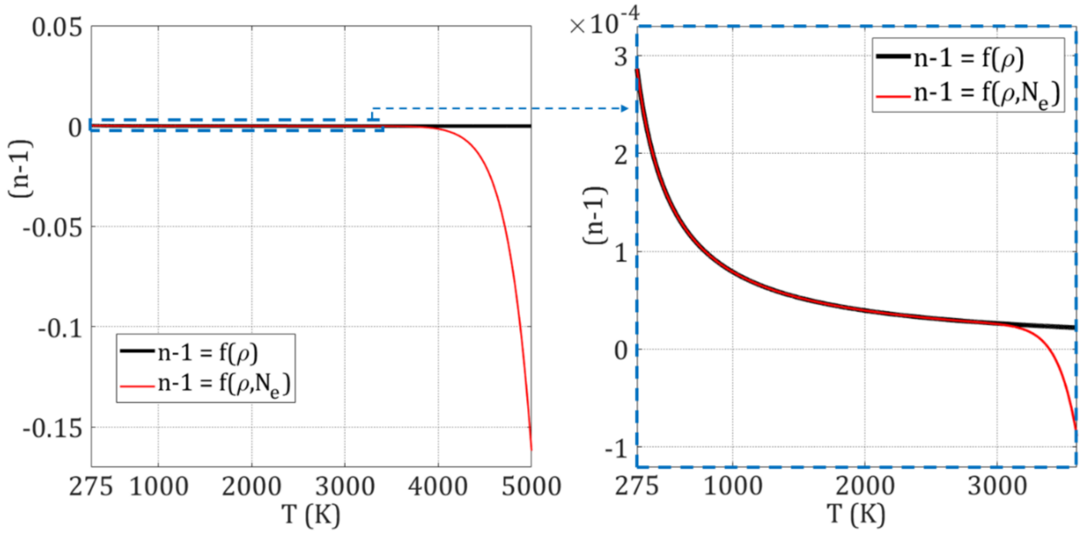

Figure 4-8: Influence of electronic density on the refractive index-temperature relation in air.

For temperatures lower than 3000 K, Gladstone-Dale equation is a linear relation with no need for electron density correction. Higher temperatures are reached only at the first moments of the discharge, or for high energy igniters: in this case the non-linear equation is solved to obtain temperature field from the refractive index field, see chapter §5.

For our pin-to-pin electrode discharges, density field is obtained directly by dividing each point of the (n-1) field by the Gladstone-Dale constant K, adding the ambient density as constant to the density field resulting from integration. With respect to Leibniz integral rule, Eq. (4.1) is coupled to Eq.(4.10), yielding the following equation:

$$\vec{\delta} = \frac{lMs_p}{n_0}\int_C \vec{\nabla} n\, dz = \frac{KlMs_p}{n_0}\vec{\nabla}\int_C \rho\, dz \tag{4.13}$$

The computed displacement fields must be then integrated. G. Acher [115] compares different integration methods. Two are considered for our study: line integration and Poisson equation integration.

4.2.3.2 Line integration

The system to integrate, as in Eq. (4.13) can be expressed as follows:

$$\vec{\delta} = \frac{KlMs_p}{n_0}\vec{\nabla}\int_C \rho\, dz \rightarrow \begin{cases} \dfrac{n_0}{KlMs_p}\delta_x = \dfrac{\partial \mathcal{J}}{\partial x} \\ \dfrac{n_0}{KlMs_p}\delta_y = \dfrac{\partial \mathcal{J}}{\partial y} \end{cases} where\ \mathcal{J} = \int_C \rho\, dz \tag{4.14}$$

One solution then is to discretize line by line, integrating with boundary conditions for each line. As $\mathcal{J}$ is a scalar field, integrating by one direction (x or y) suffices. If one of δ components have little information, e.g. when there are only horizontal refractive index gradients, integration direction is the perpendicular one. If both δ_x and δ_y are non-zeros, then the direction less affected by boundary conditions is chosen. In our case, this is δ_y.

This method is simple to implement and doesn't require much processing time. The main disadvantage is that the resulting integrated density field presents discontinuities between consecutive lines (see Figure 4-9), as they are solved independently.

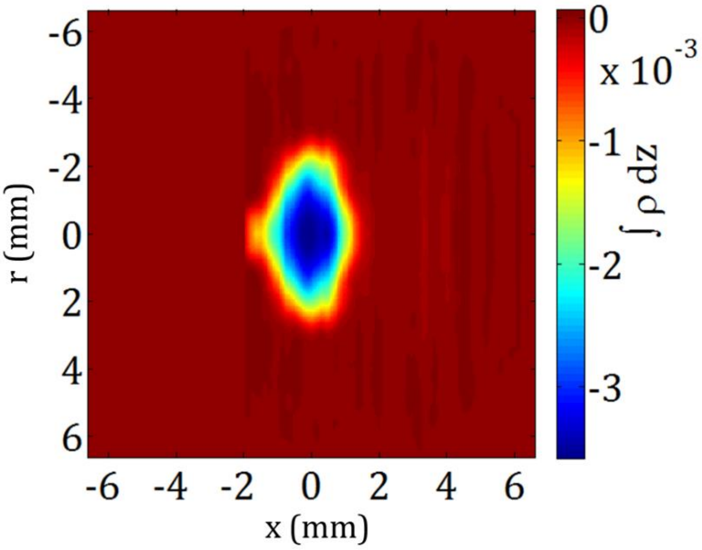

Figure 4-9: Integrated density field by line integration.

4.2.3.3 Poisson equation integration

Another method consists on solving a Poisson equation in the form $\nabla^2 u = f$. Applying the divergence operator $\vec{\nabla}_{x,y} = (\partial/\partial x\,, \partial/\partial y)^T$ to Eq. (4.13) and then taking the sum of each resulting component we obtain the Poisson equation (4.15). Calculation of the divergence field is the step ((4.11)-a) of data processing.

$$\frac{n_0}{KMls_p}\vec{\nabla}_{x,y}.\vec{\delta} = \nabla_{x,y}\int_{\mathcal{C}}\vec{\nabla}\rho\,dz = \Delta_{x,y}\int_{\mathcal{C}}\rho(x,y,z)\,dz = \Delta_{x,y}\mathcal{I} \qquad (4.15)$$
$$where\ \mathcal{I} = \int_{\mathcal{C}}\rho(x,y,z)\,dz$$

The Poisson equation, Eq. (4.16), takes the discretized form (4.17), where subscripts *i* and *j* represent the position of the discretized element in the matrix with all the elements in the field. It is solved using a second-order explicit iterative scheme, with 2nd order centered difference represented in equation (4.18). The 5 points stencil of equation (4.19) is used to iterate until the variation between consecutive iterations is lower than 10^{-6}, $\max\left(\frac{u_{i,j}|^{(n+1)} - u_{i,j}|^{(n)}}{u_{i,j}|^{(n)}}\right) < 10^{-6}$.

$$\nabla^2 u = f \overset{2D}{\Rightarrow} u_{xx} + u_{yy} = f(x,y) \tag{4.16}$$

$$u_{i,j,xx} + u_{i,j,yy} = f_{i,j} \tag{4.17}$$

$$u_{i,j,xx} = \frac{u_{i-1,j} + u_{i+1,j} - 2u_{i,j}}{\Delta x^2};\; u_{j,yy} = \frac{u_{i,j-1} + u_{i,j+1} - 2u_{i,j}}{\Delta y^2} \tag{4.18}$$

$$u_{i,j}\Big|^{(n+1)} = \frac{\left(u_{i-1,j} + u_{i+1,j}\right)\Delta y^2 + \left(u_{i,j-1} + u_{i,j+1}\right)\Delta x^2 - \Delta x^2 \Delta y^2 f_{i,j}}{2(\Delta x^2 + \Delta y^2)}\Bigg|^{(n)} \tag{4.19}$$

Boundary conditions are imposed at the image borders and along the electrode virtual surfaces. Dirichlet's conditions are used along the image borders, where the integral $\mathcal{I} = \int_{\mathcal{C}} \rho(x,y,z)\,dz$ is assumed to be zero (it represents the density field integrated along the z axis, with integration constant adjusted later so zero corresponds to ambient density). Neumann's conditions are used along the virtual electrodes or spark plug surfaces: this calculation mask, like the one used to calculate the displacement field, represents the electrode bodies without the blurry external part. Figure 4-10 represents the displacement divergence field (left) and the boundary conditions imposed for integration (right). The application of Neumann boundary conditions to our case is explained in detail in Appendix C.

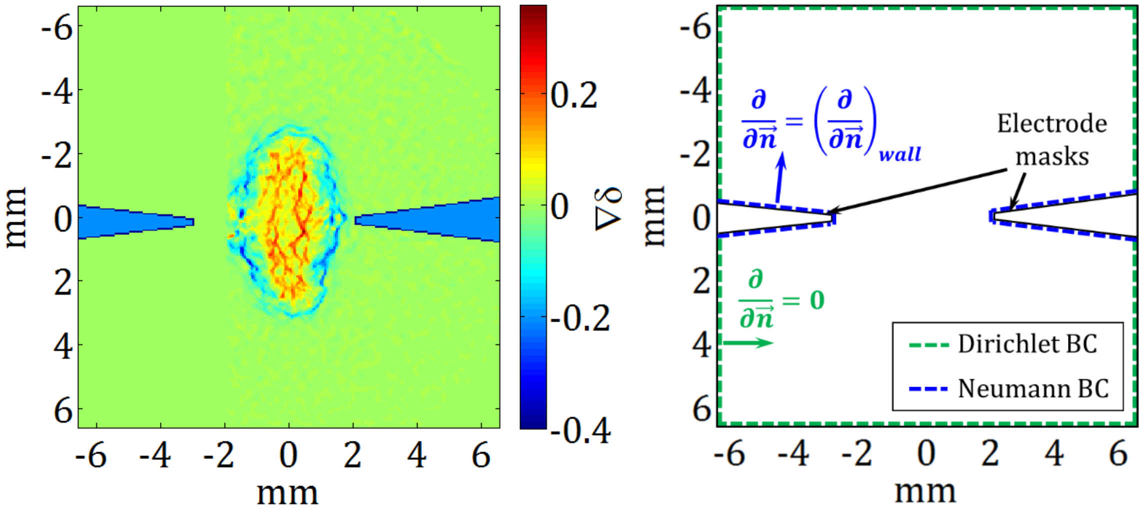

Figure 4-10: Displacement divergence field (left), with masked electrodes in blue, and boundary conditions applied to the displacement divergence field (right).

The integrated density field resulting from this method presents high resolution, without the lateral gradients of line integration method, although it requires higher computational time. It is represented in Figure 4-11.

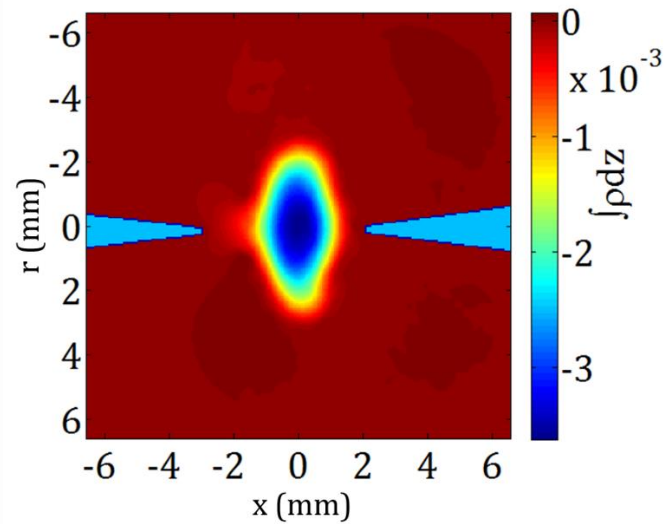

Figure 4-11: Integrated density field by integration of the Poisson equation.

4.2.4 Filtered backprojection

From the density field integrated through the line of sight, the density field is obtained by tomographic reconstruction, which represents the step (4.11)(c) of the mathematic processing. As there is only one integral field (from 1 single camera), this process is only possible for axisymmetric fields, where the projection is the same along any other radial direction.

Mathematically, the tomographic reconstruction is done via filtered backprojection, i.e. inverse Radon transform. The projection $P_\theta(t)$ of angle θ of an objet $f(t,s)$ is represented in Figure 4-12 [116] and defined in equation (4.20). The object $f(x,y)$ can be estimated from its projections $P_\theta(t)$ as in equation (4.21)[115]: the Fourier transform $S_\theta(w)$ is calculated for every projection available, and filtered by a Hamming function $H(w) = |w|$. The window filtering greatly attenuates the projection of high frequency spatial components, which are assumed to be mainly noise related and may therefore be reduced to negligible values without affecting the density distribution [117]. Additional filtering performed by directly truncating high frequency noises (up to the Nyquist value) using a reduced window width is not required. Then the inverse Fourier transform $Q(t)$ is calculated, and computing the sum of $Q(t)$ yields the object $f(x,y)$. This process is explained in detail in [115].

$$P_\theta(t) = \int_{-\infty}^{+\infty} f(t,s)\, ds \tag{4.20}$$

$$f(x,y) = \int_0^{\pi} Q(x\, cos\theta + y\, sin\theta)\, d\theta \tag{4.21}$$

$$where \begin{cases} Q(t) = \displaystyle\int_{-\infty}^{+\infty} S_\theta(w)\, |w| e^{j\, 2\pi w\, t} dw \\ S_\theta(w) = \displaystyle\int_{-\infty}^{+\infty} P_\theta(t)\, e^{-j\, 2\pi\, w\, t} dt \end{cases}$$

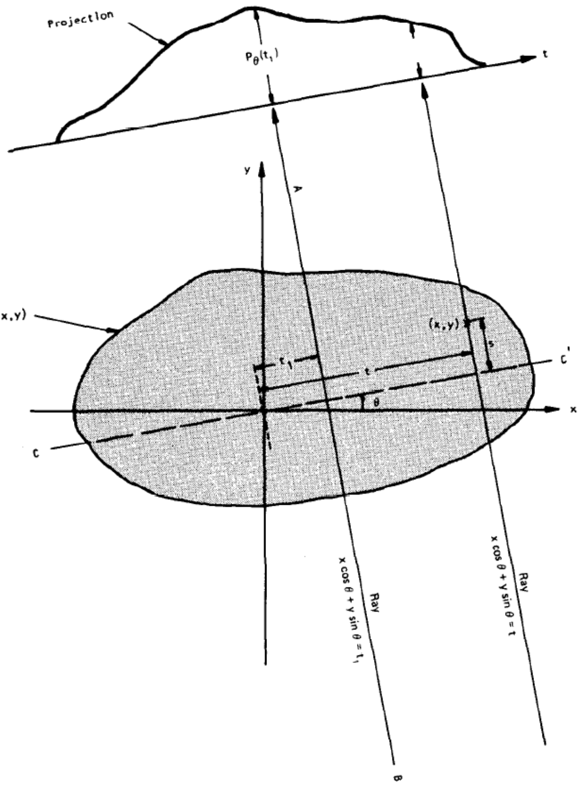

Figure 4-12: An object and its projection [116].

For an axisymmetric field, $P_\theta(t)$ is the same for every projection angle θ. First the integrated density field is centered at the middle of the image, shifting the horizontal plane (center of the discharge). Then the inverse Radon transform is performed for the integral density field using the *iradon* function of Matlab® Image Processing Toolbox, which follows the described method.

The resulting field is the density field relative to initial density $(\rho - \rho_0)$. It is centered manually, correcting the vertical deviation to place the symmetry axis in the central horizontal plane before the backprojection. Little deviations from the symmetry in the kernel are solved by averaging the resulting fields from rotation of the upper and lower halves of the integrated density field (separated by the symmetry axis). If the kernel distribution is not close to axisymmetric it cannot be processed with a single tomographic view, as this would produce a fake reconstruction, and 3D BOS would be needed [118], [119].

4.2.4.1 Temperature field

The gas heated by the electrical discharge is intended to be air of ambient composition and pressure, so we apply ideal behavior. This means that the ideal gas law applies, and temperature field is obtained from density field using ideal gas relation (step (4.11)). Figure 4-13 represents the density and temperature fields for the discharge in air.

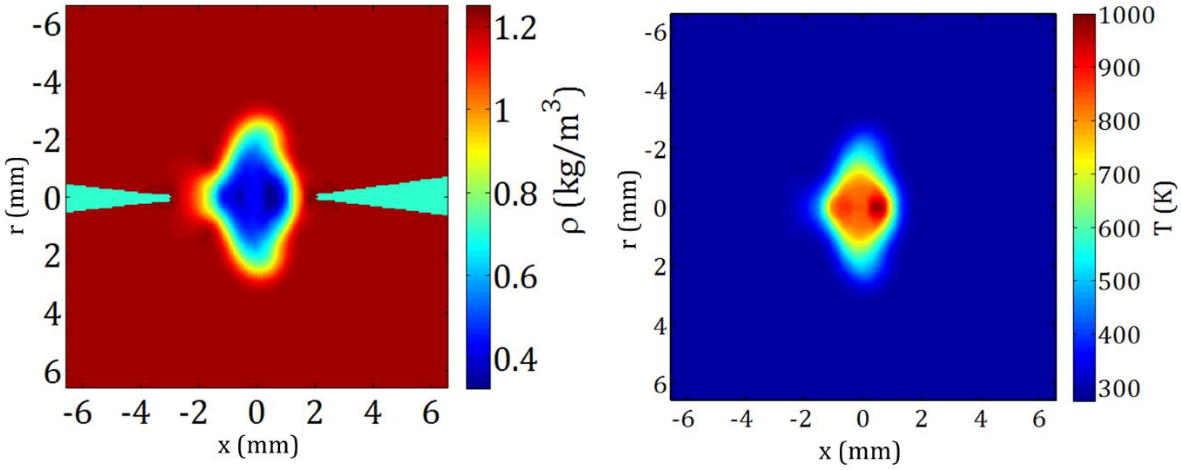

Figure 4-13: Density field obtained by backprojection and masked electrodes (left). Corresponding temperature field (right).

4.2.4.2 Kernel size

The hot kernel volume is defined from the temperature field. First a temperature threshold is set to obtain the kernel surface, e.g. the binary matrix defined as $T > T_{threshold}$. This value is chosen as atmospheric temperature + 35 K, representing an increase of 5% of the maximum temperature difference (1000 K – 300 K). Figure 4-14 shows the hot kernel boundary and centroid, extracted from the temperature field, superimposed on the temperature field.

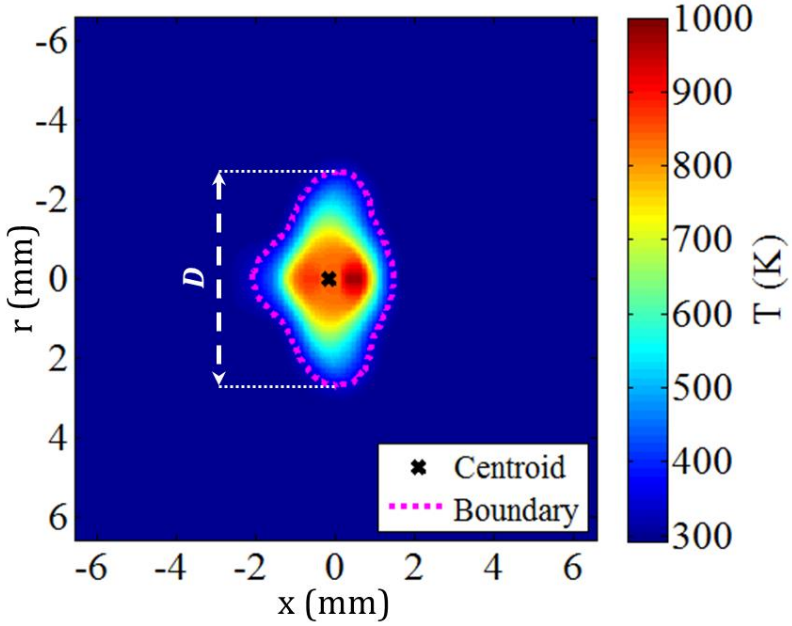

Figure 4-14: Hot kernel boundary superimposed on the temperature field.

We estimate the maximum kernel diameter from the kernel planar surface as the difference between extreme points, and radius as half the value of the diameter *D*, as signaled in the figure.

Kernel volume results from the solid of revolution generated rotating the kernel surface around the central y-axis, which passes by the surface centroid, as in equation (4.22).

$$Volume = \oiiint_{V} \pi \, (2\, r + dr)\, dr\, dy \tag{4.22}$$

For the atmospheric test with 1 mm gap shown in Figure 4-14: $Volume = 43.7\, mm^3$, $Radius = 2.73\, mm$, which represent typical values for discharges.

Kernel maximum radius and volume depend on the temperature threshold and are affected by the blur effect produced by defocus, d_{av}. Total values may vary for the same experimental conditions if the diaphragm opening change, so while total values are presented as a good estimation, they are most representative of the kernel size changes as a function of experimental conditions; i.e., if kernel size tends to increase or decrease with gap, pressure or gas mixture.

4.2.5 Energy calculation

Energy calculation starts by the estimation of the enthalpy field. As mentioned before, we suppose semi-perfect behavior of the heated gas. Heat capacity $c_p(T)$ is temperature-dependent, taken as the standard Gordon-McBride polynomial form [120]. Absolute molar enthalpy of the gas per mol is:

$$h(T) = \int_{T_{ref}}^{T} c_p(T)\, dT + {h_0}^{*} \tag{4.23}$$

Where ${h_0}^{*}$ is the enthalpy of formation. We are interested in the enthalpy distribution Δh, called kernel enthalpy variation per mol, which is the enthalpy increase per mol associated to the temperature increase in the discharge kernel. Local molar enthalpy is higher for higher temperatures, and thus its distribution resembles the temperature distribution, see Figure 4-15. It is defined in Eq. (4.24), assuming that there is no change in chemical composition:

$$\Delta h(T) = h(T) - h(T_{amb}) = \int_{T_{ref}}^{T} c_p(T)\, dT - \int_{T_{ref}}^{T_{amb}} c_p(T)\, dT \tag{4.24}$$

where c_p is the molar heat capacity at constant pressure in $J/mol/K$, and Δh is the enthalpy variation from the atmospheric temperature to the kernel temperature, in J/mol.

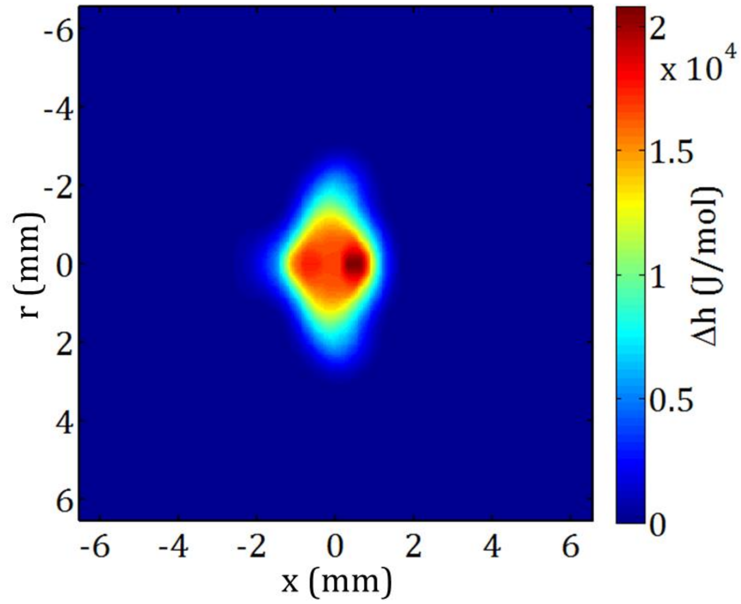

Figure 4-15: Local enthalpy, $\Delta \boldsymbol{h}(\boldsymbol{T})$, in J / mol

The kernel enthalpy variation is calculated for each element of the field taking the number of moles into account: multiplying Δh by an element with dn_m moles, see Eq. (2.2) where p is the ambient pressure in Pa (e.g. in J/m^3) and R is the ideal gas constant given in J/mol/K,. This yields the enthalpy differential dH, as in equation (4.26), with c_m molar concentration.

$$dn_m = c_m\, dV = \frac{p}{R\,T} dV \tag{4.25}$$

$$dH = \Delta h(T) dn_m = \frac{p}{RT} \Delta h(T) dV \tag{4.26}$$

The infinitesimal element of number of moles dn_m corresponds to an infinitesimal volume dV. The element of volume $dV(r)$ is one of an infinitesimally thin cylindrical shell, of internal radius r, thickness dr, external radius $(r + dr)$, and height dy, as in eq. (4.27). For numerical integration, the differentials dy and dr are equal and represent the side of an element of the matrix, which corresponds to the pixel size, re-scaled to the original image resolution $\left(s_p \cdot 4\ {}^{vect}/_{pixel} \cdot {}^{1}/_{M}\right)$.

$$dV(r) = \pi\, dy\, [(r + dr)^2 - r^2] = \pi\, dy\, (2\, r\, dr + dr^2) \tag{4.27}$$

Density field $\left(\rho = {}^{p}/_{R_g\,T} = c_m Mm, with\ R_g = {}^{R}/_{Mm}\ and\ Mm\ molecular\ weight\right)$ is inversely proportional to temperature. The enthalpy in the fluid does not concentrate on the high temperature hot spot next to electrode tips (which reaches the maximum temperature of the temperature field), but rather distributes over the interior of the kernel. The enthalpy variation per unit of volume, $c_m \Delta h$, is depicted in Figure 4-16.

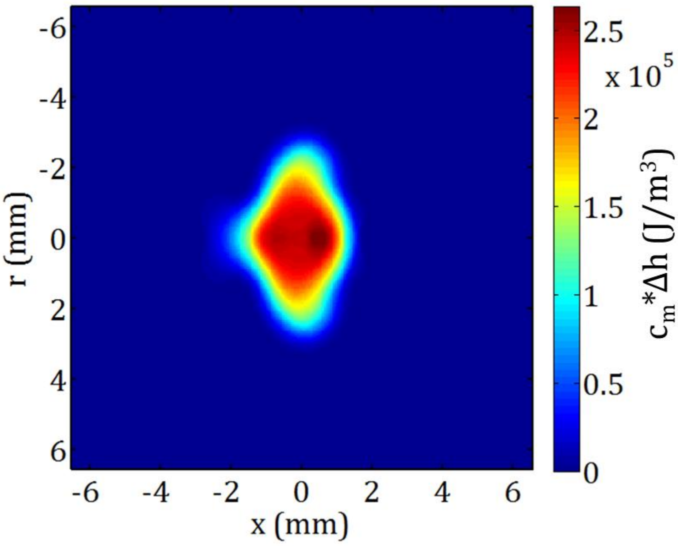

Figure 4-16: Enthalpy variation per unit of volume, $c_m(T) \cdot \Delta h(T)$

Considering an ideal gas of constant composition, the variation of $\Delta h(T)/\,T$ depends only on temperature, and is equal to zero at a ambient temperature (i.e., for an unheated gas). $\Delta h(T)/\,T$ acts as a weighting function, which, given a fixed dV, accounts for the overall balance between mass reduction with decreasing density and increasing local enthalpy content with increasing temperature difference.

Enthalpy differential dH is calculated from the enthalpy variation and temperature fields (step (4.11)-e). It represents, on a flat surface, the weighted distribution of the energy deposit in every point of the hot kernel, taking into account the posterior revolution integral. The enthalpy differential surface is represented in Figure 4-17, normalized over the total energy deposit H. dH is concentrated in the toroidal part of the kernel, due to the smaller radius of the area next to the revolution axis and the corresponding low value of dV. The tomographic field is given in cylindrical coordinates, with the reference being taken along the electrode axis.

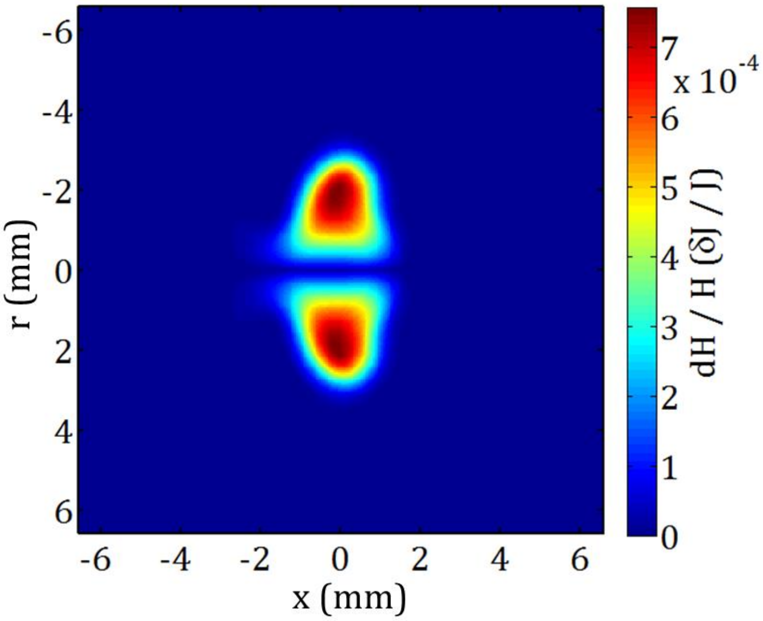

Figure 4-17: Enthalpy differential surface.

Finally total energy deposit, $E_{sbos} = H$, is estimated at the instant the test image is captured. This is the result of the volume integral of the enthalpy differential distribution over the hot kernel volume $\mathcal{V}$ – step ((4.11)-f)-. Calculations for enthalpy require the choice of a control volume $\mathcal{V}$, which is taken as a large area around the hot kernel. The integration of Eq. (4.26) over $\mathcal{V}$ yields the overall balance of enthalpy before and after electrical transfer, as in (4.28):

$$E_{sbos} = H = \oiiint_{\mathcal{V}} dH = \frac{p}{R} \oiiint_{\mathcal{V}} \frac{\Delta h\big(T(r,y)\big)}{T} dV(r,y) \qquad (4.28)$$

With the element of volume chosen, dV, the volume integral of dH corresponds to the summation of all elements in the field. Numerically, this integration equals the summation of all element of the differential enthalpy surface dH matrix. For the test shown above in air and 1 mm gap, $E_{sbos} = 6.99\, mJ$.

4.2.6 Critical control parameters

Control parameters influence greatly the final results after the multi-step data processing. Here we present the influence of these parameters and how to correctly measure, detect or set them, from the exact lengths and properties of the experimental setup to the position of the kernel center in the calculated displacement field.

4.2.6.1 Optical setup properties: Focal plane, optical magnification and defocus distance.

The focal plane of the optical setup *F* is the reference for setting the defocus distance *l*. At this focal plane the optical magnification *M* is obtained from the image of a sharp object of known size –a measured part like the electrode diameter, or distance as the electrode gap-. At image post-processing, defocus distance and magnification are constants that multiply the displacement field to obtain the integrated density field, and thus errors at determining *F*, *l* or *M* translate directly into global measurement error.

4.2.6.2 Electrical discharge and camera synchronization

Signal synchronization is controlled by the same trigger signal and the camera control program. The square signal from the trigger is doubled, so it triggers the TCI (and thus the discharge) and the WinView32 program. The leading edge of the signal starts the TCI charge, and the falling edge starts the electrical discharge at the electrodes and is detected as origin of time by the camera control. The delay between the origin of time and the image acquisition is set by the camera control.

The camera trigger return (signal with a peak of few μs width) is recorded with the oscilloscope together with the electrical signals and the differential pressure signal, so global synchronization can be checked. This is important because during the experiments it is difficult to appreciate if a SBOS image contains information about the displacement field or it does not –which is seen clearly after image and reference cross-correlation–, so the camera trigger return is very useful to verify that the image acquisition occurs as desired.

4.2.6.3 Symmetry axis location

Before solving the tomography problem, one has to locate the symmetry axis, which passes by the center of the hot kernel center (theoretical the center of pin electrodes). Then the integrated density field is re-centered to compensate the detected vertical shift in the image, and the filtered-backprojection yields the density field. This is observed in the vertical position of the kernel between Figure 4-11 and Figure 4-13.

If the symmetry axis is misplaced, then filtered-backprojection result in a wrong density field, as the input would not be axisymmetric. The axis is placed between the electrode tips, and the vertical shift remains the same for the same experimental conditions: at the camera sensor plane, the image shifts vertically if the defocus distance is modified. Camera position is adjusted manually to compensate this shift, but a remaining gap of few pixels is further corrected during image processing.

4.2.7 Advantages and Limitations

SBOS technique is chosen to study the spatial distribution of gas properties and the hot kernel during the discharge. Compared to other visualization techniques, it is relatively simple to set up, as it only requires optical access to the test cell, a laser to generate the speckle pattern, optical lenses and a camera. SBOS can measure quantitatively gas properties: refractive index, density, temperature and local enthalpy distributions. Applied to electrical discharges, it also quantifies the volume of the hot kernel formed during the discharge.

There are some considerations to be taken into account when using SBOS for electrical discharges:

- Due to the laser and the ICCD camera used for the study, measurements are obtained at one instant, when the second image (with the background pattern displaced by the phenomenon) is captured. We can only take measurements at one instant for each test.
- Discharge kernel needs to be axisymmetrical in order to obtain the temperature field, as it is constructed by tomography from the density field. Asymmetric tests are discarded for SBOS processing.
- At the early stages of the discharge (around 0.5 ms after discharge onset) with high energy discharges, electronic density has to be taken into account in the discharge kernel and high temperatures. In chapter 5 SBOS methodology is adapted to these conditions and applied to high energy discharges.

4.2.7.1 Molecular dissociation

Molecular dissociation is not considered in the calculations. The refractive index of the gas mixture depends on the mixture composition and species concentration, *n(X)*. The gas temperature is calculated from the refractive index gradient distribution, so it is *T(n, X)*. Finally, molecular dissociation, and thus gas composition depends on the temperature. An iterative loop considering variable gas composition would improve the final estimation, as in equation (4.29).

$$n_i(X_i) \rightarrow T_{i+1}(n_i, X_i) \rightarrow X_{i+1}(T_{i+1}) \rightarrow n_{i+1}(X_{i+1}) \qquad (4.29)$$

If using long-chain fuels in the gas mixture, there would be strong recombination of ionized species and gas atoms, first at the plasma channel and then in the hot gas kernel. This could yield a change in the gas composition after the first test, with molecules of shorter chain fuels instead of the original fuel, and it would affect the following tests if the gas is not renewed. In our case, we use propane mixtures at low concentration. Propane recombines as methane and ethane among other species. To investigate this effect, we estimate the change in gas composition after one discharge to verify that the changes in the gas are negligible afterwards:

The maximum propane mole fraction we employ is at 0.06 (moles of propane/total moles). Considering the discharge volume over the total volume of the chamber and a temperature of 3000 K for dissociation, an estimation of the dissociation is obtained using Cantera, yielding a 5% molar decomposition of propane. This means low change in the gas due to dissociation, with propane mole fraction changing to 0.057 instead of 0.06, which represents a global influence on the mixture of a 0.3% (0.003). Then for our case, we consider negligible the influence of molecular dissociation on the refractive index and in the number of moles of the mixture. Dissociation of other species, as those present in air, recombine during and after the discharge.

4.3 Validation and uncertainties. Application to a reference CO_2 jet in air

The application of the SBOS technique to electrical discharges requires to adapt the system to the conditions present in electrical discharges. To validate SBOS methodology, a set of experiments is performed with a reference case of similar characteristics, in terms of size and density gradient: a jet of CO_2 through a nozzle. We also study the uncertainties and accuracy of the measurements comparing the results with the known density of CO_2. A part of this work is published in [103], although the data processing is modified, and reported also in [121].

4.3.1 Validation on CO_2 jet in air

The application of SBOS technique to electrical discharges measures small density gradients and enthalpy variation in the discharge kernel. To validate the SBOS setup we choose a laminar CO_2 jet in air, as it presents similar features than the expected conditions in electrical discharges: the density and refractive index gradients from air to CO_2 are similar to those estimated for the discharge kernel. Furthermore, the size of the jet is set to a few millimeters (exit nozzle diameter), which is similar to the inter-electrode gap distance of the pin-to-pin electrodes configuration. Density can be calculated using ideal gas equations for the CO_2 jet, so the SBOS accuracy is estimated from density reconstruction results.

In a first approximation, we estimate the energy deposit of an electrical discharge as 40 mJ. According to equation (4.6), the energy deposit would cause light rays to deviate up to $\varepsilon_{max} \sim 3.4 \cdot 10^{-4}\, rad$. For CO_2 in air, in atmospheric conditions, $\varepsilon_{max} \sim -3 \cdot 10^{-4}\, rad$. This confirms that in term of light deviation the test case is representative of an electrical discharge hot kernel. The different sign in ε is related to the different physics of each case ($\rho_{CO_2} > \rho_{air}$ while $\rho_{hot\ air} < \rho_{air}$) but it does not have major consequences for the density or enthalpy deposit calculation process: there should be few differences from the method perspective when following Eq. (4.7).

The laminar CO_2 jet is generated by the gas exit through a 4 mm inner diameter nozzle, from a 60x6 mm tube machined at an 11.5° angle. The 4 mm diameter is reamed for a 60 mm distance to ensure ideal steady flow conditions. The CO_2 is supplied by a 6 bar 10 L pressure tank. This setup is depicted in Figure 4-18, which shows a schematic view of the setup and a picture of the nozzle.

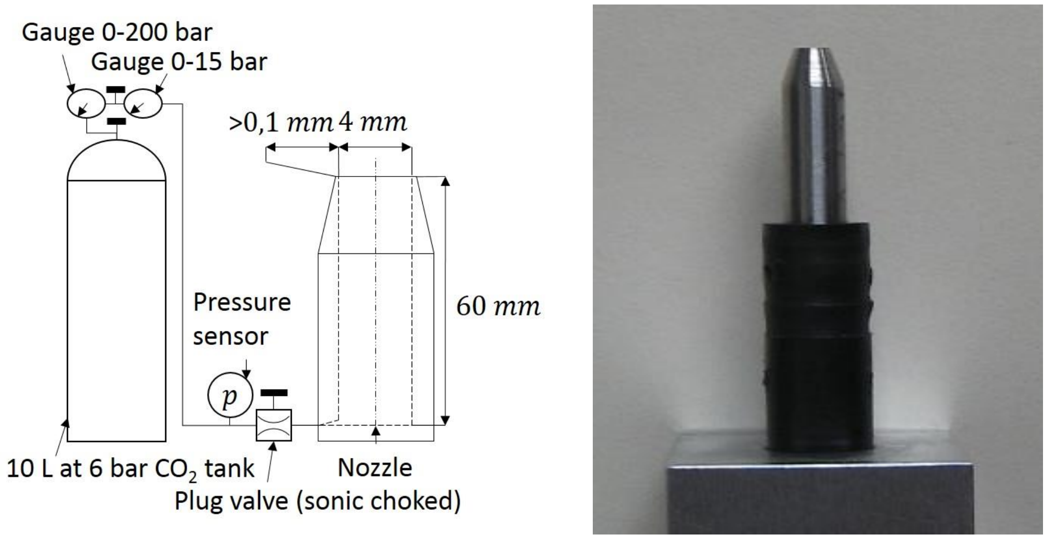

Figure 4-18: CO_2 jet setup scheme (left) [103] and picture of the exit nozzle (right).

A pressure sensor and a plug valve are placed in the tube between the tank and the nozzle. The plug valve provides choked conditions, with a Reynolds number of approximately 700. Temperature variation is found to be negligible in the jet due to the low pressure expansion. Ambient temperature in the room is $T_{ref} = 20.0 \pm 0.5\,°C$, and pressure $p = 1.00 \pm 0.01\,bar$, which yield densities of $\rho_{CO_2} = 1.806\,kg/m^3$ and $\rho_{air} = 1.190\,kg/m^3$.

A reference image is captured, and a set of 100 acquisitions is made at 0.2 Hz camera frequency. Images are processed to obtain the displacement field using Davis 8.3.1 (Lavision) for the same reference image for all the tests. Given a $\delta_{max} = 3\,px$, the cross-correlation processing uses a multi-pass interrogation window that starts at 32x32 px and ends at 16x16 for the last steps. Images of 1024x1024 px result in a 255x255 vectors field, with a resulting spatial resolution of $\Delta x = 0.208\,mm$. An averaged δ field is computed from the 100 images.

The reference image and the averaged δ field are represented in Figure 4-19 (a) and (b) respectively. The reference image (Figure 4-19 a) is obtained under no flow conditions and presents the sharp speckle background while the nozzle edges appear blurry on the bottom of the image, due to the defocusing distance ($l = -80\,mm$). The displacement field δ (Figure 4-19 b) is averaged to obtain a complete axisymmetric steady state, as expected in the laminar flow of the CO_2 jet.

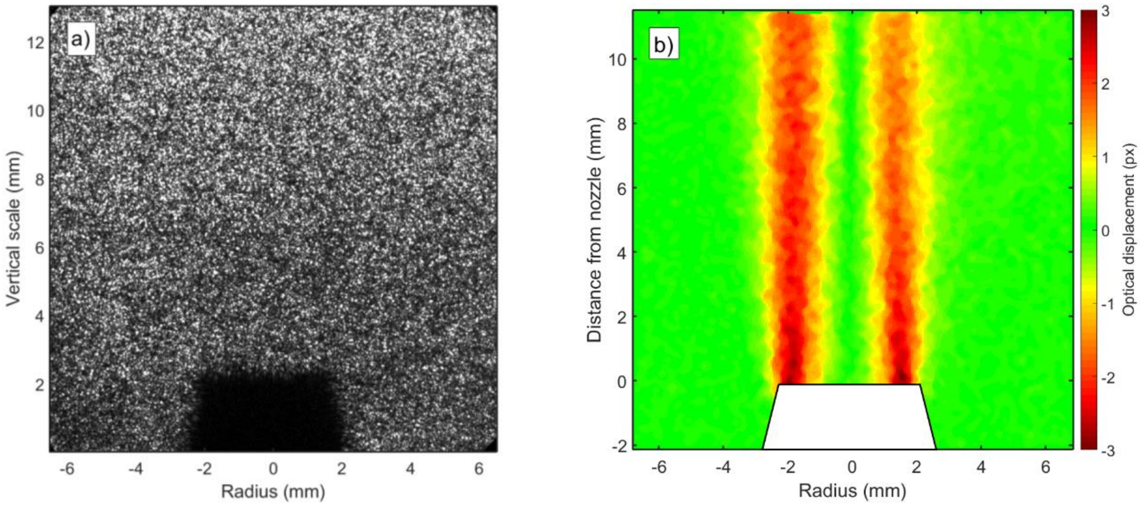

Figure 4-19: CO_2 jet SBOS images. Example of reference image under no-flow conditions (a) and mean displacement magnitude field in pixel (b), in each case the radius is the distance from the center of the nozzle [103]

BOS processing reconstructs the density field from the averaged displacement field. The integration through the line-of-sight density, is obtained by iteratively solving the equation using a second-order explicit iterative scheme (§4.2.3). For simplicity on the jet, the displacement field divergence is truncated at the nozzle. Neumann's conditions are used along the nozzle side and opposing side. Dirichlet's conditions are used along the two other boundaries, where $\mathcal{I}$ is assumed to be 0 (where $\mathcal{I} = \int_C \rho(x, y, z)\, dz$). The density field is represented in Figure 4-20 (a), in cylindrical coordinates. The slow development of a mixing layer is appreciated on the jet.

We check if the maximum gradient of density is compatible with spatial resolution. If they were incompatible, there would be a loss in information and the density distribution obtained would be inaccurate. Maximum gradient width is measured along a radial profile, as gradient is maximum in this direction. The radial profile is taken as an averaged profile at 1 mm above the nozzle, where the mixing layer is at its thinnest. Considering the variation in density from 10% to 90% of the maximum value, the maximum gradient width is 1.66 mm. Spatial resolution for this setup is, from equation (4.8), $d_{av} = 0.88\,mm$. Maximum gradient width is then compatible (smaller or in the same order) with d_{av}, then the measurements are valid.

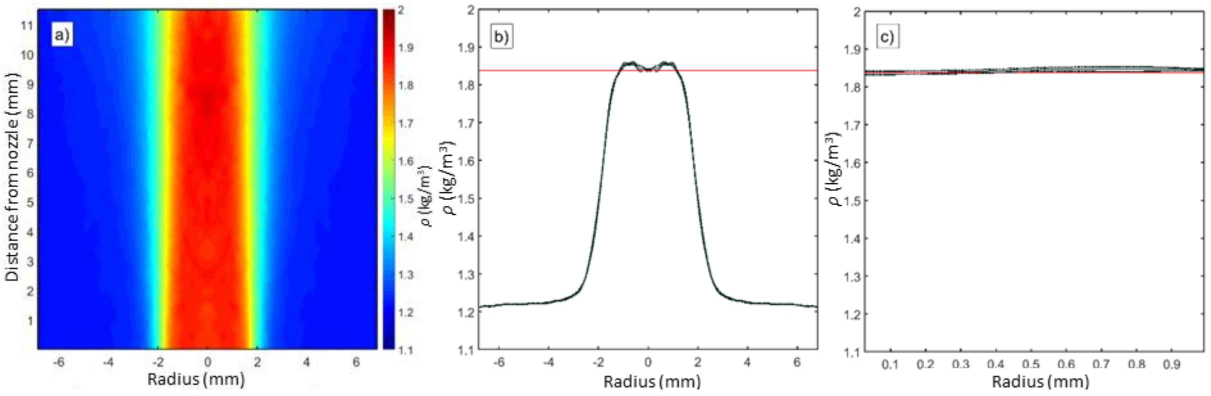

Figure 4-20: Jet CO2 – noise. Density field in cylindrical coordinates (a), density radial distribution average and deviation profiles obtained 1 mm above nozzle exit (b) and density axial distribution, average and deviation profiles in the jet core (r=0) (c) with CO_2 theoretical density for reference (in red) [103].

Measured density at the jet core should correspond to the theoretical CO_2 density. Density profiles in radial and axial directions are compared to the reference value. Density profile is represented along radial direction in Figure 4-20 (b), as the average value for all the tests and its deviation profiles 1 mm above the nozzle; and compared to the reference CO_2 density value in red. Density at the jet core $(radius = 0\,mm)$ is represented versus distance from nozzle –or height – in Figure 4-20 (c), with little variation from the reference CO_2 density represented as a red horizontal line.

Density values are compared at the nozzle exit area. We consider the exit area as a rectangle 2 mm wide centered at the jet core, and 1 mm height from the nozzle exit up to 1 mm above it. The mean relative difference for density measured at the jet core is $(\rho_{CO_2} - \rho_{jet})/\rho_{CO_2} = 0.8\% \pm 0.9\%$ (average and one std), lower than expected, which yields a 0.3 ± 0.3% relative error for the final measured CO_2 density.

4.3.2 Uncertainties and noise

Noise is generated during both steps of the SBOS density field measurement, namely acquisition and reconstruction. During acquisition, noise sources are camera sensor intrinsic noise (CCD dark current), image intensifier, background pattern generator vibration (ground glass), local room temperature gradients and laser light intensity fluctuations. Cross-correlations between different reference images measure the noise levels, as shown in Figure 4-21 as the typical mean and RMS (root-mean-square) of noise levels.

The noise results from high-frequency background displacement fluctuations (over 4 μm), partially produced by local speckle luminous intensity fluctuations during acquisition. Also, the uncertainty induced in cross-correlation is considered as white noise during reconstruction and may largely account for what is seen in Figure 4-21.

The refractive object is axisymmetric, so the overall average of the displacement field should be zero. Before reconstruction, the field residual mean displacement is subtracted to reduce noise.

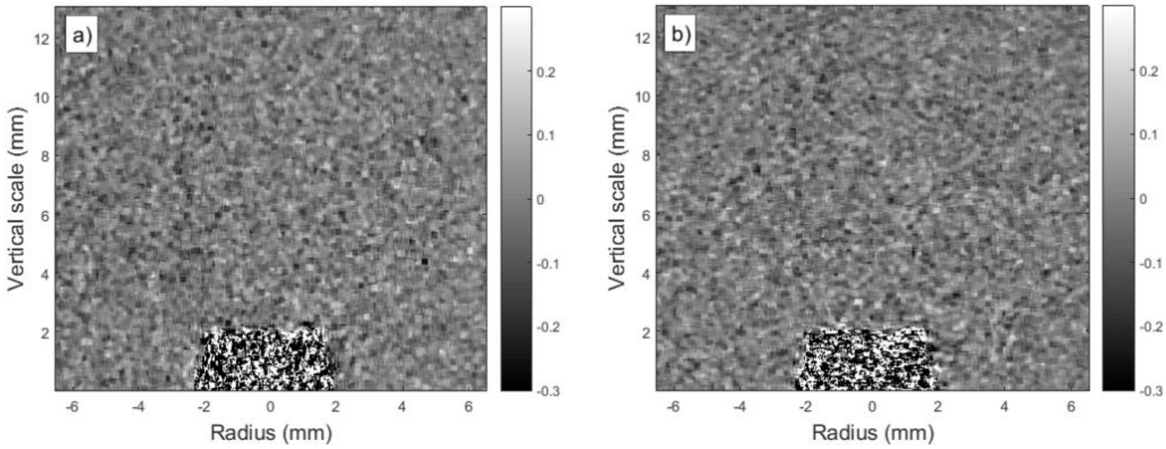

Figure 4-21: Mean horizontal displacement (a) and RMS displacement (b) in pixels for ten reference images [103].

To estimate the measurement uncertainty in the density profile (Figure 4-21 a) we apply logarithmic differentiation to integrated equation (4.15). On δ_x, it yields

$$\Delta\mathcal{I}/\mathcal{I} = \Delta n_0/n_0 + \Delta K/K + \Delta M/M + \Delta l/l + J \tag{4.30}$$

Where $\mathcal{I}$ is the integrated density and J is the uncertainty in the integral of the displacement profile, detailed below. The first and second terms are negligible according to [122].

Magnification measurement M is performed using an object of known dimensions, $(1.98^{+0.01}_{-0}mm)$, in the focal plane to measure its size in pixels, $(153 \pm 1\,px)$, and convert the measurement with the known pixel size $(s_p = 0.013\,mm/px)$. Resulting uncertainty is 1.1%. The focal plane – reference for the defocusing distance measure- is located where the hand-positioned item of interest appears sharp for the maximum diaphragm opening. Uncertainty of the defocusing distance is estimated to be 1 mm, which represents 1.3% of *l*. These two terms are constant over the field, so they only induce bias in the results. One could properly adjust the amplification factor $A = lM$, removing error from the geometrical measurement.

The term *J* is the uncertainty in the integral of the displacement profile: it represents the overall uncertainty of the cross-correlation operation, including both the cross-correlation algorithm and the acquisition white noise. Maximum dispersion occurs at the center of the reconstruction, as Figure 4-21 (a) shows. One diameter over the nozzle exit, the reconstructed value in the center of the jet should equal the CO_2 density.

J is then estimated from the stochastic fluctuation of the displacement profiles. The jet is supposed to be in steady conditions, so a temporal averaging is done on δ_x. Then the statistics are evaluated along *y*. A majorant value J_t is defined as in (4.31):

$$J \leq \sigma_y\left(\int_{-\frac{L}{2}}^{\frac{L}{2}} |<\delta_x>_t| dx\right) \Bigg/ < \int_{-\frac{L}{2}}^{\frac{L}{2}} |<\delta_x>_t| dx >_y = J_t \tag{4.31}$$

where $<>_t$ is the temporal averaging operator and L is the field radial dimension, with σ_y being the standard deviation operator in direction *y*, and $<>_y$ being the spatial averaging operator in vertical direction *y*.

If temporal averaging is not possible, as in unsteady conditions, a higher majorant J_{Ave} may be computed. In this case, the analysis should be done using the ensemble of profiles of each acquisition, as in equation (4.32):

$$J \leq J_t \leq \sigma_{y,Ave}\left(\int_{-\frac{L}{2}}^{\frac{L}{2}} |\delta_x| dx\right) \Bigg/ < \int_{-\frac{L}{2}}^{\frac{L}{2}} |\delta_x| dx >_{y,Ave} = J_{Ave} \tag{4.32}$$

where *Ave* represents a set of 100 acquisitions. These calculations yield J_t~2.6% and $J_{Ave} = 9.0\%$.

The obtained value for J is compared to the uncertainty of the cross-correlation, which is about 0.1 px. The value of the integration of $|\delta_x|$ along x is ~130 px, which is a 9.8% of the possible cross-correlation uncertainty. Given that cross-correlation intrinsic noise appears as white noise, integration and temporal averaging would reduce these values, which explains the slightly low J_t value.

Before the tomographic reconstruction, the total uncertainty for I (the line-of-sight integrated density difference) adds up to 5.0%. Computed tomography adds its own uncertainty in reconstruction. Comparing the oscillation amplitude value (2.6%) with J_t shows values that may indicate that the addition of tomography should only be of the order of a few percent.

The uncertainty of final results must take into account the reference temperature and pressure measurements, which are used to calculate the ambient gas density. This corresponds to 1.2%. The uncertainty of the measured density is thus estimated to be 6.2%, which is consistent with the low measured deviation. Temperature fields, obtained directly from density distribution, have the same 6.2% uncertainty associated.

Uncertainty propagation from temperature to enthalpy estimation is approximated from the integral of the polynomial function for $c_p(T)$, as indicated in (4.33) (with A_i being the coefficients of the polynome). Only the first term of the summation is considered for uncertainty estimation, as other terms negligible in comparison (higher power of temperature uncertainties). Then, the estimation of enthalpy variation yields the same uncertainty as for temperature, 6.2% (applying logarithmic differentiation).

$$c_p(T) = \sum_{i=1}^{7} A_i T^{i-1} \rightarrow \Delta h = \int_{T_{amb}}^{T} c_p(T)\, dT = \sum_{i=1}^{7} A_i\left(T^i - {T_{amb}}^i\right)/i \tag{4.33}$$

Energy deposit uncertainty is not simple to estimate. As specified in (4.28), energy deposit is calculated as the integration of the product of density and enthalpy variation over the kernel volume $\left(E_{sbos} = \oiiint_V \rho \Delta h\, dV\right)$. Propagation of the uncertainties of ρ and Δh through the volume integral cannot be directly calculated. The product $\rho\Delta h$ has an associated uncertainty of 12.4%. This is a good estimation for E_{sbos}, which is also in the order of variability observed from measurements.

4.4 Experiments and results

The SBOS method is employed to obtain density, temperature and volumetric energy fields, discharge kernel volume and radius, and also the total energy deposit at the moment the test image is captured.

Firstly we test discharges in atmospheric conditions, changing inter-electrode gap distance and image capture delay. Energy deposit values are compared with those obtained simultaneously by pressure rise calorimetry to compare and validate results. Secondly, we study the effect of pressure on the discharge, and lastly the effect of different gas mixtures.

The experimental setup used for this study, described in [§ Chapter 2], performs tests simultaneously by SBOS and pressure rise, Figure 4-22 pictures the experimental setup used for this study: the laser and the optical setup, the test chamber and calorimetry setup.

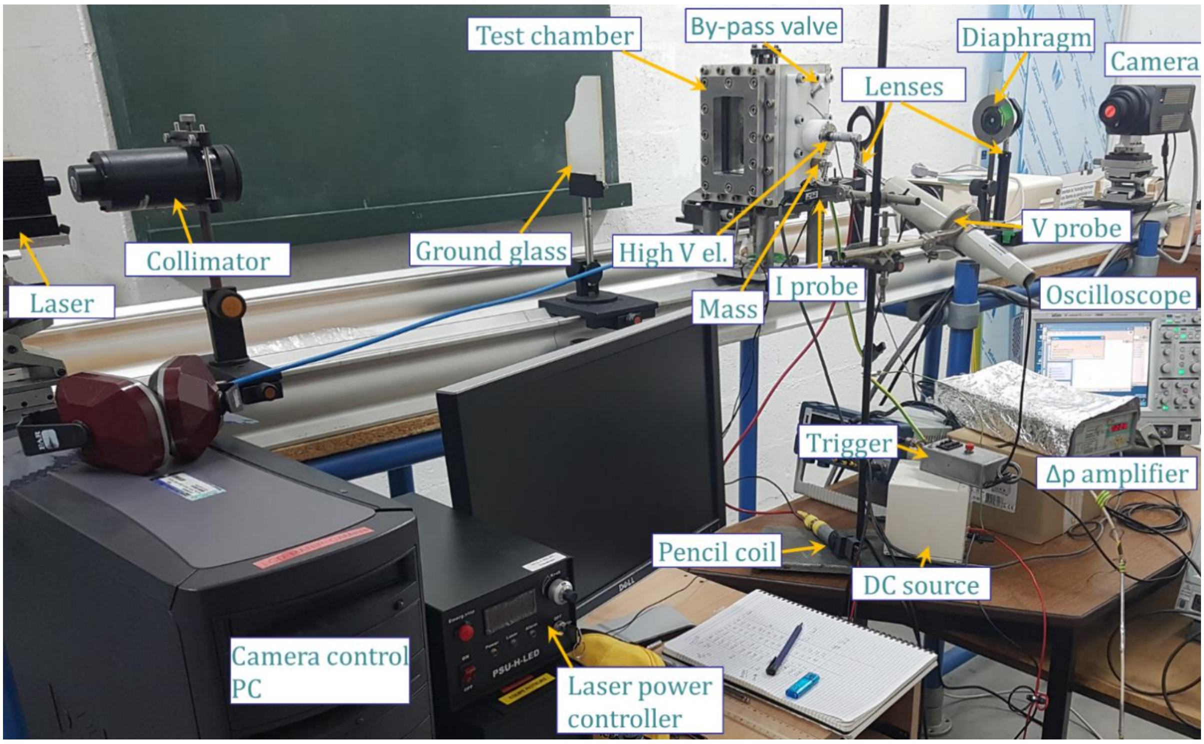

Figure 4-22: Picture of the SBOS and calorimetry experimental setup

Signal synchronization is controlled by the camera control computer and WinView32® program. The program is triggered by the TCI electrical trigger simultaneously with the discharge, and sets the picture capture delay as the one chosen for the test. First results obtained for SBOS and calorimetry were published in [123].

4.4.1 Atmospheric conditions

First tests study the influence of control parameters keeping constant the initial atmospheric conditions. Inter-electrode gap influence on the discharge is studied by SBOS, and different capture delays are set to track the kernel evolution over time, one instant at a time.

4.4.1.1 *Influence of gap*

The influence of gap is already studied in terms of discharge duration, energy deposit and efficiency by calorimetry in §3.3. The SBOS approach complements this information with the temperature distribution and kernel size.

We perform 2 series of 10 tests, at atmospheric conditions in air, one set with a 1 mm gap and the second one with a 2 mm gap. The defocus distance is set at $l = -80\ mm$. Images are captured at the end of the discharge, defined from electrical signals ($\Delta t = 3.0$ and $2.9\ ms$ for 1 and 2 mm respectively), so all the electrical energy for the discharge has been supplied to the fluid. Averaged displacement fields for each of the sets are represented in Figure 4-23, 1 mm on the left and 2 mm on the right. Displacement is higher for the 2 mm discharge (with a maximum of ~3.5 px in 1 mm and ~4.5 in 2 mm). Two different cross-correlations are applied consecutively with different number of steps each; i.e., *x1* step for *Cross-correlation 1* and *x3* steps for *Cross-correlation 2* (*x4* steps in total, not to be confused with 2). Table 4-1 summarizes the SBOS control parameters employed for these tests:

M	*Ø*	t_{gw}	*Gain*	*l*	Δt_{input}	*Cross-correlation 1*	*Cross-correlation 2*
-1.0	8 mm	1 µs	200	-80 mm	2.9 - 3 ms	64x64 px^2, 25% OL, x1	16x16 px^2, 75% OL, x3

Table 4-1: SBOS control parameters for the study of the effect of gap.

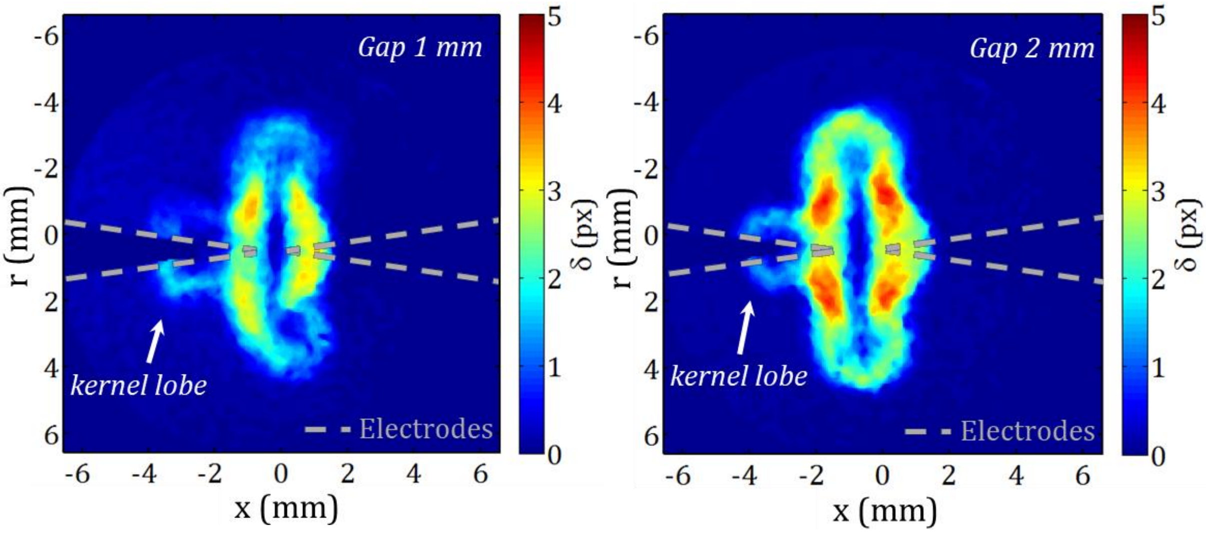

Figure 4-23: Displacement fields for 1 and 2 mm gap (left and right, respectively) at the end of the discharge averaged for each set of tests. In air at 1 bar. Δt=3.0 ms (1mm), 2.9 ms (2 mm).

A part of the kernel is projected around the anode, which is the left lobe in Figure 4-23 (indicated with a white arrow in the images). This effect appears only in half of the tests. It is neglected for enthalpy calculation by truncating the lobe: it is close to the electrode walls and interacts with the boundary conditions in masks, inducing errors in the mathematical reconstruction. This truncation induced little difference in the resulting estimated energy, less than 1 mJ difference.

Temperature distributions are obtained for each test, and represented averaged for the 10 tests in Figure 4-24. The study explained in §3 shows that for longer gap distances discharges are shorter and with a higher energy deposit.

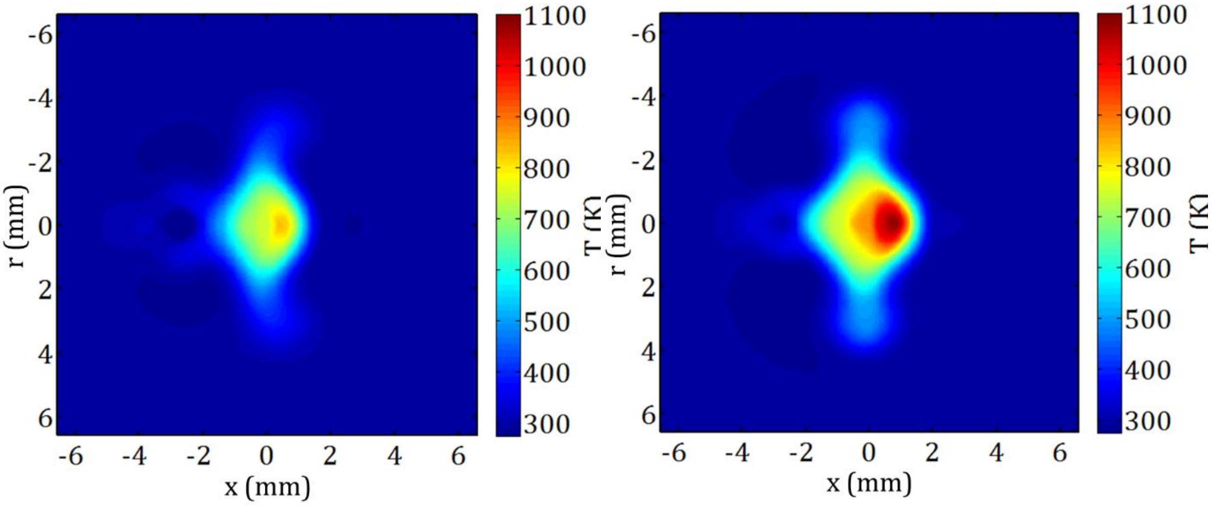

Figure 4-24: Temperature field for 1 and 2 mm gap for 3.0 and 2.9 ms, averaged for 10 tests.

The discharge kernel present higher temperatures at the end of the discharge for longer gap distances: a maximum temperature of 833 K, for 1 mm gap; and 1080 K, for 2 mm. To compare kernel temperatures, the temperature profiles along the vertical central section of the temperature distribution are analyzed instead of comparing only the hot spots. As there are temperature gradients in the x-plane, a single vertical line would miss a part of the information contained in the kernel (as there are hot spots close to the electrode tips). A vertical band is chosen instead, averaged along the horizontal x-axis and represented in Figure 4-25. The band is 0.4 mm width ($x \in (-0.2, 0.2)\ mm$), and represented on the temperature fields on the left.

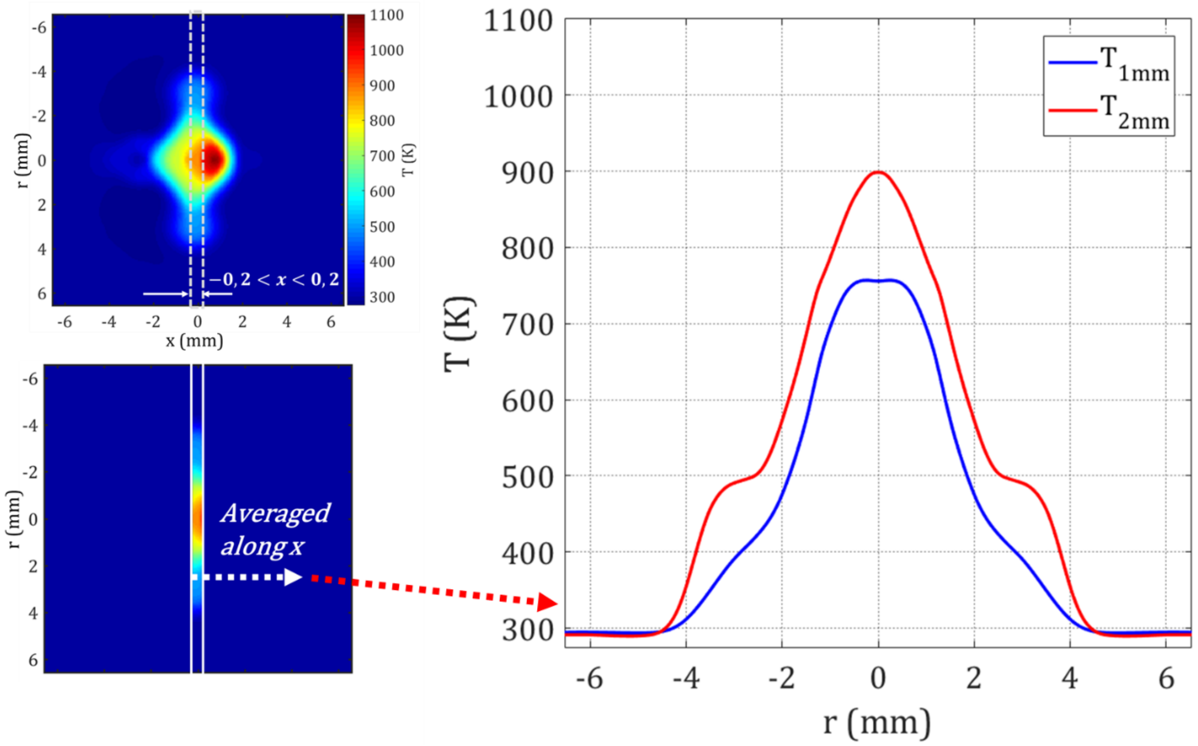

Figure 4-25: Temperature profiles along kernel diameter for 1 mm and 2 mm gap and at Δt of 3.0 and 2.9 ms respectively, averaged over a 0.4 mm band.

Gap distance also affects the hot kernel size. Kernel radius increases from 3.9 to 4.1 mm in average for the 10 tests from 1 to 2 mm gap (at the end of the discharge, which is $\Delta t = 3.0$ and $2.9\,ms$ for 1 and 2 mm respectively). Radius estimation has an accuracy of ±0.05 mm (1/255 matrix points, 13.18 mm long), although its values depend on the temperature threshold chosen for kernel edge detection. Larger radius means that the kernel expands further away from the initial conductive channel between the electrode tips. Volume of the discharge also increases with gap, from 92 to 113 mm^3 in average for discharges with 1 and 2 mm gap respectively. These results are shown in Figure 4-26, on the left graph for radius comparison and right for volume comparison vs gap distance, both expressed as the average for the 10 tests in each condition and error bars representing standard deviation. The exact values are detailed in Table 4-2.

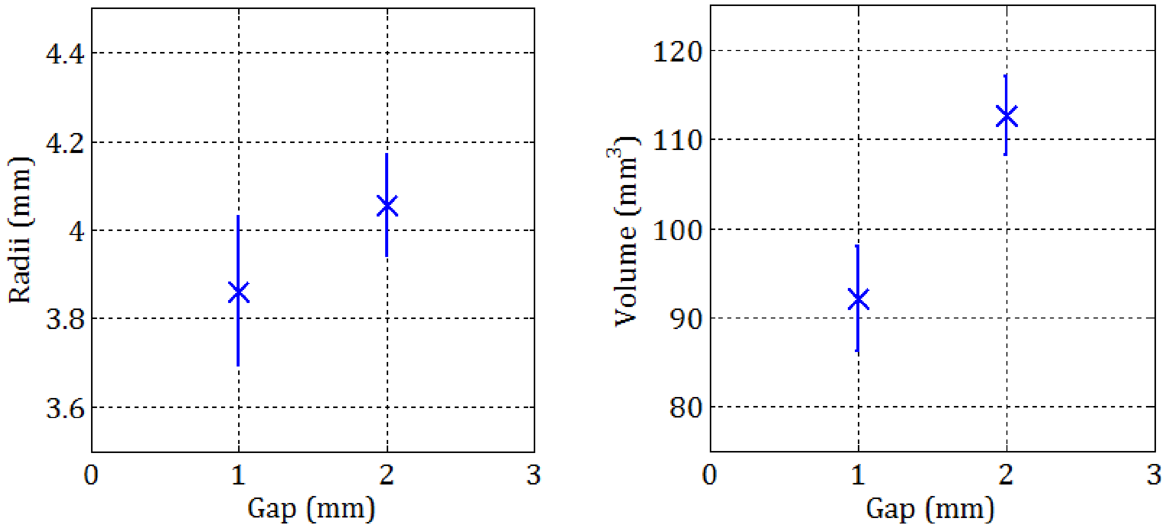

Figure 4-26: Kernel radius (left) and volume (right) for electrical discharges in atmospheric conditions at 1 and 2 mm gap.

Gap (mm)	1	2
Volume (mm^3)	92.1 ± 5.9	112.7 ± 4.5
Radius (mm)	3.86 ± 0.17	4.06 ± 0.11
Discharge duration and Δt (ms)	3.0	2.9

Table 4-2: Kernel volume and radius for 1 mm and 2 mm gap.

The temperature fields and kernel sizes obtained represent temperature at one instant at the end of the discharge. Their temporal evolutions are investigated in the next paragraph.

4.4.1.2 Time evolution of the discharge kernel

In order to monitor the kernel development over time, the delay time Δt (image acquisition time from the beginning of the discharge) is varied. Series of tests are performed for each instant.

We perform 9 series of 10 tests, with Δt from 0.5 to 2.5 ms, with an increment of 0.25 ms for each series. The tests have an inter electrode gap of 2 mm, and are made in air at 1 bar, with a defocus distance of $l = -80\,mm$. Other SBOS control parameters are specified in Table 4-3. Electrical discharges in each test condition show good repeatability, with the same kernel position and similar displacement field. The averaged displacement fields for each series are represented in Figure 4-27, where one can see the kernel expansion over time and the formation of radial lobes which indicate a toroidal structure when expanding [2].

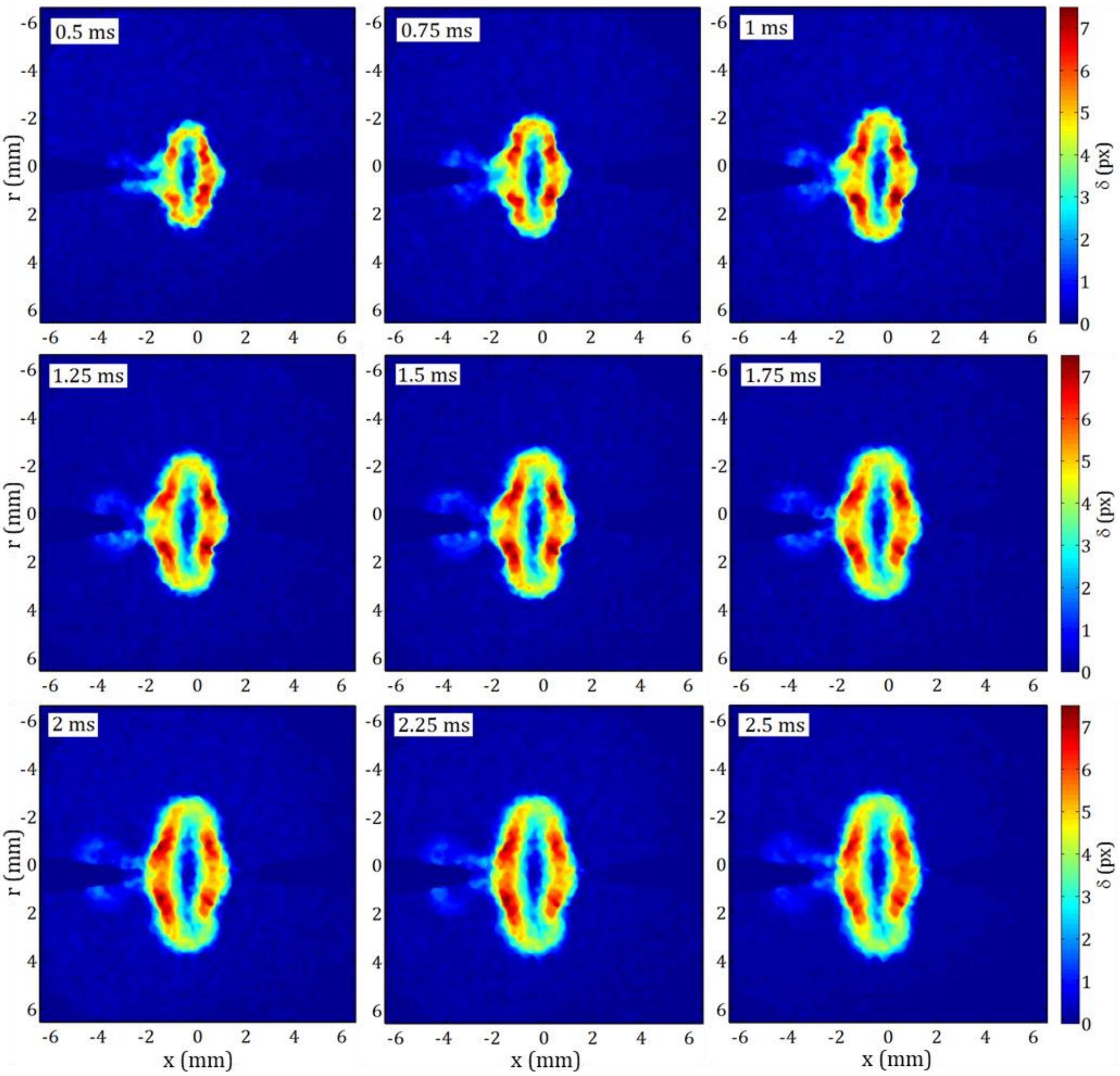

Figure 4-27: Displacement fields averaged from 10 tests, for $\Delta t = 0.5$ to 2.5 ms from left to right and top to bottom, 2 mm gap.

M	Ø	t_{gw}	*Gain*	l	Δt_{input}	*Cross-correlation 1*	*Cross-correlation 2*
-1.0	8 mm	1 µs	200	-80 mm	0.5 – 2.5 ms	64x64 px^2, 25% OL, x1	16x16 px^2, 75% OL, x3

Table 4-3: SBOS control parameters for the observation of kernel evolution

For each test, the temperature distribution is calculated, and the average temperature field for each delay time is obtained. Average temperature distributions are compared in Figure 4-28. As the figure shows, the kernel reaches higher temperatures at the earliest delay times: up to 1400 K at the first observed instant, 0.5 ms, and around 1200 K 1 ms after discharge onset. Later on, even when the discharge is still going on, the kernel cools down as it expands (1.25 to 2.5 ms).

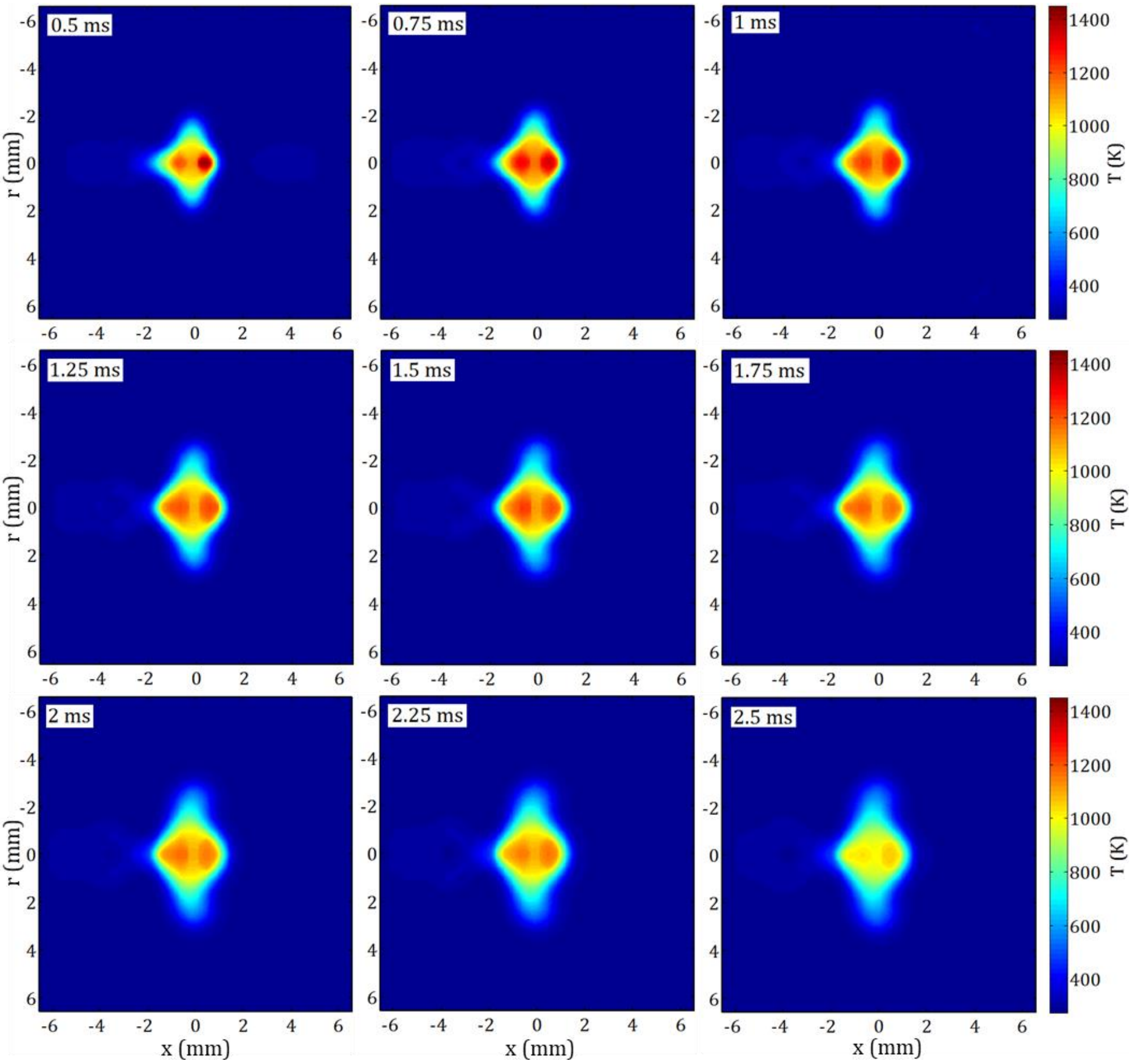

Figure 4-28: Temperature fields averaged for 10 tests, 0.5 to 2.5 ms after discharge onset, 2 mm gap.

Temperature profiles along the central band of the average temperature fields are computed, and represented in Figure 4-29. The temperature profiles are obtained averaged along the x-axis over a 0.4 mm width vertical band, as in §4.4.1.1. In the figure, each temperature profile corresponds to a delay time, following the color code in the legend. The cooling of the kernel over time is indicated by the lower temperature profiles at later instants. The radial expansion is deduced from the wider temperature profiles, with larger radius at low temperatures in later moments. In conclusion, these observations are in agreement with [5], [87]: the hot kernel reaches higher temperatures in early stages of the discharge, and then it cools down as it expands during the discharge, even during the following deposit of energy in the conductive channel in arc or glow mode.

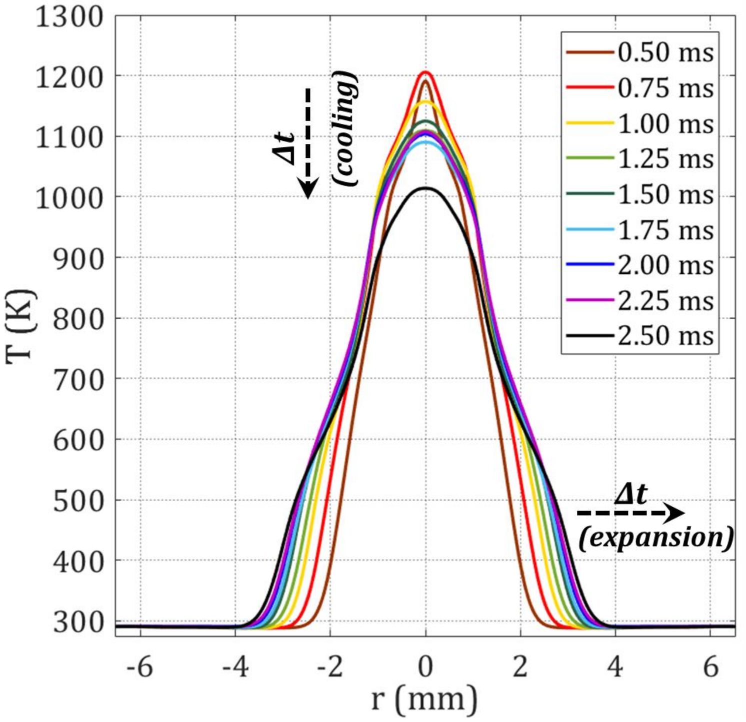

Figure 4-29: Temperature profiles along a central band of the discharge kernel for different Δt. Profiles from temperature fields averaged for 10 tests at each Δt, at 1 bar for a 2 mm gap.

Kernel expansion is clearly observed analyzing the kernel radius and volume. Kernel expands from the discharge start. In the first instants observed (Δt from *0.5* to *1 ms*), the maximum kernel radius increases at *~1 m/s*; later ($\Delta t > 1.5$ *ms*) kernel grows slower at *~0.3 m/s*. Diffusion rules the kernel expansion, although there is great influence of the convective transport induced by the shockwave, with the shockwave itself that depends on breakdown energy. Kernel size is estimated for each set of 10 tests, and maximum radius and kernel volume are presented in Figure 4-30 as mean values with standard deviation bars.

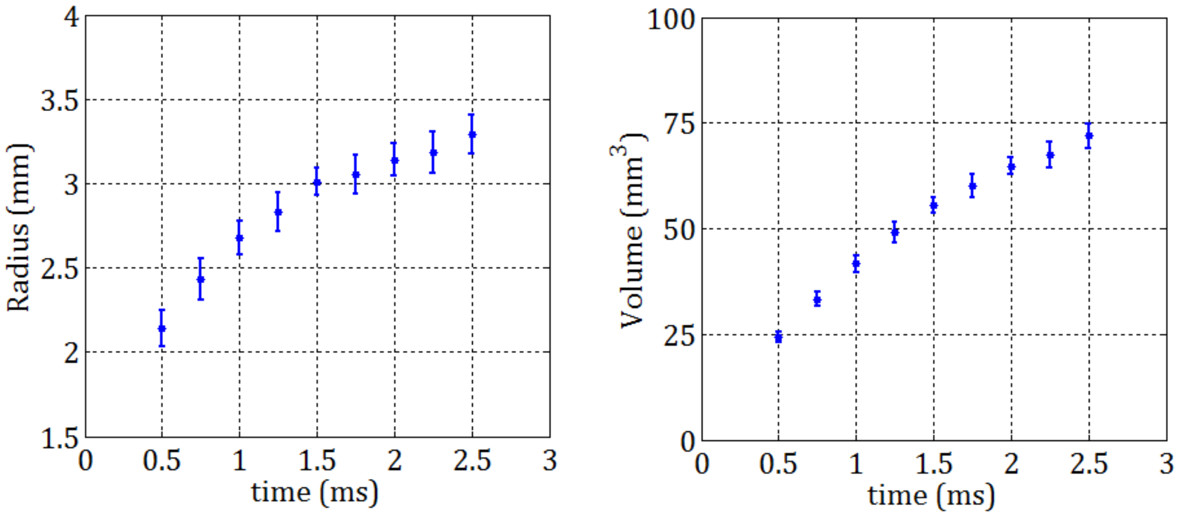

Figure 4-30: Kernel maximum radius (left) and kernel volume (right) from 0.5 to 2.5 ms after the discharge onset for a 2 mm gap.

The hot kernel expansion rate is smaller after the discharge end. Once the energy deposit finishes, the hot kernel may expand few millimeters further (from radius measurements, < 0.5 mm), but the energy measurements confirm the energy in the hot kernel does not significantly vary during this period.

4.4.1.3 Energy deposit and comparison with calorimetry

Enthalpy and energy are calculated with the SBOS technique and compared to calorimetry results obtained simultaneously for the same tests. Calorimetry tests and electrical measurements provide E_{th} and E_{el} over time for each test, but only their values at the time image capture instant are selected for comparison with E_{BOS}.

Figure 4-31 compares the energy measurements from both techniques, as mean values (x) with standard deviation bars, in green for E_{BOS}, red for E_{th} and blue for E_{el}. SBOS estimations overvalue the energy deposit compared to the E_{th} values given by pressure-rise calorimetry; E_{BOS} is 15% higher than E_{th} for the first instants studied, to 20% at the lasts. The difference is in the order of the measurement uncertainty of both methods, and results follow the same tendency. Given that pressure-rise calorimetry and SBOS are based on very different principles, for the study of the electrical discharges they both provide a good estimation of the energy deposit.

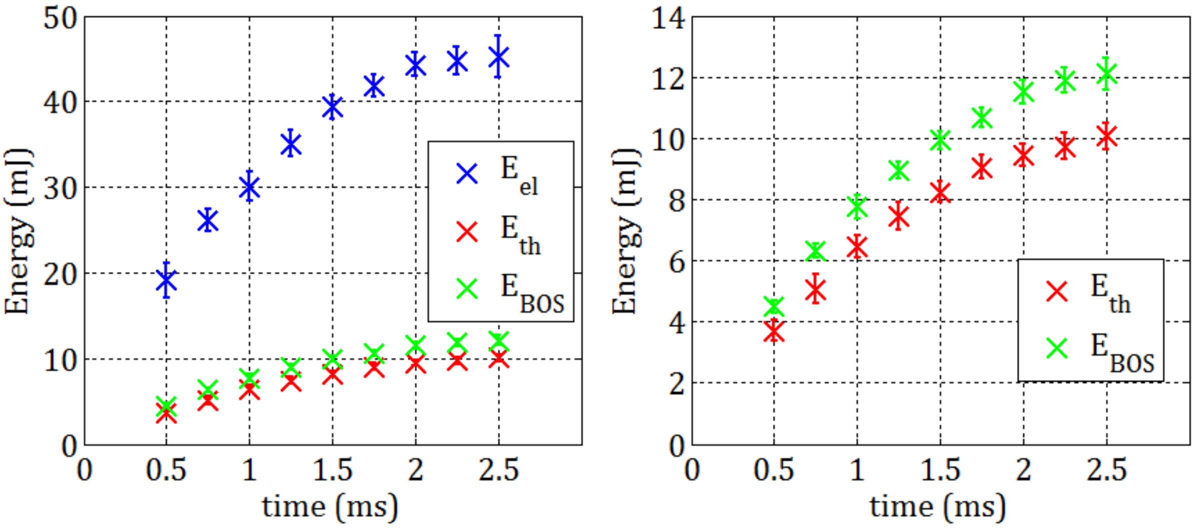

Figure 4-31: Calorimetry and SBOS cross-correlation for energy measurements over time. Left figure shows E_{el}, E_{th} and E_{BOS}. The right graph is re-scaled for a more detailed view of E_{BOS} and E_{th}.

4.4.2 Influence of pressure

To study the influence of pressure on the discharges, tests are performed from 0.5 to 2.0 bar. This range of pressure is related to the density found in aircraft engine conditions, from re-ignition at high altitude (low temperature and pressure) to sea level ignition (high temperature and pressure).

Defocusing distance *l* is adjusted for each pressure condition. The energy deposit increases with pressure, as seen in §3.4.1, so higher displacement values are expected. Too much displacement of the background pattern points would difficult the cross-correlation processing (with points that moved too far and couldn't be detected, yielding zero displacement), and too little displacement means a lower SNR (signal noise ratio). Defocus distance is set to $-80\,mm$ for low pressure, $-50\,mm$ for 1 bar and $-30\,mm$ for 1.5 and 2.0 bar, as indicated with the rest of control parameters in Table 4-4. Reference images for 0.5 and 2 bar are compared in Figure 4-32, which shows much blurry electrode tips for the longer defocusing distance at 0.5 bar than at 2.0 bar.

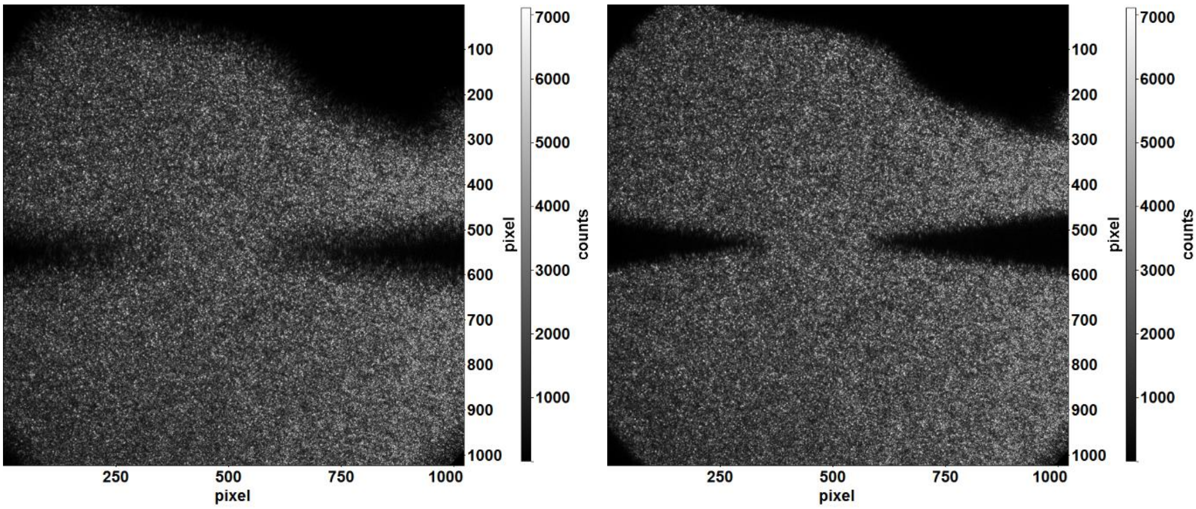

Figure 4-32: Reference background speckle pattern. Left: 0.5 bar, l = -80 mm, Right: 2.0 bar, l = -30 mm.

p (bar)	M	∅ (mm)	t_{gw} (μs)	Gain	l (mm)	Δt_{input} (ms)	Correlation 1	Correlation 2
0.5	-1.0	8	1	200	-80	2.0 -3.5	64x64 px^2, 25% OL, x1	16x16 px^2, 75% OL, x3
1.0					-50			
1.5 - 2.0					-30			

Table 4-4: SBOS control parameters for tests at different initial p. Empty cells represent no change in values.

For each pressure a series of 10 tests is performed at 1 mm gap, with one reference image captured for each series. Then they are repeated for a 2 mm gap. For each experimental condition, Δt is equal to the discharge duration (estimated in Chapter 3, §3.3.2), to ultimately obtain the total energy deposit at the end of the discharge. Experiments were performed at ambient temperature $T_{ref} = 20.0 \pm 0.5\,°C$. Displacement fields are then computed for each test; then they are represented in Figure 4-33 averaged for each series of tests at different pressures for the 2 mm gap. Discharges at lower pressure produce lower displacement fields, with $\delta_{max} < 4\,px$ at 0.5 bar and $l = -80\,mm$ compared to $\delta_{max} < 6.5\,px$ at 2.0 bar and $l = -30\,mm$.

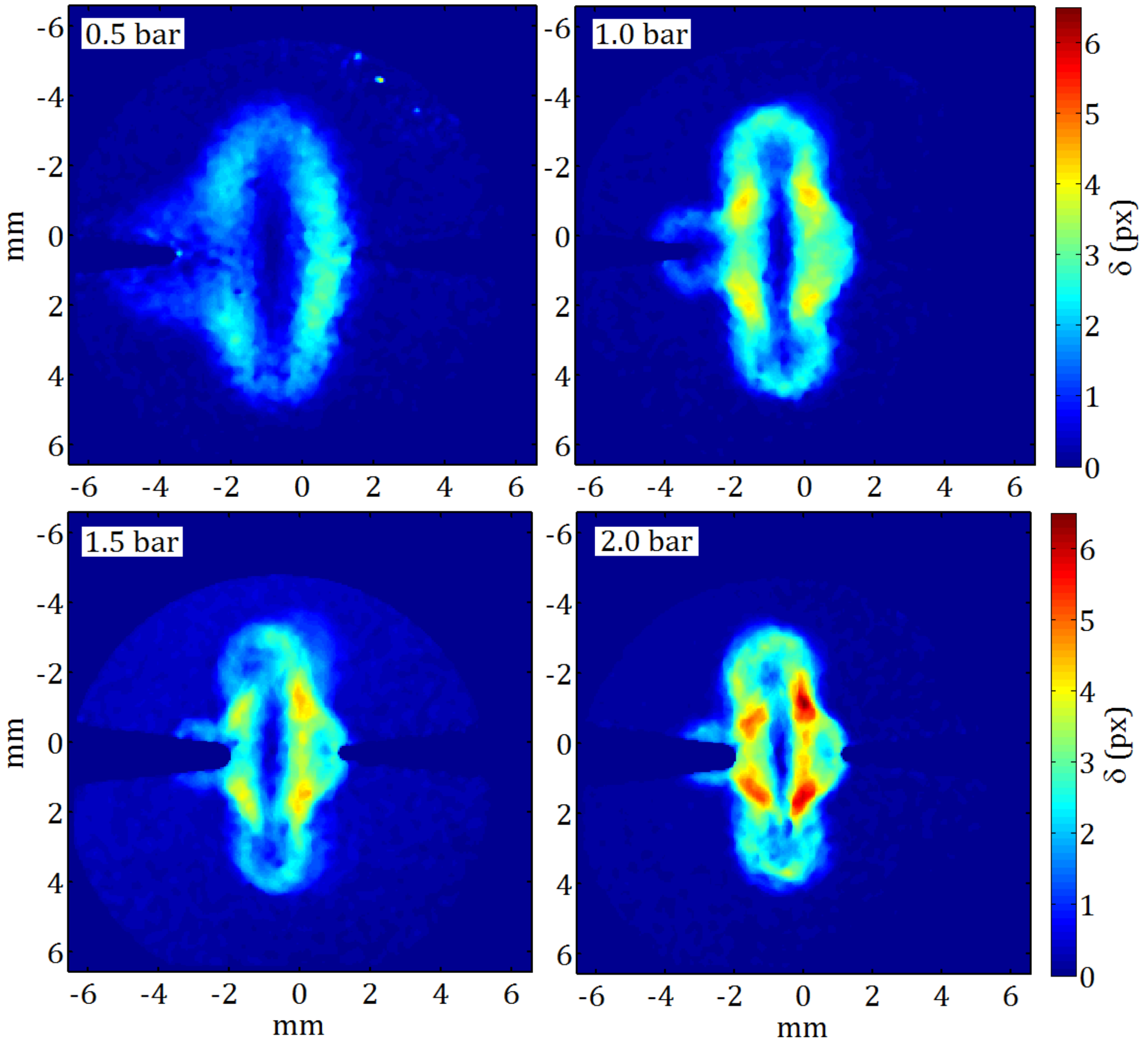

Figure 4-33: Averaged displacement field for 0.5, 1.0, 1.5 and 2 bar in air and a 2 mm gap.

In some cases isolated displacement peaks caused by light reflection induce noise, for instance in the pressure transducer protection (right corner) at the displacement field for 0.5 bar in Figure 4-33. Filtering during the refractive index and density reconstruction mitigate this effect, together with proper mask definition and image truncation.

Density and temperature fields are reconstructed from the displacement fields for each test. The average temperature field for 10 tests at each pressure is represented in Figure 4-34. Both energy deposit and the energy transfer efficiency increase with pressure, while discharge duration decreases. At the end of the discharge, the kernel temperatures tops at 610 K for 0.5 bar, at 900 K for 1.0 and 1.5 bar, and at 1100 K, and at 2.0 bar.

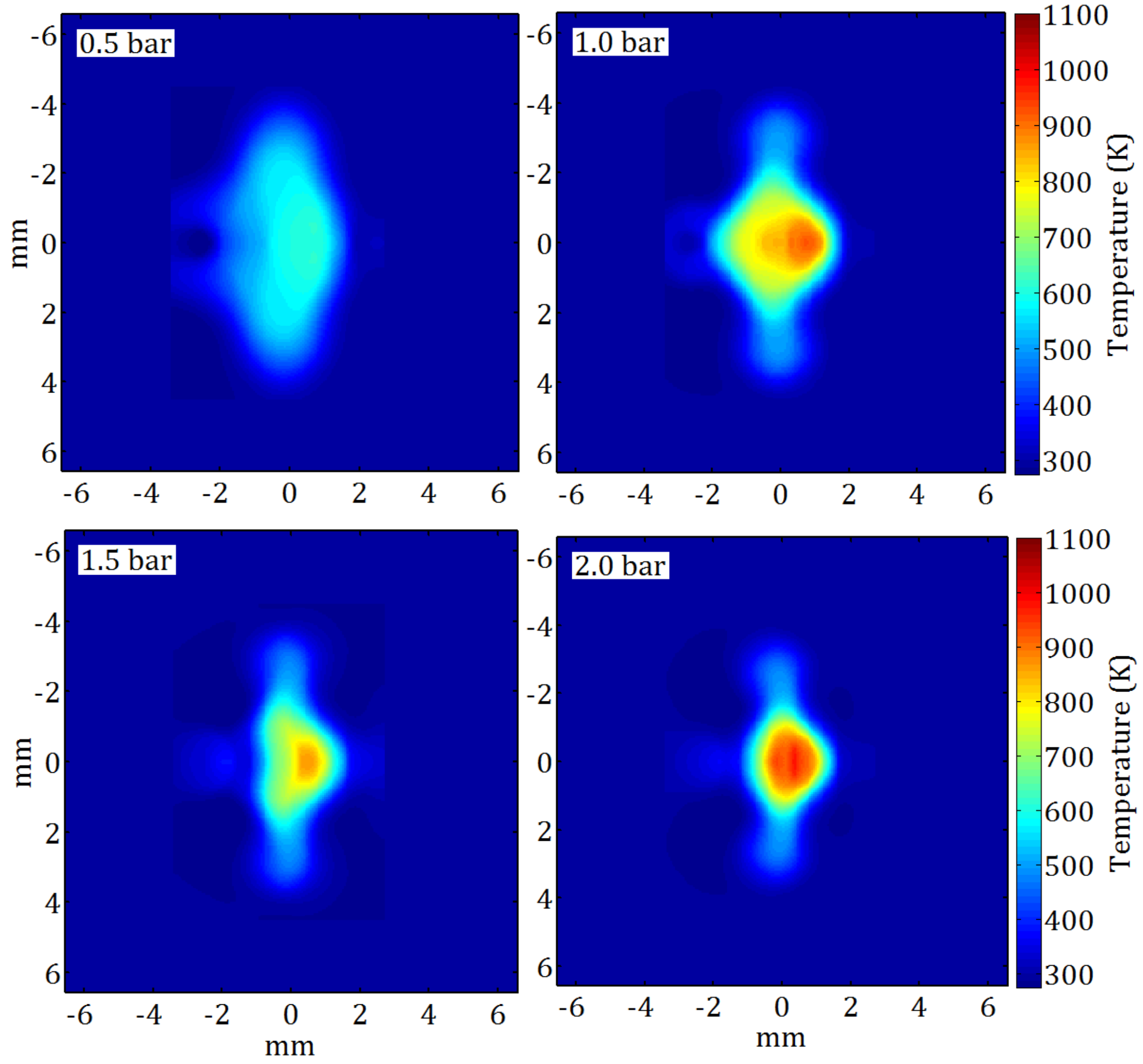

Figure 4-34: Temperature fields averaged for 10 tests, for 0.5, 1.0, 1.5 and 2 bar in air and a 2 mm gap.

From the average temperature fields one can qualitatively observe the kernel size tends to decrease with higher pressures. Temperature profiles are extracted along a vertical band, as in previous paragraphs, and plotted in Figure 4-35. They are represented for both 1 and 2 mm gap, on the left and on the right respectively (the 2 mm gap corresponding to previous figures). One should note that the profiles correspond to different instants of time (the total duration of the discharge in each condition). At the end of the discharge (a different Δt for each pressure) at lower pressures kernel temperatures are lower at both 1 and 2 mm gap. For higher pressures, at the end of the discharge, kernel remains at higher temperatures.

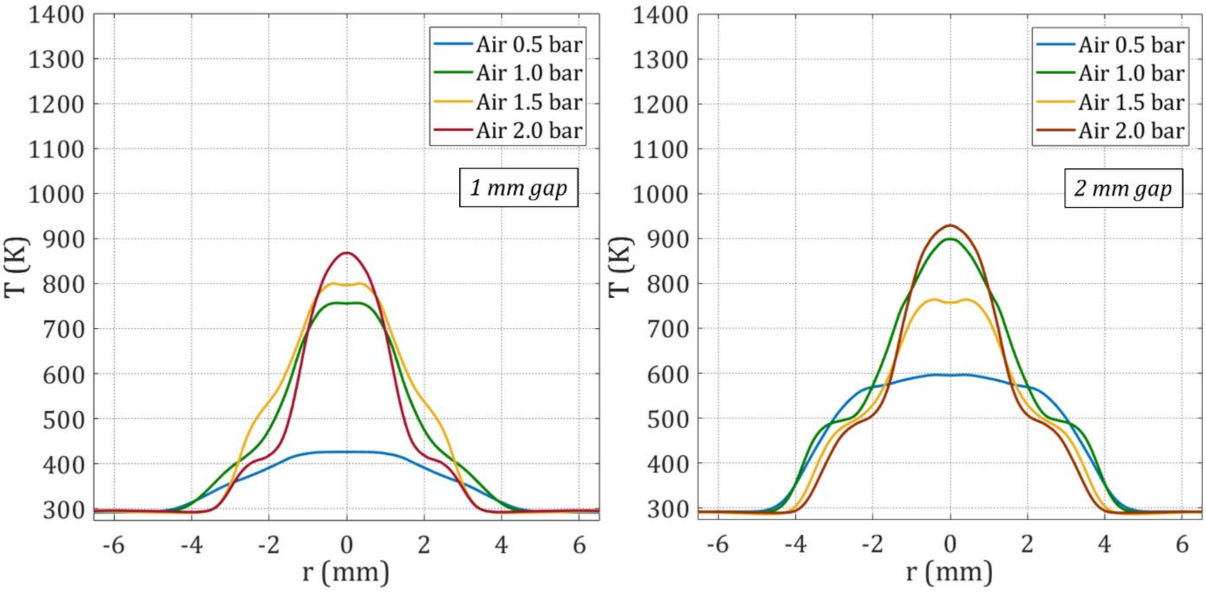

Figure 4-35: Temperature profiles along a vertical band for different pressures. From temperature fields averaged for 10 tests in each condition. Gap of 1 mm (left) and 2 mm (right).

The kernel size analysis is performed for each test, measuring the kernel size and maximum kernel radius for each gap and pressure conditions. Results show that at higher pressures the hot kernel reduces its size, both in maximum radius and in volume. Figure 4-36 shows the maximum radius (left) and kernel volume (right) for discharges at 1- and 2-mm gap, plotted versus the initial pressure. Radius decreases from 3.9 mm at 0.5 bar to 3 mm at 2.0 bar, for a 1 mm gap. The same trend is obtained for the 2 mm gap, with slightly higher values. Kernel volume decreases linearly with pressure, from 104 to 41.5 mm^3 for 1 mm gap. The same trend is observed at 2 mm gap, with larger kernel volumes (by ~40 mm^3).

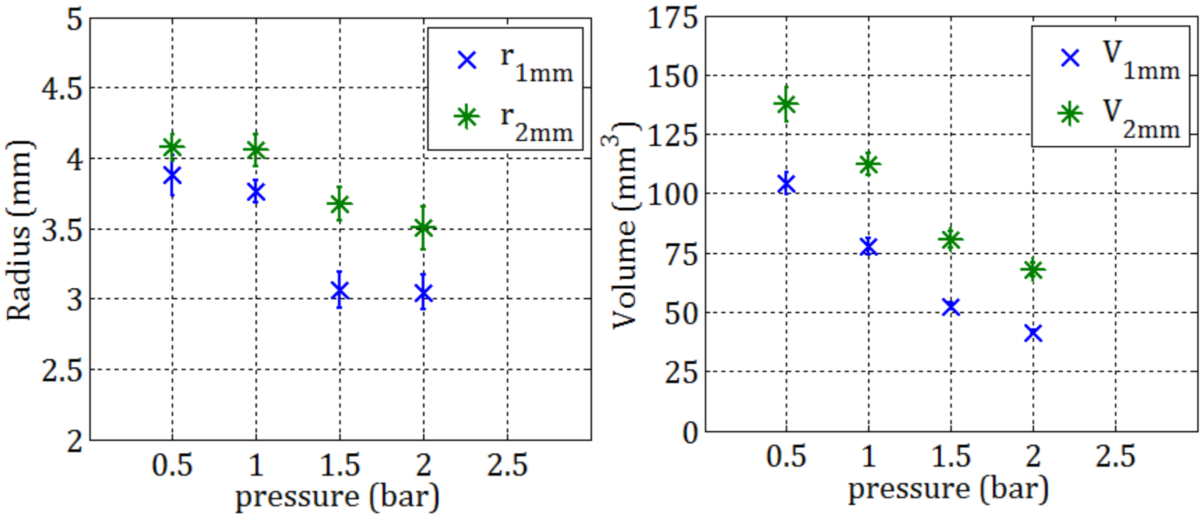

Figure 4-36: Kernel maximum radius (left) and volume (right) versus pressure, for 1 and 2 mm gap.

4.4.2.1 Energy deposit and method comparison

From the temperature distributions, the enthalpy deposit is estimated for all the tests. Results for energy deposit are compared to those obtained by calorimetry, as in §3.3.1. They are presented in Figure 4-37, for tests in 1 mm and 2 mm gap and all the tested pressures.

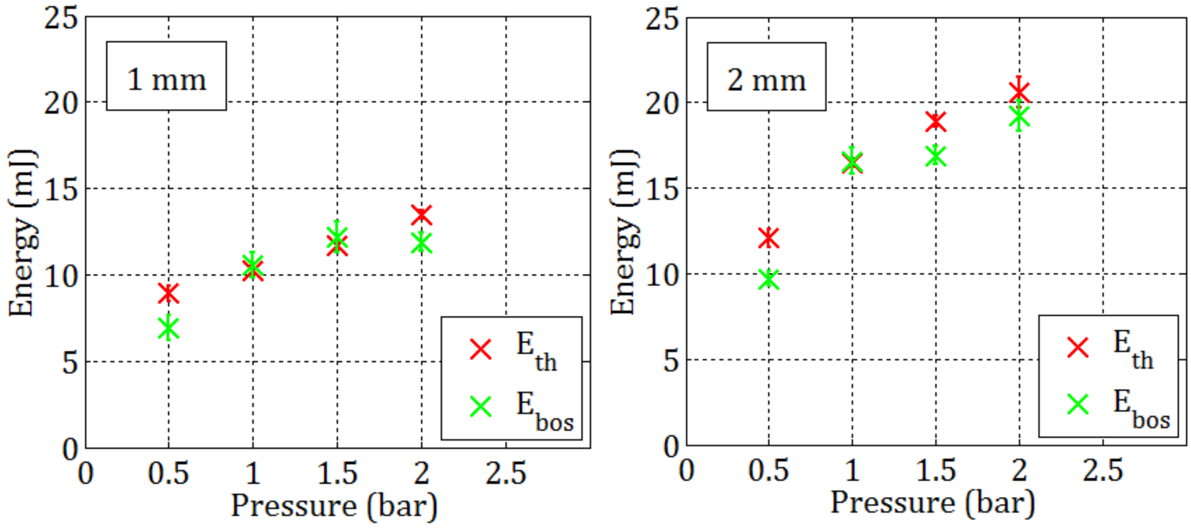

Figure 4-37: SBOS-Calorimetry results comparison. Air, 0.5 to 2 bar.

E_{BOS} measurements follow the same trend as calorimetry results: energy deposit increases with pressure. In some conditions, as in 1.0 bar pressure for both 1- and 2-mm gap, and 1.5 bar for 1 mm gap, E_{BOS} values are very close to E_{th}. For 0.5 and 2 bar, SBOS technique undervalues energy deposit, with a difference of 25%. As in previous tests, considering the uncertainties associated to each method, there is a good agreement between the results issued from the both methods.

4.4.3 Influence of gas mixture compositions

We study the effect of the presence of carbonated chains in the gas on the electrical discharges. Nitrogen-propane mixtures at different concentrations represent the fuel-air mixture in engine conditions, avoiding the extra energy that would be released by the oxidation of the fuel in the presence of oxygen –as explained in §3.4.2-.

First, gas properties such as Gladstone-Dale constant, c_p and molecular weight are calculated for the mixture. Then, the SBOS results for the gas mixtures are compared with results in air. Finally, the energy deposits measured by SBOS are compared to the ones obtained by pressure-rise calorimetry.

4.4.3.1 Gladstone-Dale constant estimation

Gladstone-Dale relation for a gas mixture is reported in equation (4.2). It is equivalent to the relation for a single gas, with $\rho = \rho_{mix}$ and $K = K_{mix}$. Gladstone-Dale constant of the mixture, K_{mix} is obtained from the components constants K_i and their density ratio, as in equation (4.34) [106]. K_{air}, K_{N_2} and $K_{C_3H_8}$ are obtained by interpolation of the different values published by A.C. Simmons [114], for our laser wavelength of 532 nm (inside the linear domain of the values published). Table 4-5 contains molecular weight and Gladstone-Dale constants of each of the gases employed, where propane-nitrogen mixtures are named for their equivalent equivalence ratio Φ_{eq}.

$$K_{mixture} = \sum_i K_i \left({}^{\rho_i}/_{\rho_{total}} \right) \tag{4.34}$$

Gas	$\boldsymbol{Mm\ (g/mol)}$	$\boldsymbol{K\ (cm^3/g)}$
Air	28.97	0.2271
Nitrogen	28.01	0.2392
Propane	44	0.5432
Mixture Φ_{eq}~1.0 $(C_3H_8 - N_2)$	28.66	0.2580
Mixture Φ_{eq}~1.5 $(C_3H_8 - N_2)$	28.97	0.2666

Table 4-5: Molecular weight and Gladstone-Dale coefficient of different gas mixtures for a 532 nm wavelength.

Specific heat capacity at constant pressure (c_p) changes for different mixtures. It is computed from Gordon-McBride polynomial coefficients of the c_p model using the molar ratio of the mixture.

4.4.3.2 Results and discussion

We perform series of 10 tests in propane-nitrogen mixtures, for different initial pressure, inter-electrode gap and propane concentrations. Two propane concentrations are compared: the first one is equivalent in propane proportion to a stoichiometric propane-air mixture, at Φ=1.0 with a mole fraction of $40.3 \cdot 10^{-3}$; and the second one is equivalent to a rich mixture at Φ=1.5, with a mole fraction of $59.3 \cdot 10^{-3}$. Tests are performed simultaneously by SBOS and pressure-rise calorimetry, with calorimetry results discussed in §3.4.2.

Defocus distance is adapted to initial pressure, as for the tests in air: $-80\,mm$ for low pressure, $-50\,mm$ for 1 bar and $-30\,mm$ for 1.5 and 2.0 bar. A reference image is recorded for each experimental condition (gap, gas composition, pressure), before performing the 10 tests. Images are captured at the end of the discharge in each condition, so that the total energy deposit can be estimated.

In the presence of fuel and at higher pressures (1.5 and 2.0 bar) spark discharges present less repeatability in terms of kernel shape: asymmetric and/or 3D structures form. The SBOS image processing is only valid for axisymmetric fields. Thus, tests presenting asymmetries – that are observed visually at the displacement field- are excluded from the SBOS data processing.

As an example of valid and invalid tests, Figure 4-38 illustrates different displacement distributions issued from single tests for the Φ_{eq} 1.5 mixture and a 2 mm gap, and their corresponding temperature fields. At 0.5 bar, as in the left image, test show high repeatability. For higher pressures there are asymmetries and 3D structures in some of the tests for the same experimental conditions. One can observe this variability in the middle and right displacement distributions, both from tests at 2.0 bar: the first one is symmetric and valid for the SBOS image processing, but the right is one not valid for not verifying the axisymmetric kernel hypothesis. Resulting temperature fields are symmetrized by the filtered backprojection of the image processing – as explained in 4.2.4-, producing a virtual temperature field which does not correspond to the real temperature distribution in the asymmetric case (right).

Table 4-6 compares the number of tests discarded for data processing for each gas, gap and pressure. This ratio could represent the variability of the discharge kernel spatial distribution in each experimental condition. In air, the ratio of asymmetric discharges is similar for all conditions. In propane-nitrogen mixtures though, discharges in 0.5 and 1 bar present high repeatability but in 1.5 and 2.0 bar most of the tests are discarded. The presence of carbonated chains, molecule recombination and change in the electrode surface at microscopic scale in each discharge may be the origin of such instabilities.

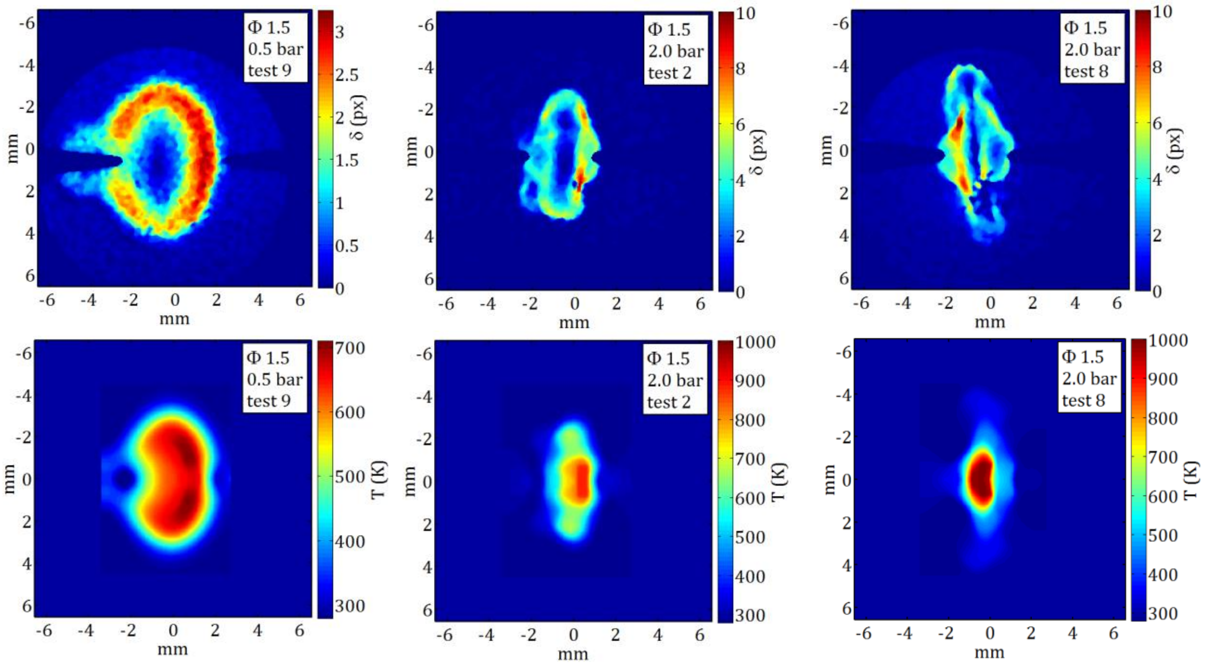

Figure 4-38: Instantaneous displacement and corresponding temperature fields for discharges with a 2 mm gap in the mixture Φ_{eq} 1.5 and different pressures. In 0.5 bar (left), high repeatability with symmetric kernel shape. At 2.0 bar, higher variability with symmetric kernels (central image) as well as asymmetric structures (right).

Gap	1 mm			2 mm		
p \ Gas	Air	Mix Φ 1.0	Mix Φ 1.5	Air	Mix Φ 1.0	Mix Φ 1.5
0.5 bar	0/6	0/10	0/10	0/9	0/10	0/10
1.0 bar	3/10	0/10	0/10	3/10	0/10	0/10
1.5 bar	0/10	0/11	3/10	4/9	6/9	8/9
2.0 bar	2/10	6/12	9/12	3/9	7/9	6/9

Table 4-6: Ratio of tests with strong asymmetries over the total number of tests at the specified conditions.

Integration of displacement distributions for symmetric cases yields the temperature distribution for each condition. Averaged temperature fields are represented in Figure 4-39 and Figure 4-40, for 1 mm and 2 mm gap respectively and together with temperature fields obtained in air at the same gap and pressure.

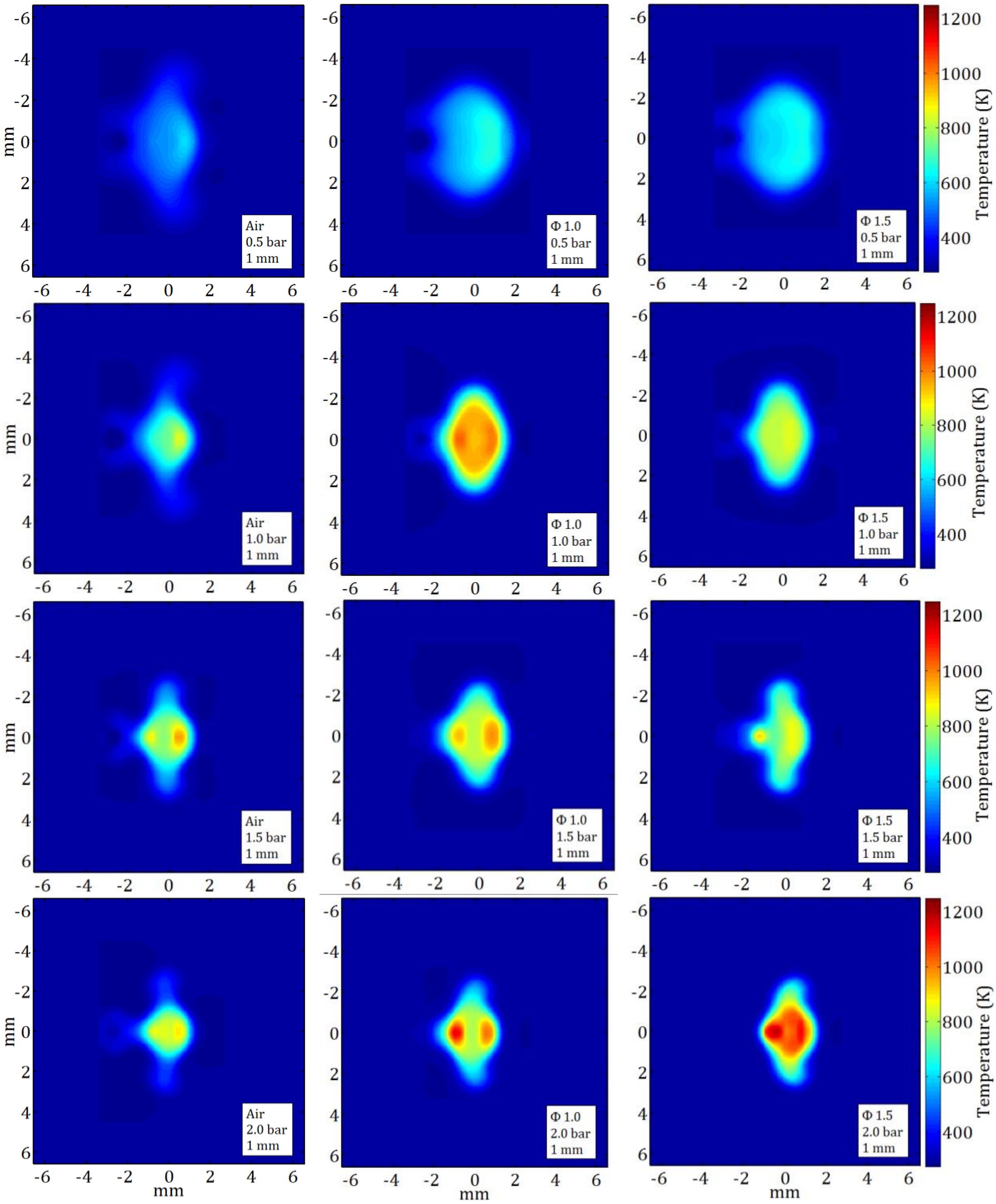

Figure 4-39: Temperature fields for different gases and pressures, 1 mm gap. From left to right: air, C_3H_8-N_2 at Φ_{eq}=1.0 and C_3H_8-N_2 at Φ_{eq}=1.5. From top to bottom, pressure from 0.5 to 2.0 bar.

Overall, average kernel temperature increases with pressure, and is higher in the C_3H_8-N_2 mixtures than in air. At a pressure of 0.5 bar, kernel temperature is below 750 K at the end of the discharge. For higher initial pressures, temperature in the center of the kernel is higher, up to 1200 K at 2 bar for the propane mixtures. Regarding tests at 2.0 bar, a high number of tests were discarded due to asymmetries for both 1 mm and 2 mm gaps.

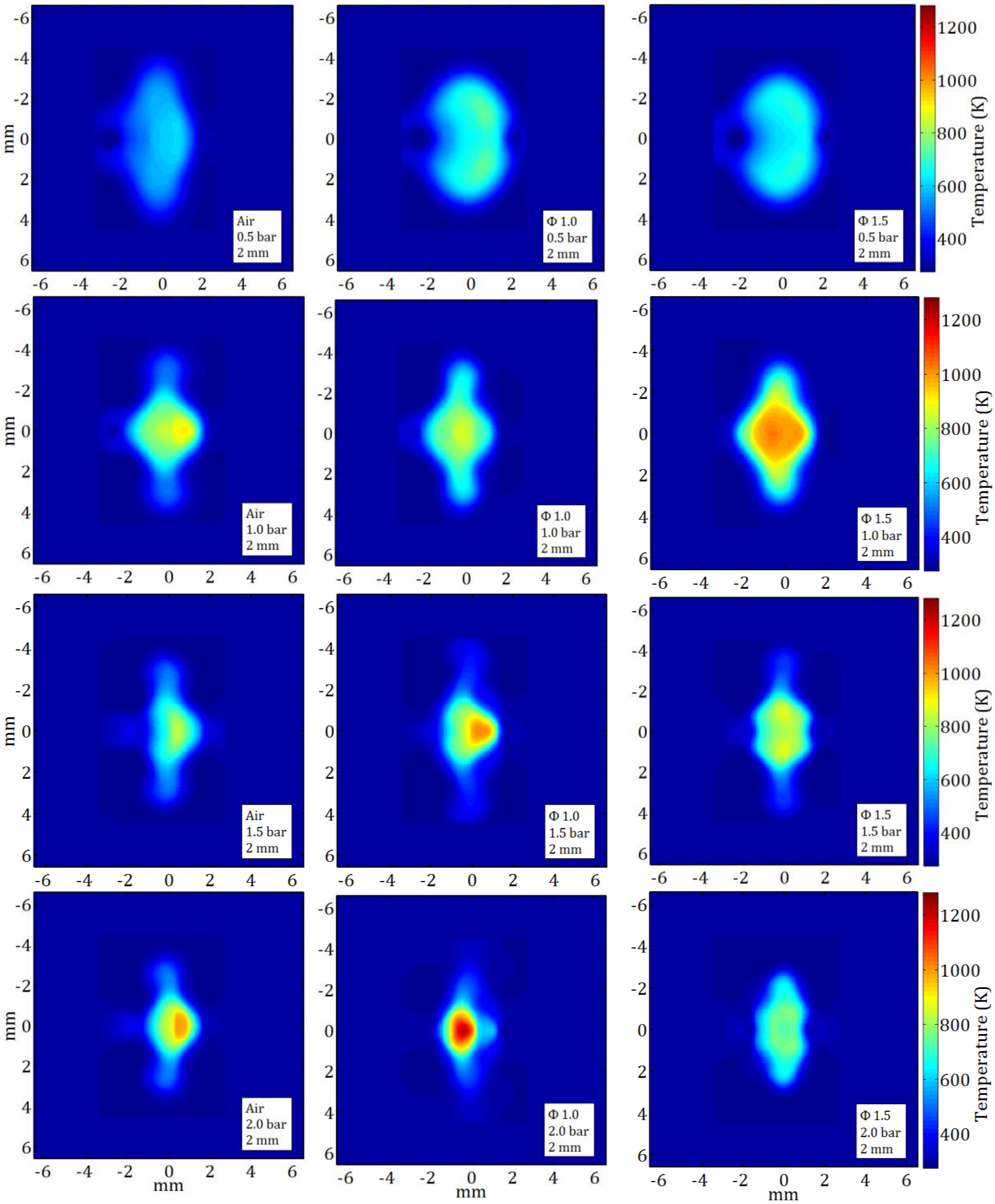

Figure 4-40: Temperature fields for different gases and pressures, 2 mm gap. From left to right: air, C3H8-N2 at Φeq=1.0 and C3H8-N2 at Φeq=1.5. From top to bottom, pressure from 0.5 to 2 bar.

Temperature profiles of the average fields are obtained. Profiles are analyzed for a vertical 0.4 mm width band, averaged along the width (x-axis), as in 4.4.1.1. Results are presented in Figure 4-41, with a color code for different pressures, at 1 mm gap (top figures) and 2 mm gap (bottom figures). The comparison of these profiles confirms the tendency towards higher temperatures at higher initial pressures and in the presence of fuel than in air. However, different profiles correspond to different delay times (end of the discharge in each condition), and in some tests a limited number of axis-symmetric tests were available. This explains why some experiments do not follow the trend evoked above.

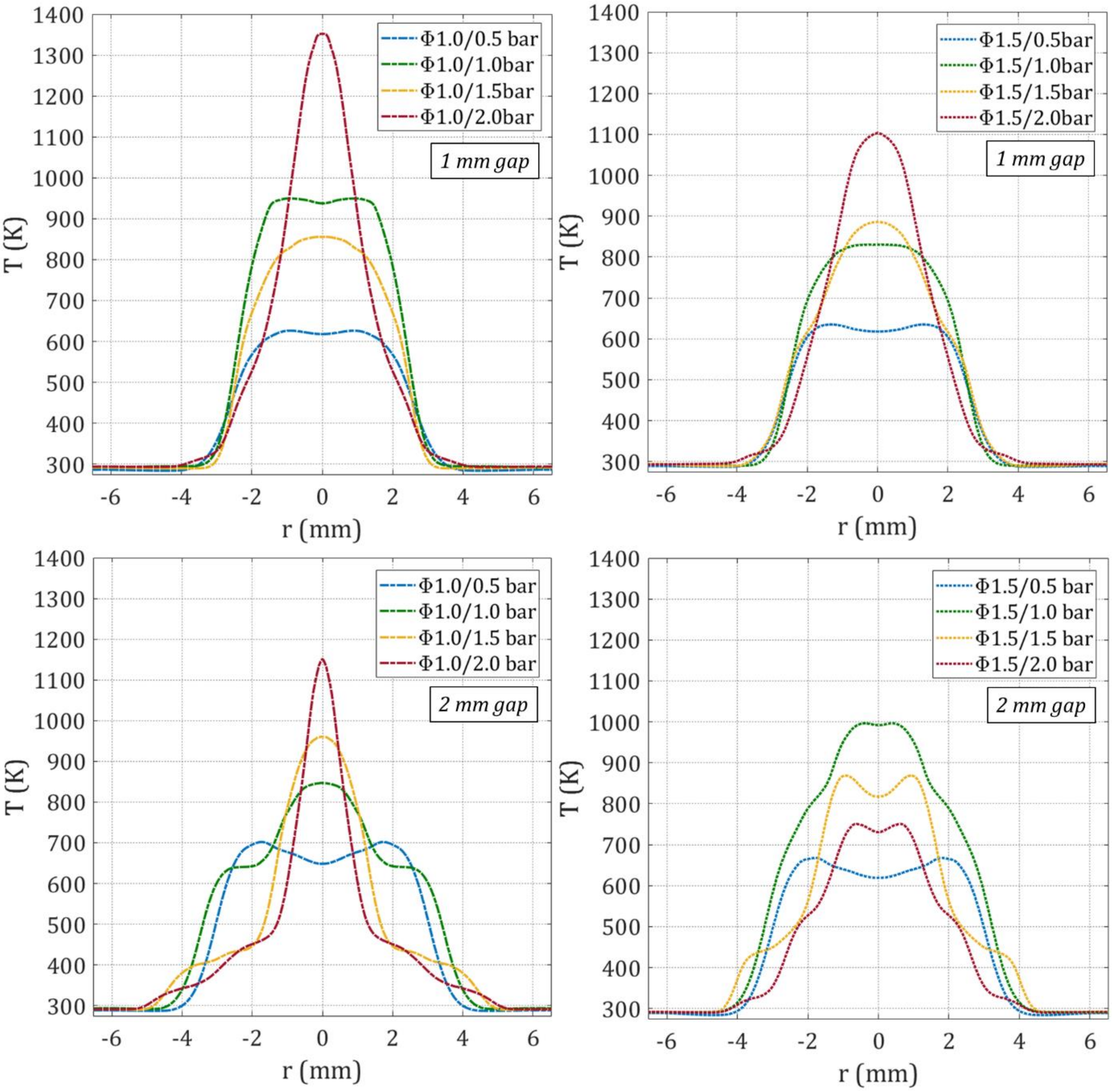

Figure 4-41: Temperature profiles of a vertical band of the central plane at the end of the discharge for different inert mixtures and pressures, for 1 and 2 mm gap.

Kernel maximum radius and volume are estimated for each test from temperature fields. Figure 4-42 represents kernel maximum radius and volume versus pressure, as mean values and standard deviation bars and for the three mixtures (air, C_3H_8-N_2 at $\Phi_{eq}=1.0$, C_3H_8-N_2 at $\Phi_{eq}=1.5$). For a gap of 1 mm, kernel radius decreases with increasing pressure, although for 2 mm gap, radius does not follow a clear tendency: the maximum radius is reached at 1.5 bar – the limited number of post-processed tests may influence this tendency-.

Higher maximum radius only means that the kernel expands more in the radial direction, not that the volume is bigger. By contrast, the kernel volume clearly decreases with pressure, with a nearly linear trend. Gas composition does not significantly affect kernel volume. It is divided by a factor two when pressure rises from 0.5 to 2 bar.

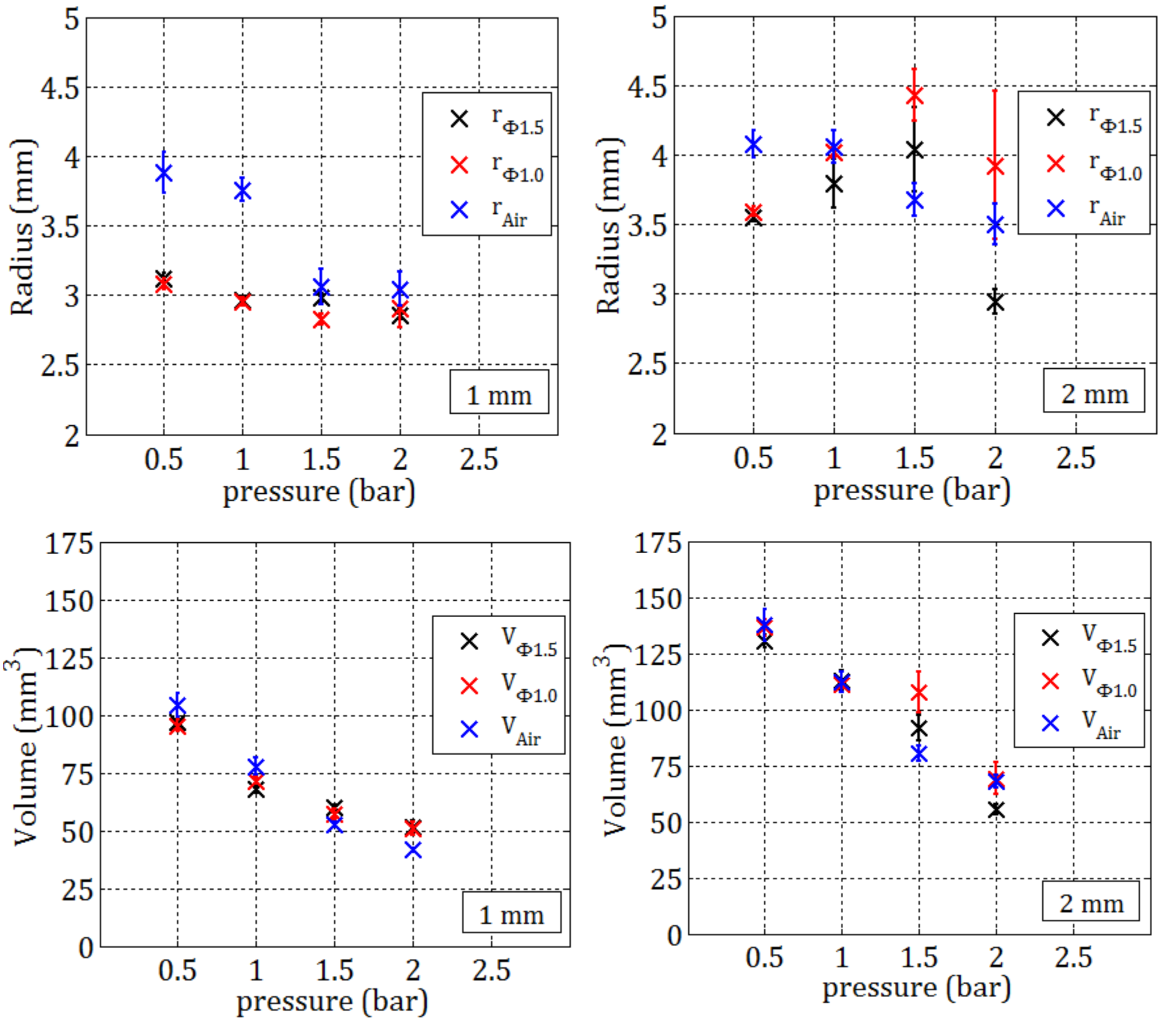

Figure 4-42: Kernel maximum radius and kernel volume, for 1 mm gap (left) and 2 mm gap (right).

4.4.3.3 Energy calculation and comparison with calorimetry

From the temperature distributions we obtain the local enthalpy fields and the energy deposit (E_{BOS}). The energy deposit E_{BOS} is presented versus initial pressure in Figure 4-43, for every gas mixture tested (blue circle for air, red triangle downward for Φ 1 and black triangle upward for Φ 1.5) as whole symbols, as mean value for the valid tests and standard deviation bars. Calorimetry results are also presented in Figure 4-43 as empty symbols, for comparison with SBOS measurements.

One can observe in E_{BOS} results the same tendency as for calorimetry E_{th}: energy deposit is higher with higher pressures, longer gaps and in presence of fuel. Both methods differ up to a 20% of the energy deposit value in some conditions. At 0.5 bar, SBOS underestimates the energy deposit in air (as seen before in 4.4.2.1) and in both propane-nitrogen mixtures. For a pressure of 1 to 2 bar, E_{BOS} is overestimated for all the gas mixtures tested.

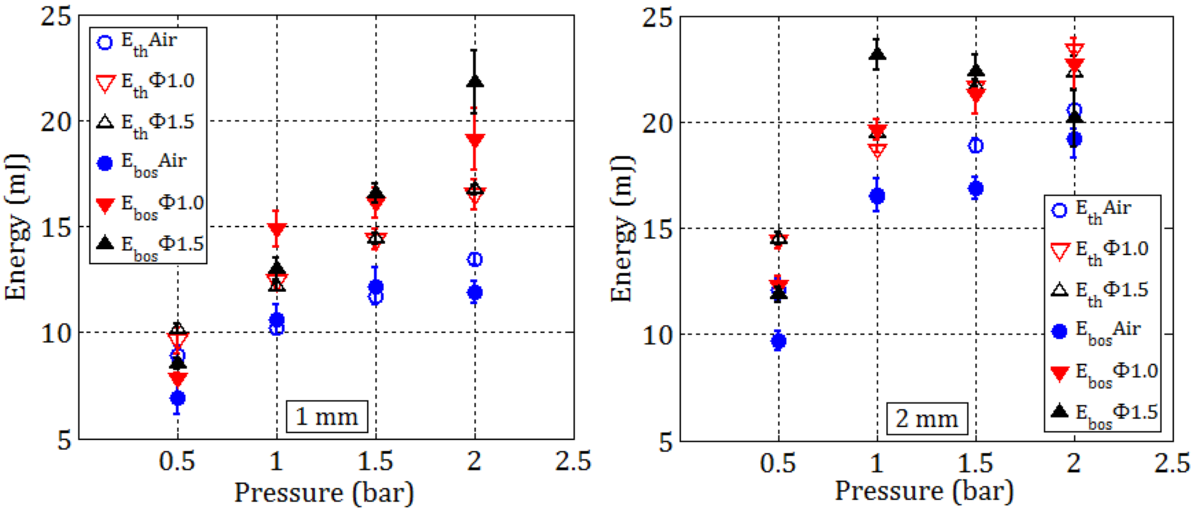

Figure 4-43: Energy deposit measured by SBOS and Calorimetry, comparison for different pressures and gas mixtures.

Figure 4-44 represents the same measurements separately for each gas and gap.

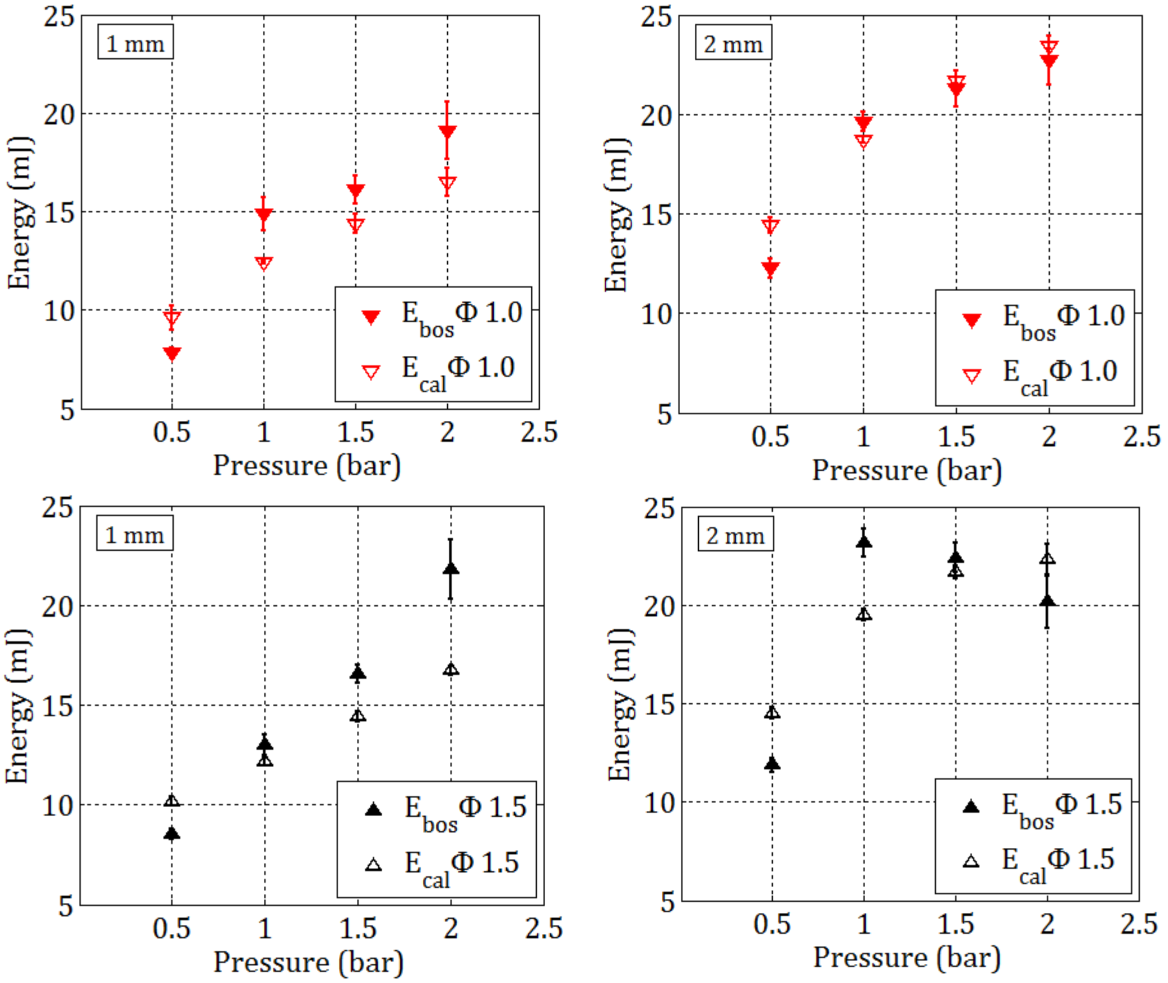

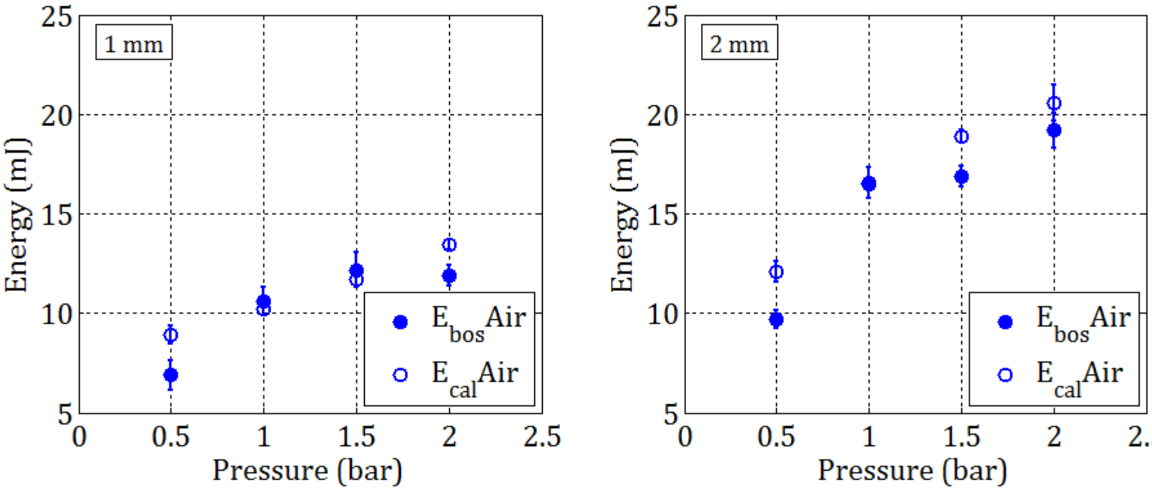

Figure 4-44: Energy deposit measured by SBOS and calorimetry, comparison for different pressures and gas mixtures

The maximum deviation of the energy deposit values measured by SBOS (E_{BOS}) deviate from the expected values (E_{th}) up to a 20%. Asymmetries, 3D effects and the multi-step image processing affect this measurement through the intermediate results; i.e., the refractive index, density or temperature fields. For each test, the difference between the energy deposit measured by SBOS and by calorimetry is calculated. Taking as reference the calorimetry result (E_{th}), this difference is defined as

$$\frac{\Delta E}{E} = \frac{|E_{th} - E_{bos}|}{E_{th}} \tag{4.35}$$

Figure 4-45 shows the energy deposit difference for each experimental condition, as the mean value and standard deviation bars of each set of tests. In the best cases, the energy difference is lower than $5 \pm 3\%$, as in air at 1 bar. In the worst scenario found, for a 1 mm gap, $\Phi = 1.0$, this difference is of 30 ±8%. In average, for the 233 analyzed results, the energy deposit difference is of 12.8 ± 8.6%.

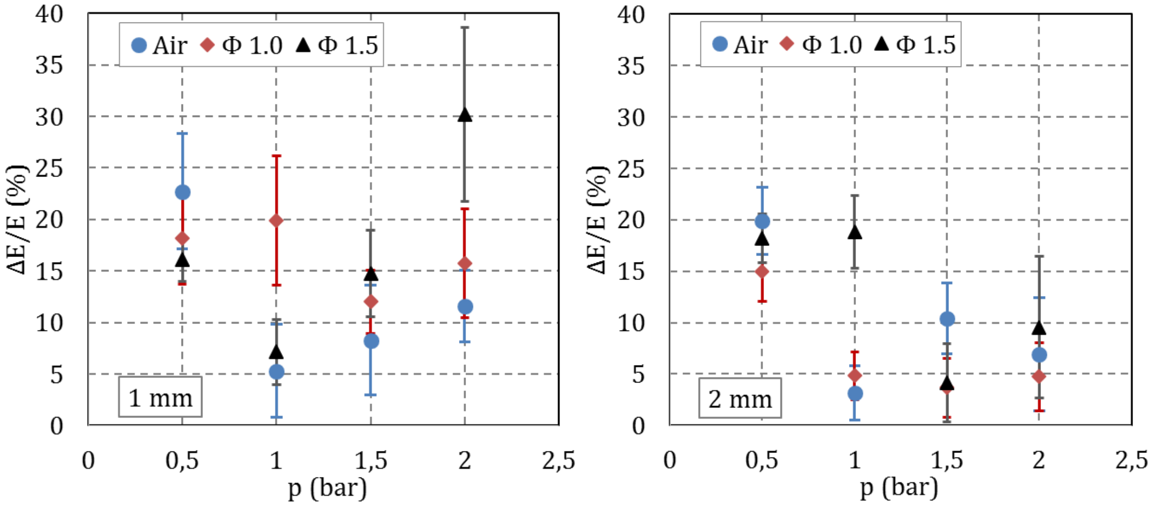

Figure 4-45: Relative difference in energy deposit measurement, between SBOS and pressure rise calorimetry. Left: 1 mm gap, right, 2 mm gap.

The estimated uncertainty for the method applied to the CO_2 jet is 6.2% (see 4.3.2). This value is lower than the obtained deviation. That result is obtained in quasi-stationary conditions, from the results of 100 tests and the same jet of CO_2. When applied to electrical discharges, kernel presents slightly different shapes in each test, sometimes developing 3D structures or not perfectly symmetric structures. The unsteady nature of the phenomena under study; using only one test image per discharge; and the stochastic variations in electrical discharges explain the higher variability in the measurements.

4.5 Conclusion

We adapted the Speckle-based Background-Oriented Schlieren technique to the study of electrical discharges. BOS technique is based on the dependence of the gas density on the refractive index, as given by the Gladstone-Dale relation for gases. The points of a background pattern displace when there are density gradients between the background and the observer camera. This is observed if the phenomenon producing the density gradient is at a defocusing distance away from the focal plane. This displacement is calculated by a multi-pass cross-correlation between a reference image of the background pattern and a test image during a phenomenon involving density gradients. The use of a laser-generated speckle pattern background improves resolution, especially in small applications, such as the electrical discharges.

The image processing is adapted to electrical discharges: speckle generation with the right speckle pattern size, and image acquisition at the desired delay, controlled by WinView32. Then the displacement field is obtained by cross-correlation with a reference image, by DaVis program. Using Matlab®, the displacement field is integrated, solving a Poisson equation, to obtain the density integrated along the line of sight. For axisymmetric fields, then a filtered backprojection yields the density field. For a semi-ideal gas behavior, temperature field is obtained directly from density field, and then the local enthalpy distribution is evaluated. The discharge hot kernel size is estimated from the temperature field, and in particular its maximum radius and its volume. Finally, the volume integral of the enthalpy distribution yields the energy deposit, as the total enthalpy increase from initial conditions.

The methodology is validated for a reference case: a jet of CO_2 with the same size and absolute density gradients as those expected in electrical discharges. A set of 100 tests are performed on the jet, obtaining the displacement fields and density distributions. As in the center of the jet the density should be that of CO_2, the results are compared to this value. The analysis of the influence of different parameters and measurement uncertainties, together with a temporal averaging of the results, yield an uncertainty of 6.2%.

The SBOS technique is then applied to electrical discharges. Tests in atmospheric conditions (in air at 1 bar) show that for a higher gap, the kernel temperature at the end of the discharge is higher, and kernel size is bigger. The energy deposit calculated for these results is also higher for higher gap. Kernel evolution is studied also, with series of tests at 0.5 to 2.5 ms after the discharge onset, and a 2 mm gap. The kernel temperature is higher at the first instants of the discharge, and the kernel cools down as it expands. It expands faster at the first moments of the discharge than later on, as diffusion rules the kernel expansion, although there is great influence of the convective transport induced by the initial shockwave. The energy deposit increases up to its maximum value at the end of the discharge. SBOS results for energy deposit evolution are compared to those of calorimetry measurements, performed simultaneously. In this first series of experiments, SBOS overestimates the energy deposit results, but they follow the same tendency over time.

Test in air are completed by changing the initial pressure, from 0.5 to 2.0 bar. The defocusing distance of the setup is adapted at each pressure to obtain an adequate displacement. The hot kernel temperature increases with pressure, as well as the energy deposit. The kernel volume decreases for higher pressures though, which is explained by the higher density: at 2.0 bar the kernel volume is half of the kernel volume at 0.5 bar.

Finally the influence of the presence of fuel is studied. Propane-nitrogen mixtures, at 0.04 and 0.06 mole fractions, are tested for 1 mm and 2 mm gap and initial pressures of 0.5 to 2.0 bar. The Gladstone-Dale constants of the different mixtures are obtained first. Tests are performed in 8 different conditions (2 gap distances and 4 initial pressures), for both gas mixtures.

For higher pressures, temperature reaches higher values than the same discharges in air, without an appreciable difference with propane concentration. Repeatability of the discharges is lower at higher pressures in the presence of propane, with a higher proportion of asymmetric kernel distributions and 3D structures, therefore discarding those tests for SBOS treatment. Kernel size decreases linearly with pressure. Gas composition does not significantly affect the kernel volume, although high variability in maximum radius is observed, as a result of differences in the kernel shapes.

The energy deposit is estimated for the different propane mixtures, and together with results in air these results are compared to results from simultaneous measurements by calorimetry. Both SBOS and calorimetry data show the same trend: energy deposit is higher for longer gap distances and higher pressure, and it increases in the presence of fuel. From a quantitative point of view, the two energy measurement techniques differ on average by 13%, which is within the range of uncertainties cumulated for the two methods.

Chapter 5

Experimental characterization of different ignition systems

Contents

5 Experimental characterization of different ignition systems

In this chapter we aim at characterizing contemporary ignition systems using the experimental techniques developed in previous chapters.

First, a helicopter engine igniter is studied by calorimetry, it allows a global measurement of the energy deposit. The experimental setup and method are adapted to the ignition system, and then the energy transfer is characterized by calorimetry. Second, the helicopter engine is studied by SBOS. The optical setup and data processing are adjusted to this kind of discharge, yielding spatial and instantaneous information. Last, we study a radio-frequency spark plug, a promising ignition system which is currently under development.

5.1 Helicopter engine igniter: calorimetry

The Ardiden 3 helicopter engine is equipped with a pair of surface-discharge igniters. This igniter produces a discharge periodically during engine ignition, at a rate of 2 to 5 Hz for several seconds. This kind of systems are usually described by the energy input they use, from 1 to 10 J depending on the engine (1-2 J for helicopter gas turbines, 10 J for higher power-turbojets). This energy is distributed to the electronic circuit and the spark plugs. A part of that energy is lost in the way to the electrodes. The energy delivered to the electrodes and to the fluid are typically in the order of hundreds of mJ [18], [19], [36].

Spark plugs in surface-discharge igniter configuration produce a fast discharge, with a duration in the order (100 μs), and high power. The discharge kernel is projected away from the igniter and the chamber wall, towards the center of the combustion chamber where conditions are better for mixture ignition.

Despite their extensive use in the aeronautic industry, we only find few studies about real aircraft igniters (c.f. §1.2.3.3.2). Our aim is to characterize the igniter discharge by calorimetry, to gain better understanding of the global energy remaining in the fluid and the efficiency of the energy transfer.

The electrical discharge produced by the aeronautic igniter differs from the case studied in previous chapters: electrode geometry is different, the discharge is shorter and the energy supply is in the order of ten times higher. First, we adapt the calorimetry method to the igniter and the discharge, and then we perform experiments in different conditions.

5.1.1 Adaptation of pressure rise calorimetry and electrical measurements

First, we adapt the measurement apparatus to the characteristics of the aeronautic igniter discharge (described in Chapter 2). Electrical signals from the studies of Sforzo [18] and George

[36] give an estimate of the electrical voltage and intensity that we will find during the discharge, as represented in Figure 5-1.

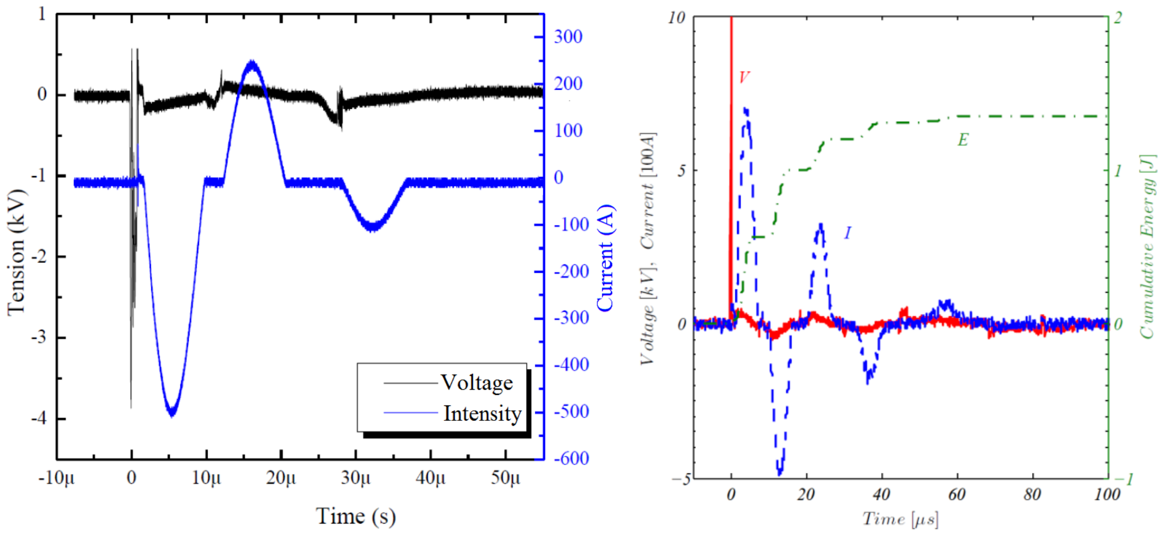

Figure 5-1: Characteristic electric signals for an aircraft igniter, George [36](left), Sforzo [18](right).

During the discharge, voltage peaks at up to 10 kV. The spark plug that will be employed in this study regulates breakdown voltage using a semi-conductive layer at the inter-electrode isolation, so maximum peak voltage is expected to be lower than in the electrical signals from other studies (as in the aforementioned studies there is no semi-conductive layer). The same probe used for the pin-to-pin electrodes discharge, the Tektronix P6015A, is appropriate for the measurement of this voltage signal. Maximum electrical current reaches 750 A during the discharge from Sforzo, so we will use a current probe with a high maximum current peak, the Pearson current monitor model 101.

A coaxial cable connects the igniter to the electric controller. This impedes direct electrical measurements: voltage probes require access to the high voltage electrode and mass electrode separately; and current probes work by Lenz's law, measuring changes in the electrical flux through the probe section, which remains constant in the case of a coaxial cable -as current is transferred in opposite ways inside the coaxial cable-.

To measure electrical voltage and current we placed an adaptive part between the igniter and the coaxial cable. A copper rod, isolated by a POM-C case, connects the high voltage electrode with its cable. A mass cable connects the mass electrode to the coaxial cable corresponding part. This setup is shown in Figure 5-2.

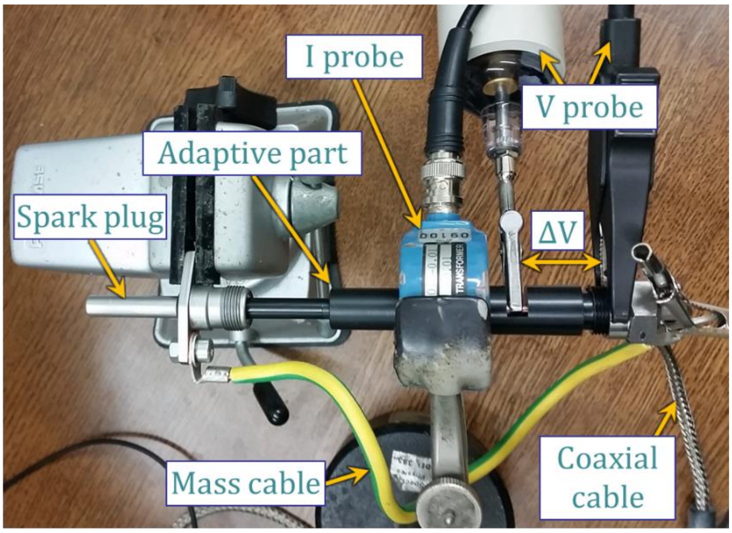

Figure 5-2: Ardiden 3 spark plug and connector adaptive part.

Regarding calorimetry measurements, we perform a set of preliminary tests to estimate the energy deposit and the pressure rise characteristics, as discussed next.

5.1.1.1 Preliminary tests - 60 ml chamber.

Sforzo [124] estimated the igniter used in his study to have a high efficiency, based on the electrical energy analysis: half of the discharge electrical energy is supplied to the spark plug in (10 μs). Initially we considered a 500 mJ thermal energy deposit, then the chamber volume that suits well our pressure transducer is of 60 ml, as detailed in Chapter 2.

We first estimate the energy deposit in a cylindrical polycarbonate plastic chamber (50 mm x Ø 40 mm). The cylinder base is pierced to hold the pressure transducer, and the cover is adapted to the igniter cylindrical head. The volume is measured by filling the closed chamber with water from a calibrated syringe, through the pressure transducer hole, which yields 63 ml. The chamber is depicted in Figure 5-3.

Figure 5-3: Atmospheric chamber for preliminary tests with different adaptive covers.

From calorimetry, we obtain the differential pressure signal during the discharge, filtered by the 10 kHz low-pass filter integrated in the signal amplifier. The filtered pressure signal presents high amplitude oscillations. An analysis of the Fourier spectrum of the pressure signal identifies the oscillations main frequency as 3.4 kHz. Acoustic waves resonating in the chamber produce these oscillations, as it is estimated in equation (5.1) from the sound speed in air at the test conditions (293 K) and twice the chamber length (considering the total distance the soundwave travels before arriving back at the pressure transducer). Figure 5-4 represents the pressure signal for a single test, and its Fourier single-sided amplitude spectrum on the right.

$$f = \frac{\sqrt{\gamma RT}}{l} = \frac{\sqrt{1.4 \cdot 287 \cdot 293}}{2 \cdot 50 \cdot 10^{-3}} \sim 3.43\ kHz \tag{5.1}$$

In the previous study, for pin-to-pin electrodes, the pressure wave produced is weaker and it is damped faster, allowing for a transient pressure measurement during the discharge time. For the aeronautical igniter we cannot measure the pressure rise during the discharge, due to the shorter discharge time, in $\mathcal{O}$(100 μs), and the intense oscillations produced by the strong shockwave and posterior pressure waves.

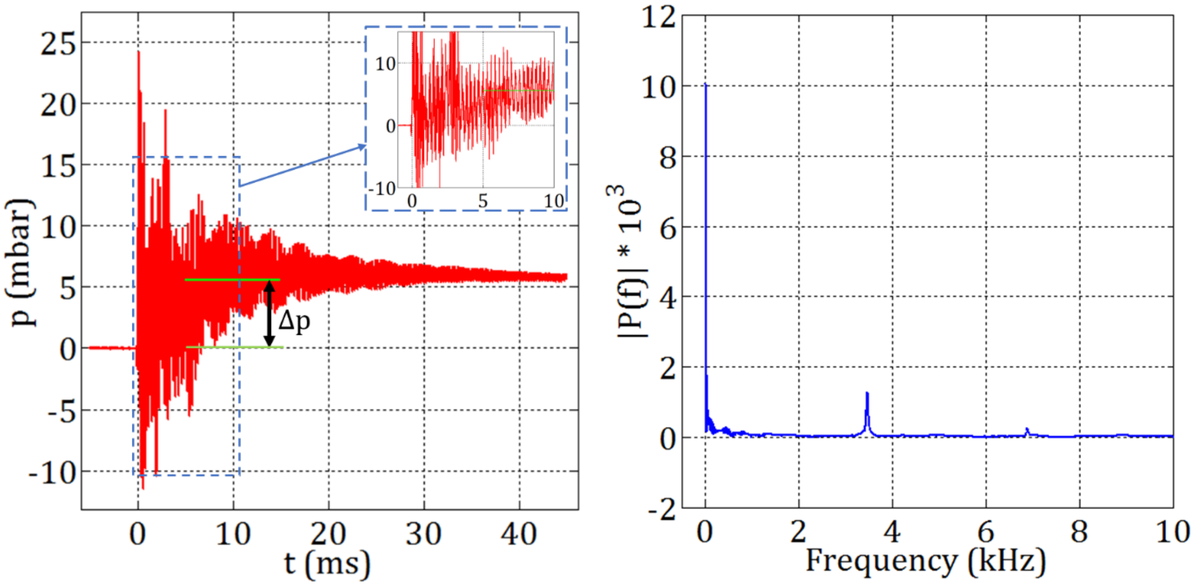

Figure 5-4: Differential pressure signal from an aeronautic igniter discharge in a 63 ml chamber (left) and its single-sided amplitude spectrum from the Fourier transform (right).

Even if temporal tracking of the differential pressure increase is not possible, the energy deposit E_{th} is estimated from the pressure difference after and before the discharge. The final pressure is taken as the mean pressure a few milliseconds after the discharge start, when acoustic oscillations are weaker. This pressure difference Δp is represented with green levels in Figure 5-4. For this single test, $\Delta p = 5.5\ mbar$, which yields an energy deposit $E_{th} = 87\ mJ$.

From a set of 90 tests, the average energy deposit is $E_{th} = 83.6 \pm 7.8\ mJ$ (± one std). This value is much lower than expected. The experimental chamber for the final calorimetry-SBOS setup is dimensioned accordingly, with a volume of 20 ml. The uncertainty of the chain of measurement is lower than 6.4% for the 20 ml volume and an energy deposit of 100 mJ (as in Figure 2-4 in

Chapter 2), and below 7.5% for a 85 mJ deposit. A protective disc of porous material is placed before the pressure transducer to protect it against the initial shockwave and help dampening the acoustic resonations. The protective disc does not affect the global pressure increase in the chamber, as it is verified comparing tests with and without the protection.

5.1.2 Results and discussion

The Ardiden 3 engine igniter is tested first at atmospheric conditions, then at different initial pressures in air, and finally at different initial pressures in nitrogen-propane mixtures. We employed the calorimetry setup described in §2 and presented in Figure 5-5, which includes the 20 ml chamber (Ø 32 mm x 25 mm) (detailed on the right of the figure).

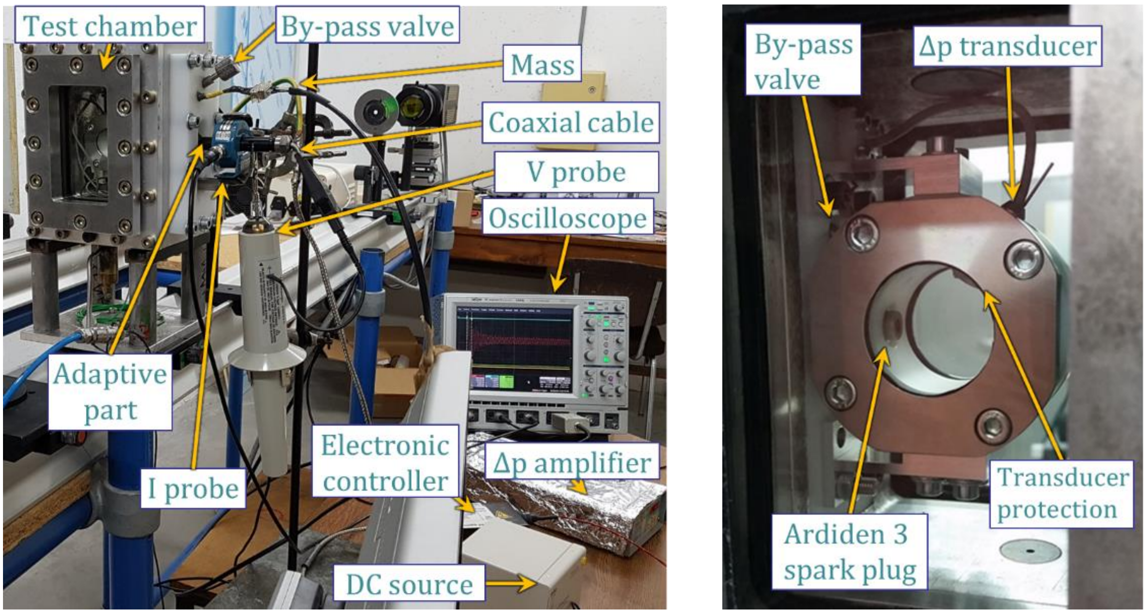

Figure 5-5: Calorimetry setup adapted to the Ardiden 3 engine igniter (left) and detail on the 20 ml chamber (right).

5.1.2.1 Atmospheric tests

To characterize the Ardiden 3 igniter we performed first a set of tests in air at atmospheric conditions of pressure and temperature (1 bar, 293 K). The chamber volume is estimated to be 19.6 ml, considering the spark plug tip and the pressure transducer protection (porous material) volumes. Differential pressure signal is presented in Figure 5-6, together with its frequency response or amplitude spectrum:

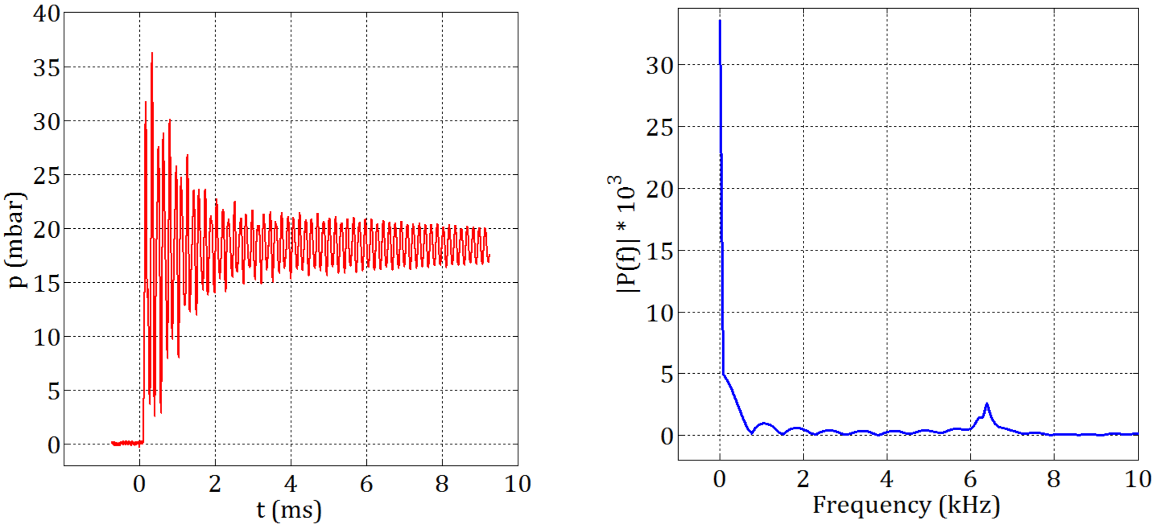

Figure 5-6: Differential pressure signal (left) and single-sided amplitude spectrum of p(t).

Acoustic resonance in this chamber oscillates at around 6.3 kHz. This corresponds to the chamber size, Ø 32 mm x 25 mm, although the simple estimation with the diameter as in equation (5.1) is not valid in this case: following equation (5.1) the resonance frequency of 6.3 kHz corresponds to a linear distance of 2x27 mm, shorter than the opposing wall (2x Ø). Pressure transducer is placed on the cylindrical wall, so the cylindrical geometry causes 3D reflections of the shockwave, which explains the difference in the obtained resonance frequency.

We filtered the signal by suppressing frequencies over 4 kHz at the Fourier transform and performing the inversed transform. Resulting filtered pressure signal and the filtered transformed are represented in Figure 5-7. The final pressure is taken as the average differential pressure for a 1 ms window, 3 ms after discharge onset, which is represented as a green level in the figure. This value equals the value of the filtered pressure in that moment (it differs in a 1%), so it is a valid estimate with lower processing cost than the Fourier filtering. The pressure increase for this test is $\Delta p = 18.4\,mbar$, which for the $19.6\,ml$ volume yields $E_{th} = 90.4\,mJ$.

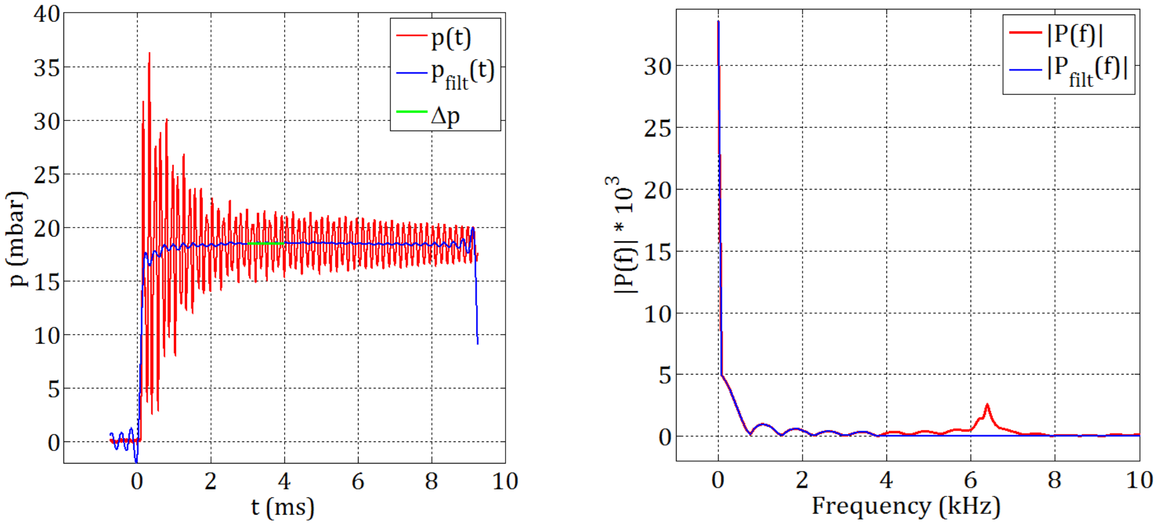

Figure 5-7: Pressure signal, pressure filtered by Fourier low pass at 4 kHz, and the averaged final pressure (left). Amplitude spectrum of the signal and filtered spectrum (right).

If we superimpose the electrical signals U and V, one can see the different time scale that we require for signal analysis. Figure 5-8 represents the three signals in the pressure rise timescale (on the left of the figure) and in the discharge timescale (on the right). The discharge lasts less than 250 µs, from the breakdown peak until electrical power zeroes. The shockwave arrives to the pressure transducer at $t = 100\ \mu s$ and bounces on the chamber walls, and the discharge ends before a mean pressure rise can be appreciated.

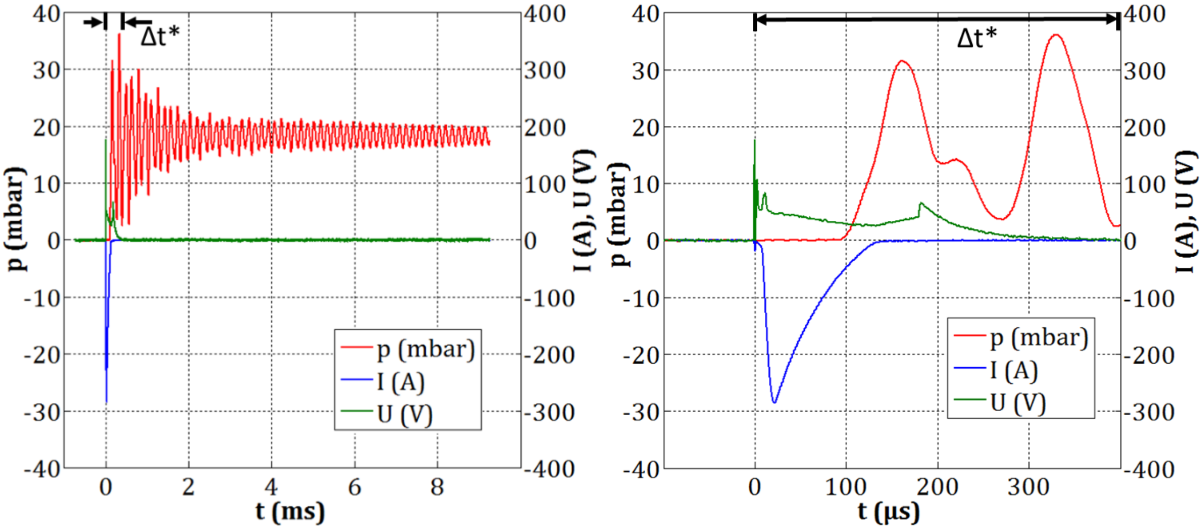

Figure 5-8: Pressure, intensity and current signals for the aeronautic igniter. Left: timescale of pressure registering. Right: timescale of the discharge duration.

The electrical signals are presented on Figure 5-9: the electrical current, inverted for clarity (left) and the electrical voltage. The electrical voltage sampling frequency is too low to record properly the several hundred V-breakdown peak, but for the calculation of E_{el}, the low intensity value during breakdown compensates this effect, as few millijoules supplied during breakdown are negligible compared to the final value of E_{el}, 625 mJ. The electrical energy E_{el} is presented in Figure 5-10 (left), together with electric power (right), with a maximum power of 13.5 kW for this discharge. Total electrical energy is taken at the end of the discharge, at 250 µs, when current is almost zero and power is low. We measure the electrical energy E_{el} over time and compare the final E_{el} value with the global thermal energy deposit E_{th} to obtain the energy transfer efficiency, which is $\eta = 14\%$ for this test.

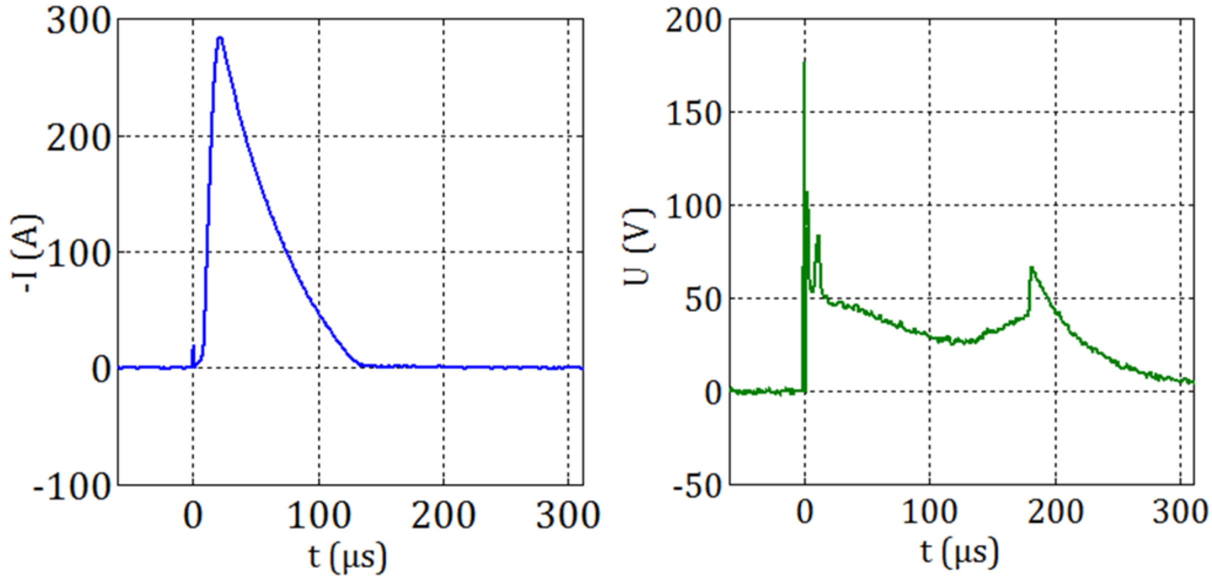

Figure 5-9: Electrical signals: Intensity (inversed, left) and Voltage (right).

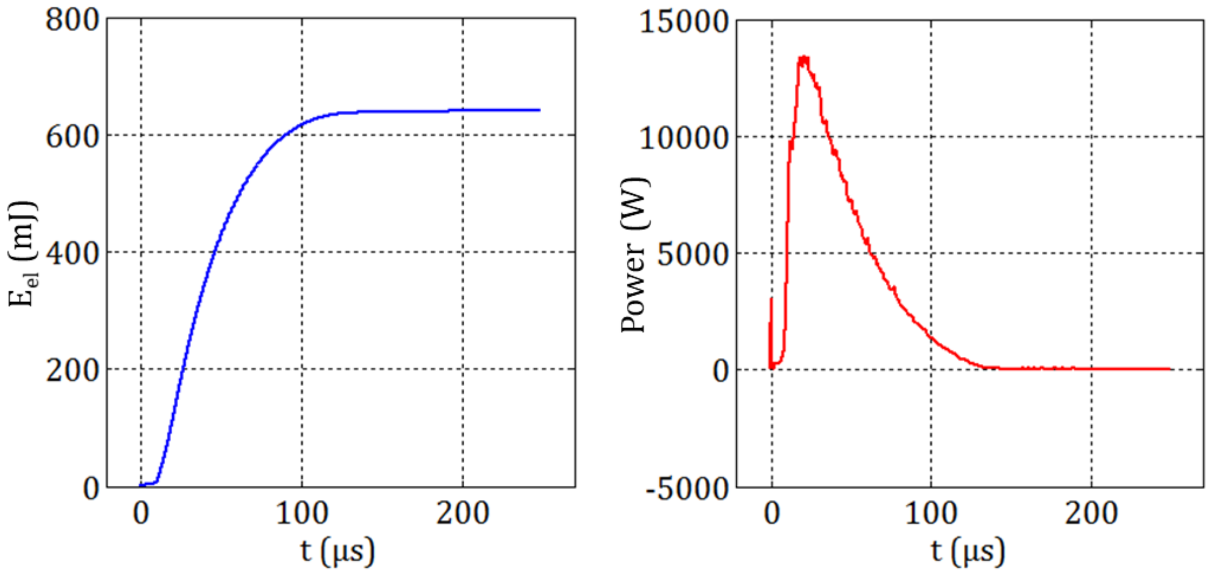

Figure 5-10: Electric energy E_{el} (left) and electric power (right).

A set of 45 tests in the same experimental conditions yields the mean and standard deviation values for $E_{el} = 624 \pm 49\, mJ$, $E_{th} = 85 \pm 7\, mJ$, and $\eta = 13.7 \pm 0.4\%$. The results for each test are presented on Figure 5-11. We observe that there is relatively high dispersion on E_{el} and E_{th} values, with a standard deviation around 8% of the energy values (49 *mJ* for E_{el} and 7 *mJ* for E_{th}), but efficiency is more stable with a deviation of 3% of the total value. This dispersion is due to the stochastic nature of electrical discharges, with microscopic differences in the surface of the electrodes between consecutive discharges and the statistical nature of the formation of the plasma channel.

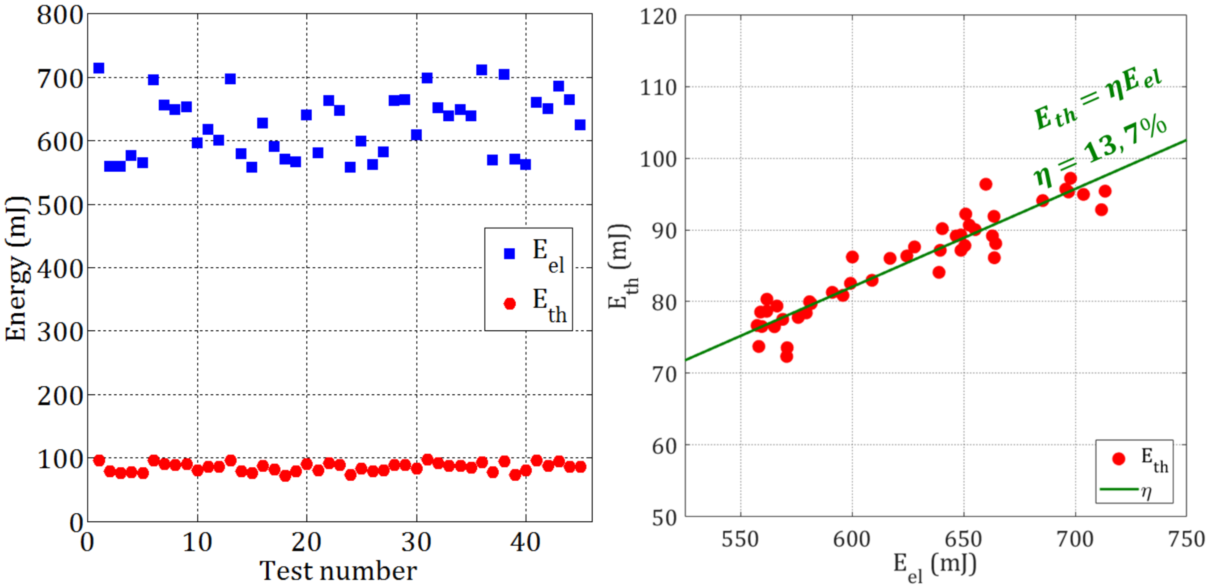

Figure 5-11: Aeronautic igniter results in atmospheric conditions, electrical and thermal energies (left) and efficiency (right).

The resulting values for the energy deposit and efficiency represent the first calorimetry measurements in this kind of igniter. The energy transfer efficiency is relatively low, in spite of the discharge short duration, which contradicts the hypothesis from Sforzo et al. [124]. The low efficiency is not an issue in the helicopter engine, as this system presents also advantages, such as the dynamic effect produced by expelling the discharge kernel away from the igniter electrodes, and therefore further from the combustion chamber walls towards the center of the chamber.

5.1.2.2 Tests in air at different initial pressures

For the next step in our study we perform tests at different pressures. This presents gas conditions closer to the ones present during engine ignition: an initial pressure ranging from 0.25 to 2.0 bar represents gas density from 0.3 to 2.4 kg/m^3, as in aircraft engine in normal ignition (higher density) and in-flight re-ignition (low density) conditions.

Series of 8 tests for each initial pressure from 0.25 to 2 bar represent the igniter performance in each case. The associated results are reported in Figure 5-12, for E_{el} and E_{th} on the left, E_{th} in the middle graph and η on the right graph, as mean values with standard deviation bars.

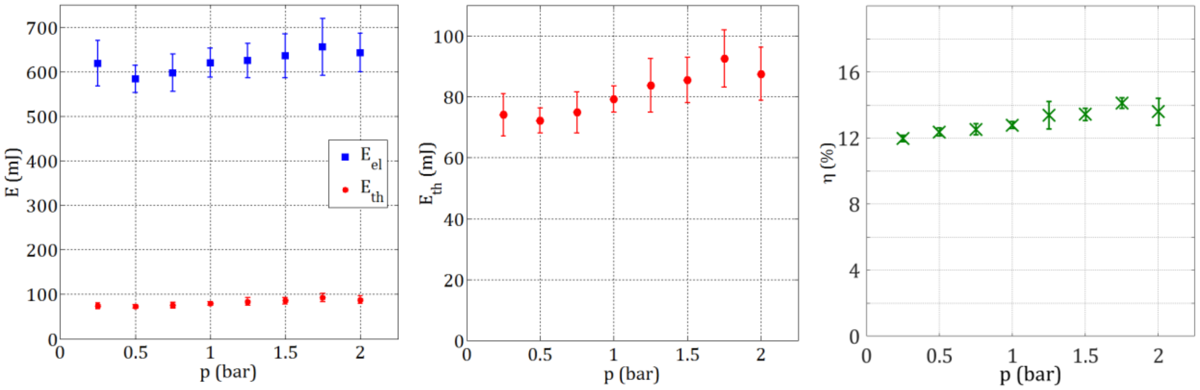

Figure 5-12: E_{el}, E_{th} and η vs pressure, as mean value with standard deviation bars.

There is some dispersion of the results, with data for energy supply and deposit superimposed for different pressures: in some tests both E_{el} and E_{th} are higher at 0.25 bar than at 2 bar. However, one can appreciate that globally E_{th} tends to increase for higher pressures, as the average increases from around 70 mJ at 0.25 bar to around 88 mJ at 2.0 bar. Efficiency rises also, in the order of 2%, from 12% at 0.25 bar up to close to 14% at 2 bar and with less deviation from the average. One can observe that for 1 bar we find a slightly lower average E_{th} than in previous tests (c.f. the previous section, 5.1.2.1), which is explained by the lower size of the sample (8 tests instead of 45) and high variability.

Compared to the pin-to-pin electrodes discharge, the aeronautic igniter behavior is very little affected by the pressure changes, as energies - both E_{el} and E_{th}- vary less than a 12% of their values from the extremes of 0.25 and 2.0 bar, with a variation in efficiency lower than 2% on average. For the pin-to-pin electrodes, energy deposit increases from 8 mJ at 0.5 bar to 12 mJ at 2.0 bar in air and a 2 mm gap (an increase of 50% of the initial value), and efficiency from 16% to 29% (a variation of ~200% of the initial efficiency). This difference in behavior is due to the presence of the semi-conductive layer that lowers and regulates breakdown voltage for the aeronautic igniter.

5.1.2.3 Experiments for different gases at different pressures.

The discharge characteristics can be different in the presence of fuel, as seen in Chapter 3. Additional tests are performed with the Ardiden 3 igniter to study this effect, in inert nitrogen-propane gas mixtures. As in chapter 3, the gas mixtures are equivalent to a stoichiometric and a rich air-propane mixtures, with $\Phi_{eq}=1.0$ and $\Phi_{eq}=1.5$ respectively. We perform series of 10 tests at four different initial pressures, from 0.5 to 2.0 bar, for both gas mixtures. Results for E_{el}, E_{th} and η are represented as mean values with standard deviation bars in Figure 5-13, for $\Phi_{eq}1.5$ in the top row and $\Phi_{eq}1.0$ in the bottom, and from left to right energies (E_{el} and E_{th}), then a zoom on E_{th}, and finally discharge efficiency η.

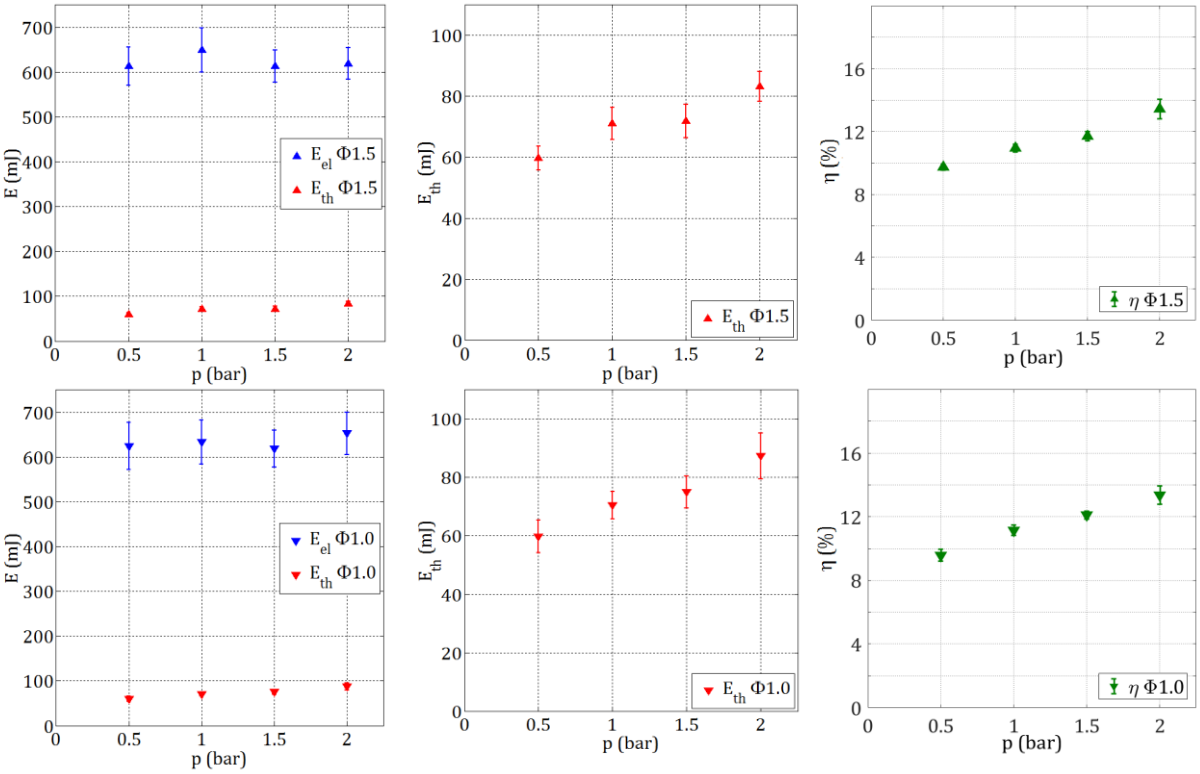

Figure 5-13: Energy results in presence of fuel at different pressures, for $\Phi_{eq}1.5$ (top) and $\Phi_{eq}1.0$ (bottom), and graphs for E_{el} (top), E_{th} (middle) and η (right).

Electrical energy (E_{el}) is almost identical in air and in propane-nitrogen mixtures for the range of pressures tested. The energy deposited by this igniter (E_{th}) is lower in presence of fuel than in air at lower pressures: at 0.5 bar the average of E_{th} equals 60 mJ in the propane mixtures while it is 73 mJ in air. The energy transfer efficiency η is thus lower in the presence of fuel than in air for lower pressures, with values lower than 10% at 0.5 bar. There is no appreciable difference between results for both propane concentrations tested.

The presence of fuel affects differently the aeronautical igniter than the pin-to-pin electrodes discharge. It can be noticed E_{th} and η are lower than in air, while the contrary was measured with the pin-to-pin electrodes discharge. This is due to the different discharge regime, as this is a high-energy fast discharge. Also, there are no changes in discharge phase composition with experimental conditions, as we can only observe breakdown and arc phases during the discharge. In the pin-to-pin electrodes setup, changes in discharge phases proportion and in breakdown energy with experimental conditions affected the discharge. The helicopter ignition system regulates breakdown voltage with a semi-conductive layer on the spark plug, and presents similar electrical characteristics of the discharge in different conditions. For the aeronautical igniter E_{th} and η are higher in air than in presence of fuel.

5.1.2.4 Helicopter igniter – Eyquem

Another model of helicopter igniter is tested. This igniter, produced by Eyquem, is exactly the one used by R. George [36]. The main differences with the Ardiden 3 engine igniter are: (i) the igniter spark plug does not use a semi-conductive layer to lower the breakdown voltage; and (ii) the alternating polarization electrical current and voltage. The igniter generator (Eyquem - HEP 502 T2) has an input power of 2 J. The experimental setup employed for testing this igniter is depicted in Figure 5-14.

Electrical signals, U and I, are plotted in Figure 5-15, together with the electrical energy measured at the igniter electrodes (E_{el}) on the right. Electrical voltage and current alternate between positive and negative values for this igniter, with a positive power output meanwhile. The total E_{el} at the end of the discharge for the test shown is 697 mJ.

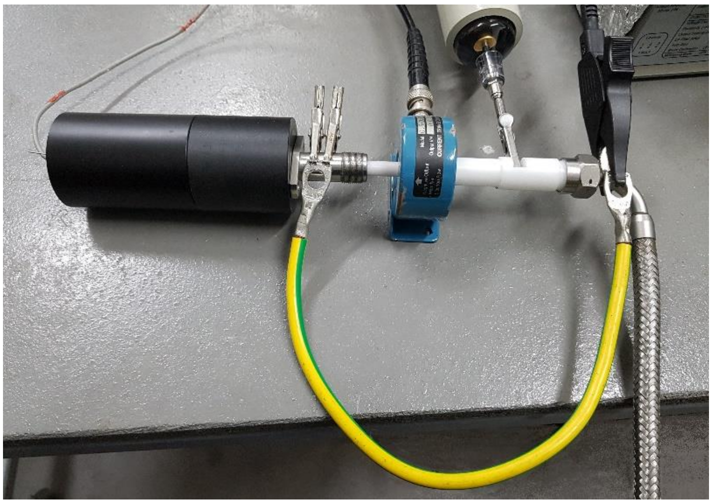

Figure 5-14: Atmospheric test with aeronautical igniter in a 60 ml chamber.

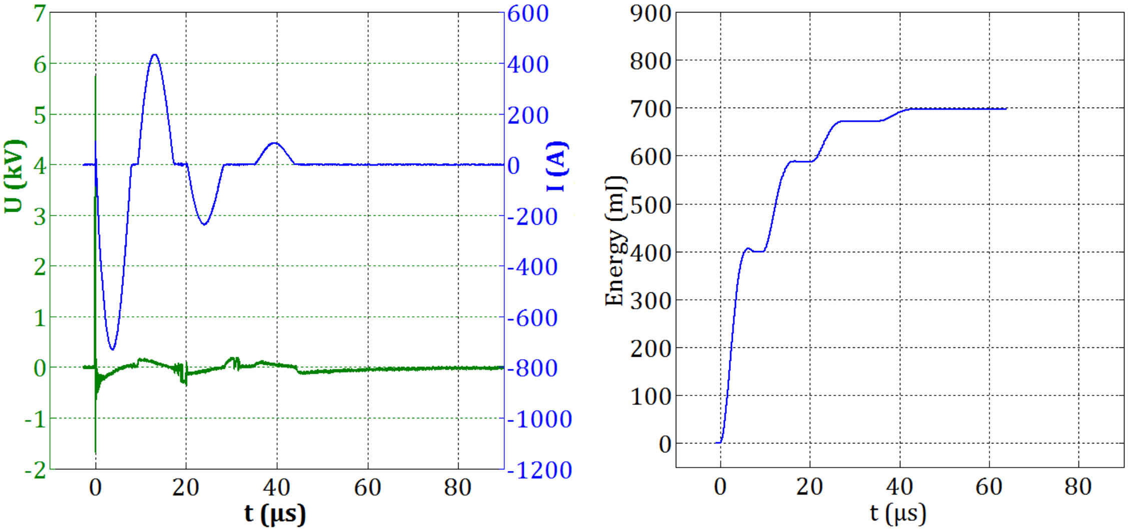

Figure 5-15: Electrical signals and E_{el} for the Eyquem helicopter igniter, in air and atmospheric conditions.

The differential pressure signal is represented in Figure 5-16. Acoustic oscillations are present, as one can see in the Fourier transform in the figure. The main pressure after the discharge reaches 19 mbar, 10 milliseconds after the discharge start. For the 63 ml chamber volume, this pressure rise would correspond to an E_{th} of 300 mJ. But for this discharge, the pressure rise is not completely caused by the energy deposit in the gas: this value also includes electrode heating effects, as explained next.

The filtered pressure signal -in blue in the figure- displays a transient pressure rise after 3 ms, even when the discharge ended 2.75 ms before. The high current, that reaches 600 A, heats greatly the electrodes. The electrodes then heat the surrounding gas by conduction, causing the pressure rise observed.

The final pressure difference is taken as the mean value 2 ms after discharge, with a 1 ms window, representing the end of the pressure rise caused by E_{th} with little influence of the heat exchange from the electrodes. This represents a good estimate of the energy deposited at the fluid by the discharge, excluding heating by the electrodes after the discharge, and the best we can obtain by calorimetry for this igniter. In the figure, it is represented by a green level. We estimate this way a value for E_{th} of 91.8 mJ.

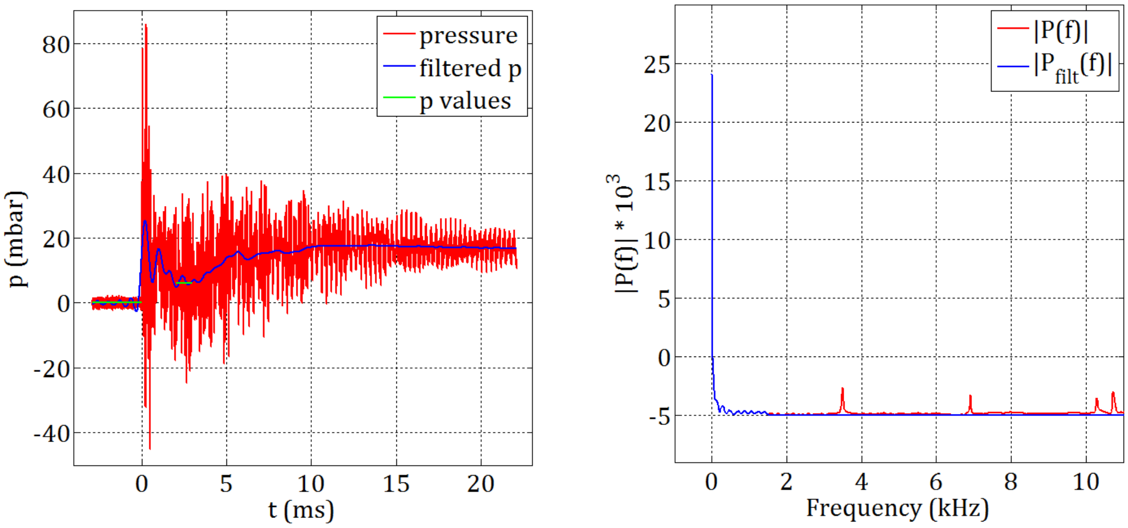

Figure 5-16: Pressure rise for a Eyquem igniter discharge in red (left); filtered using a low-pass Fourier transform, in blue; and final pressure rise (green). On the right, single-sided amplitude spectrum in red and filtered spectrum in blue.

We performed 30 tests in the same experimental conditions (1 bar, 293 K). The results for each test are plotted in Figure 5-17. Extreme results for E_{th} are caused by differences in the pressure signal, as acoustic resonance complicates the measurement of the pressure difference. For the set of tests, average and standard deviation results are $E_{el} = 675 \pm 46\, mJ$, $E_{th} = 99 \pm 36\, mJ$, and $\eta = 14.6 \pm 5.1\%$. These values are close to the energies delivered by the Ardiden 3 igniter.

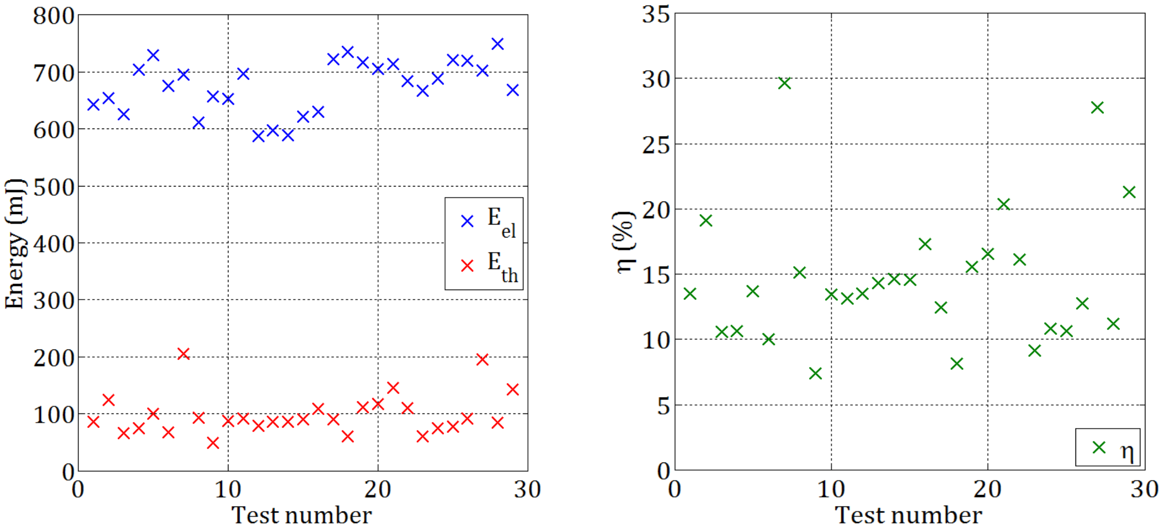

Figure 5-17: Set of tests for the Eyquem helicopter igniter. Results for E_{el} and E_{th} (left) and corresponding η (right).

5.2 Helicopter engine igniter: SBOS

We adapt and apply the SBOS technique to the visualization of the Ardiden 3 igniter. The aim is to estimate the spatial distribution of the spark kernel physical quantities, such as density and temperature. Using the SBOS technique we can obtain instantaneous spatial information, at a chosen time after the discharge starts.

First, we adapt the SBOS method to the helicopter igniter discharge. There are five meaningful changes in the method: image magnification, signal synchronization, physical filtering of light emission, the theorical model for Gladstone-Dale relation, and cross-correlation and integration masks and boundary conditions. Then simultaneous SBOS-calorimetry experiments are performed to characterize the discharge.

5.2.1 SBOS adaptation

We want to study the helicopter engine igniter using the SBOS technique. As well as in the calorimetry approach, we start by the adaptation of the setup and the methodology matured with the study of the pin-to-pin electrodes discharge to better fit the particularities of the aeronautic igniter discharge. The main modifications to the experimental procedure relate to the discharge size, signal synchronization and light emission from the discharge. Adaptations in data processing concern the electronic density influence in the Gladstone-Dale relation, and boundary conditions for the integration of the displacement field.

5.2.1.1 Discharge kernel size - Magnification

In the pin-to-pin electrodes discharge, the hot discharge kernel characteristic size is that of the inter-electrode gap. For the aircraft igniter, as observed by Sforzo [124] and Okhovat [19], the kernel grows fast up to several centimeters. The 20 ml constant volume chamber is also larger than the one used for the pin-to-pin electrodes. We compensated these differences by changing the optical setup, adjusting the distances of the lenses to obtain a magnification of $M = -0.5$. A schematic view of the optical setup is depicted in Figure 5-18.

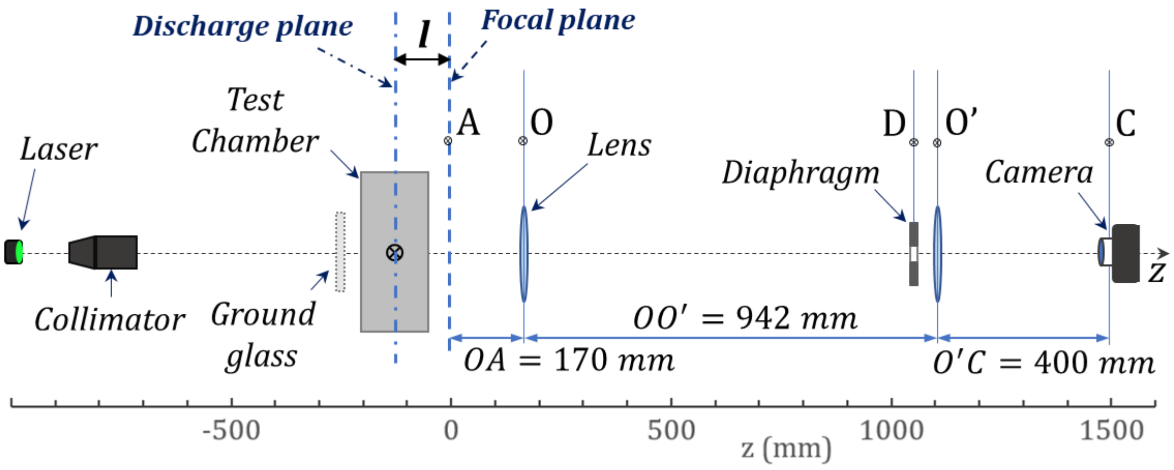

Figure 5-18: Optical setup for a magnification of M = -0.5

As the magnification is reduced, the displacement of the points of the pattern is reduced for the same refraction index gradient. Thus, we need longer defocusing distances to keep the displacement at the required values, high enough for a high SNR (signal to noise ratio) but lower than 6 pixels for a proper cross-correlation processing.

5.2.1.2 Signal synchronization

The electrical generator generally works cyclically, producing discharges at over 2 Hz, alternatively through the two spark-plug exits. With the trigger add-on, a 300 ms square signal triggers the charge of the igniter capacitance, and after 263 ms the discharge starts, with a jitter of about 40 μs.

We synchronize the discharge with the camera system using a delay generator (Standford Research Systems, Model DG645 Digital Delay Generator). Two output channels are employed, one to produce a 300 ms square signal - “Discharge trigger”-, and another to produce a 1 ms square signal at $t = 262\,ms$, which triggers the camera system on the trailing edge, setting the time reference for the WinView32 program –“Camera PC trigger”-. The image acquisition delay is adjusted further using the WinView32 program, where an input delay (input Δt) is set. The camera feedback signal is used to obtain the real image acquisition delay by comparison with the measured electrical signals. Signal synchronization is pictured in Figure 5-19, with the delay generator output channels on the left graph, and discharge event and image acquisition synchronization on the right graph.

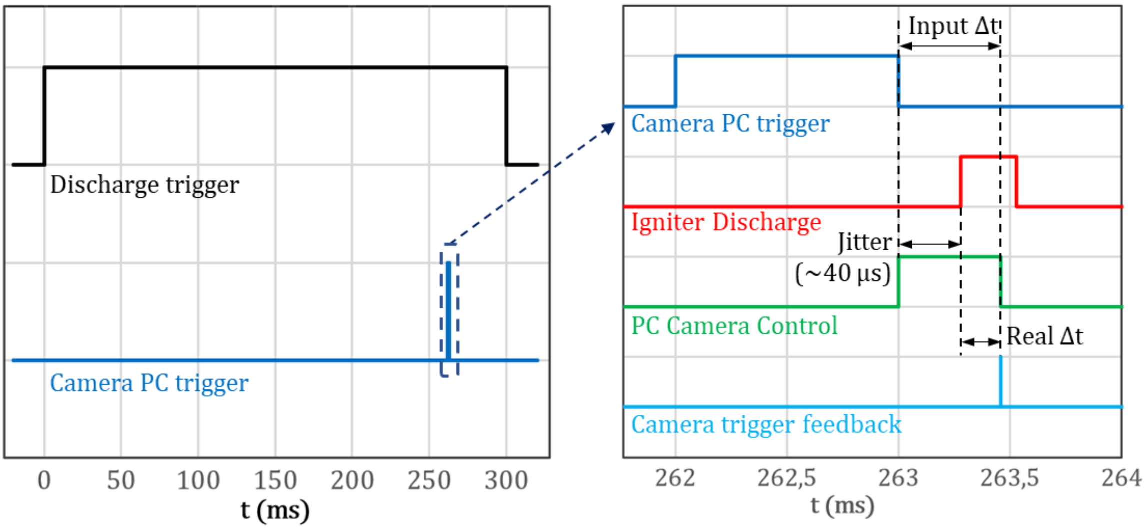

Figure 5-19: Camera and discharge control synchronization. Signals generated by the delay generator (left) and camera-discharge events synchronization (right).

The camera trigger feedback sends a 2 V peak when the camera acquisition occurs, with an accuracy in the order of the nanosecond. The camera trigger feedback is recorded with the electrical and pressure signals. The image acquisition delay is measured from the time difference between the discharge start, i.e. the beginning of the breakdown voltage peak; and the camera trigger feedback. If the image acquisition delay is negative, the image will contain no information of the discharge and it will be equivalent to a reference image (no displacement of the background pattern points).

Figure 5-20 shows the oscilloscope input signals for p, U, I and camera trigger feedback, on the left; and the delay detection from the comparison of the camera feedback and electrical voltage signals, on the right, for a Δt of $48.6\ \mu\mathrm{s}$.

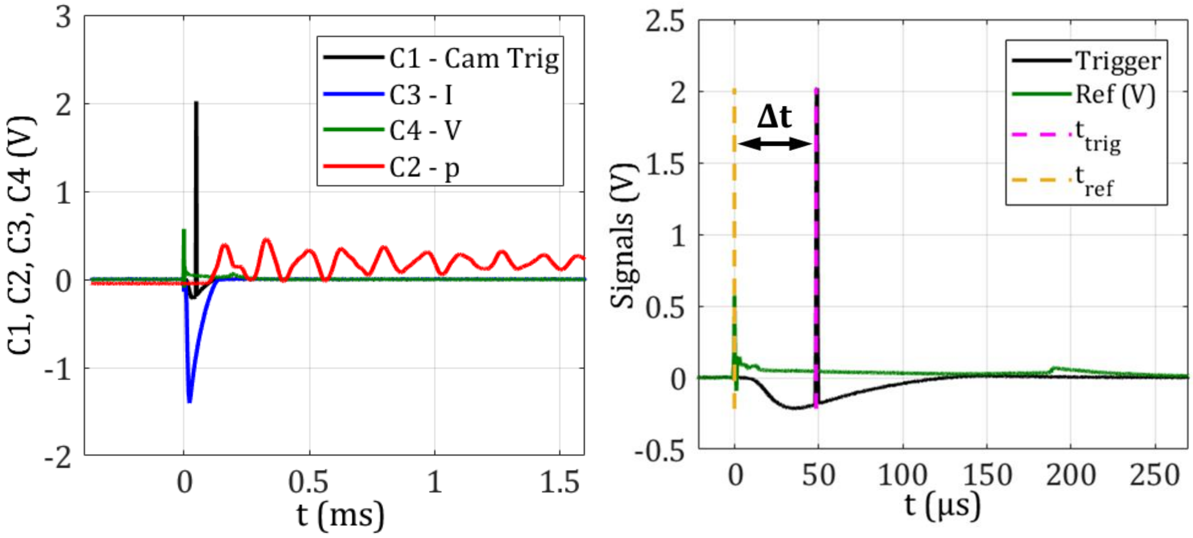

Figure 5-20: Oscilloscope input signals (left) and real delay detection from voltage and camera trigger feedback (right). Camera trigger feedback is represented in yellow in the left graph and in blue in the right graph for a better contrast.

5.2.1.3 *Light emission from the high-power discharge – optical filter.*

The high-power discharge (see Figure 5-10) from the aeronautic igniter presents strong light emission in the first moments of the discharge, about 40 μs after the discharge onset. The emission of light in the discharge kernel hides the background speckle pattern, and even saturates the camera sensor.

Other works [19], [125] discarded the study of the first moments of the discharge because of this effect. We tested the implementation of different filters to analyze if the light emission hides completely the SBOS signal (displacement of the background points) or if it can be filtered.

Two filters are tested: a high-pass 400 nm filter, which filters the UV emission; and an interferometric filter for the 532 nm wavelength, as it is the wavelength of the speckle pattern generated by our laser. Several tests show that the low-pass filter does not prevent the camera sensor saturation, but the interferometric filter compensates the light emission and allows for SBOS measurements. The filters showed no influence on the speckle characteristics, as one can see in Figure 5-21.

Figure 5-21 shows three SBOS test images: the first with a delay $\Delta t = 73\ \mu s$, without filter and presenting camera sensor saturation; the second at $\Delta t = 46\ \mu s$, with a high-pass filter at 400 nm and camera sensor saturation; and the third one with the interferometric filter at $\Delta t = 59\ \mu s$, with no trace of the light emission. The infrared emission produced during the discharge explains this effect. The corresponding displacement fields are represented in the bottom row, showing that sensor saturation makes the background pattern points to “disappear” in the test image, so the cross-relation with the reference image tends to find the missing points outside the light emission area, yielding erroneous displacement vectors for the saturated areas.

The interferometric filter for the 532 nm wavelength is used for the SBOS experiments. The filter 532 nm bandwidth reduces light intensity to 60%, so the camera intensification gain is adjusted from 200 to 250 (closer to the maximum of 255) to compensate this effect.

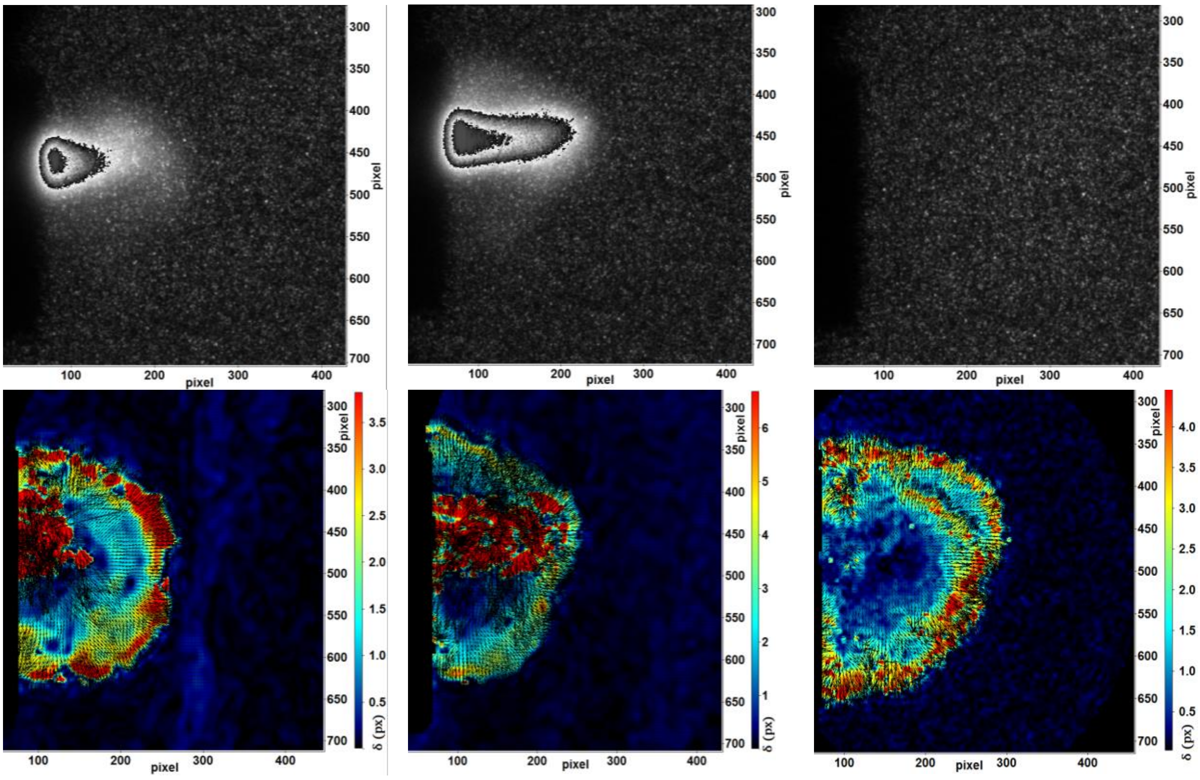

Figure 5-21: SBOS tests images without filter (left), with the low-pass filter (middle) and the interferometric filter (right). On the bottom row, the corresponding displacement fields from cross-correlation processing.

5.2.1.4 Electronic density

Electronic density affects the Gladstone-Dale (G-D) relation at high temperatures. According to Sforzo estimation [124], temperature reaches 4000 K in the discharge kernel 50 µs after the discharge start. As presented in Chapter 4, the effect of the electrons on the refractive index is negligible below 3000 K, but the G-D model must be changed for higher temperatures, as in this case.

As presented in Chapter 4, equation (4.3) describes the G-D relation for an ionized gas. According to [113], the electron contribution is much higher than the ion contribution (electron contribution represents ~20 times the ion contribution and ~19 times the gas atom contribution). Gas atom contribution is present in the original G-D relation and is more important at lower temperatures. Ion contribution is only present at high temperatures (with ionized gas), and it would be necessary to consider all the possible ions present in the gas, with little impact on the final result. Therefore we neglect ion contribution to the refractive index in our model.

$$n - 1 = \rho[(1 - \alpha_I)K_A + \alpha_I K_I] + N_e K'_e \qquad (4.3)$$

The electronic density N_e in air is related to temperature. In our case we use the NASA9 model for air included in the Cantera module, which we have integrated into our Matlab program. This model solves the ionization level depending on thermodynamic conditions (T and p). Electronic density is sampled between 275 and 5000 K, and the resulting $N_e(T)$ function is recorded as a vector. The function represented by equation (5.2) models $n - 1$ as a function of temperature:

$$n - 1 = K_A \frac{p}{R_g T} 10^{-3} + K'_e\, N_e(T) = K_A\, \rho\,(T) + K'_e\, N_e(T) \qquad (5.2)$$

Where $K_A = 0.2274\, cm^3 g^{-1}$, $R_g = 287\, J\, kg^{-1} K^{-1}$, and $K'_e = -4.46 \cdot 10^{-14} \lambda^2$ [113], with $\lambda = 532 \cdot 10^{-7} cm$. Density units are expressed in $g \cdot cm^{-3}$ (hence the first term is multiplied by 10^{-3}).

In SBOS image post-processing, summarized in eq. (4.11) from chapter 4, first we integrate the displacement field, and for low temperatures we substituted at the equation refractive index with density, as G-D relation is linear and their derivates are proportional (times the Gladstone-Dale constant). But the high temperature G-D relation is non-linear, and temperature dependent. Thus, the integration of the Poisson equation and the filtered back-projection are solved first to obtain the refractive index field -up to the step (d) of Eq. (4.11)-, and then the non-linear equation is solved to obtain the temperature field.

$$\vec{\boldsymbol{\delta}} \overset{(a)}{\rightarrow} \boldsymbol{\nabla}_{x,y} \vec{\boldsymbol{\delta}} \overset{(b)}{\rightarrow} \int_{\mathcal{C}} \boldsymbol{n}\, \boldsymbol{dz} \overset{(c)}{\rightarrow} \boldsymbol{n}(\boldsymbol{x},\boldsymbol{y}) \overset{(d)}{\rightarrow} \begin{Bmatrix} \boldsymbol{\rho}(\boldsymbol{x},\boldsymbol{y}) \\ \boldsymbol{T}(\boldsymbol{x},\boldsymbol{y}) \end{Bmatrix} \overset{(e)}{\rightarrow} \boldsymbol{dH}(\boldsymbol{r}) \overset{(f)}{\rightarrow} \boldsymbol{H} = \boldsymbol{E}_{\boldsymbol{SBOS}} \qquad (4.11)$$

The non-linear equation at step (d) is solved with the $n - 1$ field obtained from the SBOS images, $(n - 1)_{SBOS}$; and the equation (5.2), $(n - 1)_{f(T)}$; zeroing $\left[(n - 1)_{SBOS} - (n - 1)_{f(T)}\right]$ for each point of the $n - 1$ field with the *fzero* function in Matlab®.

5.2.1.5 Masks and boundary conditions

SBOS test images show, apart from the background speckle pattern, the chamber walls, the aeronautic igniter and the pressure transducer protective disc. These elements are hidden for the obtention of the displacement field δ by cross-correlation between the test image and the reference image. The masks used to obtain δ are set in DaVis program, excluding the area inside the spark plug and outside an ellipse inscribed in the chamber walls shadow. Figure 5-22 shows a test image with superimposed masks and the area that they hide, in the left figure.

Similarly, the boundary conditions (BC) applied for the integration of the displacement field are depicted in the Figure 5-22 (right image). The kernel is projected away from the igniter, so the image can be cut at the spark plug surface for simplicity of the boundary conditions -this way we avoid boundary conditions in the corner of the igniter-. A Dirichlet BC is applied to the edges of the image and the truncation plane, except for the igniter surface. A Neumann BC is applied at the igniter surface, giving the derivate (the $u_{i,j}\big|^{(n+1)}$ term in the iterative scheme, see Eq. (4.19)) the same value inside the wall than outside $\left(u_{i,j}\big|^{(n+1)}{}_{inner} = u_{i,j}\big|^{(n+1)}{}_{outer}\right)$.

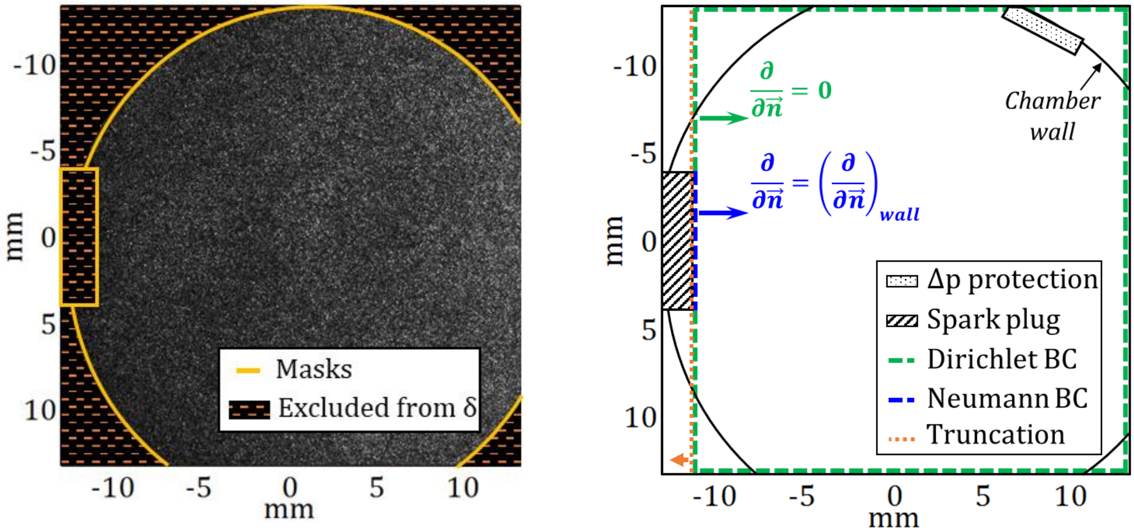

Figure 5-22: Displacement field masks for cross-relation (left) and schema of the boundary conditions for Poisson equation integration (right).

After the displacement field integration, the vertical area of the image that contains the spark plug (to the left of the truncation line in the image) is set to zero to compensate numerical diffusion.

5.2.2 Results and discussion

In this section, the helicopter igniter discharge is studied by SBOS and calorimetry simultaneously. First, we observe the discharge kernel at different instants after the discharge onset, by varying the test image acquisition delay time (Δt). Then, we post-process the SBOS images for a discharge in air at atmospheric conditions to obtain the air properties and the energy deposit at the instant of image acquisition. The same process is applied to a set of tests in air in different initial pressures. Last, we present an approach which could estimate the density gradient through the discharge initial shockwave.

For the study of the discharge kernel by SBOS we use the optical setup described in section 5.2.1.1, and shown in Figure 5-23.

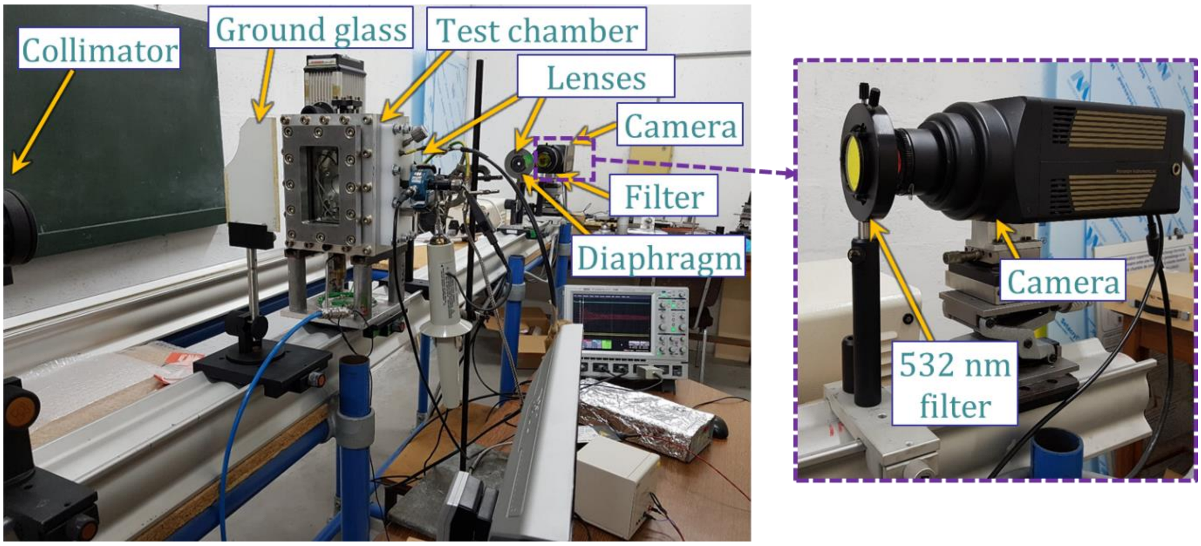

Figure 5-23: SBOS experimental setup.

5.2.2.1 Evolution of the discharge kernel.

To characterize the helicopter igniter discharge by SBOS we first need to know how the hot discharge kernel develops with time. The aim is to find the time window during which the discharge fulfills the required conditions for SBOS processing (axis-symmetry, mainly). As only one image per test can be recorded and because of the jitter of the discharge occurrence, series of tests have been performed for several acquisition delays (Δt) considering the same experimental conditions (1 bar, 293 K).

The first series of experiments is composed of 121 tests, with an input delay Δt_{input} ranging from 20 to 300 μs, and 48 tests with Δt_{input} ranging from 300 μs to 9 ms. The jitter in the electronic system is taken into account thanks to electrical signals and camera trigger return signal. Events in the first moments occur in the order of 10 μs. Hence for the first series, the input delay Δt_{input} is increased of 5 μs every five tests to obtain several images at different times. For the second series, input delay is increased by 0.5 ms every 3 tests.

The control parameters that affect the optical setup, the image acquisition and the cross-correlation processing for these tests are as described in the Table 5-1:

M	Ø	t_{gw}	*Gain*	*l*	Δt_{input}	*Cross-Correlation 1*	*Cross-Correlation 2*
-0.5	8 mm	1 μs	250	-120 mm	20 μs – 9 ms	64x64 px^2, 25% OL, x1	16x16 px^2, 75% OL, x3

Table 5-1: SBOS control parameters for kernel evolution observation

Where *M* is the Magnification, Ø the diaphragm opening diameter, t_{gw} the camera acquisition gate width, *Gain* the optical sensor gain, *l* the defocusing distance, Δt_{input} the input delay, and *Cross-Correlation* specifies the cross-correlation processing window width, overlap (*OL*) and number of steps.

The displacement field obtained 1 ms after the discharge onset is shown in Figure 5-24. Image acquisition and displacement field are obtained as described in Chapter 4, section 4.2. In the recorded discharge evolution, the hot kernel only extends into a part of the chamber. In the following figures of this section, we zoom to the area marked out by the white dashed line in the Figure 5-24 for clarity.

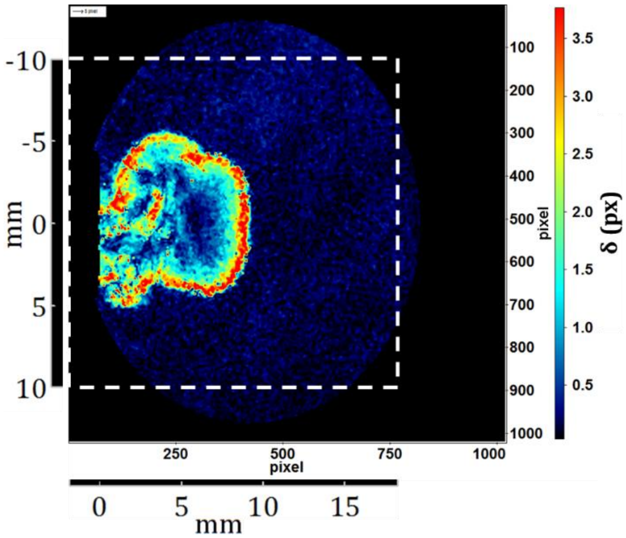

Figure 5-24: Displacement field 1 ms after the discharge start. White: investigation zone for kernel evolution

Figure 5-25 shows SBOS displacement fields at different delay times, ranging from 20 μs to 8.5 ms, representative of different moments of the discharge kernel evolution. In this figure, the color scale is adapted to each image maximum displacement to highlight the kernel structure. The delay time of each test is deduced from the electrical and camera trigger signals (see 5.2.1.2). To clarify, each image of a discharge kernel is obtained from a single test, so different images correspond to different discharges, which explains different structures in the kernel. Maximum displacement ranges from 4.5 px (tests in the first 100 μs) to 2.5 px for the longer delays. For the shorter delay times, as kernel size is still reduced compared to the full image, a part of the background is masked (in black in the images) to reduce computing time.

First images are taken 20 μs after the discharge onset. The hot kernel is first a small ellipsoid around the area of the spark plug at the discharge location. It is surrounded by a shockwave. Then the hot kernel expands and the shockwave propagates, as shown in the first line of images in Figure 5-25, e.g. for a Δt value ranging from 20 to 40 μs.

Then the discharge kernel moves away from the spark plug, with a quasi-symmetric structure up to about 70 μs. At this instant, 3D structures such as lobes start forming in the kernel surface as a result of the gas dynamics: part of the shockwave bounces at the wall next to the spark plug and at the flat walls – windows – of the chamber and affects kernel structure on contact with it, before the main part of the shockwave travels back and forth the opposite side of the chamber from the spark. For the same condition, the observed location of the 3D structures vary from test to test. With time, the kernel expands away from the spark plug.

The projection of the kernel away from the spark plug is positive for combustion initiation: away from the wall chamber, the kernel is less prone to wall heat transfer and to extinction, and may be located in a zone where conditions are more favorable for ignition (e.g. velocity, fuel equivalence ratio...).

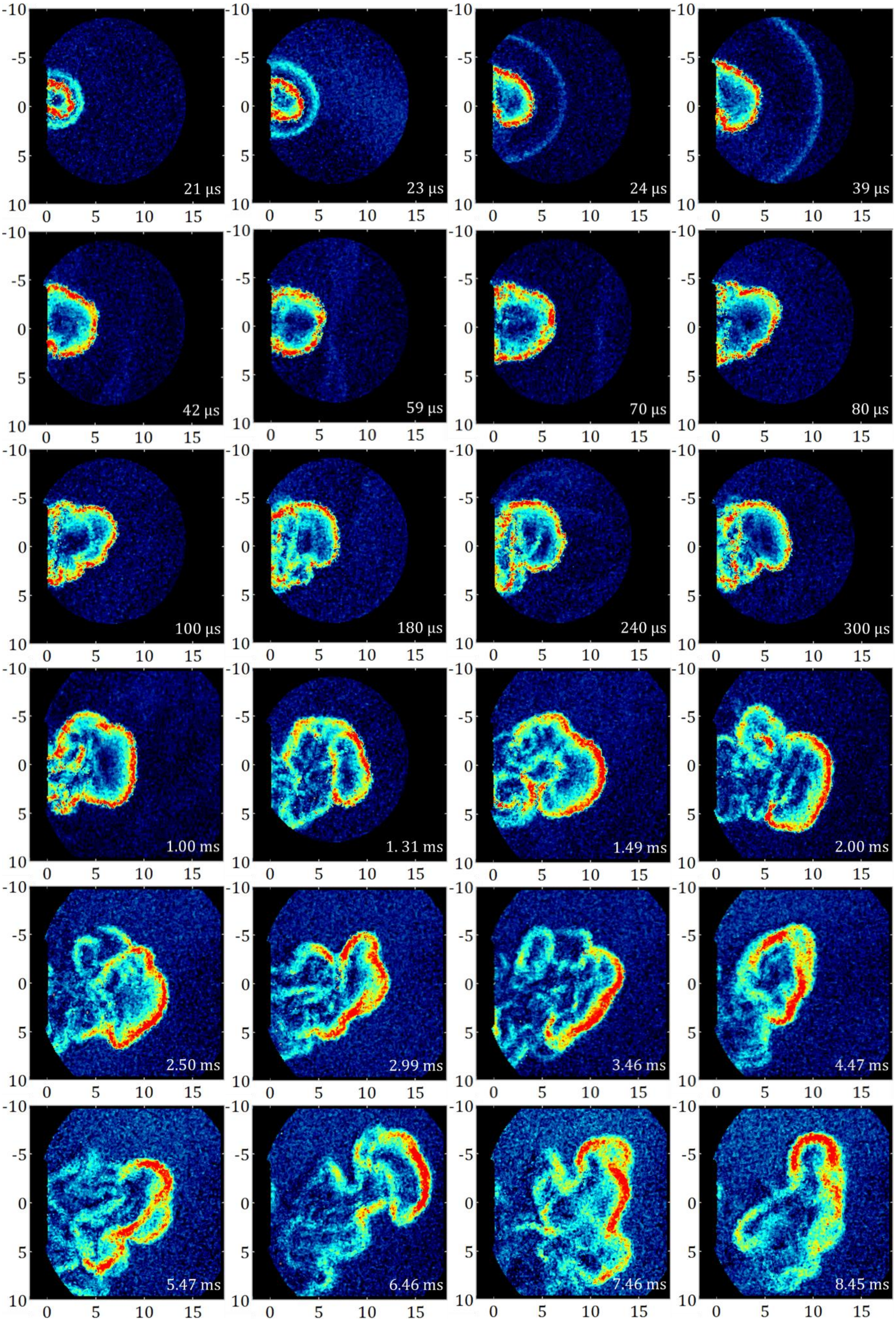

Figure 5-25: Helicopter igniter discharge kernel evolution, as SBOS δ fields with Δt from 21 µs to 8.45 ms. Each image correspond to a different test.

Sforzo studied the ignition kernel projection and time-evolution, as it is shown in Figure 5-26 ([124], pp. 58-64). The spark plug in Sforzo's study does not use a semi-conductive layer to lower breakdown voltage. However, both discharge kernels show at the first instants (up to 80 µs) the same trajectory. For longer delays the sparks in their study are projected further and faster. These differences are due to several factors: first, the visualization method: their kernel edge detection is observed by direct light emission, while in our case the kernel edge is materialized by density gradients. Then, electrode geometry: differences at the spark plug geometry influence kernel projection. Last, gas confinement is greater in our case because of the reduced size of our chamber that affects kernel dynamics at later instants.

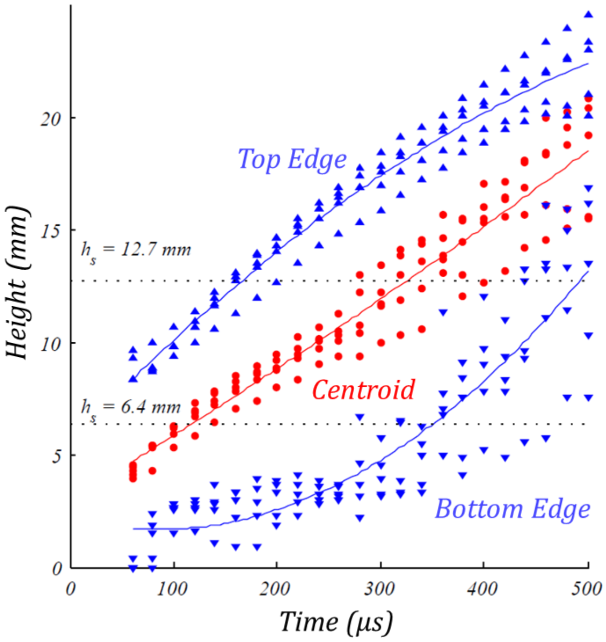

Figure 5-26: Kernel location heights from wall at different times for five kernel events [124].

Based on the observed kernel evolution we can determine the image acquisition delay time adequate for the SBOS image processing. In very short delays ($\Delta t < 25\ \mu s$),the shockwave is too close to the hot kernel to estimate the conditions between the shockwave and the discharge kernel; i.e., pressure is not yet in equilibrium between the shockwave and the kernel. During the valid Δt window, the shockwave is far from the kernel (at least 1 cm) and expanding towards the chamber wall, where it will bounce and complete its oscillating period of 160 µs – from the acoustic resonance found in the pressure signal-. In longer delays ($\Delta t > 100\ \mu s$), repeatability decays and 3D structures develop in the kernel surface, so the axis-symmetry condition for SBOS processing is not fulfilled. For these reasons, we only post-process images for a ∆t ranging from 25 to 100 µs after discharge onset, selecting the axis-symmetric cases.

5.2.2.2 Discharge energy calculation.

We estimate the gas properties and the energy deposit during a test in air at atmospheric conditions (1 bar, 291 K) for a quasi-axis-symmetric discharge. Each step of this calculation is described in detail in section 4.2. This section describes this process briefly to highlight the different results in the case of the helicopter igniter.

Image acquisition and displacement field calculation are performed as in 5.2.2.1, with an input delay time Δt_{input} of 54 μs and a second cross-correlation processing phase with a 8x8 px^2 window, a 50% overlap and 3 iterative steps. Figure 5-27 shows the reference image (a), test image (b) and the resulting displacement field (c) obtained using a 5x5 px^2 median filter to reduce noise. In the δ field, we observe the hot kernel on the left, with high displacement in its edges, and the shockwave, near the limit of the elliptic mask used for cross-correlation processing.

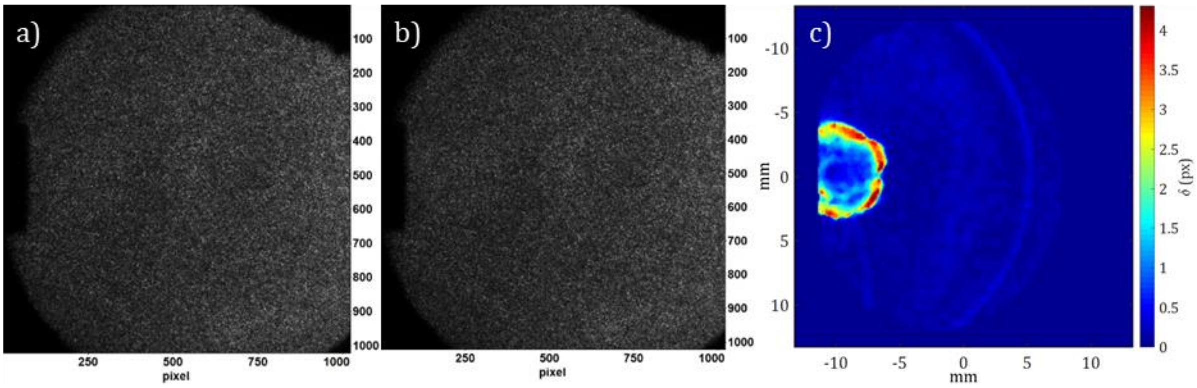

Figure 5-27: SBOS test in atmospheric conditions: a) reference image, b) test image, c) displacement field.

Image processing is shown in Figure 5-28, with a), b) and c) corresponding to the following fields respectively: $\vec{\nabla}_{x,y}.\vec{\delta}$, $\int_C n\,dz$ and $n(x,y)$.

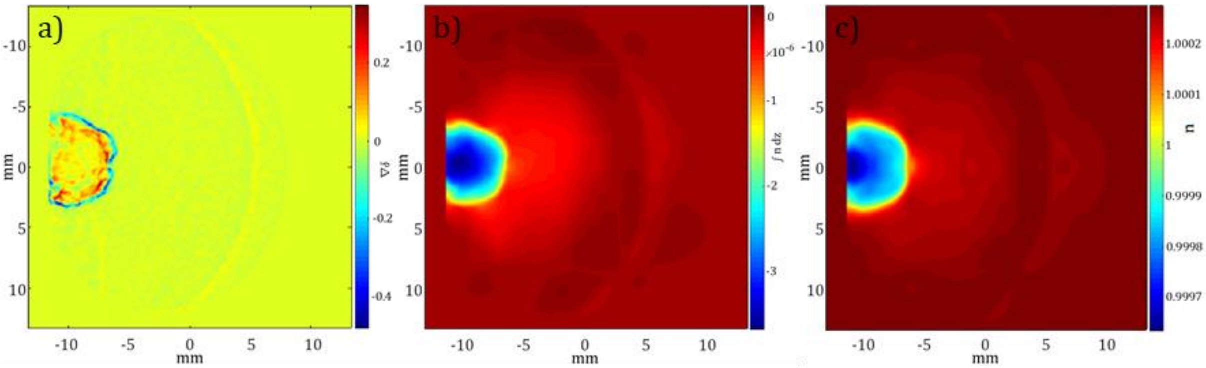

Figure 5-28: SBOS image processing: a) divergence, b) integration, c) filtered back-projection.

Both temperature and density fields are depicted in Figure 5-29: T and ρ profiles along the symmetry axis are represented on the right of the figure, with the x-axis adjusted to zero at the spark plug surface so one can estimate the kernel front position. Temperature reaches the maximum value of 3772 K close to the discharge kernel origin. Temperature T is over 3500 K inside the kernel and decreases abruptly at the kernel border to reach the initial temperature. Density distribution is, of course, the opposite: a minimum density in the hottest zones, increasing up to the initial value at the kernel border.

Kernel boundary is detected from the temperature field. The temperature threshold for boundary detection is set at $T_{threshold} = 620\,K$, which corresponds to a 10% increase of the total temperature from the ambient temperature $\left(T_{threshold} = T_{amb} + 0.1(T_{max} - T_{amb})\right)$. Kernel boundary is highlighted on the temperature field, as a dashed cyan line, with the centroid of the equivalent ellipse as a black cross. The detected kernel volume is $V_{kernel} = 187.3\, mm^3$, obtained as in section 4.2. From the axial temperature profile we obtain the kernel front depth; i.e. the distance from the spark plug surface to the furthest point of the kernel along the axis: $x_{front} = 5.4\, mm$.

We can observe that temperature and density do not reach the ambient value right outside the kernel: there is an area before the kernel front where temperature is between ambient T (291 K) and 500 K, and density is lower than initial density. After the shockwave passes, we suppose that the relaxation time is long enough for gas characteristic to be the same as before the test. Then, the differences of T and ρ to the ambient values are due to the "numerical diffusion" produced by the different filters and integrations through the displacement field processing. That is why temperature threshold is chosen to exclude these zones from the kernel volume. Density gradient through the shockwave is further analyzed later, in section 5.2.2.4.

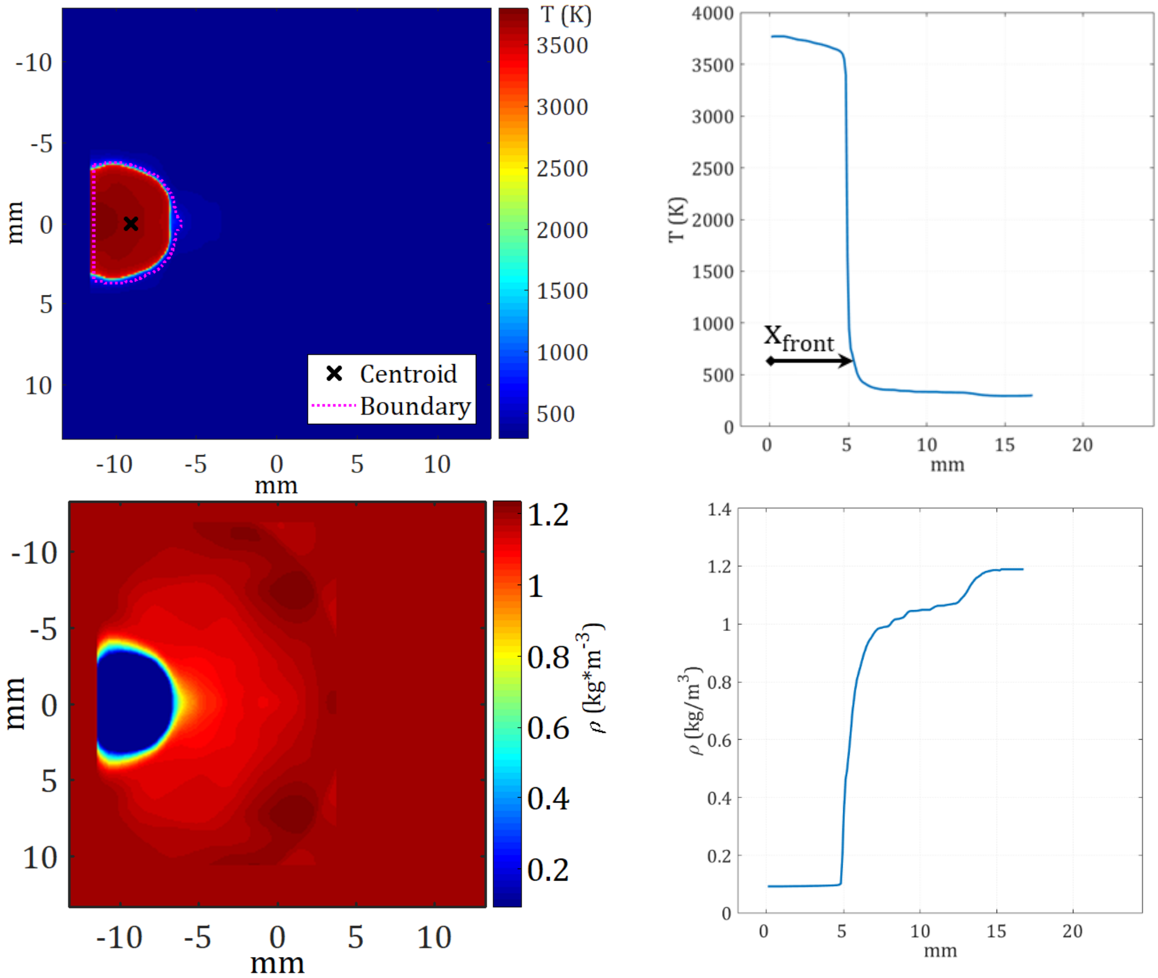

Figure 5-29: Temperature and density fields (left) , and T and ρ along the symmetry axis (right); in air, at 1 bar, Δt= 48.6 µs.

From the temperature and density fields we obtain the associated enthalpy and energy. We calculate the total enthalpy deposit by a revolution integral. The kernel temperature is extended to its surroundings by numerical diffusion, which would cause us to over-estimate the energy deposit in the integration. To avoid this over-estimation, we only consider the enthalpy inside the detected kernel (where $T > T_{threshold}$). The resulting enthalpy variation per mol Δh, enthalpy variation per unit of volume $c_m \cdot \Delta h$, and enthalpy differential (normalized over the total enthalpy deposit) dH/E_{SBOS} are represented in Figure 5-30 (a, b and c images respectively).

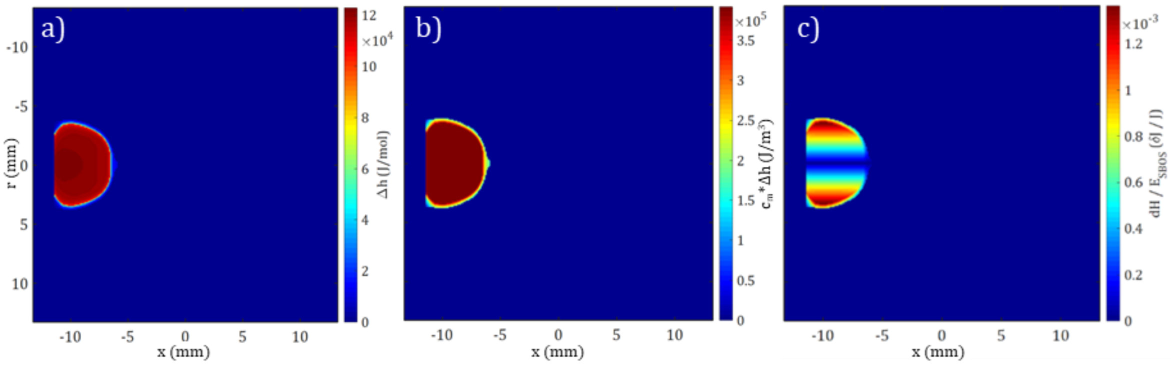

Figure 5-30: SBOS energy calculation: a) molar enthalpy, b) enthalpy per unit of volume, c) total enthalpy planar distribution.

Total energy deposit at image acquisition time, measured by SBOS, is $E_{bos} = 66.3\,mJ$ for Δt = 48.6 μs. The electrical energy supplied to the spark plug at Δt, $E_{el}(\Delta t)$, is only a fraction of the total E_{el} at the end of the discharge: $E_{el}(\Delta t) = 424\,mJ$, while at the end of the discharge $E_{el} = 643\,mJ$. Figure 5-31 represents the image acquisition time Δt as in signal synchronization, on the left, and the electrical energy $E_{el}(\Delta t)$ in cyan over the total electrical energy E_{el} in blue, on the right.

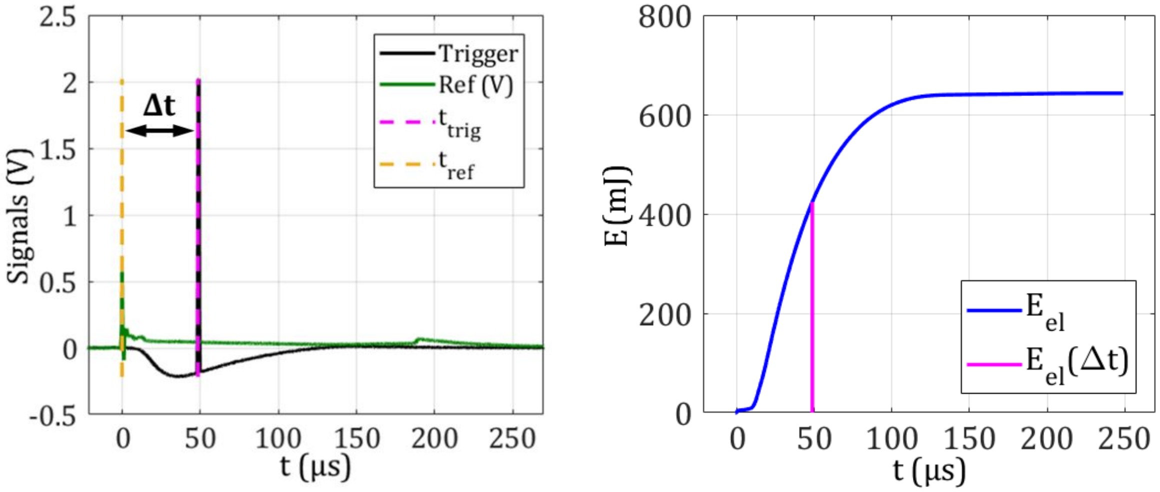

Figure 5-31: Image acquisition delay Δt (left) and electrical energy E_{el} (right). $E_{el}(\Delta t)$ is the E_{el} supplied at the time of image acquisition.

The energy transfer efficiency at Δt, $\eta_{bos} = E_{bos}(\Delta t)/E_{el}(\Delta t)$, is compared to the global efficiency of the discharge obtained by calorimetry. For this discharge, $E_{th} = 83.4\,mJ$, and $\eta_{th} = 13\%$ (from simultaneous calorimetry measurements, see 5.1.2.1). Based on the approach proposed above, efficiency is then higher in the first moments of the discharge for this test: $\eta_{bos} = 15.6\%$.

5.2.2.3 Discharge energy for different pressures.

We study the energy deposit for different initial pressures. We perform series of 8 experiments, from 0.25 to 2 bar every 0.25 bar. Measurements are performed simultaneously by SBOS and calorimetry, so both results can be compared. The corresponding calorimetry results are analyzed in 5.1.2.2. The control parameters for SBOS setup and cross-correlation calculations are referenced in Table 5-2:

M	∅	t_{gw}	*Gain*	*l*	Δt_{input}	*Cross-Correlation 1*	*Cross-Correlation 2*
-0.5	8 mm	1 µs	250	-120 mm	40 - 60 µs	64x64 px^2, 25% OL, x1	8x8 px^2, 50% OL, x3

Table 5-2: SBOS control parameters for energy calculation tests

We set the input delay Δt_{input} for each set of tests, but as a result of jitter, different values of the real delay Δt are obtained for each experiment from the recorded signals. As discussed before, the test fulfills the conditions for the SBOS processing only if 25 µs < Δt < 100 µs.

For the series of 8 tests at each pressure, only around a quarter of the tests respect the SBOS criteria. Hence only 14 tests can be validated for SBOS analyses ranging 8 different pressures and for different delays. It is clear that tests present a low repeatability as Δt is not the only factor affecting symmetry, in particular: 1) location of the spark over the sparkplug; 2) 3D reflection of the shockwave in the close wall cause lateral reflections of the shockwave reaching the kernel at the first stages of kernel development, deforming the kernel and inducing asymmetries early after the discharge. The ratio of valid tests over the total number of experiments in each condition is represented in the following table:

Pressure (bar)	0.25	0.5	0.75	1.0	1.25	1.5	1.75	2.0
Symmetric tests	2/8	2/8	2/8	2/8	1/8	1/8	2/8	2/8

Table 5-3: Ratio of tests presenting a quasi-symmetric discharge kernel.

The energy deposit is presented for each test versus the reference number of the test, in Figure 5-32 (left). Filled symbols represent E_{BOS}, and empty symbols represent E_{th}. The initial pressure for each test is specified by the color code. In Figure 5-32 (right) the electrical energy is plotted, both as the instantaneous energy supplied up to image acquisition, $E_{el}(\Delta t)$, in whole symbols; and as the global E_{el} of the discharge, as empty symbols. As observed in 5.1.2.1, during the first 100 µs most of the electrical energy is already delivered to the electrodes: $E_{el}(90\ \mu s) \sim 0.95\ E_{el}(250\ \mu s)$.

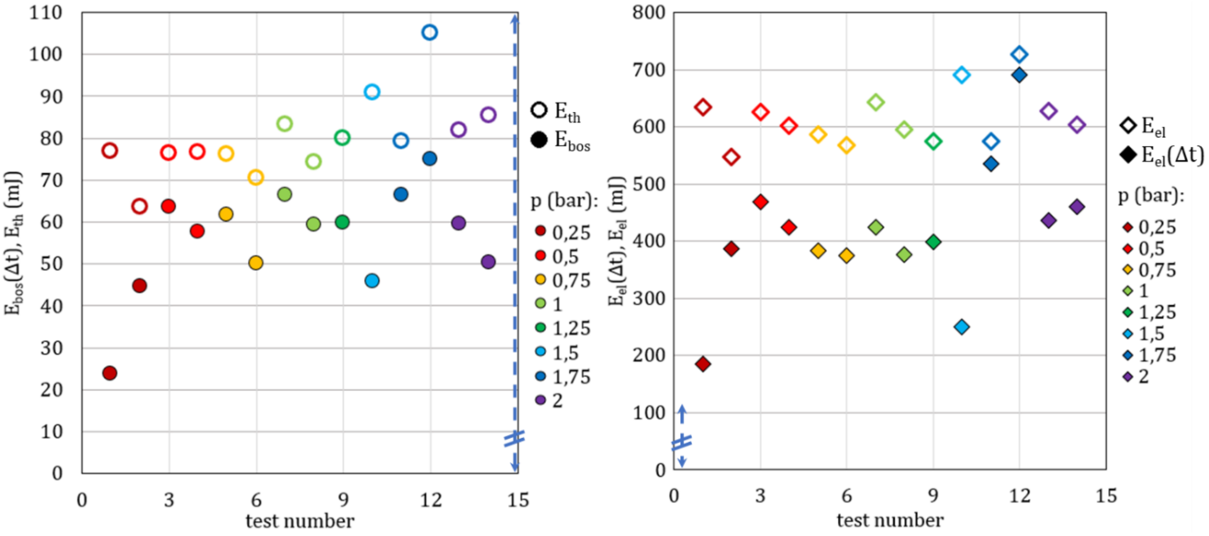

Figure 5-32: Energies calculated by SBOS and calorimetry for each test. E_{BOS} and E_{th} vs test number (left), and $E_{el}(\Delta t)$ and E_{el} vs test number (right).

Energy transfer efficiency, both instantaneous from SBOS, $\eta_{bos} = E_{bos}/E_{el}(\Delta t)$; and global, $\eta_{th} = E_{th}/E_{el}$; are plotted for each test in Figure 5-33 (left). Each test has its own image acquisition delay, Δt, which is obtained from the trigger signal, and represented in Figure 5-33 (right). Each result is associated to a different pair p-Δt, so we cannot compare directly these results yet: we need to isolate some of them.

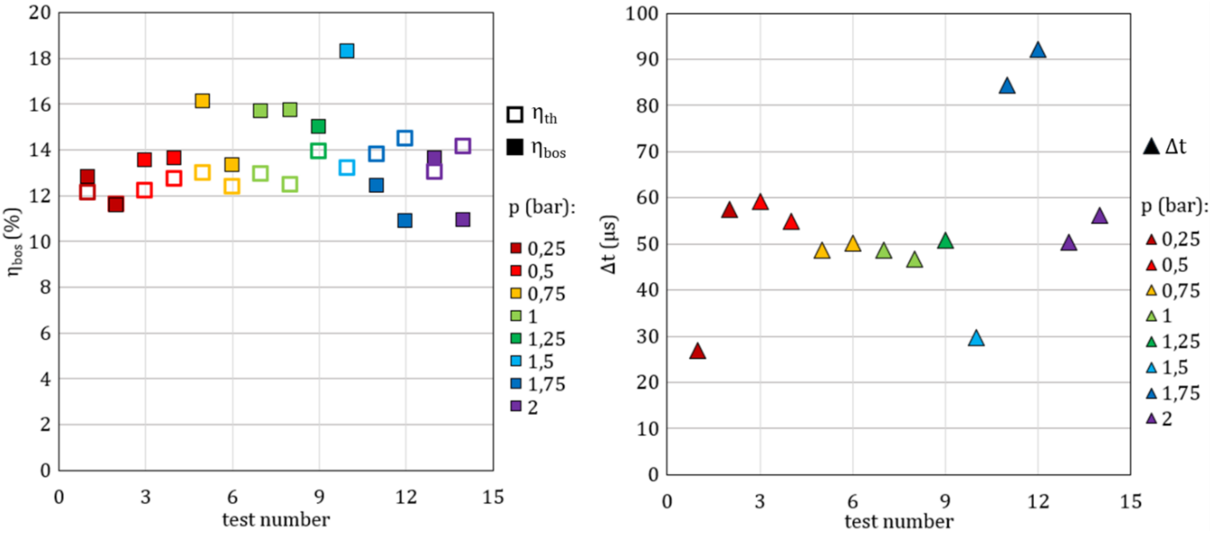

Figure 5-33: Efficiency (left) and delay (right) for each test.

To further analyze the data, we group the results in four different groups Δt_i, depending of their delay: $\Delta t_1 = (25,30)\,\mu s$, $\Delta t_2 = (45,51)\,\mu s$, $\Delta t_3 = (54,60)\,\mu s$, and $\Delta t_4 = (80,95)\,\mu s$. Data in each group are quasi-iso-delay, so we can observe the single effect of pressure, see Figure 5-34.

Energy deposit, measured by SBOS, is little affected by pressure. As one can see in Figure 5-34 (left) which plots E_{BOS} versus pressure, if there is an influence of pressure on the energy deposit it is lower than test-to-test variation for each Δt_i. Calorimetry results showed high variability for the helicopter igniter, so the influence of pressure, if it exists, is hidden by dispersion of the data.

We find the same result regarding the instantaneous efficiency η_{bos} vs pressure, represented in Figure 5-34 (right).

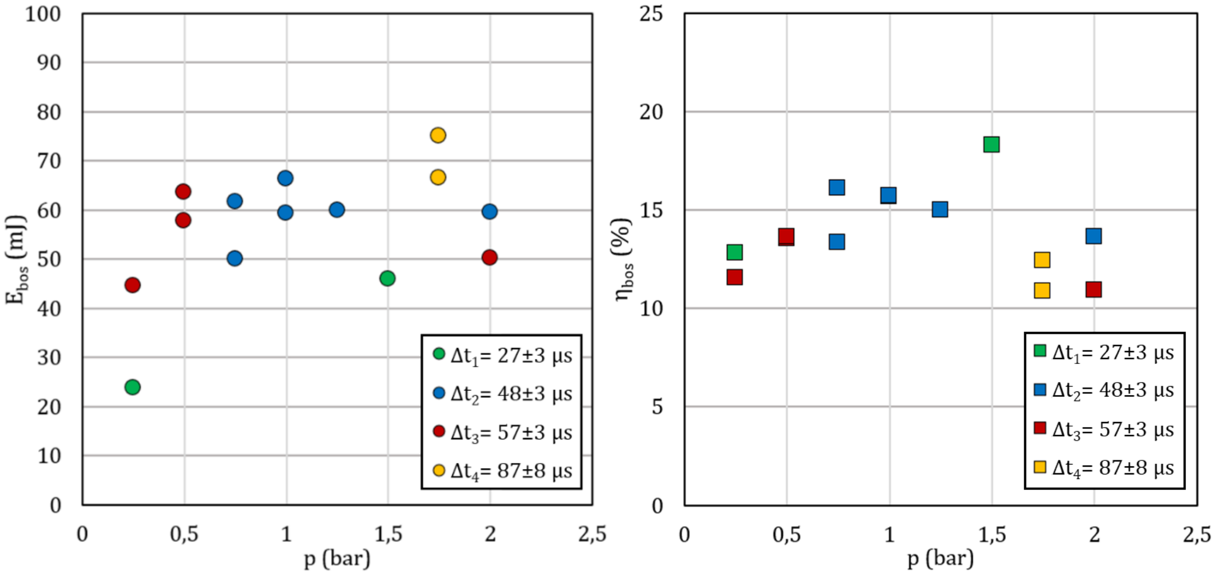

Figure 5-34: E_{BOS} (left) and efficiency at Δt (right), versus pressure at iso-Δt

We normalize the energy deposit E_{BOS} and the instantaneous electrical energy $E_{el}(\Delta t)$ by dividing them by their corresponding global measurements at the end of the discharge: E_{th} and E_{el} respectively (from the simultaneous calorimetry and electrical measurements). This yields the deposit energy ratio E_{BOS}/E_{th} and the electrical energy ratio $E_{el}(\Delta t)/ E_{el}$. We represent in Figure 5-35 the deposit energy ratio versus the electrical energy ratio, for different pressures (see the color code) and delay intervals (symbol shape).

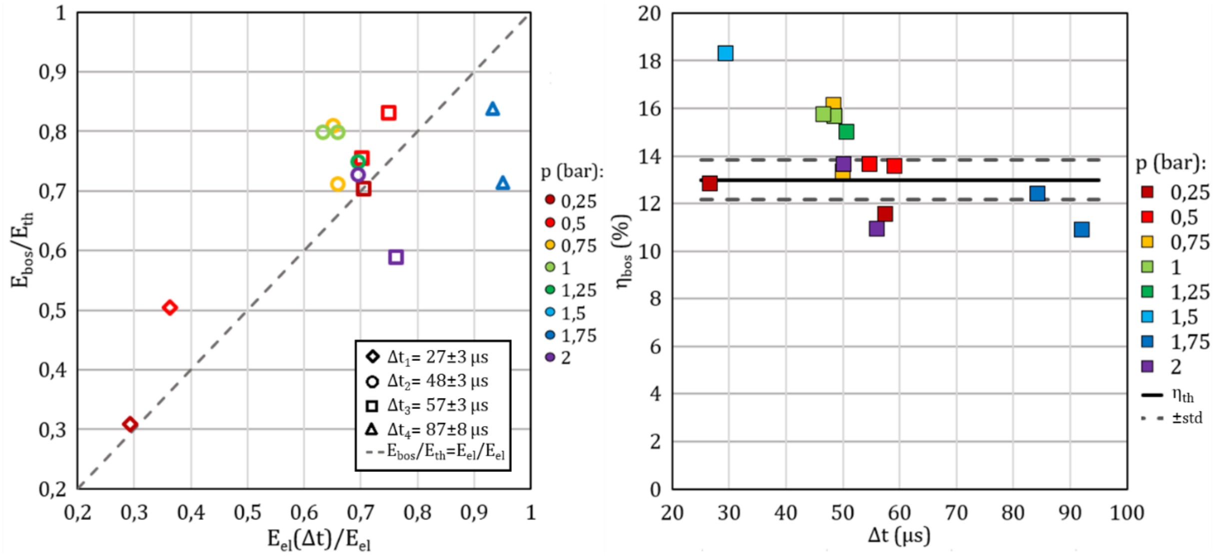

Figure 5-35: Energy deposit ratio vs Energy supplied ratio (E_{BOS}/E_{th} vs $E_{el}(\Delta t)/E_{el}$). For all tests at different Δt (left), and efficiency by SBOS at Δt versus Δt (right).

The deposit energy ratio increases with the electrical energy ratio increase for shorter delays ($\Delta t<60$ µs). For shorter delays, E_{BOS}/E_{th} is higher than $E_{el}(\Delta t)/E_{el}$ (over the diagonal dashed line), which suggests that energy transfer efficiency is better at the first moments of the discharge. At longer acquisition delays, deposit energy ratio is lower than electrical energy ratio (below the diagonal dashed line), as when $E_{el}(\Delta t)/E_{el}$ tends to 1, E_{BOS}/E_{th} tops at 0.85. Globally, E_{BOS}/E_{th} is close to $E_{el}(\Delta t)/E_{el}$ for different delays Δt, which gives consistency to our results; i.e., for every portion of total E_{el} supplied to the electrodes at a given Δt ($E_{el}(\Delta t)/E_{el}$), a comparable portion of total E_{th} is deposited in the gas (E_{BOS}/E_{th}).

Efficiency measured by SBOS (η_{bos}) is represented versus delay in Figure 5-35 (right). Thermal efficiency at the end of the discharge (η_{th}), measured by calorimetry, is represented as the average for the 14 tests ± one standard deviation. Globally, efficiency is higher at the first moments after the discharge ($\eta_{bos} > \eta_{th}$). As delay is closer to 100 µs, η_{bos} should tend towards η_{th}, as efficiency measured by SBOS and by calorimetry should be equal at the end of the discharge. As η_{bos} is lower than η_{th}, the value of energy deposit may be slightly underestimated by SBOS, compared to the same value for calorimetry. This discrepancy may be due to some factors:

- Shockwave: Energy dissipated by the shockwave is partially included in calorimetry measurements but not in SBOS. Indeed, we supposed isobaric conditions after the occurrence of the shockwave and the associated expansion wave: we measured after the shockwave detaches and before it bounces back to the kernel.
- Temperature: High gradients of refractive index, density and temperature for this discharge have limited resolution. The temperature threshold as kernel boundary detector may cause to underestimate the energy deposit.

Taking into account measurement uncertainties, the low number of valid tests for our post-processing and the low repeatability of the aeronautic discharge, the difference in η_{bos} and η_{th} may be lower in reality. A higher number of valid tests would be necessary for future studies and to confirm and analyze better these differences.

SBOS still provides an insight of the energy deposit in the early stages of the discharge (volume and overall energy), while calorimetry measures the global energy deposit at the end of the discharge.

For each test, from the temperature field we analyze the temperature profile along the axis of the kernel (as in Figure 5-29). Temperature inside the discharge kernel is close to 3700 K for all the tests. Maximum temperature is not affected appreciably by pressure variation, which is explained by the spark plug semi-conductive layer, that lowers breakdown voltage and reduces pressure influence on breakdown. During the interval of time under study (with observed Δt ranging between 25 and 100 µs) the expanding kernel remains at high temperatures because the electrical discharge continues delivering energy to the gas. According to Maly [5] temperature rises during breakdown phase, and electrical energy delivered to the gas after breakdown slows the cooling of the kernel. Temperature profiles along the axis are plotted for the 14 tests in Figure 5-36, grouped by initial pressure (color code). The dashed line in the figure signals the temperature threshold (620 K) chosen for kernel volume and kernel front depth (x_{front}) detection. Each temperature profile in the figure represents a different delay time, which explains the differences in kernel size.

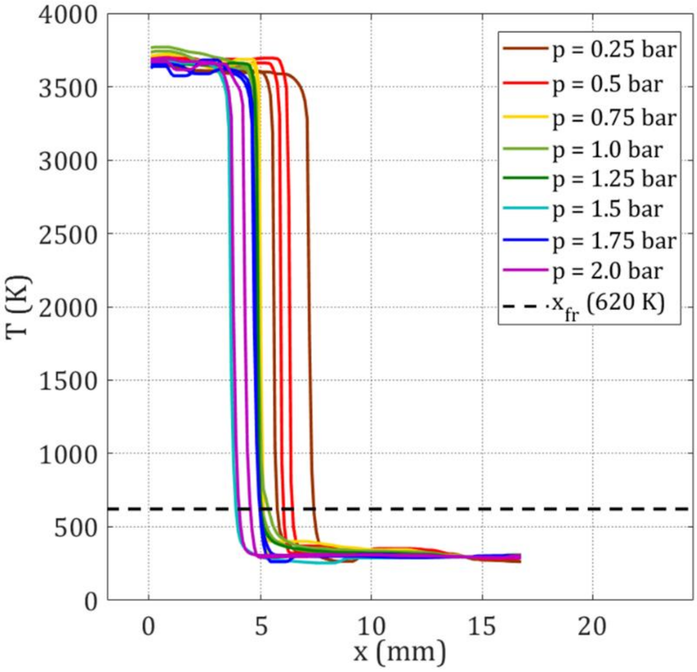

Figure 5-36: Temperature profiles along the kernel axis for 14 tests.

From the temperature fields we estimate kernel size. Kernel size is characterized by the kernel front penetration length x_{front} (obtained from the temperature profile along the axis) and the kernel volume V_{kernel}, which are represented versus pressure in Figure 5-37, grouped by delay ranges Δt_i (colors).

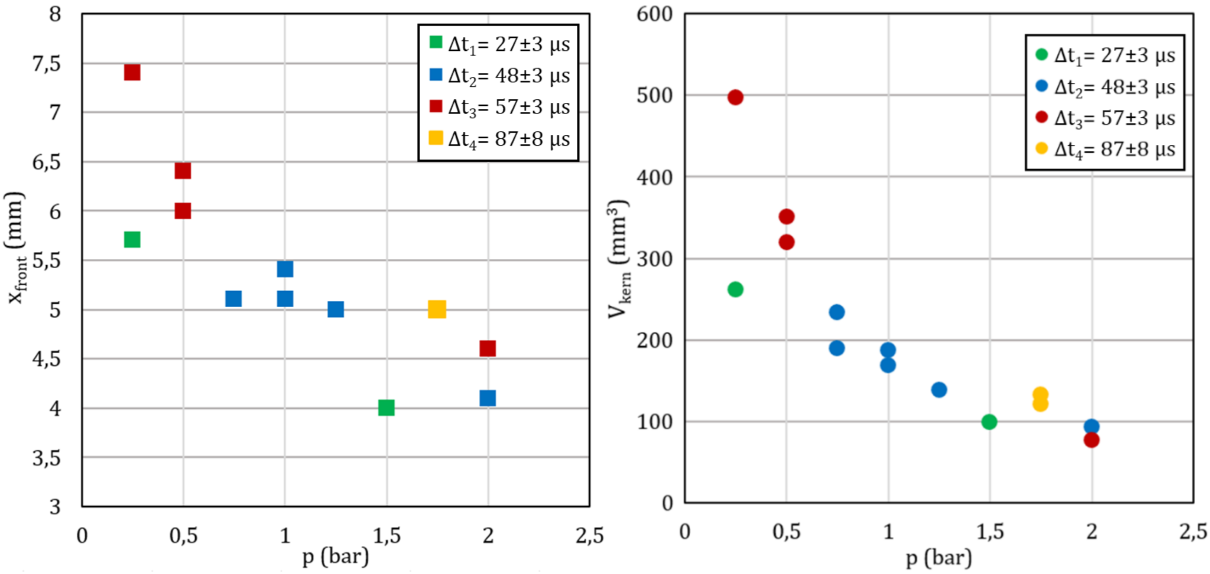

Figure 5-37: Kernel front penetration length and kernel volume versus pressure, at iso-Δt.

Although in terms of energy the initial pressure has little influence on the discharge, it affects considerably the kernel size, as both x_{front} and V_{kernel} decrease with pressure.

5.2.2.4 Density gradient through the shockwave – an approach.

In addition to measuring the energy deposit by the electrical discharge, we also attempt to estimate the density gradient through the shockwave by SBOS. The setup and control parameters used to obtain the displacement field at the kernel are not optimal for the study of the shockwave:

the shockwave width in previous figures is ~0.5 mm; and during the image acquisition gate width t_{gw}, a shockwave travelling at 340 ms^{-1} covers 0.34 mm, so most of the observed shockwave signal is a result of the displacement of the shockwave during the acquisition gate.

As the shock moves, t_{gw} should be short enough that the shockwave appears still; i.e., that the object displaces less than the test resolution during the acquisition time gate. This requirement is expressed in the next equation:

$$x_{measured} = v_{obj}\, t_{gw} \leq s_p \tag{5.3}$$

Where $x_{measured}$ stands for the measured size of the object, v_{obj} for the object speed, and s_p is the system resolution (pixel scale). For our system parameters and the shockwave speed:

$$t_{gw} \leq \frac{s_p}{v_{obj}} = 1\, px_{cam} \frac{1\, px_{real}}{0.5\, px_{cam}} \frac{0.013\, mm}{1\, px_{real}} \frac{ms}{340\, mm} = 76.4\, ns \tag{5.4}$$

In order to have an image of the shockwave with a correct time resolution, $t_{gw} \leq 76.4\, ns$ is needed. Shortening the acquisition gate width reduces the amount of light the camera sensor receives. In a first attempt, we performed a test at $t_{gw} = 75\, ns$. The lower levels of light that correspond to a shorter gate duration reduces the Signal-Noise Ratio (SNR). In the case of $t_{gw} = 75\, ns$, SNR is reduced so much that the kernel and shockwave locations can be confused with noise: the SNR is ~1, with both δ and noise in the order of 0.3 pixels. Figure 5-38 shows the displacement field resulting from the test at $t_{gw} = 75\, ns$. The shockwave is highlighted to properly differentiate it from noise.

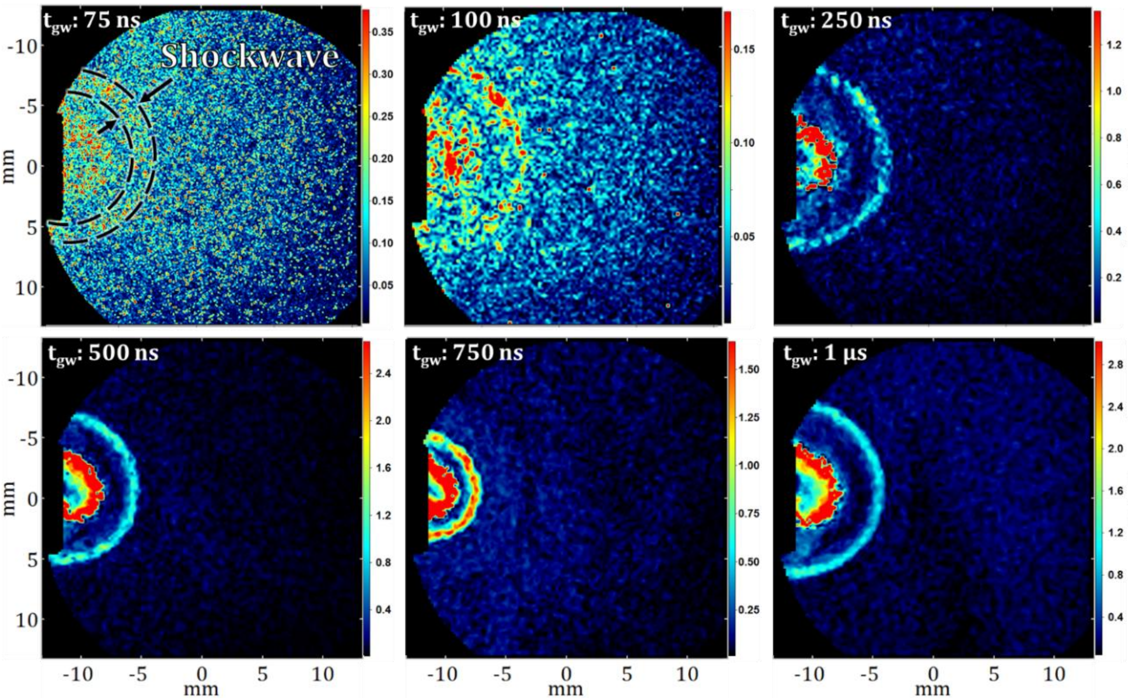

Figure 5-38: Displacement fields with initial hot kernel and shockwave, for different acquisition gate widths.

We performed several tests, with the intermediate t_{gw} to find out setup limit. The obtained displacement fields at 75, 100, 250, 500, 750 and 1000 ns are shown in Figure 5-38. The control parameters for the tests are specified in Table 5-4: the interrogation window size and overlap are reduced for the 75 ns case, as the displacement would be lower. SNR rapidly rises for longer gate width, up to SNR~4 at $t_{gw} = 250\,ns$ (displacement at the shockwave over noise).

t_{gw}	Δt	*Cross-Correlation 1*	*Cross-Correlation 2*
75 ns	22 µs	64x64 px^2, 25% OL, x1	8x8 px^2, 50% OL, x3
0.1 – 1 µs	22-26 µs	64x64 px^2, 25% OL, x1	16x16 px^2, 75% OL, x3

Table 5-4: SBOS control parameters for shockwave-related tests

Shockwave width in the displacement field is not reduced for shorter t_{gw}. The cross-correlation processing, the effect of overlap and interrogation window size thicken the apparent shockwave in the δ field, so we are unable to obtain displacement field with enough resolution to estimate properly the density gradient behind the shockwave.

In order to measure the gradient $\vec{\nabla}\rho$ close to the shockwave, we are limited mainly by three factors: first, the camera speed, as a faster camera (faster as receiving more light per second) would allow to lower the gate width keeping acceptable values of SNR. Second the laser power, as with a more powerful laser the light level with short t_{gw} is higher. A pulsed laser suits the needs for this experiment, as it emits high amounts of energy in a short pulse, hence enough light for the image; and also, the pulse duration would be equivalent to the t_{gw}, as there is no laser light (and thus no signal) but during the pulse duration, even if t_{gw} is longer. Last, image resolution, as the image processing thicken the apparent shockwave higher resolution would allow to reduce this effect.

5.3 Radio-frequency igniter

Innovative radiofrequency (RF) igniters produce a non-equilibrium plasma discharge to initiate combustion. This system has been tested in automobile-engine conditions [24], [25], [27], [126]. The cold-plasma discharge lowers the energy losses, as heat transfer to the electrodes is lower.

The RF system consists in an electronic controller, an electrical transformer and the spark plug. As explained in §2, the RF spark plug has one electrode and a built-in RLC circuit, with a resonance frequency f_R. When the RF spark plug is supplied with a high-tension alternative signal at f_R, it transfers the electrode tip a polarized high voltage. The fast change in the polarization of the high tension ionizes the fluid around the electrode tip, producing a non-equilibrium plasma at low temperature and forming streamers that develop in a multi-branch structure. The electronic controller and the electrical transformer supply the appropriate electrical signal to the spark plug.

5.3.1 Adaptation

The setup is adapted to the radio-frequency spark plug when possible, for our experimental techniques:

5.3.1.1 Electrical measurements

Our ignition system works with an input signal of adjustable voltage, with $f_R = 3.58\, MHz$. The electronic controller regulates voltage at the primary of the electric transformer, from 70 to 110 V, and the discharge duration, from several hundreds of µs to several ms. The electronic controller requires an input square signal of 5 V amplitude and $f = f_R$.

We dispose of current and voltage probes, connected at the secondary of the high-voltage transformer. This enables the measure of the electrical energy delivered to the spark plug, E_{el}. To analyze the energy transfer from the spark plug point to the fluid, we would need to connect the electrical probes at the electrode tip, but it would short circuit the electric circuit, affecting the discharge. Figure 5-39 shows electrical measurements for a 0.5 ms discharge and a voltage of 90 V at the electrical controller: at the timescale of the whole discharge (on the left) and the timescale of the 3.58 MHz signals oscillations (on the right).

From the electrical measurements, we directly obtain the electrical energy supplied to the spark plug as the integral of the electric power $E_{el} = \int U\, I\, dt$. The electric power remains almost the same, $P = 86.3\, W$ during the whole discharge duration, as we can see in the constant slope of the electrical energy E_{el}, represented in Figure 5-40. E_{el} at the end of the discharge is $E_{el} = 45.8\, mJ$. Compared to the 13.5 kW as maximum power from the helicopter igniter, this discharge is a low-power discharge.

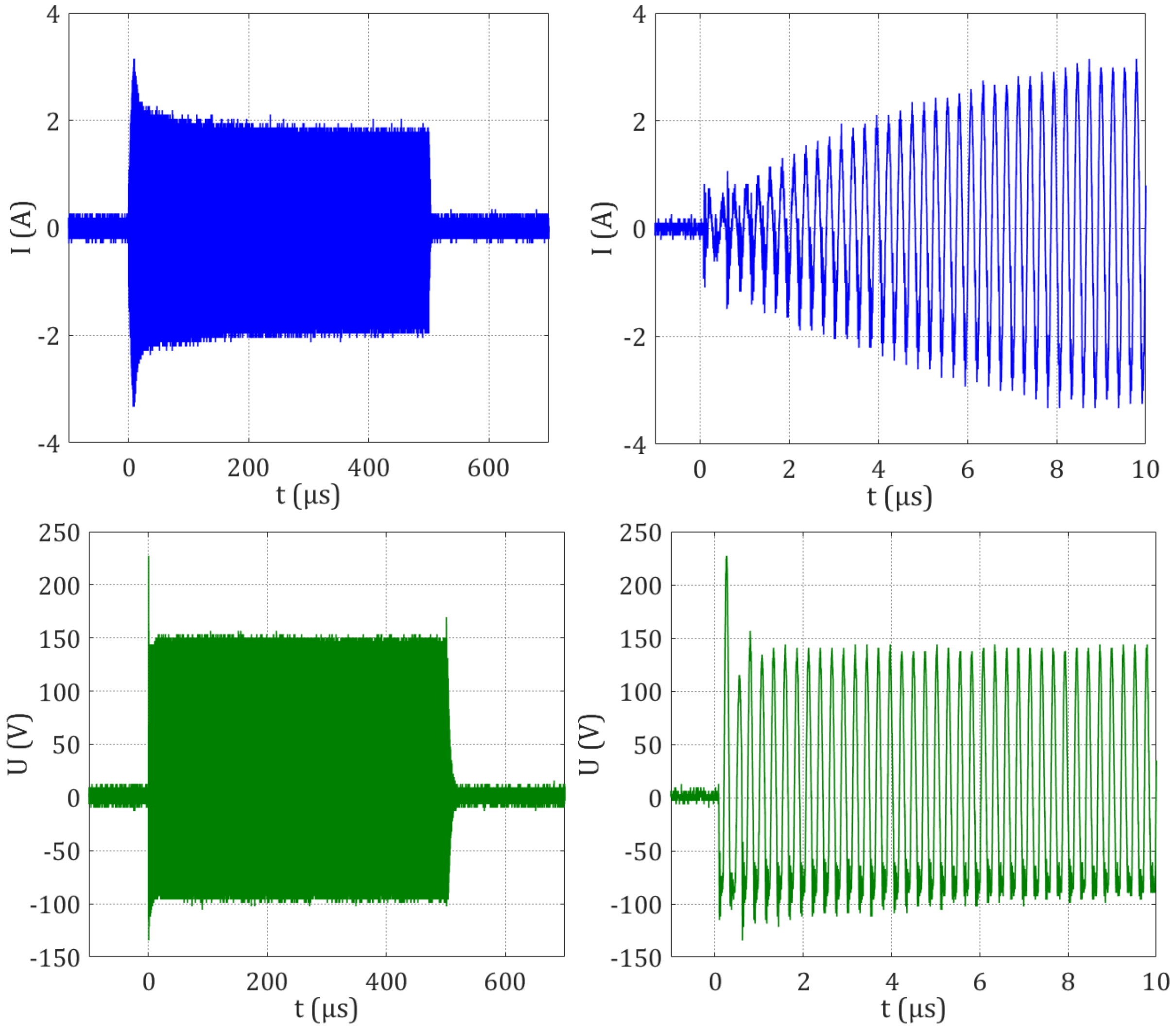

Figure 5-39: Electrical signals during RF discharge

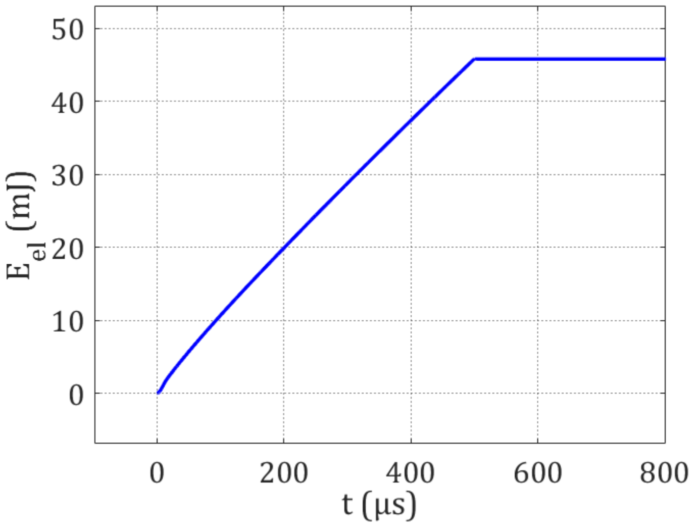

Figure 5-40: Electrical energy supplied to the RF spark plug, controller voltage of 90 V for 0.5 ms.

5.3.1.2 Calorimetry

We test the RF spark plug inside a constant volume chamber. The experimental chamber is cylindrical (Ø 60 mm x 35 mm), with a 99 ml volume and made of POM-C; it is similar to the one depicted in Figure 5-3. The spark plug is placed in the flat wall, with the pressure transducer in the other end of the chamber.

The high electric field during the radio-frequency discharge saturates the pressure transducer amplifier, so we cannot measure the pressure rise during the discharge. After the discharge ends the electromagnetic interference disappears, and then we obtain the mean pressure rise. We estimate the pressure rise as the increase from the initial level before the discharge to the average pressure in a 1 ms window after the discharge ends (t=0.5 ms). The pressure signal is presented in Figure 5-41, for several milliseconds after discharge on the left, and at a shorter timescale on the right, with a detail on the pressure rise calculation. Pressure signal is filtered by a moving-average filter to highlight the pressure decay after the discharge.

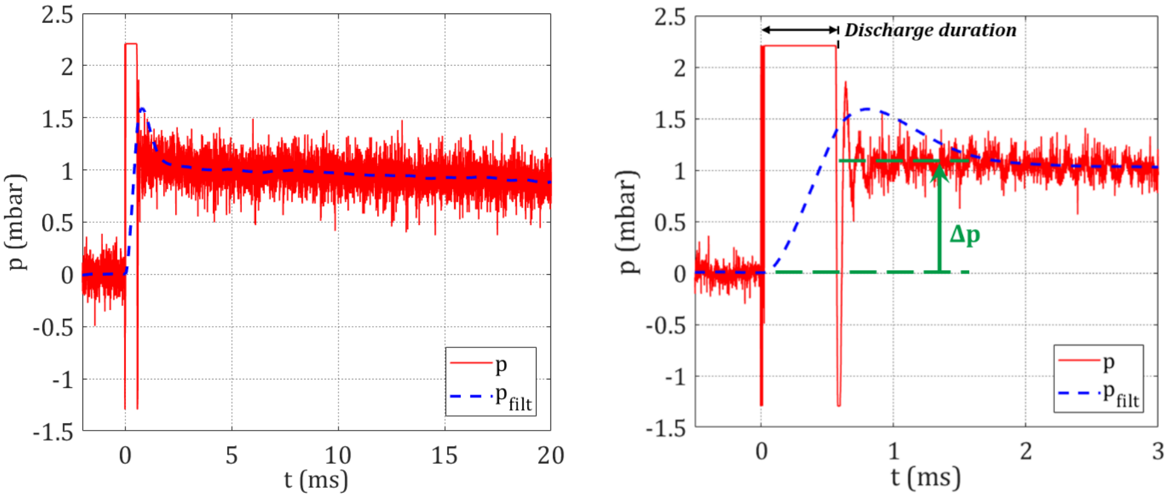

Figure 5-41: Pressure signal during a radiofrequency discharge of E_{th} = 26.6 mJ at 1 bar.

The pressure difference of the figure, $\Delta p = 1.1\, mbar$ in the 99 ml chamber, corresponds to an energy deposit $E_{th} = 26.6\, mJ$.

5.3.1.3 SBOS

In the RF discharge the streamers develop into irregular ramifications, so the origin of the discharge kernel is strongly asymmetric. Axis-symmetry is a necessary condition for us to solve the back-projection problem in the SBOS image processing, so we cannot use the SBOS technique for this type of discharge. Furthermore, the non-equilibrium plasma produced by the RF discharge (cold-plasma) presents a high degree of ionization at low temperatures. Thus, there is a high electron density at low temperatures too, so the Gladstone-Dale relation requires an adapted model for $\rho_e(T)$ in order to obtain the temperature from the refractive index field.

5.3.2 Results and discussion

A complete parametric study of the radio-frequency discharge was carried out by Auzas [24]. In this PhD dissertation the discharge formation, spatial development and electrical properties are characterized. The thermal energy deposit in the fluid was not measured in that study though. An example of multi-filamentary discharge is shown in Figure 5-42 [24], showing the influence of pressure on the discharge structure and spatial development.

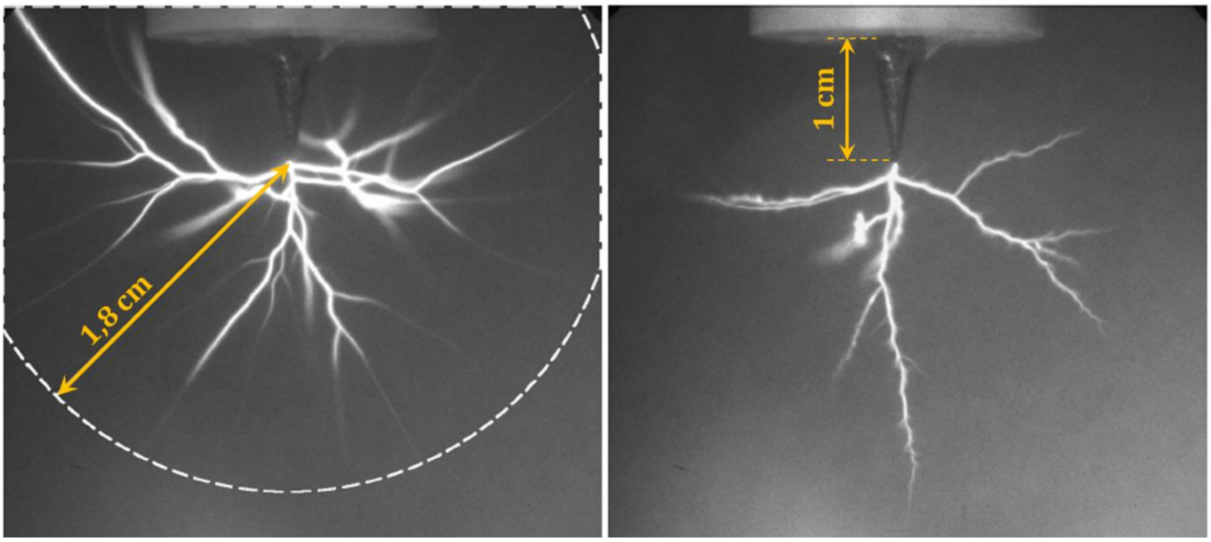

Figure 5-42: Radio-frequency discharge at 1 bar (left) and at 5 bar (right) [24].

We perform 3 sets of experiments, for three different voltage levels at the electronic controller and the same discharge duration of 0.5 ms. E_{el} and E_{th} are measured for 5 tests at 90 V, 3 at 120 V, 4 at 140 V, in air at atmospheric conditions (293 K, 1 bar). We also obtain the spark plug efficiency E_{th}/E_{el}. The results are represented in Figure 5-43:

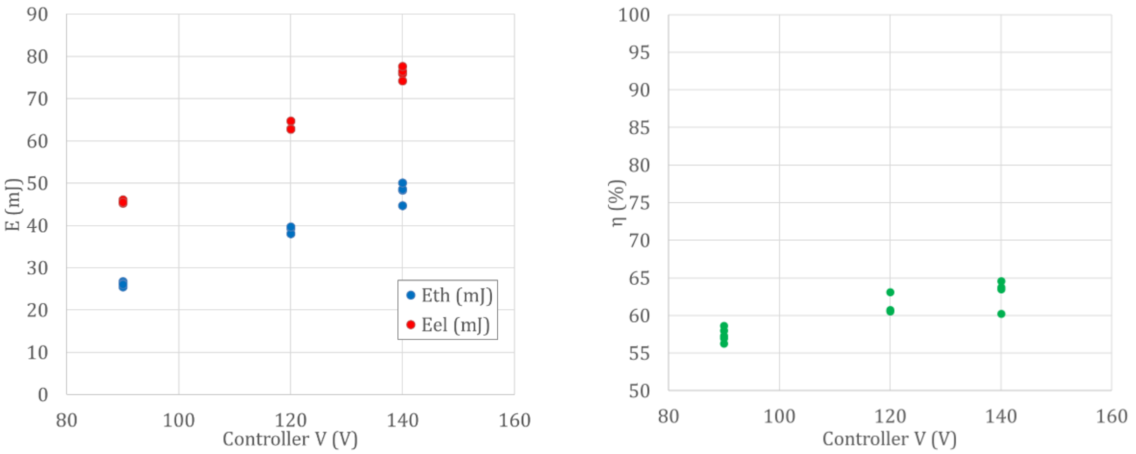

Figure 5-43: Experiments in air for the RF igniter, E_{el} and E_{th} (left) and η (right) versus controller voltage.

Energy increases linearly with voltage at the controller, with E_{th} ranging from 25 to 50 mJ and E_{el} ranging from 45 to 78 mJ. A wide interval of energy deposit can be obtained by regulating controller voltage and duration. Efficiency of the spark plug is close to 60%, increasing for higher voltage values at the controller.

The spark plug internal resistance should be considered, as it dissipates a part of the electrical energy supplied to the spark plug. This electrical energy supplied to the electrode pin would then be: $E_{pt} = E_{el} - R\, I^2$. We could not measure the internal resistance. The energy transfer efficiency from the electrode pin to the fluid is expected to be higher than the spark plug efficiency.

The high efficiency of the radiofrequency spark plug (~60%) compared to the pin-to-pin electrodes with TCI system (~20%) or the helicopter igniter (~20%) is due to the reduced heat losses produced in the discharge, because of the nature of the discharge and the spark plug setup. As it is a low temperature plasma discharge, the temperature of the molecules of gas in the discharge kernel is much lower than in equilibrium plasma discharges: energy is mainly deposited through electronic excitation instead of full ionization, thus ions and molecules of gas are not directly heated. Then the difference of temperature between the electrode and the molecules of the discharge kernel is greatly reduced compared to equilibrium plasma discharge, so are the heat losses. On top of that, the RF discharge produces a discharge kernel with only a small fraction of its volume in contact with the single electrode, which also explains the reduced heat losses.

5.4 Conclusion

Pressure-rise calorimetry and SBOS techniques are applied to a helicopter engine igniter and a radio-frequency igniter. The discharges produced by these igniters are studied by measuring the electrical energy they deliver to the spark plug, the thermal energy deposit in the fluid, the energy transfer efficiency and the spatial characterization of the discharge.

The energy deposited in the fluid by the Ardiden 3 helicopter engine igniter is measured by calorimetry, in air and different gas mixtures, for a range of initial pressures from 0.25 to 2.0 bar. Both the electrical energy supplied to the spark plug and the energy deposit remaining in the fluid at the end of the discharge differ from the values that typically describe the ignition system, which is the energy input for the system.

For our ignition system with an electrical input of 2 J (from the power source), at the spark plug electrical energy is on average $E_{el} = 624 \pm 49\, mJ$ (± one std). The energy deposit in the gas by the discharge, measured for the first time by calorimetry, is $E_{th} = 85 \pm 7\, mJ$, for a discharge duration of 250 μs. The discharge is too short to allow energy deposit measurement over time during the discharge , so the energy is estimated as the global deposit after the discharge ends. This yields an efficiency of $\eta = 13.7 \pm 0.4\%$.

Tests at different initial pressures showed that there is low influence of pressure over E_{th} and η. The presence of fuel, tested by experiments in propane-nitrogen mixtures, lower the energy deposit around 10 mJ, and the efficiency at 2%.

The Ardiden 3 igniter is also studied by SBOS, after adapting the methodology to the discharge characteristics in terms of size, energy, and light emission. The discharge kernel evolution shows the kernel structure in the first moments of the discharge, from 20 μs up to 8.5 ms after the discharge start. The reconstruction of the temperature field by SBOS requires an axis-symmetric field, so from kernel evolution images we set the valid window for image acquisition delay for complete SBOS processing between 25 and 100 μs. Refractive index, temperature, density and enthalpy distributions are estimated for discharges in air in different pressures, and the energy deposit. The influence of pressure over the discharge energy is too low to be observed in the results, as there is a variability in the energy deposit. Nevertheless, initial pressure directly affects the discharge kernel size, as both the kernel volume and kernel penetration depth decrease for higher initial pressures.

A radio-frequency igniter is characterized by calorimetry for a 0.5 ms discharge. As the discharge produces a non-equilibrium plasma that develops into a three-dimensional multi-branch structure, we could not measure gas conditions by SBOS for this igniter. We performed calorimetry experiments for different energies in air, yielding E_{el} ranging from 45 to 78 mJ of electrical input to the spark, and E_{th} ranging from 25 to 50 mJ. These values were obtained by changing the discharge duration and supply voltage. The efficiency of this type of discharge is much higher than for conventional sparks, with an spark plug efficiency of $\eta > 60\%$.

Conclusion and perspectives

Research and development in air transport is nowadays oriented towards increasing efficiency and reducing pollutant emissions. Aircraft propulsive systems have been optimized to a point where there is little margin for further improvement. New engine concepts that employ different thermodynamic cycles are potentially more efficient but are still under development.

Successful ignition of these aeronautic engines in different conditions is a crucial issue for engine manufacturers: the ignition system must perform properly even in challenging conditions, such as in-flight re-ignition using lean mixtures or ignition in engine configurations which differ from traditional engines.

Spark ignition systems are generally defined by the electrical energy input used to operate them. Little information has been published about the properties of the electrical discharge that produces the hot gas kernel needed to ignite the fuel-gas mixture in gas-turbine engine applications. A better understanding of the electrical discharge and energy deposit produced by modern aeronautic ignition systems would provide essential knowledge for combustion simulation and for the design of new engines.

Summary

This work is focused on the characterization of the thermal energy deposit of electrical discharges, and on the development of different methodologies dedicated to this purpose. It was carried out at the Institut Pprime and financed by Nouvelle Aquitaine region, and collaborated with the CAPA industrial research project and Radiμs research programs.

The properties of the discharge that we needed to measure were the energy deposit delivered to the fluid by the discharge, the electrical properties of the electrical discharge (current, voltage, duration and energy supplied to the electrodes), and the spatial distribution of gas properties at the discharge (kernel evolution over time, discharge kernel volume and gas temperature and density fields).

Chapter 1 first presented the principles of electrical discharges and spark ignition and then described the state-of-the art on spark ignition research. When the electrical voltage between two electrodes increases, the electrical field in the inter-electrode gap rises. As the voltage reaches the breakdown value for the gas conditions, the gas in the gap is ionized and a conductive channel forms in an equilibrium plasma discharge. Electrical energy stored in the gap discharges then in the fast breakdown phase, and if the electrical circuit connected to the electrodes has more energy stored, this energy discharges in the following arc and glow phases. Electrical energy is then transformed into thermal energy at the discharge hot kernel, producing also ionized species of gas molecules that start and enhance combustion.

Commercial automobile ignition systems use either an electrical capacity (CDI systems) or a coil (TCI systems) to produce electrical discharges, while gas turbine engine igniters consist on a high energy capacitive system and a coaxial spark plug. Other ignition systems, currently in the final steps of development, utilize non-equilibrium plasmas or laser for ignition. A non-equilibrium plasma discharge takes place if the voltage is increased at a fast-enough rate.

A bibliographic review revealed that although many published works on the electrical discharges characterize discharge properties, kernel evolution, and – to a lesser extent – energy transfer from electrical supply to thermal deposit; experimental works on available ignition systems rarely study simultaneously the thermal energy deposit and the kernel evolution. In many ignition studies, the spark energy is still characterized as the electrical energy supply to the electrodes (E_{el}) or as the energy stored in the capacitor of the electrical circuit (E_c). Instead, the thermal energy deposit in the gas (E_{th}) is desirable for electrical discharge and ignition modeling, as it is needed to start the simulations or verify the results, together with early kernel spatial evolution. The energy transfer is produced differently in the different discharge phases, and only a few studies measured arc and glow phase efficiencies. This motivated the research for experimental methodologies able to fully characterize electrical discharges and kernel formation for existing and new ignition systems.

Chapter 2 presented electrical discharges under study in this thesis and the choice of experimental methods, materials and setups. Three different electrical discharge systems were employed: first, an academic configuration of pin-to-pin electrodes with an inductive TCI pencil coil system. This system can supply an E_{el} from ~10 to 50 mJ in a duration of 1-3 ms, depending on experimental conditions. Second, a helicopter engine ignition system that uses a coaxial spark plug. This high-energy system supplies an E_{el} value of around 700 mJ in a duration in the order of ~100 μs. Third, a radio-frequency spark plug igniter. This system can be regulated to supply a wide range of E_{el} from ~30 to 200 mJ, in 0.1 to 5 ms.

The experimental methods chosen for the study were the pressure rise calorimetry and the Speckle-based Background Oriented Schlieren (SBOS). Pressure rise calorimetry measures the thermal energy deposit E_{th} transferred to the fluid by the electrical discharge, electrical measurements estimate the electrical energy supplied to the electrodes E_{el}, and SBOS measures the spatial distribution of density gradients at a chosen instant during or after the discharge.

The experimental setup was composed by a test chamber that holds the electrodes and a differential piezo-resistive pressure transducer. Different test chambers were available, with an inner volume of 6 or 20 ml, to reduce measurement uncertainties for low-energy or high-energy discharges. The test chamber was contained inside a larger chamber that serves as reference pressure, with a larger volume of gas (0.64 L). Both chambers were connected by a by-pass valve, which was open to change pressure or gas for the experiments and closed during tests. Electrical probes measured voltage and current at the electrodes. The system had optical access through windows on the sides of the two chambers, enabling the implementation of the SBOS method simultaneously to the pressure calorimetry measurements. The setup consisted of a series of lenses, a diaphragm and intensified CCD camera; placed at different distances to set the system optical magnification, speckle size and defocusing distance. The subjective speckle pattern background was generated by the interaction of a collimated laser beam from a diode-pumped continuous solid-state laser, a ground glass, the lenses and camera sensor.

Chapter 3 presented the pressure rise calorimetry methodology for the study of electrical discharges produced by a pin-to-pin electrodes and TCI pencil-coil setup. Calorimetry, coupled with electrical measurements, globally characterized the electrical discharge in a pin-to-pin electrodes configuration. E_{th} was calculated from the increase in transient pressure inside a 6 ml constant volume vessel during the discharge, using a piezo-resistive differential pressure transducer. Simultaneously, electrical current and voltage were measured with respective current and voltage probes to obtain the electrical energy supplied to the electrodes E_{el}. Measurement uncertainties were under 15% for E_{th} and under 4.1% for E_{el}.

The effects of control parameters E_{el} and inter-electrode gap on the electrical discharge were studied in air at atmospheric conditions (1 bar and 293 K). Electrical energy E_{el} was set varying the TCI pencil coil charge time set by the discharge trigger. Coil charging time varied from 0.5 to 5 ms, with saturation of the TCI at 3.5 ms and no changes for charging times longer than saturation time. E_{el} increased with charging time from 6 to 42 mJ, with E_{th} also increasing from 2 to 10 mJ. The ratio of E_{th} over E_{el}, which is the energy transfer efficiency η, decreased with charging time, from 34% to 25%. Inter-electrode gap affected greatly the energy transfer, as the longer the gap the more gas molecules there are between the electrodes. E_{el} and E_{th} values increased with increasing gap: from 37 and 7.5 mJ at 1 mm gap respectively to 45 and 15 mJ at 3 mm gap; in average.

Energy transfer efficiency η also increased with gap, from 19% at 1 mm gap to 33% at 3 mm. An analysis of the phases of the discharge showed that for longer gap distance there is a higher portion of the energy transferred in arc phase and less in glow phase. This affected the global efficiency of the discharge, together with the decrease in energy losses with increasing gap. The efficiencies for each discharge phase were estimated for different gap distances, with η_{arc} and η_{glow} of 55% and 25% respectively at 2 mm gap.

The effects of pressure and gas composition on the discharge were also studied. Tests were performed at 0.5, 1, 1.5 and 2 bar; in air and in two inert nitrogen-propane mixtures with different molar fraction of propane. Pressure affected the discharge in a similar way as gap distance: E_{th} and η increased for increasing pressure, and a higher portion of the discharge occurred in arc mode. Breakdown energy was also higher for higher pressure, with higher breakdown voltage values. In presence of fuel the same tendency with pressure was observed. The proportion of arc phase of the total discharge increased much in presence of fuel, with more than a 80% of E_{el} corresponding to the arc phase at higher pressures and propane mixtures, while this value was under 60% in air.

Chapter 4 presented the development of the SBOS technique for electrical discharges from pin-to-pin electrodes and the measurements of the instantaneous spatial distribution of gas properties in the discharge kernel in different conditions. SBOS is a visualization method that yields the spatial distribution of density gradient at a chosen time. A reference image of a background pattern was compared with another image of the pattern disturbed by the electrical discharge. We used a speckle background pattern generated by laser to improve resolution at the size of the electrical discharge kernel. The displacement of the points in the background pattern was caused by gradients in the refractive index.

From the displacement field, we calculated the refractive index gradient and the density gradient field using the Gladstone-Dale relation. The density field integrated through the line-of-sight was obtained from the Poisson integral of the divergence of the density gradient. Filtered back-projection yielded the density field. For a semi-ideal gas behavior, temperature field is obtained directly from density field, and then the local enthalpy distribution is evaluated. The discharge hot kernel size is estimated from the temperature field, and in particular its maximum radius and its volume. Finally, the volume integral of the enthalpy distribution yields the energy deposit.

SBOS methodology was first validated using a CO_2 jet. The jet was chosen for it had an absolute difference of refractive index with atmospheric air representative of a hot gas kernel from an electrical discharge and the same characteristic size. A set of 100 tests was performed. Density distribution on the jet was obtained and matched the reference value for CO_2 with very low error ($<$ *0.6%*). For the application to electrical discharges, SBOS measurement uncertainties were estimated to be under 6.2% for temperature and density distribution. The uncertainty of the energy deposit obtained by SBOS (E_{BOS}) was in the order of ~12%.

Then the SBOS technique was applied to electrical discharges produced by pin-to-pin electrodes. The influence of gap distance, the time evolution of the discharge kernel and the energy deposit were analyzed in atmospheric conditions first. For longer gap distances, kernel temperature was higher at the end of the discharge, as it reached 900 K for 2 mm gap and 750 K for 1 mm gap. Longer gap distance was associated to a larger volume of the hot kernel too. Kernel evolution was studied with series of tests measuring kernel properties at 0.5 to 2.5 ms after the discharge onset. Kernel temperatures were higher at the first instants of the discharge, with a maximum temperature of 1200 K at 0.5 ms after the discharge onset. Then the kernel cooled down to 1000 K at 2.5 ms even while the discharge was still going on. Kernel expanded fast during the first instants, with an increase of the kernel radius about 1 m/s between the first time frames and slower later on, at 0.3 m/s. E_{BOS} was measured during kernel evolution and compared to simultaneous E_{th} measurements by calorimetry. Even though SBOS slightly overestimated the energy deposit, differences between E_{BOS} and E_{th} were in the order of measurement uncertainties, so both techniques provided good estimates of the energy deposit.

The effects of pressure and gas composition were tested, for air and two N_2-C_3H_8 mixtures in 8 different conditions: 1 mm and 2 mm gap and 4 different initial pressures of 0.5 to 2.0 bar. Temperature and energy deposit increased and kernel size decreased with higher pressures: at the end of the discharge kernel temperature was around 900 K for 2 bar, while it was lower than 600 K at 0.5 bar in air. Discharges in nitrogen-propane mixtures reached higher temperatures than in air at the end of the discharge, with temperatures over 1100 K at 2.0 bar. Tests with propane mixtures presented high variability of kernel shapes, some of which could not be processed as only axis-symmetric distributions were valid for our SBOS methodology. Kernel volume decreased linearly with pressure as density is higher: at 2.0 bar, kernel volume is half of the kernel volume at 0.5 bar. The energy deposit was estimated for all the tests in air and propane mixtures. These results were compared to simultaneous measurements of the energy deposit by calorimetry. Both SBOS and calorimetry data showed the same trend: energy deposit increased with gap and pressure, and also in the presence of fuel. Differences in the values provided by SBOS and calorimetry were within the range of uncertainties cumulated for the two methods.

Chapter 5 presented the application of the developed methodologies to the characterization of a gas turbine engine igniter. Both pressure rise calorimetry and SBOS were first adapted to the characteristics of the helicopter igniter: high power and energy with a shorter discharge duration that produce a larger kernel volume. These techniques were then applied to the study of this electrical discharge for the first time. Thermal energy deposit was obtained by calorimetry, and spatial distribution of thermodynamic properties in the spark kernel were obtained by SBOS. Tests were performed in air and different gas mixtures, for a range of 8 initial pressures from 0.25 to 2.0 bar.

Calorimetry tests revealed that both the electrical energy supplied to the spark plug and the energy deposit remaining in the fluid at the end of the discharge differ from the values that typically describe the ignition system, which is the energy input for the system. For our ignition system with an electrical input of 2 J (from the power source), at the spark plug electrical energy was on average $E_{el} = 624 \pm 49\, mJ$ (± one std) in air and 1 bar. The energy deposit transferred to the gas by the discharge, measured for the first time by calorimetry, was $E_{th} = 85 \pm 7\, mJ$, for a discharge duration of 250 μs. Most of the electrical energy E_{el} was supplied in the first instants, with E_{el} about ~95% of the total E_{el} already 100 μs after the discharge onset. The discharge was too short to allow energy deposit measurement over time during the discharge, so the energy was estimated as the global deposit after the discharge ended. This yielded an efficiency of $\eta = 13.7 \pm 0.4\%$ for the energy transfer from the igniter electrodes to the fluid.

The helicopter igniter presented was not significantly affected by changes in experimental conditions, compared to the pin-to-pin electrodes and TCI configuration. Tests in air varying with initial pressure showed that the energy deposit increased in average from $74 \pm 8\, mJ$ at 0.25 bar to $94 \pm 8\, mJ$ at 1.75 bar, with values for E_{th} that overlapped at different pressures (E_{th} around 80 mJ was obtained for some of the tests in any pressure). The increase in η was of only 2% from 0.25 to 2.0 bar. The semi-conductive coating of the spark plug isolation was the reason for the low effect of pressure. The semi-conductor set the breakdown voltage to around 700 V, which otherwise greatly change with pressure. The presence of fuel lowered the energy deposit around 10 mJ and the efficiency around 2%.

SBOS methodology allowed us to track the discharge kernel evolution and to estimate gas properties and the energy deposit. SBOS was first adapted to the discharge characteristics in terms of size, energy, and light emission. Then the kernel structure was analyzed during kernel evolution, varying the image delay from 20 µs up to 8.5 ms after the discharge start. The reconstruction of the temperature field by SBOS required an axis-symmetric field, so the valid window for image acquisition delay for complete SBOS processing was set between 25 and 100 µs, from kernel evolution images. Refractive index, temperature, density and enthalpy distributions were estimated for discharges in air in different pressures, and the energy deposit. Temperature inside the hot kernel was about 3750 K for the valid tests. The influence of pressure over the discharge energy was too low to be observed in the results, as there was a variability in the energy deposit. Nevertheless, initial pressure affected the discharge kernel size directly, as both the kernel volume and kernel penetration depth decreased for higher initial pressures.

Lastly, a radio-frequency igniter was characterized by calorimetry for a 0.5 ms discharge. As this igniter produced a non-equilibrium plasma discharge that develops into three-dimensional multi-branch structures, SBOS was not applied to this igniter. We performed calorimetry experiments for different energies in air, yielding $\mathrm{E_{el}}$ ranging from 45 to 78 mJ of electrical input to the spark, and $\mathrm{E_{th}}$ ranging from 25 to 50 mJ. These values were obtained by changing the discharge duration and supply voltage. The efficiency of this type of discharge was much higher than for conventional sparks, with a spark plug efficiency of $\eta > 60\%$.

Conclusion

This paragraph remarks the main findings and conclusions of this thesis:

- We adapted and developed two methodologies to the study of electrical discharges: pressure rise calorimetry, that provided a global measurement of the energy deposit in the gas E_{th}; and SBOS, that allowed us to calculate the spatial distributions of density, temperature and enthalpy at a chosen time after the discharge start, as well as the energy deposit in the gas up to that time E_{BOS}.
- Calorimetry was applied to discharges in a pin-to-pin electrodes and TCI configuration. The energy deposit E_{th} that was transferred to the fluid by an electrical discharge ranged from 7 to 18 mJ, with an electrical energy supplied to the electrodes E_{el} from 33 to 48 mJ. The energy transfer efficiency η was about 20 to 40%. E_{th} and η were increased with pressure and inter-electrode gap distance. The increase in the efficiency was due to reduced losses with high pressure or gap and to a higher proportion of the discharge produced in the arc mode. The presence of fuel, tested with propane-nitrogen mixtures, increased further the energy deposit E_{th} and the efficiency η.
- Speckle-based Background-Oriented Schlieren was adapted for the study of discharges in the same pin-to-pin configuration. Refractive index, density and temperature distributions of the discharge kernel were obtained for different moments of the discharge in air and at the end of the discharge in multiple experimental conditions of pressure and gas mixtures. Temperature is higher at the beginning of the discharge, and is affected by the initial pressure, the inter-electrode gap and the gas composition, reaching over 1400 K in some conditions. The energy deposit E_{BOS} was estimated and compared with simultaneous calorimetry results. Estimation of the energy deposit by two methods based on different physical properties yielded good results, with differences within the uncertainty interval of the methodologies.
- For the first time, calorimetry was applied to the study of a gas-turbine engine igniter: the Ardiden 3 helicopter engine igniter. This ignition system had a nominal input energy to the electrical system of 2 J. However, the electrical energy supplied to the electrodes per discharge were about 625 mJ, and the energy deposit to the gas was of 85 mJ; with an efficiency under 14%, even for the short duration of 250 μs. A semi-conductive coating on the spark plug insulation lowers the breakdown voltage, reducing greatly the influence of pressure and gas composition on the discharge characteristics.
- The discharge kernel produced by the helicopter igniter was studied by SBOS. Temperatures inside the kernel were measured to be up to 3700 K, 50 μs after discharge onset. This discharge was not significantly affected by changes in pressure.

Perspectives

The present study proposes experimental methodologies to characterize spark discharges at spark ignition. It also provides valuable insights about the energy transfer from the electrical system to the fluid during spark ignition and the characteristics of the hot discharge kernel, both for a pin-to-pin electrodes configuration and for a helicopter igniter. To complete the characterization of the ignition phase, additional tests should be performed, some of them would lead to experimental conditions closer to engine conditions:

- As a first step, stagnant gas mixtures were considered, but at the combustion chamber aerodynamics play an important role. The experimental setup could be adapted to study crossflow conditions and how they affect the energy deposit and kernel formation.
- In-depth study of the discharge phases: breakdown, arc and glow discharge phases were studied for commercial ignition electrical circuits. A more fundamental study would be possible limiting electrical voltage to produce a discharge composed of breakdown plus arc or glow. Calculation of the efficiency of the discharge phases in different experimental conditions would be more direct using this approach.
- In this study we used experimental chambers with reduced volume to have high sensitivity in our measurements and low uncertainties, and simultaneous calorimetry-SBOS tests to obtain results for the energy deposit in the gas. However, the proximity of the chamber walls to the discharge kernel could affect kernel development, especially in the case of the helicopter igniter. SBOS tests in a large chamber or in open air would study discharge kernel projection without the effect of confinement.
- For the Ardiden 3 helicopter engine igniter, the temporal jitter and the asymmetries made impossible to process a high proportion of the SBOS tests. A higher number of tests would be necessary to have more representative SBOS results.
- The application of calorimetry to the radio-frequency discharge showed that it is possible to characterize this type of discharge. The application of SBOS to the radio-frequency discharge would require an adapted non-equilibrium plasma ionization model for the Gladstone-Dale relation, and the use of more cameras to assess asymmetries. A full parametric study of the radio-frequency discharge was out of the scope of this work, but it could be performed using these methods.

Bibliography

[1] Advisory Council for Aviation Research and innovation in Europe (ACARE), "Flightpath 2050 Europe's vision for aviation," 2011.

[2] R. Maly, "Spark Ignition: Its Physics and Effect on the Internal Combustion Engine," *Fuel Econ. Road Veh. Powered by Spark Ignition Engines*, no. 4, pp. 91–148, 1984.

[3] R. R. Maly and R. Herweg, "Spark Ignition and Combustion in Four-Stroke Gasoline Engines," in *Flow and combustion in reciprocating engines*, C. Arcoumanis and T. Kamimoto, Eds. Berlin, Heidelberg: Springer Berlin Heidelberg, 2009, pp. 1–66.

[4] Y. P. Raizer, *Gas discharge physics*. 1991.

[5] R. Maly and M. Vogel, "Initiation and propagation of flame fronts in lean CH4-air mixtures by the three modes of the ignition spark," in *Symposium (International) on Combustion*, 1979, vol. 17, no. 1, pp. 821–831.

[6] J. S. Townsend, "The conductivity produced in gases by the motion of negatively-charged ions," *Nature*, vol. 62, no. 1606, pp. 340–341, 1900.

[7] E. Sher, J. Ben-Ya'ish, and T. Kravchik, "On the birth of spark channels," *Combust. Flame*, vol. 89, no. 2, pp. 186–194, 1992.

[8] J. M. Meek and J. D. Craggs, *Electrical Breakdown of gases*. 1953.

[9] P. Tardiveau, E. Marode, A. Agneray, and M. Cheaib, "Pressure effects on the development of an electric discharge in non-uniform fields," *J. Phys. D. Appl. Phys.*, vol. 34, no. 11, pp. 1690–1696, 2001.

[10] D. B. Go and A. Venkattraman, "Microscale gas breakdown: Ion-enhanced field emission and the modified Paschen's curve," *J. Phys. D. Appl. Phys.*, vol. 47, no. 50, 2014.

[11] G. Meng *et al.*, "Demonstration of field emission driven microscale gas breakdown for pulsed voltages using in-situ optical imaging," *Phys. Plasmas*, vol. 25, no. 8, 2018.

[12] B. Saggau, "Kalorimetrie der drei Entladungsformen des elektrischen Zündfunkens," *Arch. für Elektrotechnik*, vol. 64, no. 3–4, pp. 229–235, May 1981.

[13] K. Eisazadeh-Far, F. Parsinejad, H. Metghalchi, and J. C. Keck, "On flame kernel formation and propagation in premixed gases," *Combust. Flame*, vol. 157, no. 12, pp. 2211–2221, 2010.

[14] P. J. Bruggeman, F. Iza, and R. Brandenburg, "Foundations of atmospheric pressure non-equilibrium plasmas," *Plasma Sources Sci. Technol.*, vol. 26, no. 12, Nov. 2017.

[15] G. Meyer and A. Wimmer, "A thermodynamic model for the plasma kernel volume and temperature resulting from spark discharge at high pressures," *J. Therm. Anal. Calorim.*, pp. 1–11, 2018.

[16] R. R. Maly, “State of the art and future needs in S.I. engine combustion,” *Symp. Combust.*, vol. 25, no. 1, pp. 111–124, 1994.

[17] ATSM, “Standard test method for minimum ignition energy and quenching distance in gaseous mixtures.” ASTM Int, 2007.

[18] B. Sforzo, J. Kim, J. Jagoda, and J. Seitzman, “Ignition Probability in a Stratified Turbulent Flow With a Sunken Fire Igniter,” *J. Eng. Gas Turbines Power*, vol. 137, no. 1, p. 011502, Aug. 2014.

[19] N. S. Okhovat, J. M. Hauth, and D. L. Blunck, “Temperatures of Spark Kernels Discharging into Quiescent or Crossflow Conditions,” *J. Thermophys. Heat Transf.*, vol. 31, no. 1, pp. 120–129, 2016.

[20] S. M. Starikovskaia, “Plasma assisted ignition and combustion,” *J. Phys. D. Appl. Phys.*, vol. 39, no. 16, pp. R265–R299, Aug. 2006.

[21] A. Starikovskiy and N. Aleksandrov, “Plasma-assisted ignition and combustion,” *Prog. Energy Combust. Sci.*, vol. 39, no. 1, pp. 61–110, Feb. 2013.

[22] S. M. Starikovskaia, “Plasma-assisted ignition and combustion: Nanosecond discharges and development of kinetic mechanisms,” *J. Phys. D. Appl. Phys.*, vol. 47, no. 35, 2014.

[23] Y. Ju and W. Sun, “Plasma assisted combustion: Dynamics and chemistry,” *Prog. Energy Combust. Sci.*, vol. 48, pp. 21–83, 2015.

[24] F. Auzas, “Décharge radiofréquence produite dans les gaz à pression élevée pour le déclenchement de combustion,” Paris 11, 2008.

[25] V. Prevost, “Autoinflammation de mélanges pauvres assistée par plasma,” Ecole National Supérieur de Méchanique et d’Aérotechnique, 2013.

[26] A. Mariani, F. Foucher, and B. Moreau, “The Effects of a Radio Frequency Ignition System on the Efficiency and the Exhaust Emissions of a Spark-Ignition Engine,” 2013.

[27] A. Mariani and F. Foucher, “Radio frequency spark plug: An ignition system for modern internal combustion engines,” *Appl. Energy*, vol. 122, pp. 151–161, 2014.

[28] D. R. Topham, P. R. Smy, and R. M. Clements, “An investigation of a coaxial spark igniter with emphasis on its practical use,” *Combust. Flame*, vol. 25, pp. 187–195, 1975.

[29] P. R. Smy, R. M. Clements, J. D. Dale, D. Simeoni, and D. R. Topham, “Efficiency and erosion characteristics of plasma jet igniters,” *J. Phys. D. Appl. Phys.*, vol. 16, no. 5, pp. 783–791, May 1983.

[30] C. Letty, A. Pastore, E. Mastorakos, R. Balachandran, and S. Couris, “Comparison of electrical and laser spark emission spectroscopy for fuel concentration measurements,” *Exp. Therm. Fluid Sci.*, vol. 34, no. 3, pp. 338–345, 2010.

[31] I. A. Mulla, S. R. Chakravarthy, N. Swaminathan, and R. Balachandran, “Evolution of flame-kernel in laser-induced spark ignited mixtures: A parametric study,” *Combust. Flame*, vol. 164, pp. 303–318, 2016.

[32] C. Cardin, B. Renou, G. Cabot, and A. M. Boukhalfa, “Experimental analysis of laser-induced spark ignition of lean turbulent premixed flames: New insight into ignition transition,” *Combust. Flame*, vol. 160, no. 8, pp. 1414–1427, 2013.

[33] Marrero Santiago *et al.*, “On the extinction and ignition mechanisms along the ignition events in the KIAI spray burner . A joint experimental and numerical approach,” 2017.

[34] S. A. O’Briant, S. B. Gupta, S. S. Vasu, S. A. O’Briant, S. B. Gupta, and S. S. Vasu, “laser ignition for aerospace propulsion,” *Propuls. Power Res.*, vol. 5, no. 1, pp. 1–21, 2016.

[35] T. X. Phuoc, “Laser-induced spark ignition fundamental and applications,” *Opt. Lasers Eng.*, vol. 44, no. 5, pp. 351–397, May 2006.

[36] R. George, “Développement de nouvelles stratégies d’allumage laser: application à la propulsion aéronautique et/ou spatiale,” Université Paris-Saclay, 2017.

[37] M. Champion, B. Deshaies, G. Joulin, and K. Kinoshita, “Spherical flame initiation: Theory versus experiments for lean propane-air mixtures,” *Combust. Flame*, vol. 65, no. 3, pp. 319–337, Sep. 1986.

[38] A. P. Kelley and C. K. Law, “Nonlinear effects in the extraction of laminar flame speeds from expanding spherical flames,” *Combust. Flame*, vol. 156, pp. 1844–1851, Sep. 2009.

[39] B. Galmiche, “Caractérisation expérimentale des flammes laminaires et turbulentes en expansion,” Université d’Orleans, 2014.

[40] S. McAllister, J.-Y. Chen, and A. C. Fernandez-Pello, *Fundamentals of Combustion Processes*. New York, NY: Springer New York, 2011.

[41] D. R. Ballal and A. H. Lefebvre, “The influence of spark discharge characteristics on minimum ignition energy in flowing gases,” *Combust. Flame*, vol. 24, pp. 99–108, 1975.

[42] J. E. Shepherd, J. C. Krok, and J. J. Lee, “Spark ignition energy measurements in Jet A,” California Institute of Technology, 2000.

[43] J. J. Lee and J. E. Shepherd, “Spark ignition measurements in jet a: part II,” California Institute of Technology, 2000.

[44] S. P. Moffett, S. G. Bhanderi, J. E. Shepherd, and E. Kwon, “Investigation of Statistical Nature of Spark Ignition,” *Fall Meet. theWestern States Sect. Combust. Institute, Sandia Natl. Lab.*, pp. 1–19, 2007.

[45] S. P. M. Bane, J. E. Shepherd, E. Kwon, and A. C. Day, “Statistical analysis of electrostatic spark ignition of lean H2/O2/Ar mixtures,” *Int. J. Hydrogen Energy*, vol. 36, no. 3, pp. 2344–2350, 2011.

[46] S. P. M. Bane, J. L. Ziegler, P. A. Boettcher, S. A. Coronel, and J. E. Shepherd, “Experimental investigation of spark ignition energy in kerosene, hexane, and hydrogen,” *J. Loss Prev. Process Ind.*, vol. 26, no. 2, pp. 290–294, Mar. 2013.

[47] A. Er-raiy, “Étude des processus élementaires impliqués en combustion à volume

constant," Ecole Nationale Supérieure de Mécanique et Aérotechnique, 2018.

[48] R. Maly, "Ignition model for spark discharges and the early phase of flame front growth," *Symp. Combust.*, vol. 18, no. 1, pp. 1747–1754, 1981.

[49] E. Sher and J. C. Keck, "Spark ignition of combustible gas mixtures," *Combust. Flame*, vol. 66, no. 1, pp. 17–25, 1986.

[50] Y. Ko, V. S. Arpaci, and R. W. Anderson, "Spark ignition of propane-air mixtures near the minimum ignition energy: Part II. A model development," *Combust. Flame*, vol. 83, no. 1–2, pp. 88–105, Jan. 1991.

[51] Y. Ko, R. W. Anderson, and V. S. Arpaci, "Spark ignition of propane-air mixtures near the minimum ignition energy: Part I. An experimental study," *Combust. Flame*, vol. 83, no. 1–2, pp. 75–87, Jan. 1991.

[52] M. Anbarasu, D. L. Abata, and P. C. Moilanen, "Modeling of early pressure rise and flame growth in a spark ignition engine," 1994.

[53] M. Akram and E. Lundgren, "The evolution of spark discharges in gases: I. Macroscopic models," *J. Phys. D. Appl. Phys.*, vol. 29, no. 8, p. 2129, 1996.

[54] M. Akram, "The evolution of spark discharges in gases: II. Numerical solution of one-dimensional models," *J. Phys. D. Appl. Phys.*, vol. 29, no. 8, p. 2137, 1996.

[55] M. N. Plooster, "Shock Waves from Line Sources. Numerical Solutions and Experimental Measurements," *Phys. Fluids*, vol. 13, no. 11, p. 2665, 1970.

[56] M. N. Plooster, "Numerical Simulation of Spark Discharges in Air," *Phys. Fluids*, vol. 14, no. 10, p. 2111, 1971.

[57] M. N. Plooster, "Numerical Model of the Return Stroke of the Lightning Discharge," *Phys. Fluids*, vol. 14, no. 10, p. 2124, 1971.

[58] M. Akram, "Two-dimensional model for spark discharge simulation in air," *AIAA J.*, vol. 34, no. 9, pp. 1835–1842, Sep. 1996.

[59] M. Thiele, J. Warnatz, and U. Maas, "2D-Simulation of Ignition Induced by Electrical Discharges," in *SAE Technical Paper Series*, 1999, vol. 1, no. 724.

[60] M. Thiele, S. Selle, U. Riedel, J. Warnatz, and U. Maas, "Numerical simulation of spark ignition including ionization," *Proc. Combust. Inst.*, vol. 28, no. 1, pp. 1177–1185, 2000.

[61] O. Ekici, O. A. Ezekoye, M. J. Hall, and R. D. Matthews, "Thermal and Flow Fields Modeling of Fast Spark Discharges in Air," *J. Fluids Eng.*, vol. 129, no. 1, p. 55, 2007.

[62] R. E. Teets and J. A. Sell, "Calorimetry of ignition sparks," 1988.

[63] F. Collin-Bastiani *et al.*, "DNS of spark-ignition in an anode-cathode configuration: impact of plasma chemical kinetics," in *7th European conference for aeronautics and aerospace sciences*, 2017, pp. 1–12.

[64] F. B. Silsbee, L. B. Loeb, and E. L. Fonseca, "Heat energy of various ignition sparks,

Report No. 56," 1920.

[65] S. Kumagai, T. Sakai, and N. Yasugahira, "Calorimetry of spark energy," *Combust. Sci. Technol.*, vol. 6, no. 4, pp. 233–239, 1972.

[66] W. Roth, P. G. Guest, G. von Elbe, and B. Lewis, "Heat generation by electric sparks and rate of heat loss to the spark electrodes," *J. Chem. Phys.*, vol. 19, no. 12, pp. 1530–1535, 1951.

[67] L. R. Merritt, "A spark calorimeter," *J. Phys. E.*, vol. 11, no. 3, pp. 193–194, 1978.

[68] R. Reinmann and M. Akram, "Temporal investigation of a fast spark discharge in chemically inert gases," *J. Phys. D. Appl. Phys.*, vol. 30, no. 7, p. 1125, 1997.

[69] B. Wolk and I. Ekoto, "Calorimetry and Atomic Oxygen Laser-Induced Fluorescence of Pulsed Nanosecond Discharges at Above-Atmospheric Pressures," in *Ignition Systems for Gasoline Engines*, M. Günther and M. Sens, Eds. Cham: Springer International Publishing, 2016, pp. 169–189.

[70] B. M. Wolk and I. Ekoto, "Calorimetry and Imaging of Plasma Produced by a Pulsed Nanosecond Discharge Igniter in EGR Gases at Engine-Relevant Densities," *SAE Int. J. Engines*, vol. 10, no. 3, Mar. 2017.

[71] G. Discepoli *et al.*, "Experimental assessment of spark and corona igniters energy release," *Energy Procedia*, vol. 148, no. September, pp. 1262–1269, 2018.

[72] R. A. Freeman and J. D. Craggs, "Shock waves from spark discharges," *J. Phys. D. Appl. Phys.*, vol. 2, no. 2, pp. 421–427, Mar. 1969.

[73] Q. Liu and Y. Zhang, "Shock wave generated by high-energy electric spark discharge," *J. Appl. Phys.*, vol. 116, no. 15, p. 153302, 2014.

[74] N. D. Peters, D. M. Coombs, and B. Akih-Kumgeh, "Thermomechanics of laser-induced shock waves in combustible mixtures," *Shock Waves*, vol. 28, no. 5, pp. 1039–1051, 2018.

[75] D. Arnal *et al.*, *Vélocimétrie laser pour la mécanique des fluides*, Lavoisier. Hermes Science, 2012.

[76] S. Barbosa *et al.*, *Métrologie laser pour la mécanique des fluides*, Lavoisier. Hermes Science, 2012.

[77] G. F. W. Ziegler, E. P. Wagner, and R. R. Maly, "Ignition of lean methane-air mixtures by high pressure glow and arc discharges," in *Symposium (International) on Combustion*, 1985, vol. 20, no. 1, pp. 1817–1824.

[78] M. Kono, K. Niu, T. Tsukamoto, and Y. Ujiie, "Mechanism of flame kernel formation produced by short duration sparks," in *Symposium (International) on Combustion*, 1989, vol. 22, no. 1, pp. 1643–1649.

[79] A. Borghese, A. D'Alessio, M. Diana, and C. Venitozzi, "Development of hot nitrogen kernel, produced by a very fast spark discharge," *Symp. Combust.*, vol. 22, no. 1, pp. 1651–1659, Jan. 1989.

[80] D. Verhoeven, “Interferometric spark calorimetry,” *Exp. Fluids*, vol. 28, no. 1, pp. 86–92, 2000.

[81] D. Verhoeven, “Spark heat transfer measurements in flowing gases,” *Rev. l’Institut Français du Pétrole*, vol. 52, no. 4, pp. 453–464, 1997.

[82] A. Dreizler, S. Lindenmaier, U. Maas, J. Hult, M. Aldén, and C. F. Kaminski, “Characterisation of a spark ignition system by planar laser-induced fluorescence of OH at high repetition rates and comparison with chemical kinetic calculations,” *Appl. Phys. B Lasers Opt.*, vol. 70, no. 2, pp. 287–294, Feb. 2000.

[83] M. Thiele *et al.*, “Spark ignited hydrogen/air mixtures: two dimensional detailed modeling and laser based diagnostics,” *Combust. Flame*, vol. 128, no. 1–2, pp. 74–87, 2002.

[84] S. P. M. Bane, J. L. Ziegler, and J. E. Shepherd, “Investigation of the effect of electrode geometry on spark ignition,” *Combust. Flame*, vol. 162, no. 2, pp. 462–469, 2015.

[85] R. Ono, M. Nifuku, S. Fujiwara, S. Horiguchi, and T. Oda, “Gas temperature of capacitance spark discharge in air,” *J. Appl. Phys.*, vol. 97, no. 12, 2005.

[86] B. Sforzo, A. Lambert, J. Kim, J. Jagoda, S. Menon, and J. Seitzman, “Post discharge evolution of a spark igniter kernel,” *Combust. Flame*, vol. 162, no. 1, pp. 181–190, 2015.

[87] C. Lacour *et al.*, “Characterisation of electric discharge in laminar flow with optical diagnostics,” 2016.

[88] B. Singh, L. K. Rajendran, M. Giarra, P. P. Vlachos, and S. P. M. Bane, “Measurement of the flow field induced by a spark plasma using particle image velocimetry,” *Exp. Fluids*, vol. 59, no. 12, p. 0, 2018.

[89] B. Singh, L. K. Rajendran, P. Gupta, C. Scalo, P. P. Vlachos, and S. P. Bane, “Experimental and Numerical Study of Flow Induced by Nanosecond Repetitively Pulsed Discharges,” in *AIAA Scitech 2019 Forum*, 2019, no. January, pp. 1–15.

[90] J. De Dale, M. D. Checkel, and P. R. Smy, “Application of high energy ignition systems to engines,” *Prog. energy Combust. Sci.*, vol. 23, no. 5–6, pp. 379–398, 1997.

[91] A. Franke and R. Reinmann, “Calorimetric Characterization of Commercial Ignition Systems,” in *SAE Technical Paper Series*, 2000, p. 11.

[92] W. Mitianiec, “Factors Determing Ignition and Efficient Combustion in Modern Engines Operating on Gaseous Fuels,” in *Internal Combustion Engines*, InTech, 2012.

[93] A. Kastengren *et al.*, “Time-Resolved X-Ray Radiography of Spark Ignition Plasma,” *SAE Int. J. Engines*, vol. 9, no. 2, pp. 693–703, Apr. 2016.

[94] N. Kawahara, E. Tomita, S. Takemoto, and Y. Ikeda, “Fuel concentration measurement of premixed mixture using spark-induced breakdown spectroscopy,” *Spectrochim. Acta Part B At. Spectrosc.*, vol. 64, no. 10, pp. 1085–1092, 2009.

[95] N. Kawahara, S. Hashimoto, and E. Tomita, “Spark discharge ignition process in a spark-ignition engine using a time series of spectra measurements,” *Proc. Combust. Inst.*, vol.

36, no. 3, pp. 3451–3458, 2017.

[96] H. H. Foster and D. M. Straight, “Effect of ignitor design and ignitor spark-gap environment on ignition in a turbojet combustor,” 1954.

[97] D. Sepulveda and E. E. Striebel, “Starting means for a gas turbine engine,” 4417439, 1983.

[98] D. W. Naegeli and G. D. Lee, “Ignition study in a gas turbine combustor,” *Combust. Sci. Technol.*, vol. 80, pp. 165–184, 1991.

[99] D. L. Blunck, B. V Kiel, L. Goss, and A. Lynch, “Spatial development and temperature of spark kernels exiting into quiescent air,” *J. Propuls. Power*, vol. 28, no. 3, pp. 458–465, 2012.

[100] M. J. Hargather and G. S. Settles, “A comparison of three quantitative schlieren techniques,” *Opt. Lasers Eng.*, vol. 50, no. 1, pp. 8–17, Jan. 2012.

[101] R. Le Dortz, “Détermination des caractéristiques fondamentales de combustion de pré-mélange air-kérosène, de l’allumage à la vitesse de flamme : représentativité de surrogates mono et multi-composants,” ISAE-ENSMA Ecole Nationale Supérieure de Mécanique et d’Aérotechnique, 2018.

[102] G. Hartmann and I. Gallimberti, “The influence of metastable molecules on the streamer progression,” *J. Phys. D. Appl. Phys.*, vol. 8, no. 6, p. 670, 1975.

[103] Q. Michalski, C. J. B. Parejo, A. Claverie, J. Sotton, and M. Bellenoue, “An application of speckle-based background oriented schlieren for optical calorimetry,” *Exp. Therm. Fluid Sci.*, vol. 91, pp. 470–478, 2018.

[104] A. H. Meier and T. Roesgen, “Improved background oriented schlieren imaging using laser speckle illumination,” *Exp. Fluids*, vol. 54, 2013.

[105] G. S. Settles, *Schlieren and Shadowgraph Techniques*. Berlin, Heidelberg: Springer Berlin Heidelberg, 2001.

[106] W. Merzkirch, “Density Sensitive Flow Visualization,” in *Methods in Experimental Physics*, vol. 18, Elsevier, 1981, pp. 345–403.

[107] N. A. Fomin, *Speckle Photography for Fluid Mechanics Measurements*, vol. 11, no. 7. 2002.

[108] W. R. Keagy, H. H. Ellis, and W. T. Reid, “Schlieren techniques for the quantitative study of gas mixing.” p. 69, 1949.

[109] A. B. Gojani, B. Kamishi, and S. Obayashi, “Measurement sensitivity and resolution for background oriented schlieren during image recording,” *J. Vis.*, vol. 16, no. 3, pp. 201–207, 2013.

[110] G. E. Elsinga, B. W. van Oudheusden, and F. Scarano, “Evaluation of aero-optical distortion effects in PIV,” *Exp. Fluids*, vol. 39, no. 2, pp. 246–256, Aug. 2005.

[111] E. D. Iffa, A. R. A. Aziz, and A. S. Malik, “Gas Flame Temperature Measurement Using

Background Oriented Schlieren," *J. Appl. Sci.*, vol. 11, no. 9, pp. 1658–1662, Sep. 2011.

[112] M. Ota, K. Hamada, and K. Maeno, "Quantitative 3D Density Measurment of Supersonic Flow By Colored Grid Background Oriented Schlieren (CGBOS)," in *27th International Congress of the Aeronautical Sciences*, 2010.

[113] F. S. Meidanshahi, K. Madanipour, and B. Shokri, "Measurement of temperature and electrons density distribution of atmospheric arc plasma by moiré deflectometry technique," *Opt. Lasers Eng.*, vol. 51, no. 4, pp. 382–387, Apr. 2013.

[114] A. C. Simmons, "The refractive index and Lorentz-Lorenz functions of propane, nitrogen and carbon-dioxide in the spectral range 15803--22002 cm- 1 and at 944 cm- 1," *Opt. Commun.*, vol. 25, no. 2, pp. 211–214, 1978.

[115] G. Acher, "Three Dimensional Density Measurement using Background Oriented Schlieren," 2014.

[116] A. C. Kak and M. Slaney, *Principles of computerized tomographic imaging*. New York: Institute of Electrical and Electronics Engineers, Inc., 1988.

[117] L. Venkatakrishnan and G. E. A. Meier, "Density measurements using the Background Oriented Schlieren technique," *Exp. Fluids*, vol. 37, no. 2, pp. 237–247, 2004.

[118] E. Goldhahn, O. Alhaj, F. Herbst, and J. Seume, "Quantitative Measurements of Three-Dimensional Density Fields Using the Background Oriented Schlieren Technique," in *Imaging Measurement Methods for Flow Analysis. Notes on Numerical Fluid Mechanics and Multidisciplinary Design*, vol. 106, 2009, pp. 135–144.

[119] V. Todoroff, "Mesure d'un champ de masse volumique par Background Oriented Schlieren 3D. tude d'un dispositif experimental et des methodes de traitement pour la resolution du probleme inverse POUR LA RESOLUTION DU PROBLEME INVERSE. Ecole," Université de Toulouse, 2013.

[120] J. Mcbride, A. Reno, and G. Sanford, "Coefficients for calculating thermodynamic and transport properties of individual species," *Nasa Tech. Memo.*, vol. 4513, p. 98, 1993.

[121] Q. Michalski, "Mise en place d'une technique de mesure de température par BOS," 2015.

[122] A. Bideau-Mehu, Y. Guern, R. Abjean, and A. Johannin-Gilles, "Interferometric determination of the refractive index of carbon dioxide in the ultraviolet region," *Opt. Commun.*, vol. 9, no. 4, pp. 432–434, Dec. 1973.

[123] C. Benito Parejo, Q. Michalski, C. Strozzi, J. Sotton, and M. Bellenoue, "Characterization of Spark Ignition energy transfer by optical and non-optical diagnostics," in *8Th European Combustion Meeting*, 2017.

[124] B. A. Sforzo, "High energy spark ignition in non-premixed flowing combustors," Georgia Institute of Technology, 2014.

[125] B. Sforzo, J. Kim, A. Lambert, J. Jagoda, S. Menon, and J. Seitzman, "High Energy Spark Kernel Evolution: Measurements and Modeling," in *Proceedings of the 8th US National*

Combustion Meeting, 2013.

[126] C. Strozzi, A. Claverie, V. Prevost, J. Sotton, and M. Bellenoue, "HCCI and SICI combustion modes analysis with simultaneous PLIF imaging of formaldehyde and high-speed chemiluminescence in a rapid compression machine," *Combust. Flame*, vol. 202, pp. 58–77, Apr. 2019.

A. Experimental procedure

Experimental procedures are presented step-by-step, showing the tasks and their order to obtain correct measurements for Calorimetry and SBOS at simultaneous experiments, see Table A-1 to Table A-5. Lastly the remarks of some precautionary measures to take into account when performing the experiments.

Test initialization:

Step	Item	Action	
1	Setup (connections)	Check connections and by-pass valve position (open)	
2	Gas bottles and setup	Check connections and pressure	
3	Oscilloscopes, computer	Initialize (turn on, load program WinView32)	
4	Meggitt Signal Amplifier	Turn on, set parameters (gain, sensitivity)	
5	Camera sensor switch	Turn ON (camera covered)	
6	Calibration Process* if needed	(See SBOS Calibration)	
7	Optical setup	Check distances (l, OO', OA, diaphragm opening)	
8	Visualization program WinView32	Set config: gain = 200 Gate width = 1 µs Trigger = external Mode = Acquisition	
9	Spark plug	Check connections, set gap (pin-to-pin electrodes config.)	
10	Vacuum pump	Empty test chamber (By-pass Open)	By-pass OPEN
11	Gas system	Fill test chamber	
12	I probe (CP031)	Offset (Degauss probe) and connection	
13	By-pass Valve	Close	By-pass CLOSED
14	Lights	Turn OFF	
15	Camera cover	Take OFF	
16	Eye Protection!	Put on	Eye-protected
17	Laser	Turn ON (max power, 6.34 (3 W)	Eye-protected

Table A-1: Initialization sequence

Reference test: Reference SBOS pattern

1	Trigger switch	Turn ON (Δt: same as for spark)	Eye-protected
2	WinView32	Acquisition Start	Eye-protected
3	Timing	10 seconds (sensor collecting light)	Eye-protected
4	Trigger	Trigger	Eye-protected
5	WinView32	Save Image (Reference SBOS image)	Eye-protected

Table A-2: Reference image sequence

Test:

1	DC Source	Turn ON	Eye-protected
2	Trigger	Trigger	Eye-protected
3	Oscilloscope	Get spark duration (dt = dt image SBOS)	Eye-protected
4	WinView32	Set: time after trigger = dt image SBOS	Eye-protected
5	WinView32	Acquisition Start	Eye-protected
6	Timing	10 seconds (sensor collecting light)	Eye-protected
7	Trigger	Trigger	Eye-protected
8	Oscilloscope	Save waveforms (p, I, V, image trigger)	Eye-protected
9	WinView32	Save Image (Reference SBOS image)	Eye-protected

Table A-3: Electrical discharge test

1	Laser	Turn off	Eye-protected
2	Camera	Cover	Eye-protected
3	Lights	Turn on (Eye-protection off)	
4	Electrical setup	Turn off	
5	By-pass valve	Open	
6	Vacuum pump	Empty chamber	
7	Gas (room air)	Fill to atmospheric pressure	
8	Data	Save and copy	
9	Computer, oscilloscopes	Turn off	

Table A-4: Test finalization sequence

* SBOS Calibration: At the focal point image should be properly focused, showing no blur.

1	SBOS Calibration	Focal point (OA) and Magnification	
2	Test cell	Position (focal plane, l = 0)	
3	Diaphragm	Open (max diameter)	
4	Visualization program WinView32	Set gain = 0 Gate width = 1 ms Trigger = internal	
5	Camera sensor protection	Take off	
6	Lights	Turn Off	
7	Eye protection!	Put on	Eye-protected
8	Laser	Turn ON, low power (1.1)	Eye-protected
9	Image Acquisition	Start (Focus Mode)	Eye-protected
10	Test cell	Set to fit the best focus on sharp objects (electrode tips, references)	Eye-protected
11	Image Acquisition	Stop and save. M measurement.	Eye-protected
12	Laser	OFF	Eye-protected
13	Camera sensor protection	Put on	Eye-protected
14	Lights	ON	
15	Test cell position	Set as reference (l = 0)	

Table A-5: SBOS calibration sequence

Special cautions:

- By-pass valve and differential pressure transducer: the latter only stands several psi (1 psi ~ 69 mbar) so skipping the opening of the by-pass valve when changing reference pressure would damage the pressure transducer.
- Laser: As it is a class 4 laser (> 500 mW), appropriate eye protection must be used all the time the laser is on.

B. Windows influence on SBOS optical setup

The effect of test cell windows over the SBOS optical setup is estimated. Refraction in the chamber windows modify the optical path and shift the virtual position of the origin of the SBOS signal, changing the defocus distance l.

In our optical setup (Figure 2-8), windows widths (included in the “test cell” in the optical setup figure) are in the order of the characteristic length of the optical setup $l = 80\,mm$. They are considered then as thick windows and their influence on the light path is taken into account. Light beams pass through the inner chamber and the outer chamber windows, which have different refractive index n than air. They are affected by windows between the refraction index variation and the optical sensor, i.e. one window of each chamber. At an electrical discharge, light beams passing through it deviate an angle ε and are then also affected by windows.

Window refraction is represented in Figure B-1: For a light beam with an incident angle α, light refracted inside the window presents an angle $\alpha' = {}^{\alpha}/_{n_w}$(Eq. B.1) where $n_w \sim 1.46$ is window refraction index $\left({}^{n_{gas}}/_{n_w} \cong {}^{1}/_{n_w}\right)$. Height difference between light beam entry to and exit from the window is called δ_0. δ_{01} represents δ_0 without angular deflection. Considering small angles ($\tan\alpha \sim \alpha$) one obtains δ_0 and δ_{01} (equations B.2, B.3):

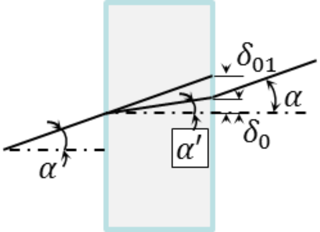

Figure B-1: Window influence on optical path (refraction)

$$\alpha' = {}^{\alpha}/_{n_w} \quad (B.1)$$

$$\delta_{01} \cong e_w \alpha \quad (B.2)$$

$$\delta_0 \cong e_w \alpha' = e_w\, {}^{\alpha}/_{n_w} \quad (B.3)$$

Applying this principle to an optical setup we find that a single window of thickness e_w produces a shift on the virtual image along the z axis l_w. Figure B-2 represents the optical setup with one window, a lens and electrodes at the position of an electrical discharge -and the origin or light path- A_1. Projecting the δ difference to find the virtual point A_0 and the y difference Δ_w, the observed point $A_1{}'$ is displaced a distance δ_w from the original observed point –without window influence- $A_0{}'$.

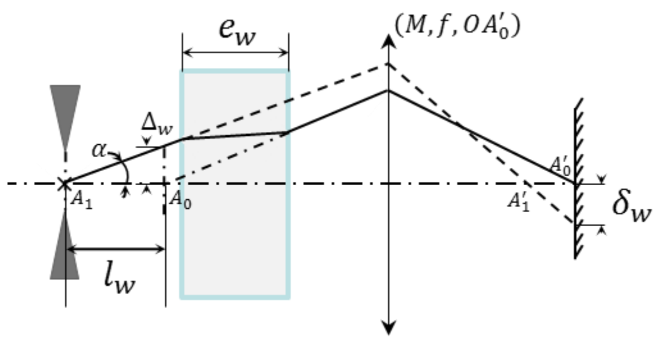

$$\delta_w = \Delta_w M \quad (B.4)$$

$$\Delta_w = \delta_{01} - \delta_0 = \alpha e_w \left(1 - \frac{1}{n_w}\right) = \alpha\, l_w \quad (B.5)$$

Figure B-2: Window influence on optical path and focal point

An electrical discharge will deflect the light an angle ε. The observed shift related to the change in refraction index and due to the window (Figure B-3) is called $\delta_{w\varepsilon}$ and estimated in equation B.6:

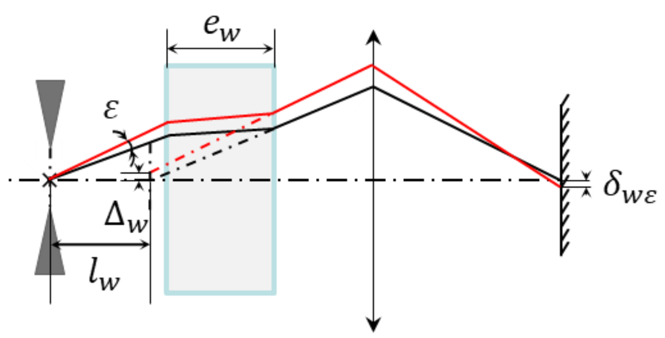

$$\delta_{w\varepsilon} = M\varepsilon e_w \left(1 - \frac{1}{n_w}\right) \quad (B.6)$$

Figure B-3: Window effect on optical path after angle deviation

For the SBOS technique, the origin of the optical signal is displaced a defocus distance (l) to obtain better sensitivity. The displacement of the origin A_1 to A_0 due to windows changes the effective defocus distance l.

We calculated the influence of two windows $W_1$and W_2 of thickness e_1 and e_2 over the SBOS optical setup we used. Figure B-4 represents the light path. S represents the spark point, O and O' the lenses, and D and C the diaphragm and the camera, respectively. $S_1$and S_2 are the apparent S point after W_1 and W_2 deviations, as in the detailed zoom of Figure B-5. The estimation is done for both $M = -0.5$ and $M = -1$, using optic equations B.7, B.8 and B.9.

$$\frac{1}{OB'} = \frac{1}{OB} + \frac{1}{f} \quad (B.7)$$

$$M = \frac{OB'}{OB} \quad (B.8)$$

$$M = \frac{f}{l + m - f} \quad (B.9)$$

For a magnification $M = -1$ optical setup is represented in Figure B-4. Reference SBOS light path is represented as a blue line with an initial angle α. SBOS test light path is the orange line, with an angle $\alpha + \varepsilon$. The lens O is at the origin of the z axis. $S = -250 = l + OA$, where $l = -80\,mm$ is the defocus distance and OA is the distance from the focal point to A to O. Internal window W_1 is at $S + 12$ and is 6 mm thick (e_1). Internal window W_2 is at $S + 33$ and is 30 mm thick (e_2). Window refraction index is $n_w = 1.458$. Lens O' is at $OO' = 492\,mm$, and the camera at $OA' = 992\,mm$. Diaphragm is at $OD = 447$ mm. Diaphragm opening is set as 5 mm and limits the maximum initial angle α and deflection ε.

Windows W_1 and W_2 shift the origin S to virtual points S_1 (due to W_1) and S_2 (W_2). Figure B-5 details this displacement. The virtual points are projected on the camera plane, and the displacement δ caused by the initial ε is obtained. The effective distance $l + \Delta l$ is related to δ and ε by equation B.10 (from Eq.(4.7), §4.1.2), as Δl represents the distance shift caused by windows:

$$\vec{\delta} = (l + \Delta l)M\vec{\varepsilon} \quad \text{(B.10)}$$

For different initial angle α and angular deviation ε, Δl was $\Delta l = 11.46\,mm$. For the $M = -0{,}5$ optical setup represented in Figure B-6 (where $S = -330$, $l = -160$, $OO' = 942$, $OD = 889$, $OA' = 1342$, and same window relative position to S and thicknesses), $\Delta l = 11.5\,mm$, similar to the $M = -1$ setup as window relative position are similar.

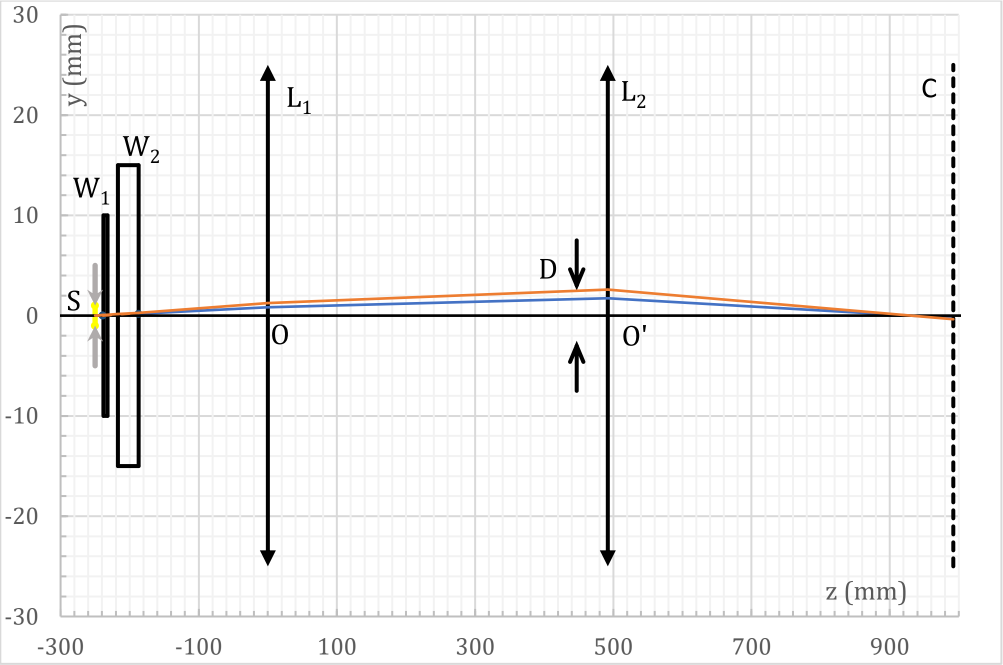

Figure B-4: Optical setup scheme for magnification M = -1. Y and Z axis in mm, in different scales for a better visualization. In blue the reference light path and in orange the light path deflected an angle ε by the spark.

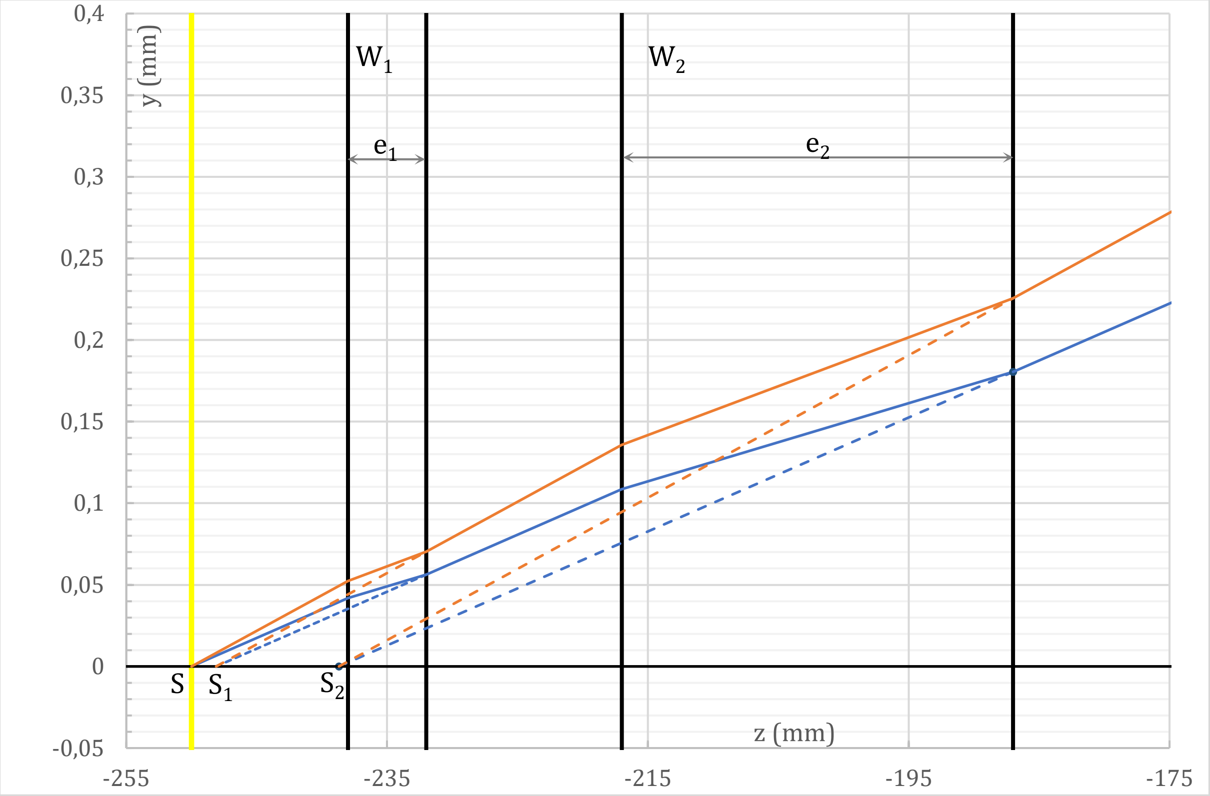

Figure B-5: Detail of window influence on light beams, zoomed at the window passage. Dashed lines represent virtual projections.

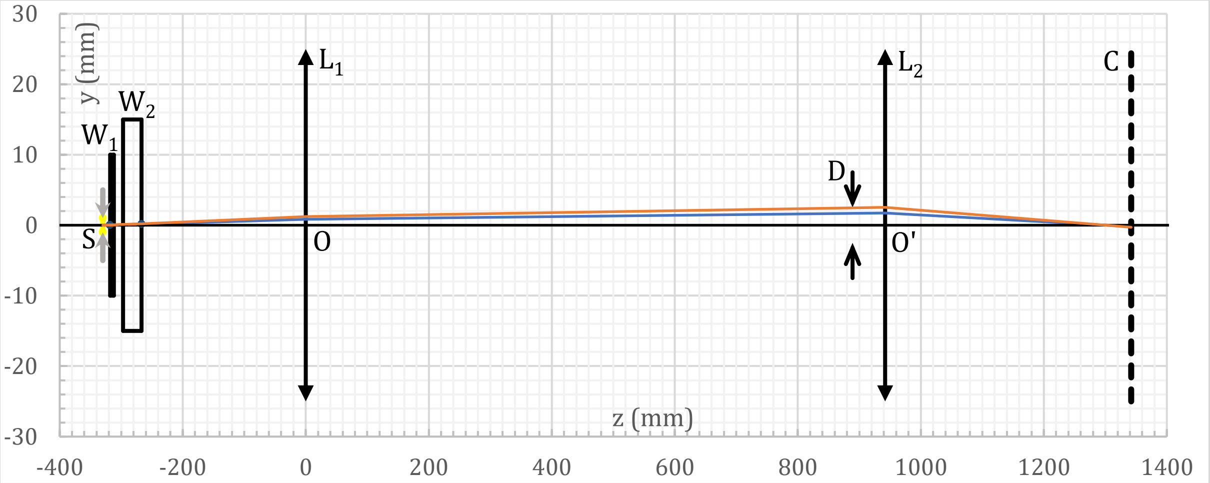

Figure B-6: Optical setup for magnification M = -0.5

This shift Δl not only affects the origin of the optical signal S, but also the setup focal point A. Experimentally, A is determined focusing a sharp image at the test cell (electrode tips), with and without windows installed. Focal point position with windows is $\sim 13\,mm$ further $(\Delta z = -13\,mm)$, which corresponds to calculated shift Δl. As the reference point A shifted, the defocus is produced from that point.

To correct this shift, a new reference point A is chosen with windows installed on the chamber, and then defocus distance l is measured from that point. Experimentally, the same displacement field was observed for the same defocus distance with and without windows.

C. Boundary conditions at the electrode masks: a practical solution.

The application of Neumann Boundary Conditions (BC) at the electrode locations presents difficulties. The 5-point stencil of equation (4.19) was used to integrate the Poisson equation, as mentioned in §4.2.3. For the 5 point stencil, Neumann Boundary Conditions are applied setting the value of the points next to the wall inside it to the value of the points out next to the wall outside it after every iterative step of the integration; i.e., after applying equation (4.19) to obtain $u_{i,j}|^{(n+1)}$ the BC is applied by setting: $u_{int\,pts}|^{(n+1)} = u_{ext\,pts}|^{(n+1)}$ where *int pts* are interior points next to the wall and *ext pts* are exterior points next to the wall. For a vertical wall, this is pictured in Figure C-1, where the BC results as $u_{\square}|^{(n+1)} = u_{\triangle}|^{(n+1)}$.

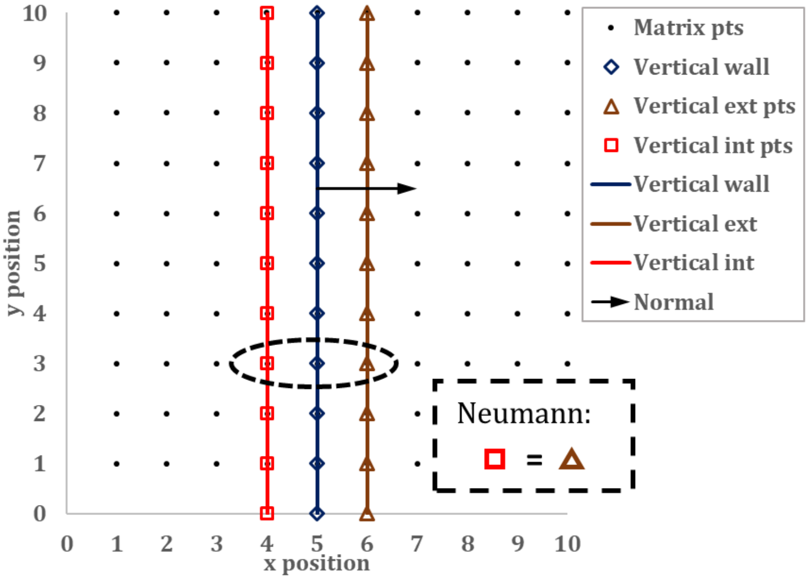

Figure C-1: Neumann Boundary Condition on a vertical wall

If the wall is neither vertical nor horizontal, the points of the wall are represented by the matrix points closer to the real wall location. The interior and exterior points are approximated in the same way, as represented in Figure C-2. Applying the BC requires assigning the exterior point that corresponds to each interior point by either approximating the normal for each point or through interpolation of different exterior points by proximity to the real point location. In our case, we assigned the corresponding pairs approximating the normal to the wall, as in the Figure C-2. In this case, the BC is applied as $u_{\blacksquare}|^{(n+1)} = u_{\blacktriangle}|^{(n+1)}$ in the figure for each point next to the wall in the matrix.

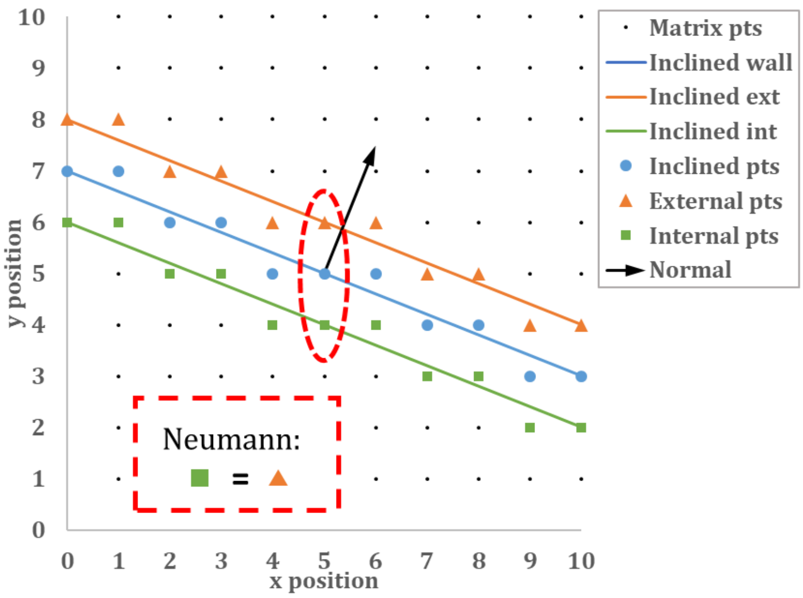

Figure C-2: Neumann BC on an inclined wall

The difficulties arise when applying the BC to a corner. The electrode masks, as explained in chapter 4, represent the electrodes without the blur in the edges originated by the SBOS acquisition process. The electrode masks are thus truncated at the tips. The top corner of the electrode tip is then the intersection of an inclined wall (the electrode cone) and a vertical wall (the truncated tip). Figure C-3represents the corner of the electrode tip as the points of the matrix that correspond to the mask. If we tried to apply the BC at the corner, the interior points of both walls would be assigned to multiple values causing singularities, as $u_{\square}|^{(n+1)} = u_{\triangle}|^{(n+1)}$ and $u_{\blacksquare}|^{(n+1)} = u_{\blacktriangle}|^{(n+1)}$.

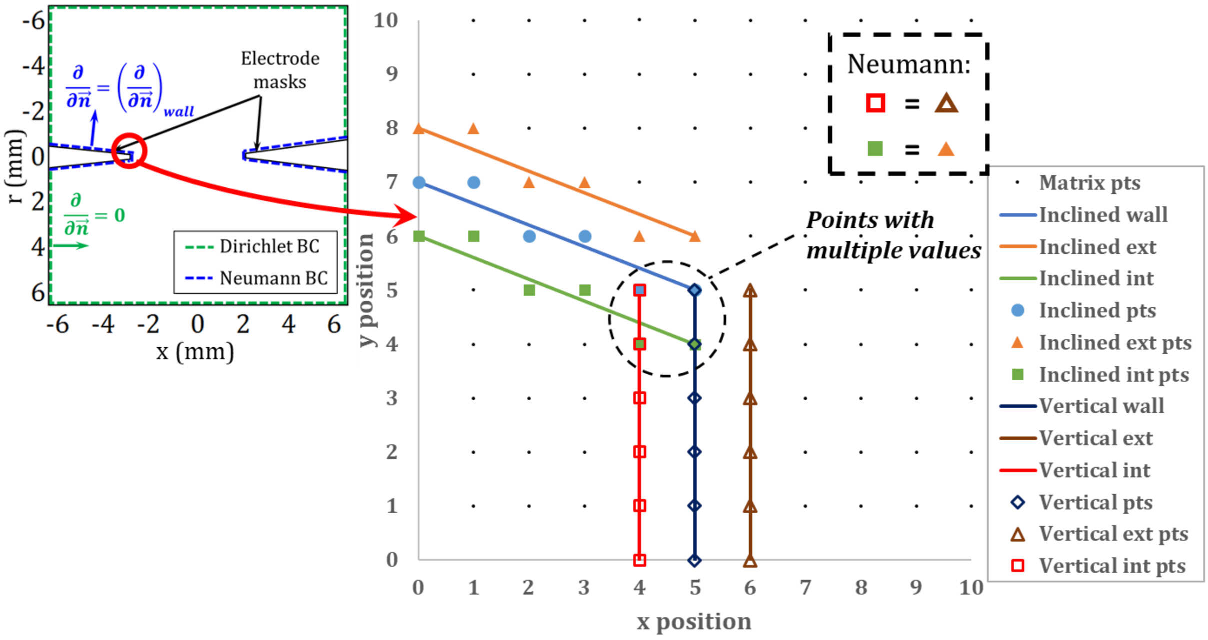

Figure C-3: Neumann BC applied to a corner

Then it is not possible to apply the BC as it is to the corner. We chose to change the assignation of the values to reduce this effect at the corner. Thus, the applied BC was inverted, to apply the values inside the wall to the points outside the wall: $u_{\triangle}|^{(n+1)} = u_{\square}|^{(n+1)}$ and $u_{\blacktriangle}|^{(n+1)} = u_{\blacksquare}|^{(n+1)}$. The influence of this BC on the integration was estimated comparing the effect on a single wall. The resulting field reached similar values, with a difference at the matrix points next to the wall: a 3-point-thickness layer separated the wall and the solution. Comparison of the integrated field using Neumann BC and the modified one showed good agreement of the results.

Other solutions to this problem would be the use of immersed BC or the application of different BC. The proximity of the strong density gradients in the discharge kernel to the electrodes prevented us from employing immersed BC. Another BOS study [89] employed a long inter-electrode gap (5 mm) in their setup, and employed images of the inter-electrode gap that contained the whole kernel. Then they applied Dirichlet BC at the borders of the image, which excluded the electrodes. This solution is not useful in our case, where the discharge kernel surrounds the electrode tips so truncation of the electrode tips would truncate a substantial portion of the kernel.

The Boundary Conditions discussed here was applied to solve the Poisson integration for the pin-to-pin electrodes setup, then for the results presented in Chapter 4. For the helicopter igniter, as presented in Chapter 5, the Neumann BC was applied along the frontal electrode surface, with no modification.

Abstract

Spark ignition systems are generally defined by the electrical energy input used to operate them. However, the physical characteristic that directly affects the ignition process is the energy deposit supplied to the fluid by the system. This work focuses on the development of two proposed methodologies for the characterization of the thermal energy deposit of electrical discharges produced by different ignition systems, and their implementation through a parametric study. An experimental device is developed for this purpose, using simultaneously a non-optical and an optical technique. The experimental techniques are first validated in a reference configuration: a pair of pin-to-pin electrodes with an automobile-type inductive ignition system.

Constant volume calorimetry measures a thermal energy deposit supplied to the fluid via the pressure rise inside a reduced volume chamber. The ratio between thermal energy deposit and electrical energy supply represents the efficiency of energy transfer, which is between 15 and 40% for the reference configuration. Energy deposit and efficiency are higher as pressure and inter-electrode gap increase. Tests with an inert propane-nitrogen mixture show that energy deposit is greater in the presence of fuel than in clean air.

SBOS (Speckle-based Background-Oriented Schlieren) is an optical method that quantifies changes in the optical index generated by the phenomenon under study. This technique has been adapted to the spatial and temporal specificity of an electrical discharge. Image-processing procedure has been developed to obtain density, temperature and local energy fields at the time of image acquisition. The volume of the hot kernel produced by the plasma and the energy deposit are deduced from it. These properties are measured at different times during the evolution of the kernel. Temperatures in the hot kernel reach higher values (up to 1400 K) at longer inter-electrode gaps and higher pressures, or in the presence of gaseous fuel. Energy deposit measurements performed by SBOS are in good agreement with calorimetry results.

Finally, both methodologies are adapted to the study of different ignition systems. Two igniters were tested: an innovative multi-filament radiofrequency discharge igniter and a capacitive helicopter engine igniter. For the latter, the energy deposit is measured for different initial pressures and gas mixtures to simulate the actual engine conditions. The electrical energy input is 2 J, the electrical energy measured at the electrodes is 625 mJ and finally the thermal energy deposited in the gas is about 85 mJ. The estimated efficiency of 14% is not very pressure dependent. The SBOS technique is used to estimate the temperature in the hot kernel at the first moments of discharge (around 3700 K) and the thermal energy deposit, which is in good agreement with the calorimetric measurement.

Keywords: Electrical discharge, energy transfer, spark ignition, calorimetry, SBOS, aircraft igniter.

Résumé

Les systèmes d'allumage par étincelle sont généralement définis par l'énergie électrique utilisée pour leur fonctionnement. Cependant, la caractéristique physique qui affecte directement le processus d'allumage est l'énergie déposée dans le fluide par le système. Ce travail porte sur le développement de deux méthodologies proposées pour la caractérisation du dépôt d'énergie thermique de décharges produites par différents systèmes d'allumage et de leur mise en œuvre au travers d'une étude paramétrique. Un dispositif expérimental est mis au point afin de développer et mettre en œuvre simultanément une technique optique et une non optique. Les méthodes sont validées d'abord dans une configuration de référence d'un allumeur inductif alimentant une paire d'électrodes pointe-pointe.

La calorimétrie à volume constant mesure un dépôt d'énergie thermique fournie au fluide par l'analyse de la montée en pression à l'intérieur d'une chambre de petit volume. Le rapport entre le dépôt d'énergie thermique et l'apport d'énergie électrique représente l'efficacité du transfert d'énergie, qui est comprise entre 15 et 40% pour la configuration de référence. Le dépôt d'énergie et l'efficacité du transfert d'énergie sont plus élevés à mesure que la pression et l'écart inter-électrode augmentent. Des essais avec un mélange inerte azote-propane montrent que le dépôt d'énergie est plus important en présence de carburant que dans l'air pur.

La SBOS (Speckle-based Background-Oriented Schlieren) est une méthode optique permettant de quantifier les variations d'indice optique générés par le phénomène étudié. Cette technique est ici adaptée aux contraintes d'échelles spatiale et temporelle d'une décharge électrique. Une procédure de traitement a été développée afin d'obtenir les champs de masse volumique, de température et l'énergie locale au moment de l'acquisition de l'image. Le volume du noyau chaud produit par le plasma et le dépôt d'énergie en sont déduits. Ces propriétés sont mesurées à différents instants de l'évolution du noyau. Dans la configuration de référence, les températures dans le noyau chaud atteignent des valeurs plus élevées (jusqu'à 1400 K) pour des distances inter-électrodes et des pressions plus élevées ou en présence de carburant. Des mesures simultanées de dépôt d'énergie par SBOS et calorimétrie montrent un très bon accord.

Enfin, les deux méthodologies sont adaptées à l'étude de différents systèmes d'allumage. Ainsi, deux allumeurs ont été testés, un allumeur à décharge radiofréquence multi filamentaires innovant et un allumeur capacitif typique d'un moteur d'hélicoptère. Pour ce dernier, le dépôt d'énergie est mesuré pour différentes pressions initiales et mélanges gazeux afin de simuler les conditions réelles du moteur. Dans des conditions standard, l'énergie électrique est de 2 J, l'énergie électrique mesurée aux électrodes de 625 mJ et enfin l'énergie thermique déposée dans le gaz de l'ordre de 85 mJ. Le rendement du 14% semble peu dépendant des conditions thermodynamiques du mélanges. La technique SBOS est utilisée pour estimer la température dans le noyau chaud aux premiers instants de la décharge (jusqu'á 3700 K) et le dépôt d'énergie thermique qui est en bon accord avec la mesure calorimétrique.

Mots-clés : Décharge électrique, allumage par étincelle, transfert d'énergie, calorimétrie, SBOS, allumeurs aéronautiques.